MPM SCIENTIFIC JOURNAL

ISSN 1605-2730
E-ISSN 1605-8119

MATERIALS PHYSICS AND MECHANICS

Vol. 52, No. 5, 2024

MATERIALS PHYSICS AND MECHANICS

"Materials Physics and Mechanics" Editorial Office:
Phone: +7(812)552 77 78, ext. 224 **E-mail:** mpmjournal@spbstu.ru **Web-site:** http://www.mpm.spbstu.ru

International scientific journal "**Materials Physics and Mechanics**" is published by Peter the Great St. Petersburg Polytechnic University in collaboration with Institute for Problems for Mechanical Engineering in the Russian Academy of Sciences in both hard copy and electronic versions. The journal provides an international medium for the publication of reviews and original research papers written in English and focused on the following topics:

- Mechanics of composite and nanostructured materials.
- Physics of strength and plasticity of composite and nanostructured materials.
- Mechanics of deformation and fracture processes in conventional materials (solids).
- Physics of strength and plasticity of conventional materials (solids).
- Physics and mechanics of defects in composite, nanostructured, and conventional materials.
- Mechanics and physics of materials in coupled fields.

Owner organizations: Peter the Great St. Petersburg Polytechnic University; Institute of Problems of Mechanical Engineering RAS.

Materials Physics and Mechanics is indexed in Chemical Abstracts, Cambridge Scientific Abstracts, Web of Science Emerging Sources Citation Index (ESCI) and Elsevier Bibliographic Databases (in particular, SCOPUS).

МЕХАНИКА И ФИЗИКА МАТЕРИАЛОВ

Materials Physics and Mechanics

Том 52, номер 5, 2024 год

Учредители:
ФГАОУ ВО «Санкт-Петербургский политехнический университет Петра Великого»
ФГБУН «Институт проблем машиноведения Российской академии наук»

Тел.: +7(812)552 77 78, доб. 224 **E-mail:** mpmjournal@spbstu.ru **Web-site:** http://www.mpm.spbstu.ru

Тематика журнала

Международный научный журнал "Materials Physics and Mechanics" издается Санкт-Петербургским политехническим университетом Петра Великого в сотрудничестве с Институтом проблем машиноведения Российской академии наук в печатном виде и электронной форме. Журнал публикует обзорные и оригинальные научные статьи на английском языке по следующим тематикам:

- Механика композиционных и наноструктурированных материалов.
- Физика прочности и пластичности композиционных и наноструктурированных материалов.
- Механика процессов деформации и разрушения в традиционных материалах (твердых телах).
- Физика прочности и пластичности традиционных материалов (твердых тел).
- Физика и механика дефектов в композиционных, наноструктурированных и традиционных материалах.
- Механика и физика материалов в связанных полях.

Редколлегия принимает статьи, которые нигде ранее не опубликованы и не направлены для опубликования в другие научные издания. Все представляемые в редакцию журнала "Механика и физика материалов" статьи рецензируются. Статьи могут отправляться авторам на доработку. Не принятые к опубликованию статьи авторам не возвращаются.

Журнал "Механика и физика материалов" ("Materials Physics and Mechanics") включен в систему цитирования Web of Science Emerging Sources Citation Index (ESCI), SCOPUS и РИНЦ.

Contents

MATERIALS PHYSICS AND MECHANICS RESEARCH ARTICLE

Submitted: October 6, 2024 Revised: October 29, 2024 Accepted: November 20, 2024

Determination of the contribution of an imperfectly bonded inhomogeneity to macroscopic diffusivity

K.P. Frolova [1]✉, **N.M. Bessonov** [1], **E.N. Vilchevskaya** [2]

[1] Institute for Problems in Mechanical Engineering RAS, St. Petersburg, Russia

[2] Flugsnapparegatan 6, Mölndal, Sweden

✉ fkp@ipme.ru

ABSTRACT

The paper contributes to the development of micromechanical approaches for determining the effective diffusivity of micro-heterogeneous materials, taking into account segregation, which is the accumulation of impurities at the phase interface. Two analytical approaches are investigated and compared with numerical simulation. In the first analytical approach, segregation is expressed in terms of a segregation parameter that prescribes the jump in concentration at the phase interface. In the second approach, an inhomogeneity with an ultra-thin mass isolating coating is introduced, and segregation is expressed in terms of equivalent surface resistivity. The developed numerical method considers inhomogeneities with an outer weakly permeable shell of thickness that tends to zero. Comparison among various models made it possible to estimate their limitations and perspectives.

KEYWORDS

effective properties • imperfect contacts • segregation • diffusion • homogenization problem

Acknowledgements. *The reported study was funded by Russian Science Foundation, Grant No. 23-79-01133 (https://rscf.ru/project/23-79-01133/).*

Citation: Frolova KP, Bessonov NM, Vilchevskaya EN. Determination of the contribution of an imperfectly bonded inhomogeneity to macroscopic diffusivity. *Materials Physics and Mechanics*. 2024;52(5): 1–17. http://dx.doi.org/10.18149/MPM.5252024_1

Introduction

Determination of the effective diffusivity of micro-heterogeneous materials is one of advanced problems in mechanics. Indeed, the internal structure of a material affects its permeability and, as a result, the total amount of a diffusing substance. The accumulation of harmful impurities, in turn, can lead to the degradation of the mechanical properties of materials [1–5]. Therefore, a comprehensive analysis of the influence of microstructure on macroscopic diffusivity is of great importance. One of the problems of fundamental interest in this area is the issue of accounting for segregation that is accumulation of impurities along the phase interface [6,7]. Typically, the effective properties of various natures are determined within classical micromechanical approaches, which assume that fields at the phase interface are continuous. However, the presence of segregation disrupts the continuity of the concentration field at the internal boundaries of heterogeneous materials [8]. In this case, the phase interface becomes “imperfect” and surface effects must be taken into account [9,10].

Only a small number of works are dedicated to accounting for the presence of imperfect contacts at the phase interface within micromechanical models. In [9,11–16], diffusivity problem was investigated and segregation was accounted for in terms of a segregation parameter, which is the ratio of concentrations on the outer and inner sides of the inhomogeneity boundary. Thus, in this approach, a jump in concentration across the phase interface is prescribed. In [12,13], the segregation parameter was introduced in the modified effective media homogenization method. In [14,16], it was incorporated into effective field methods expressed in terms of property contribution tensors that reflect the contribution of individual inhomogeneities to the property of interest. Another approach to account for imperfect interfaces involves considering inhomogeneities with an interface possessing extreme properties. Usually such an approach is used within conductivity problem [9,17–25]. Within the approach some models express jump in the field in terms of surface conductivity [17–22], whereas another models consider an ultra-thin outer shell and realize limit transitions [9,23–25]. Note that in the context of the diffusivity process accompanied by segregation, the coating should function as an insulator. Consequently, segregation can be expressed within this approach in terms of equivalent surface diffusion resistivity. The question of the most appropriate approach to account for segregation remains open.

The problem of analytical determination of effective diffusivity consists of two parts: solution of one-particle problem and application of this solution within some homogenization scheme to account for the presence of multiple inhomogeneities [26]. The problem of a single inhomogeneity placed in an infinite matrix is known as the (second) Eshelby problem [27], which originally refers to elasticity under assumption on perfect phase interfaces. Solution of the Eshelby problem for conductivity in the case of perfect contacts was derived by Fricke [28].

In general, the presence of imperfect phase interfaces must be taken into account at both steps. In [29,30], we compared the analytical solution of the first part of the problem obtained using two aforementioned approaches for accounting for imperfect contacts: the approach in which segregation is expressed in terms of a segregation parameter and the approach in which segregation is expressed in terms of equivalent surface resistivity. In particular, it was shown that, for certain parameters of the internal structure, the results obtained within the two approaches exhibit significant qualitative differences that can be quite consequential. A detailed investigation of these differences was beyond the scope of papers [29,30]. In the present research, we further develop the numerical method to account for imperfect contacts and compare the analytical solutions with the numerical results. Such a comparison could facilitate an analysis of the qualitative differences between the two analytical approaches and help in answering the question of which approach is most accurate. Additionally, numerical simulation may help in overcoming difficulties related to the complexity of solving the problem for inhomogeneities with a non-spherical shape and, more generally, with non-ellipsoidal shapes. Unlike spherical inhomogeneities, ellipsoidal and even spheroidal inhomogeneities have imperfect interfaces of non-constant curvature, which complicates the introduction of an outer shell of constant thickness within the corresponding analytical approach, making it less physically justifiable. Furthermore, an analytical solution for a single inhomogeneity embedded in an infinite matrix exists only for ellipsoidal inhomogeneities. However, considering irregular shapes is often necessary for accurately modeling real materials.

Single inhomogeneity problem

Effective properties of micro-heterogeneous materials can be expressed in terms of various microstructural parameters. In the present research, we follow [26] and consider property contribution tensors, the sum of which serves as a relevant microstructural parameter reflecting the contributions of individual inhomogeneities to the macroscopic property of interest. This takes into account physical and geometrical characteristics of inhomogeneities, such as properties, shape, and orientation in the matrix. The property contribution tensor is to be derived from the solution of the single inhomogeneity problem, while the effective properties of the material can be determined using a homogenization scheme written in terms of the corresponding microstructural parameters. We will focus on the first part of the problem of determining effective properties by introducing the diffusivity contribution tensor of a single ellipsoidal inhomogeneity with an imperfect boundary.

Let us consider the representative volume element (RVE) V, which is a typical point of continuum at the macro level, consisting of an isotropic ellipsoidal inhomogeneity with volume $V_1 << V$ and diffusivity $\mathbf{D}_1 = D_1\mathbf{I}$, along with an isotropic matrix with diffusivity $\mathbf{D}_0 = D_0\mathbf{I}$. We seek the solution of a stationary diffusion problem in the absence of inner sources and under the assumption on linear constitutive relations in each phase of the heterogeneous material:

$$\nabla \cdot \mathbf{J}(\mathbf{r}) = 0,\ \ \mathbf{J}(\mathbf{r}) = -\,\mathbf{D}(\mathbf{r}) \cdot \nabla c(\mathbf{r}), \tag{1}$$

where $\mathbf{r}$ is the position vector, $\mathbf{J}$ is the diffusion flux, c is the concentration, $\mathbf{D}(\mathbf{r}) = D_0\mathbf{I}$ if $\mathbf{r}$ belongs to the matrix and $\mathbf{D}(\mathbf{r}) = D_1\mathbf{I}$ if $\mathbf{r}$ is in the inhomogeneity.

The macroscopic properties must be independent on the type of the boundary conditions (BCs) prescribed on the boundary Σ of the RVE. Therefore, any BCs can be used. It is convenient to work with uniform BCs within analytical approaches. In the case of prescribed concentration, these are defined as follows:

$$c(\mathbf{r})|_\Sigma = \mathbf{G}_0 \cdot \mathbf{r}, \tag{2}$$

where $\mathbf{G}_0$ is a constant vector. $\mathbf{G}_0$ also represents a uniform field that would exist everywhere in the RVE in the absence of inhomogeneity. In this case, first, effective properties are automatically compatible with their definition in energy terms [26], and second, the averaged concentration gradient coincides with $\mathbf{G}_0$ ($\langle \nabla \mathrm{c}(\mathbf{r}) \rangle_V = \mathbf{G}_0$). In the same manner, one could consider uniform BCs for the normal component of the flux.

We assume that the material satisfies linear constitutive relations, so the flux and concentration gradient at the continuum point are related by classical Fick's law through the effective diffusivity tensor $\mathbf{D}^{eff}$:

$$\langle \mathbf{J} \rangle_V = -\mathbf{D}^{eff} \cdot \langle \nabla \mathrm{c} \rangle_V, \tag{3}$$

here $\langle \ldots \rangle_V = \int_V \ldots dV$ denotes averaging over the RVE, and the averaged field values correspond to values at a continuum point at the macro-level.

In the linear case, the volume average of the diffusion flux can be represented as follows [14]:

$$\langle \mathbf{J} \rangle_V = -\mathbf{D}_0 \cdot \mathbf{G}_0 + \Delta \mathbf{J}, \tag{4}$$

where $\Delta \mathbf{J}$ is an additional flux caused by the presence of the inhomogeneity that can be expressed in terms of the diffusivity contribution tensor $\mathbf{H}$ such that

$$\Delta \mathbf{J} = -\frac{V_1}{V} \mathbf{H} \cdot \mathbf{G}_0. \tag{5}$$

Hence,

$$\mathbf{D}^{eff} = \mathbf{D}_0 + \frac{V_1}{V}\mathbf{H}, \tag{6}$$

here the effective diffusivity tensor can generally be orthotropic. In the case of isotropy of the phases' material, the overall anisotropy is induced solely by the shape of the inhomogeneity. Specifically, for ellipsoidal shapes, the tensor is orthotropic; for spheroidal shapes, it exhibits transverse isotropy; and it becomes isotropic in the case of a sphere.

Diffusivity contribution tensors of inhomogeneities with imperfect contacts caused by segregation, modeled in different ways, differ from one another. We will now discuss a few mathematical models of imperfect contact and introduce corresponding property contribution tensors.

Diffusivity contribution tensors

Within the framework of the present paper, we consider two analytical approaches for modeling segregation. The first approach involves prescribing a jump in the concentration field, while the second approach considers an inhomogeneity with an ultra-thin isolating coating. For further details, we refer to our previous works [16,29,30] as well as the works of Levin and Markov [24,25]. Below, we briefly outline the main ideas and provide the key formulas associated with each approach.

In both analytical approaches, the diffusivity contribution tensor can be expressed in terms of the concentration tensor of concentration gradient $\mathbf{\Lambda}$, which linearly relates the field inside the inhomogeneity to the applied one ($\nabla c(\mathbf{r}) = \mathbf{\Lambda}(\mathbf{r}) \cdot \mathbf{G}_0$ when $\mathbf{r}$ belongs to inhomogeneity). The presence of imperfect contacts must be considered at two stages within the homogenization problem: during the averaging of fields as presented in Eq. (3), and when calculating the concentration tensor. Both the averaging procedure and the determination of the concentration tensor are influenced by the geometry of the internal boundaries and the boundary conditions applied to them. Consequently, the property contribution tensors obtained within the two approaches are expressed in terms of different variables that account for the effects of imperfect contacts.

In the first analytical approach to accounting for imperfect contacts, the influence of these contacts is modeled using a segregation parameter s_c, defined as the ratio of the concentration values on the outer and inner sides of the interface Γ between the matrix (+) and the inhomogeneity (-). The geometry of the inhomogeneity in the ($\mathbf{e}_1$, $\mathbf{e}_3$) plane is shown in Fig. 1. So, the following boundary conditions hold:

$$D_0 \frac{\partial c(\mathbf{r})}{\partial n_\Gamma}\bigg|_{r\to\partial\Gamma+} = D_1 \frac{\partial c(\mathbf{r})}{\partial n_\Gamma}\bigg|_{r\to\Gamma-}, c(\mathbf{r})|_{r\to\Gamma+} = s_c c(\mathbf{r})|_{r\to\Gamma-}, \tag{7}$$

where $\mathbf{n}_\Gamma$ is the outer normal vector to Γ. Note that the jump in concentration can be calculated as $[c] = (s_c - 1)c(\mathbf{r})|_{r\to\Gamma-}$.

The averaged fields are as follows:

$$\langle\nabla c\rangle_V = \left(1 - \frac{V_1}{V}\right)\langle\nabla c\rangle_{V_0} + s_c\frac{V_1}{V}\langle\nabla c\rangle_{V_1}, \langle\mathbf{J}\rangle_V = \left(1 - \frac{V_1}{V}\right)\langle\mathbf{J}\rangle_{V_0} + \frac{V_1}{V}\langle\mathbf{J}\rangle_{V_1}, \tag{8}$$

here $\langle \dots \rangle_{V_0} = \int_{V_0} \dots \mathrm{d}V_0$ represents the averaging over the volume V_0 of the matrix, while $\langle \dots \rangle_{V_1} = \int_{V_1} \dots \mathrm{d}V_1$ denotes the averaging over the volume of the inhomogeneity.

Diffusivity contribution tensor can be found then by the following equation:

$$\mathbf{H} = (D_1 - s_c D_0)\mathbf{\Lambda}_c, \tag{9}$$

where constant concentration tensor $\mathbf{\Lambda}_c$ ($\langle\nabla c\rangle_{V_1} = \mathbf{\Lambda}_c \cdot \mathbf{G}_0$) of an ellipsoidal inhomogeneity is as follows:

$$\mathbf{\Lambda}_c = \sum_{j=1}^{3} \frac{\mathbf{1}}{s_c\left(1 + A_j\left(\frac{D_1}{s_c D_0} - 1\right)\right)} \mathbf{e}_j \mathbf{e}_j, \tag{10}$$

here

$$A_j = a_1 a_2 a_3 \int_0^\infty \left(p + a_j^2\right)^{-1} \Big/ \left(2\sqrt{(p + a_1^2)(p + a_2^2)(p + a_3^2)}\right) dp, \tag{11}$$

where a_1, a_2, a_3 are the lengths of the semi-axes of the ellipsoidal inhomogeneity.

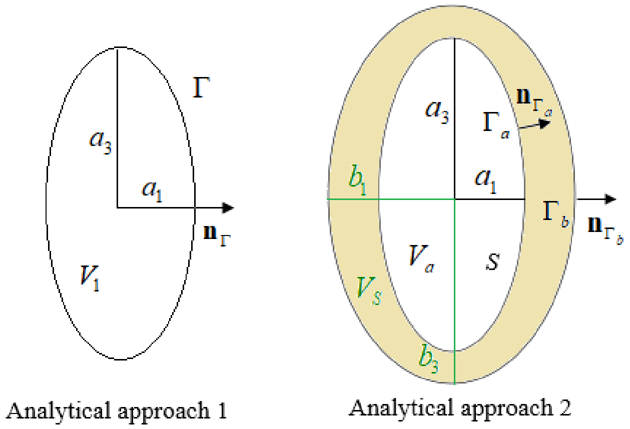

Fig. 1. Geometry of inhomogeneity considered in two analytical approaches

In the second analytical approach to accounting for imperfect contacts, a two-component layered ellipsoid is introduced (as shown in Fig. 1 in the ($\mathbf{e}_1$, $\mathbf{e}_3$) plane). The diffusivity of the inner ellipsoid coincides with that of the original inhomogeneity, while diffusivity of the outer layer, denoted as D_s, differs (material of the layer is assumed to be isotropic). The lengths of the semi-axes of the inner and outer ellipsoids, represented as a_1, a_2, a_3 and b_1, b_2, b_3, respectively, are related through a constant component ξ associated with confocal ellipsoids as:

$$b_i^2 = a_i^2 + \xi. \tag{12}$$

The bounds Γ_a of the inner ellipsoid and Γ_b of the outer ellipsoid are assumed to be perfect, so fields are continuous:

$$\begin{aligned} &D_0 \left.\frac{\partial c(\mathbf{r})}{\partial n_{\Gamma_b}}\right|_{r\to\partial\Gamma_b+} = D_s \left.\frac{\partial c(\mathbf{r})}{\partial n_{\Gamma_b}}\right|_{r\to\Gamma_b-}, c(\mathbf{r})|_{r\to\Gamma_b+} = c(\mathbf{r})|_{r\to\Gamma_b-} \\ &D_s \left.\frac{\partial c(\mathbf{r})}{\partial n_{\Gamma_a}}\right|_{r\to\partial\Gamma_a+} = D_1 \left.\frac{\partial c(\mathbf{r})}{\partial n_{\Gamma_b}}\right|_{r\to\Gamma_a-}, c(\mathbf{r})|_{r\to\Gamma_a+} = c(\mathbf{r})|_{r\to\Gamma_a-} \end{aligned}. \tag{13}$$

The thickness of the outer shell of the two-component layered ellipsoid is assumed to tend to zero that is modeled by letting $\xi \to 0$. This extremely thin coating is considered to be an isolator, resulting in $D_s \to 0$. Consequently, it becomes convenient to express the imperfect contact in terms of the equivalent surface diffusion resistivity β:

$$\beta = \frac{V_s}{D_s S} = \frac{4\pi(a_1^2 a_2^2 + a_1^2 a_3^2 + a_2^2 a_3^2)}{6 a_1 a_2 a_3 S} \lim_{\xi\to 0, D_s\to 0} \frac{\xi}{D_s}, \tag{14}$$

where V_s is the volume of the outer shell, S is the surface area of the inner ellipsoid (see Fig. 1). In the specific case of a spherical inhomogeneity, where $a_1 = a_2 = a_3 = a$, Eq. (14)

simplifies to $\beta = \lim_{\delta \to 0, D_s \to 0} \delta / D_s$, where δ is a constant thickness of the outer shell that tends to zero.

The averaged fields are as follows:

$$\begin{gathered}\langle \nabla c \rangle_V = \left(1 - \frac{V_1 + V_s}{V}\right) \langle \nabla c \rangle_{V_0} + \frac{V_1}{V} \langle \nabla c \rangle_{V_a} + \frac{V_s}{V} \langle \nabla c \rangle_{V_s} \\ \langle \mathbf{J} \rangle_V = \left(1 - \frac{V_1 + V_s}{V}\right) \langle \mathbf{J} \rangle_{V_0} + \frac{V_1}{V} \langle \mathbf{J} \rangle_{V_a} + \frac{V_s}{V} \langle \mathbf{J} \rangle_{V_s}\end{gathered}, \tag{15}$$

here $\langle \dots \rangle_{V_a} = \int_{V_s} \dots \mathrm{d}V_a$ and $\langle \dots \rangle_{V_s} = \int_{V_s} \dots \mathrm{d}V_s$ denotes the averaging over the volume of the inner ellipsoid and over the outer shell respectively.

Diffusivity contribution tensor can be found as:

$$\mathbf{H} = (D_1 - D_0)\mathbf{\Lambda}_a - \frac{V_s}{V_a} D_0 \mathbf{\Lambda}_s, \tag{16}$$

where constant concentration tensors $\mathbf{\Lambda}_a$ ($\langle \nabla \mathrm{c} \rangle_{V_a} = \mathbf{\Lambda}_a \cdot \mathbf{G}_0$) and $\mathbf{\Lambda}_s$ ($\langle \nabla \mathrm{c} \rangle_{V_s} = \mathbf{\Lambda}_s \cdot \mathbf{G}_0$) are as follows:

$$\begin{gathered}\mathbf{\Lambda}_a = D_0 \sum_{j=1}^{3} \frac{\mathbf{1}}{A_j D_1 + (1 - A_j) D_0 + (1 - A_j) D_0 D_1 \beta \left(A_j - \frac{F_j}{H}\right)} \mathbf{e}_j \mathbf{e}_j \\ \mathbf{\Lambda}_s = \sum_{j=1}^{3} A_j \frac{D_1}{D_s} \mathbf{\Lambda}_{a_{jj}} \mathbf{e}_j \mathbf{e}_j\end{gathered}, \tag{17}$$

here $H = \frac{a_1^2 a_2^2 + a_1^2 a_3^2 + a_2^2 a_3^2}{2 a_1^2 a_2^2 a_3^2}$, $F_1 = \frac{\left(\sum_{k=1}^{3} a_k^{-2}\right) A_1 - \frac{a_1 a_2 a_3}{2} \int_0^\infty \frac{3(p + a_2^2)(p + a_3^2) + (p + a_1^2)(p + a_2^2) + (p + a_1^2)(p + a_3^2)}{\sqrt{(p + a_1^2)^5 (p + a_2^2)^3 (p + a_3^2)^3}} dp}{2}$,

expressions for F_2 and F_3 can be obtained by the last equation with appropriate permutation of indices.

In our paper [30], we compared the two analytical approaches discussed above. It was shown that they yield the same result only in the case of spherical inhomogeneity, specifically when $a_1 = a_2 = a_3 = a$. In this scenario, the segregation parameter s_c and the equivalent surface resistivity β are related by the equation: $s_c = 1 + D_1 \beta / a$.

Let us now discuss the numerical approach for accounting for segregation. In this approach, we consider an inhomogeneity with a mass-isolating coating representing a shell. The procedure for numerically solving Eq. (1) for concentration is described in Appendix A. The diffusivity contribution tensor is determined through the effective diffusivity based on Eq. (6). The effective diffusivity tensor, in turn, is calculated from the solution of the following system of equations:

$$\begin{cases} \langle \mathbf{J} \rangle_1 = -\mathbf{D}^{eff} \cdot \langle \nabla \mathbf{c} \rangle_1, \\ \langle \mathbf{J} \rangle_2 = -\mathbf{D}^{eff} \cdot \langle \nabla \mathbf{c} \rangle_2, \\ \langle \mathbf{J} \rangle_3 = -\mathbf{D}^{eff} \cdot \langle \nabla \mathbf{c} \rangle_3, \end{cases} \tag{18}$$

here the indices 1, 2, 3 correspond to three calculations where the linear boundary condition (2) is alternately applied along three mutually orthogonal directions $\mathbf{e}_1$, $\mathbf{e}_2$, $\mathbf{e}_3$ (here $\mathbf{e}_1$, $\mathbf{e}_2$, $\mathbf{e}_3$ are unit vectors aligned with semi-axes of the ellipsoidal inhomogeneity. Note that the equalities $\langle \nabla c \rangle_j = \mathbf{G}_0$ are satisfied automatically for j =1, 2, 3 respectively.

To find the effective diffusivity, we multiply Eq. (18) by $\mathbf{e}_1$, $\mathbf{e}_2$, $\mathbf{e}_3$ respectively and then sum them. This leads to the following equality:

$$\mathbf{D}^{eff} = -\left(\left(\sum_{j=1}^{3} \mathbf{e}_j \langle \nabla c \rangle_j\right)^{-1} \cdot \sum_{j=1}^{3} \langle \mathbf{J} \rangle_j \mathbf{e}_j\right)^{\mathbf{T}}. \tag{19}$$

Within the numerical approach we consider different shapes for the outer shell:

1. The outer shell is represented by two ellipsoids (Numerical method 1).
2. The outer shell is characterized by a constant thickness (Numerical method 2).

Let us further discuss these methods.

In the case of Numerical method 1, when the semi-axes of the inner and outer ellipsoids are related by Eq. (12), the numerical solution can be directly compared with the corresponding analytical solution. However, consideration of such a shape of the outer shell is meaningful only within analytical approach based on the solution of a single inhomogeneity problem for confocal ellipsoids. Additionally, within the numerical approach, we examine a second case where the semi-axes of the two ellipsoids are related as $b_i = a_i + \delta$, with δ being a constant. To facilitate the comparison of the two numerical solutions, we relate the parameter ξ introduced in the first case to the parameter δ introduced in the second case in the following way:

$$\xi = \delta(2a_{max} + \delta), \tag{20}$$

where a_{max} corresponds to the largest semi-axis. In the case of confocal ellipsoids, δ represents the minimum value of the thickness of the outer shell.

In the case of Numerical method 2, the inner figure is an ellipsoid, while the outer one is not. This model is particularly significant for materials containing inhomogeneities with real coatings of finite thickness. At the same time, even in scenarios involving an ultra-thin coating used to model segregation, the model offers advantages, as in this case the thickness δ approaches zero, rather than ξ, making it a more physically relevant representation. To compare the two numerical methods, we relate δ and ξ using Eq. (20). The technical complexity associated with forming a layer of constant thickness arises from the need to calculate the distance between the surface of the ellipsoid and any point outside it to determine whether that point belongs to the layer [31,32]. The proposed method for solving this problem is described in Appendix B.

To simulate a micro-heterogeneous material in Numerical methods 1 and 2, we create three types of cubic cells based on the material they represent: inhomogeneity, layer, or matrix. When the thickness of the isolating layer approaches zero, matrix cells and inhomogeneity cells can become neighbors, resulting in no isolating cells between them. This situation gives rise to the issue of "penetration" which violates isolation. To avoid the "penetration" problem, we must consider a layer of finite thickness that, in fact, does not accurately model segregation on a real ultra-thin phase interface. To accurately simulate the case of an ultra-thin coating of interest, we propose to extrapolate the dependencies of the components of the diffusivity contribution tensor on ξ (or δ) and estimate the values at $\xi = 0$ (or $\delta = 0$).

In conclusion, we would like to emphasize that the consideration of an isolating coating—both in analytical models and numerical methods—allows the modeling of impurity accumulation solely outside the inhomogeneities. On the other hand, prescribing a jump in concentration enables the modeling of impurity accumulation in both the exterior and interior of the inhomogeneities. Segregation typically occurs along grain boundaries and within pores. In the first case, it is essential to model the grains as inhomogeneities and the grain boundaries as the matrix when employing the isolating coating approach (as opposed to modeling grains as the matrix and grain boundaries as inhomogeneities). Notably, this approach cannot be applied to model segregation in the case of pores at all.

Results and Discussion

We calculate the diffusivity contribution tensor of a less mass-conductive inhomogeneity with an imperfect boundary, which is embedded in a more mass-conductive matrix. This approach allows us to model segregation in polycrystalline materials within the framework of all the investigated models (where grains are modeled as inhomogeneities, and grain boundaries are modeled as the matrix, with segregation occurring along the grain boundaries). Inhomogeneity is assumed to have the shape of a prolate spheroid (where $a_1 = a_2 = a$ and $\gamma = a_3/a > 1$) or a sphere (where $a_1 = a_2 = a_3 = a$ and $\gamma = 1$).

To compare the results obtained within the framework of two investigated analytical approaches for accounting for imperfect contacts, we relate the segregation parameter s_c, which is responsible for the jump in concentration, to the equivalent surface resistivity β, which accounts for the surface effect in the following manner:

$$s_c = 1 + R, \quad R = \frac{D_1\beta}{a} = \frac{D_1(1+2\gamma^2)}{3a^2\gamma\left(1+\frac{\gamma^2}{\sqrt{\gamma^2-1}}\arcsin\frac{\sqrt{\gamma^2-1}}{\gamma}\right)} \lim_{\xi\to 0, D_s\to 0} \frac{\xi}{D_s}, \tag{21}$$

since in this case the application of both analytical approaches leads to the same result [29].

An ultra-thin isolating coating emerges when $\xi \to 0$ and $D_s \to 0$. The ratio $\lim_{\xi\to 0, D_s\to 0} \xi/D_s$ and the parameter R introduced in accordance with Eq. (21) are constant values. As discussed in the previous section, direct consideration of $\xi \to 0$ in numerical method presents technical challenges. To compare the numerical solution with the analytical ones, we evaluate the numerical solution at several small values of ξ while keeping ξ/D_s constant, and then we extrapolate the results.

We start with calculating the components of diffusivity contribution tensor of a spherical inhomogeneity (when $\gamma = 1$). In this case, not only do both analytical approaches yield the same result, but all numerical methods do as well, since the thickness of the coating remains constant along the inhomogeneity border. Specifically, we consider a material with a ratio of the diffusion coefficient of the inhomogeneity to that of the background matrix given by $\alpha = D_1/D_0 = 0.1$.

Figure 2 shows the dependence of the components of the diffusivity contribution tensor of a spherical inhomogeneity with imperfect contact on δ, which remains constant along the phase interface, at a constant ratio ξ/D_s. Note that in this case, an ultra-thin coating emerges when $\delta \to 0$. It is seen that for small values of the thickness of the outer shell, the dependencies can be well approximated by linear functions. The results are extrapolated to facilitate the limit transition. The numerical and analytical results are found to be in close agreement, with an error of less than 1 %. Additionally, in the absence of the coating, the components of the property contribution tensor calculated both analytically and numerically yield $H_{11} = H_{22} = H_{33} \approx 1.3$. Thus, in all models – both analytical and numerical – increasing R enhances the "negative" contribution of low mass-conducting inhomogeneities, meaning that the presence of such inhomogeneities will decrease macroscopic mass permeability.

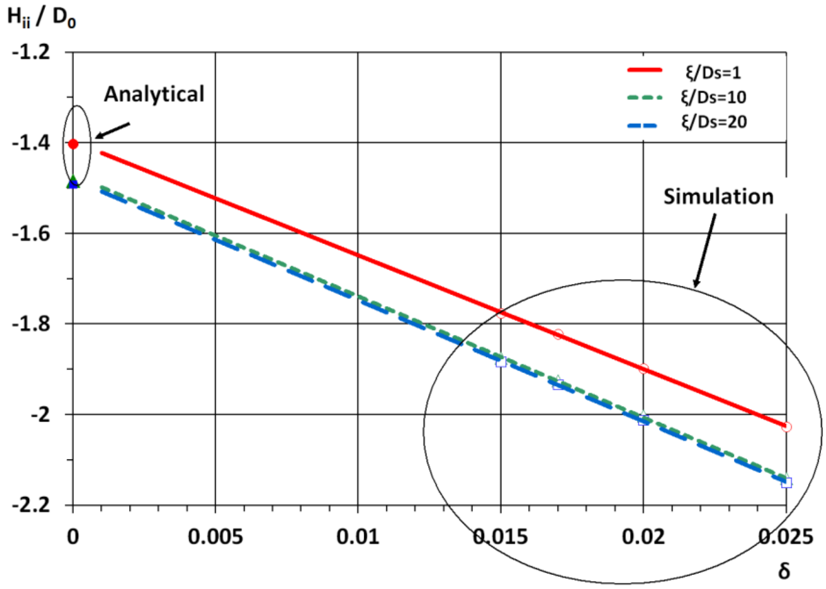

Fig. 2. Extrapolation of the numerical dependencies of the components of the diffusivity contribution tensor with respect to the thickness of the outer shell

We now turn our attention to spheroidal inhomogeneities. As previously mentioned, the two analytical approaches yield different results for any relationship between the segregation parameter s_c and equivalent surface resistivity *β*. Consequently, a quantitative comparison of the results is not particularly valuable. However, the qualitative differences are significant.

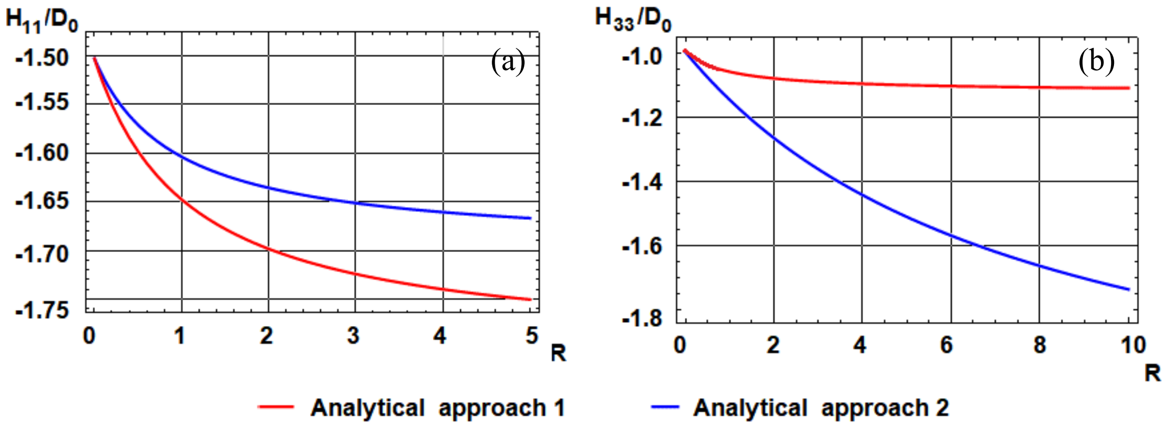

Fig. 3. Dependencies of the dimensionless components of the diffusivity contribution tensor H_{11}/D_0 (a) and H_{33}/D_0 (b) with respect to the parameter *R*

According to [26], the increase in the dimensionless parameter *R*, introduced by Eq. (21) and indicative of an imperfect contact, impacts the results obtained through the two analytical approaches in different ways. When *R* is unknown, the application of one approach allows for a border range of values for H_{ii} and, consequently, for effective properties. This can be critical when comparing theoretical results with experimental data. Note that both approaches – Analytical approach 1, which accounts for an imperfect contact via a jump prescription, and Analytical approach 2, which considers imperfect contact through an isolating coating – can yield a wider range of the results than the other, depending on the internal structure parameters. For instance, as shown in Fig. 3, at γ = 3 and α = 0.1, the increase in R affects H_{33} calculated using Analytical approach 2 significantly more than it does in Analytical approach 1. However, the influence on H_{11} is comparatively less. Notably, the difference in H_{33} calculated by the two approaches is greater than in H_{11}.

There is another significant qualitative difference between the two analytical approaches. In Analytical approach 1, the magnitudes of all components of the diffusivity contribution tensor increase with an increasing R, which is physically justified. This is because the degradation of mass permeability in the inhomogeneity should enhance its contribution to the effective properties of a material comprised of less mass-conducting inhomogeneities and a more mass-conducting matrix. In contrast, in Analytical approach 2, for certain values of the inner structure parameters, an opposing trend occurs. In Fig. 4(a) it is shown that for a given γ, the magnitude of the component H_{11} decreases with increasing R when $\alpha < \alpha_{crit}$ (where α_{crit} represents some "critical" value). An increase in γ leads to a decrease in α_{crit}. The dependence of α_{crit} on the aspect ratio is shown in Fig. 4(b). It is seen that the problem does not arise when $\alpha > 0.043$ for any value of γ. Additionally, as α decreases, the range of "critical" values of γ becomes wider (see the region under the line in Fig. 4(b)).

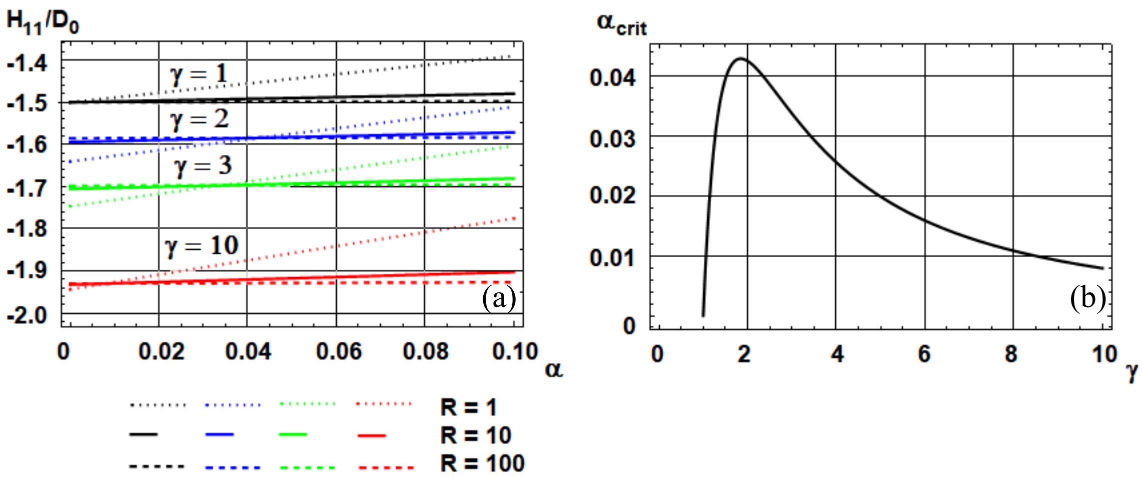

Fig. 4. (a) Dependencies of the dimensionless components of the diffusivity contribution tensor H_{11}/D_0 with respect to the ratio of the diffusivities of the inhomogeneity and the matrix; (b) dependence of the "critical" value the diffusivity ratio with respect to the aspect ratio

Figures 5 and 6 compare the analytical and numerical solutions for the components of the diffusivity contribution tensor. The numerical solution obtained using Numerical method 1 when semi-axes of the inner and outer ellipsoids are related by Eq. (12) is shown. The results are extrapolated to implement the limit transition. Figure 5 presents the results for a material with parameters $\gamma = 2,\ \alpha = 0.1$. In this case, the dependencies H_{11} on R obtained within the framework of the two analytical approaches exhibit similar behavior, with their magnitudes increasing as R increases. It is seen that an increase in R results in a greater contribution of inhomogeneity with an imperfect interface estimated within numerical approach. The results calculated using Analytical model 1 are closer to the numerical results than those obtained from Analytical model 2. This may be due to the fact that the dependency of the components of the property contribution tensors on *R* is less pronounced in the case of Analytical model 1 and in the numerical solution. It appears that Analytical model 2 can be used for small values of *R*, which holds true for small values in the limit $\lim_{\xi \to 0, D_s \to 0} \xi / D_s$.

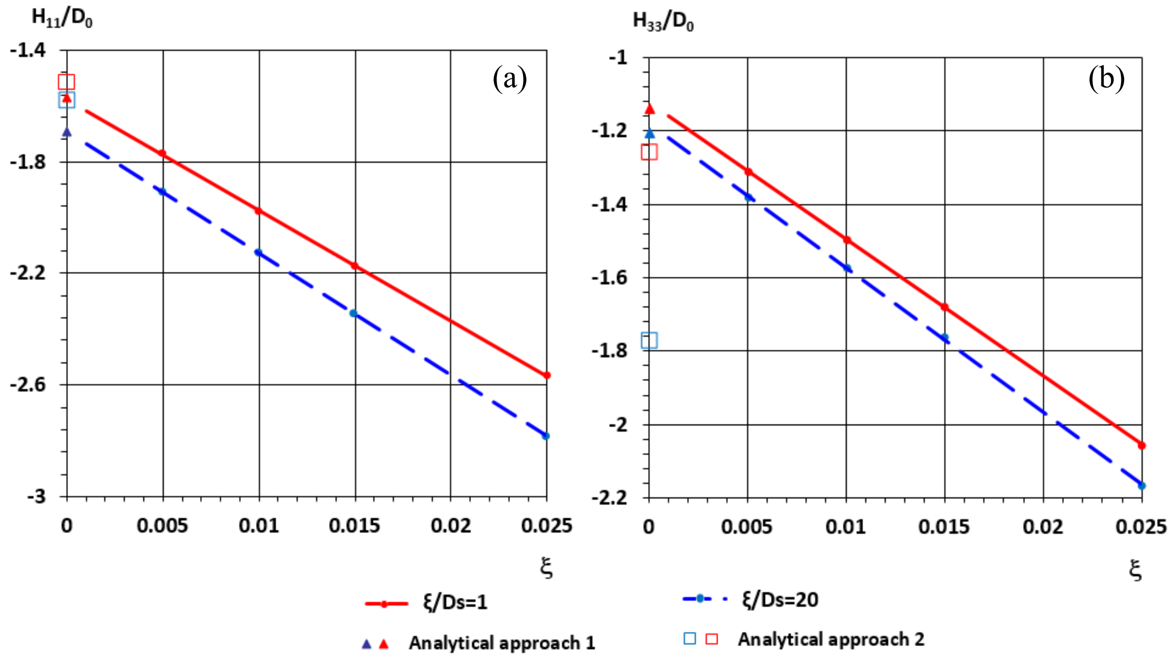

Fig. 5. Extrapolation of the dependencies of the dimensionless components of the diffusivity contribution tensor H_{11}/D_0 (a) and H_{33}/D_0 (b) with respect to the parameter ξ at γ = 2, α = 0.1

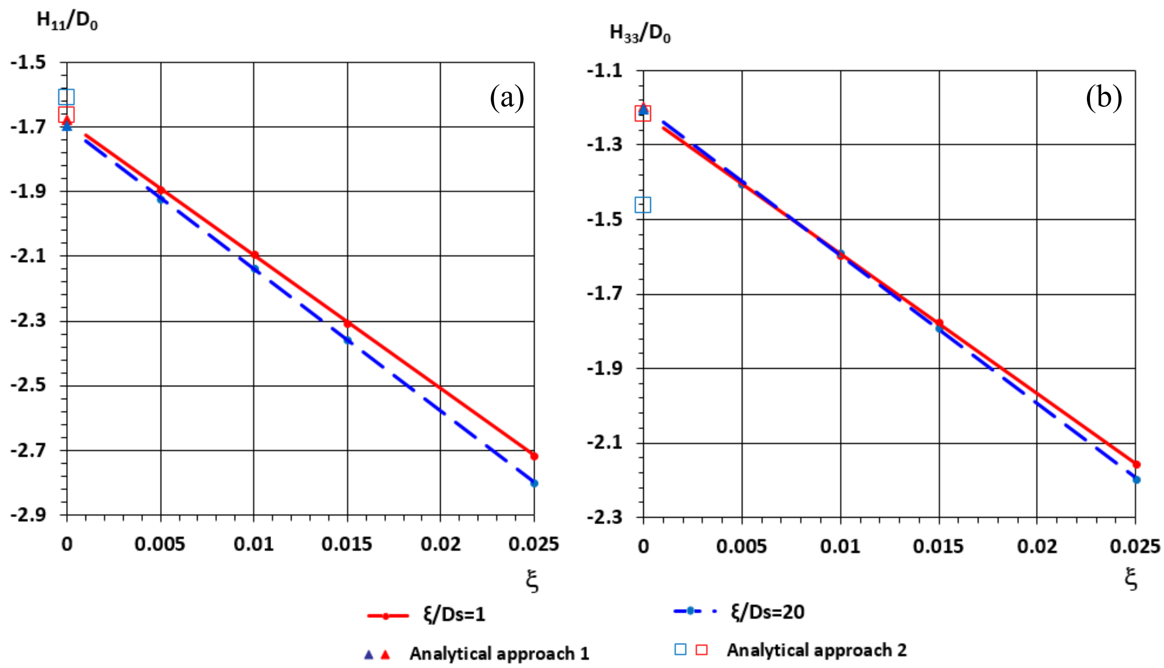

Fig. 6. Extrapolation of the dependencies of the dimensionless components of the diffusivity contribution tensor H_{11}/D_0 (a) and H_{33}/D_0 (b) with respect to the parameter ξ at γ = 2, α = 0.01

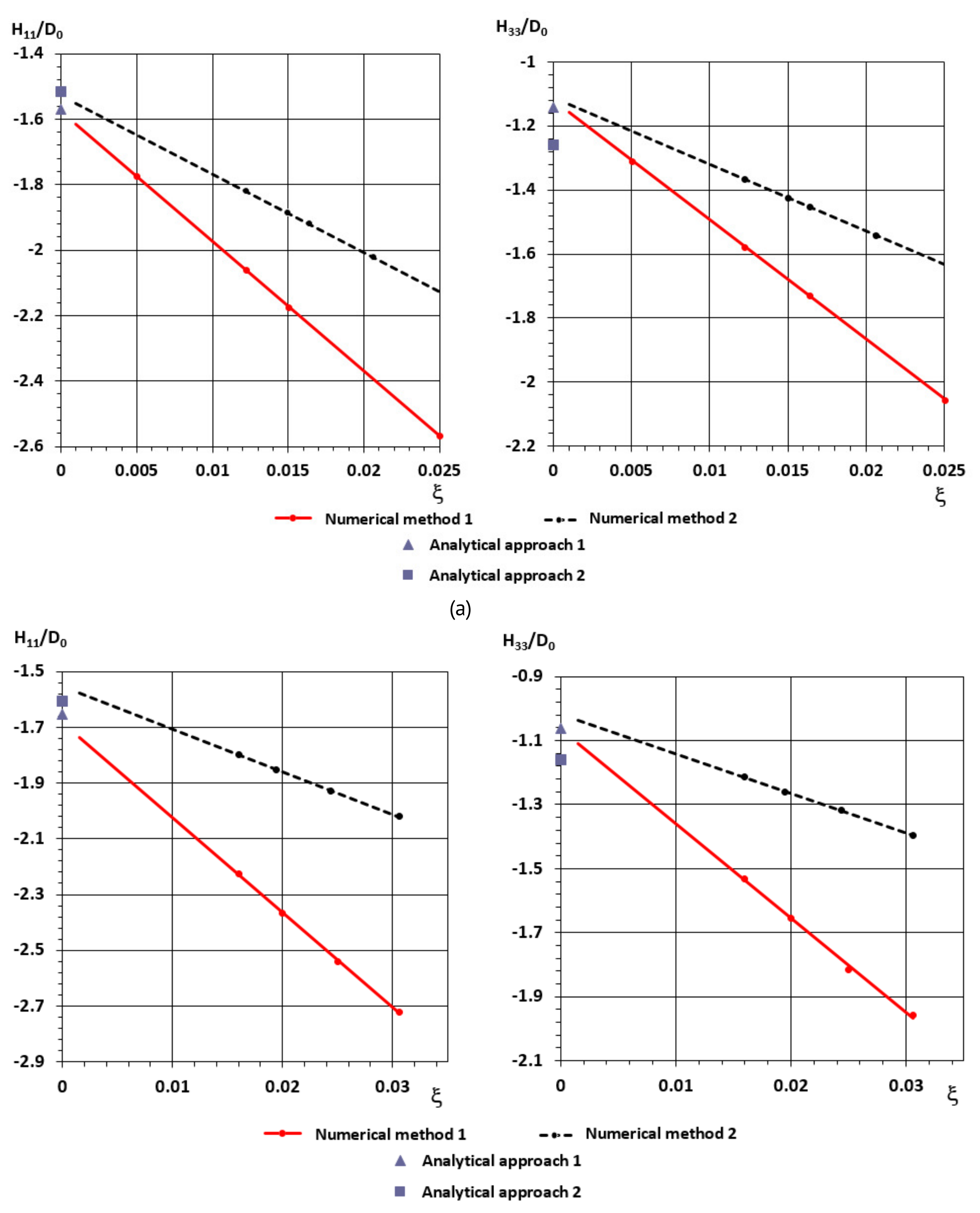

(a)

(b)

Fig. 7. Comparison of numerical methods at $\gamma = 2$ (a) and $\gamma = 3$ (b) at $\xi / D_s = 1$

Figure 7 compares the results obtained from different numerical methods: Numerical method 1, which introduces the coating using a constant parameter ξ, and Numerical method 2, which introduces the coating through a constant thickness δ along the inhomogeneity boundary. Both approaches yield similar results, allowing either model to be used for simulating an ultra-thin coating. However, the analysis of a layer with constant thickness results in outcomes that are less dependent on the absolute thickness.

Notably, for a slightly elongated spheroid with $\gamma = 2$, the results obtained within the framework of Numerical method 1.2 using a constant thickness δ along the inhomogeneity axes, coincide with those from Numerical method 2 applying the same constant thickness δ across the entire inhomogeneity boundary, with the difference being less than 1 %. The distinction between these two cases becomes apparent at larger values of γ, as shown in Fig. 8. It is seen that increasing the aspect ratio of spheroidal inhomogeneity leads to a greater difference between Numerical method 1.2 and Numerical method 2 (the value of $\left|H_{ii}^{\mathrm{NM1.2}} - H_{ii}^{\mathrm{NM2}}\right| / H_{ii}^{\mathrm{NM2}}$ is shown, where $H_{ii}^{\mathrm{NM1.2}}$ and H_{ii}^{NM2} are components of H_{ii} calculated within the framework of Numerical method 1.2 and Numerical method 2 respectively).

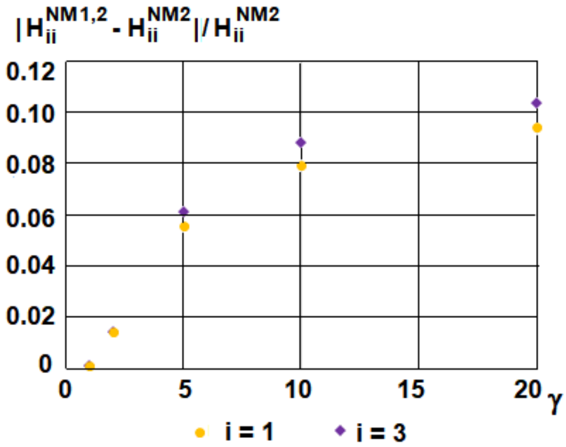

Fig. 8. Dependencies of the slot-relative difference between the components of the diffusivity contribution tensor calculated using Numerical method 1.2 and Numerical method 2 with respect to the aspect ratio of spheroidal inhomogeneity

In summary, the analytical approach that incorporates segregation via prescription of a jump in concentration shows advantages over the alternative method that models segregation through inhomogeneity with a mass isolating coating. The first analytical approach effectively describes segregation both inside and outside inhomogeneities, avoids unphysical outcomes across various internal structure parameters, and yields results that align more closely with numerical findings. Additionally, we have confirmed that our developed numerical methods are capable of accurately simulating segregation occurring outside of inhomogeneities.

Conclusions

Various analytical approaches and numerical methods that account for segregation when determining the effective diffusivity of micro-heterogeneous materials were compared in the paper based on evaluating the diffusivity contribution tensors of individual inhomogeneities. Two analytical approaches and one numerical approach were utilized. In the first analytical approach, segregation was modeled by introducing a concentration jump characterized by a constant segregation parameter. In the second analytical approach and the numerical approach, segregation was addressed by considering inhomogeneities with a mass-isolating ultra-thin coating. Moreover, in the framework of the numerical approach, different methods of simulating the coating were applied: the layer formed by two ellipsoids and the layer of constant thickness were both considered

The comparison of analytical and numerical solutions demonstrated that the first analytical approach offers more advantages than the second one. This is because it enables the description of segregation in materials with diverse internal structures and provides results that closely match numerical findings, despite its simplicity. Additionally, the developed numerical methods can be further employed to calculate the effective properties of materials with inhomogeneities featuring real mass-isolating coatings of finite thickness and inhomogeneities with irregular shapes.

References

1. Ahn DC, Sofronis P, Dodds R. Modeling of hydrogen-assisted ductile crack propagation in metals and alloys. *International Journal of Fracture*. 2007;145: 135–157.
2. Indeitsev DA, Semenov BN. About a model of structural-phase transformations under hydrogen influence. *Acta Mechanica*. 2008;195: 295–304.
3. Belyaev AK, Polyanskiy VA, Yakovlev YA. Stresses in a pipeline affected by hydrogen. *Acta Mechanica*. 2012;223(8): 1611–1619.
4. Polyanskiy VA, Frolova KP, Sedova YS, Yakovlev YA, Belyaev AK. Behavior of Pipeline Steels in Gaseous Hydrogen-Containing Mixtures. In: Polyanskiy VA., Belyaev AK. (eds.) *Mechanics and Control of Solids and Structures*. Cham: Springer;2022. p.535–556.
5. Sedova YS, Polyanskiy VA, Belyaev AK, Yakovlev YA. Modeling the skin effect, associated with hydrogen charging of samples, within the framework of the HEDE mechanism of cracking. *Materials Physics and Mechanics*. 2023;51(6): 152–159.
6. Herzig C, Mishin Y. Grain boundary diffusion in metals. In: Heitjans P, Kärger J. (eds.) *Diffusion in Condensed Matter*. Berlin: Springer; 2005. p.337–366.
7. Zhang X, Qiao L, Zhang H, Wang P. Influence of impurity gas seeding into deuterium plasma on the surface modification, sputtering erosion and deuterium retention in W and W-La2O3 alloy. *International Journal of Hydrogen Energy*. 2023;48(6): 2075–2089.
8. Zhang Y, Liu L. On diffusion in heterogeneous media. *American Journal of Science*. 2012;312(9): 1028–1047.
9. Markov KZ. Elementary micromechanics of heterogeneous media. In: Markov K, Preziosi L. (eds.) *Heterogeneous Media. Modeling and Simulation in Science, Engineering and Technology*. Boston, MA: Birkhäuser; 2000. p.1–162.
10. Javili A, Kaessmair S, Steinmann P. General imperfect interfaces. *Computer Methods in Applied Mechanics and Engineering*. 2014;275: 76–97.
11. Kaur I, Mishin Y, Gust W. *Fundamentals of Grain and Interphase Boundary Diffusion*. Wiley; 1995.
12. Kalnin JR, Kotomin EA, Maier J. Calculations of the effective diffusion coefficient for inhomogeneous media. *Journal of Physics and Chemistry of Solids*. 2002;63(3): 449–456.
13. Belova IV, Murch GE. Calculation of the effective conductivity and diffusivity in composite solid electrolytes. *Journal of Physics and Chemistry of Solids*. 2005;66(5): 722–728.
14. Knyazeva AG, Grabovetskaya GP, Mishin IP, Sevostianov I. On the micromechanical modelling of the effective diffusion coefficient of a polycrystalline material. *Philosophical Magazine*. 2015;95(19): 2046–2066.
15. Umbanhowar PB, Lueptow RM, Ottino JM. Modeling segregation in granular flows. *Annual Review of Chemical and Biomolecular Engineering*. 2019;10: 129–153.
16. Frolova KP, Vilchevskaya EN. Effective diffusivity of transversely isotropic material with embedded pores. *Materials Physics and Mechanics*. 2021;47(6): 937–950.
17. Miloh T, Benveniste Y. On the effective conductivity of composites with ellipsoidal inhomogeneities and highly conducting interfaces. *Proceedings of the Royal Society of London. Series A: Mathematical, Physical and Engineering Sciences*. 1999;455(1987): 2687–2706.

18. Duan HL, Karihaloo BL. Effective thermal conductivities of heterogeneous media containing multiple imperfectly bonded inclusions. *Physical Review B—Condensed Matter and Materials Physics.* 2007;75(6): 064206.
19. Le Quang H, Pham DC, Bonnet G, He QC. Estimations of the effective conductivity of anisotropic multiphase composites with imperfect interfaces. *International Journal of Heat and Mass Transfer.* 2013;58(1-2): 175–187.
20. Kushch VI., Sevostianov I, Belyaev AS. Effective conductivity of spheroidal particle composite with imperfect interfaces: Complete solutions for periodic and random micro structures. *Mechanics of Materials.* 2015;89: 1–11.
21. Pham DC, Nguyen TK. Thermal conductivity in spherical and circular inclusion composites with highly- and lowly-conducting imperfect interfaces. *International Journal of Heat and Mass Transfer.* 2022;196: 123245.
22. Kushch VI, Mogilevskaya SG. Higher order imperfect interface models of conductive spherical interphase. *Mathematics and Mechanics of Solids.* 2022;29(12): 2386–2410.
23. Endres AL, Knight RJ. A model for incorporating surface phenomena into the dielectric response of a heterogeneous medium. *Journal of Colloid and Interface Science*. 1993;157(2): 418–425.
24. Levin V, Markov M. Effective thermal conductivity of micro-inhomogeneous media containing imperfectly bonded ellipsoidal inclusions. *International Journal of Engineering Science*. 2016(109): 202–215.
25. Markov M, Levin V, Markova I. Determination of effective electromagnetic parameters of concentrated suspensions of ellipsoidal particles using Generalized Differential Effective Medium approximation. *Physica A: Statistical Mechanics and its Applications.* 2018;492: 113–122.
26. Kachanov M, Sevostianov I. Micromechanics of materials, with applications. In: *Solid Mechanics and Its Applications*. Cham: Springer; 2018. p.249.
27. Eshelby JD. Elastic inclusions and inhomogeneities. In: *Collected works of JD Eshelby.* Dordrecht: Springer; 2006. p.297–350.
28. Fricke H. A mathematical treatment of the electric conductivity and capacity of disperse systems I. The electric conductivity of a suspension of homogeneous spheroids. *Physical Review.* 1924;24(5): 575.
29. Frolova KP, Vilchevskaya EN, Polyanskiy VA. Modeling of Imperfect Contacts in Determining the Effective Diffusion Permeability. *Vestnik St. Petersburg University, Mathematics.* 2023;56(4): 459–469.
30. Frolova KP, Vilchevskaya EN. Comparison of approaches to accounting for imperfect contacts when determining the effective permeability of material. *St. Petersburg State Polytechnical University Journal. Physics and Mathematics*. 2023;16(4): 146–159.
31. Eberly D. *Distance from a point to an ellipse, an ellipsoid, or a hyperellipsoid*. 2011.
32. Pope SB. *Algorithms for ellipsoids*. 2008.
33. Yanenko NN. Simple Schemes in Fractional Steps for the Integration of Parabolic Equations. In: Holt M. (ed.) *The Method of Fractional Steps*. Berlin: Springer; 1971. p.17–41.

About Authors

Ksenia P. Frolova
Candidate of Physico-Mathematical Sciences
Senior Researcher (Institute for Problems in Mechanical Engineering RAS, St. Petersburg, Russia)

Nikolay M. Bessonov
Doctor of Physico-Mathematical Sciences
Chief Researcher (Institute for Problems in Mechanical Engineering RAS, St. Petersburg, Russia)

Elena N. Vilchevskaya
Doctor of Physico-Mathematical Sciences
Associate Professor (Flugsnapparegatan 6, Mölndal, Sweden)

Appendix A. Numerical procedure

To solve Eq. (1) for concentration, we employed an implicit numerical procedure based on the Alternating Direction Implicit (ADI) algorithm [33].

We can express Eq. (1) for concentration in symbolic form as follows:

$$L(\mathrm{c}) = 0, \tag{A.1}$$

where L is a differential operator defined in Cartesian coordinates (x, y, z) as

$$L = \frac{\partial}{\partial x}\left(D(\mathbf{r})\frac{\partial}{\partial \mathrm{x}}\right) + \frac{\partial}{\partial \mathrm{y}}\left(D(\mathbf{r})\frac{\partial}{\partial \mathrm{y}}\right) + \frac{\partial}{\partial \mathrm{z}}\left(D(\mathbf{r})\frac{\partial}{\partial \mathrm{z}}\right) \equiv L_1 + L_2 + L_3.$$

To find the solution of Eq. (A.1), we treat it as the stationary solution of the unsteady equation using an implicit scheme:

$$\frac{\xi^{n+1}}{\tau} = L(c^{n+1}), \tag{A.2}$$

where $\xi^{n+1} = c^{n+1} - c^n$, τ is a "pseudo-time" step, n is the iteration number.

Equation (A.2) can be rewritten in the following manner:

$$\frac{\xi^{n+1}}{\tau} = L(c^n) + L(\xi^{n+1}). \tag{A.3}$$

Equation (A.3), in turn, is convenient to rewrite as:

$$(I - \tau L)\xi^{n+1} = \tau L(c^n), \tag{A.4}$$

where *I* is the identity operator.

Equation (A.4) can be factored in the following way:

$$(I - \tau L_1)(I - \tau L_2)(I - \tau L_3)\xi^{n+1} = \tau L(c^n) + O(\xi^{n+1}). \tag{A.5}$$

Then the main steps of algorithm are as follows:

$$\begin{cases} \text{Step 1:} & \xi^n = \tau L(c^n) \\ \text{Step 2:} & (I - \tau L_1)\xi^{n+1/3} = \xi^n \\ \text{Step 3:} & (I - \tau L_2)\xi^{n+2/3} = \xi^{n+1/3} \\ \text{Step 4:} & (I - \tau L_3)\xi^{n+1} = \xi^{n+2/3} \\ \text{Step 5:} & c^{n+1} = c^n + \xi^{n+1} \end{cases}. \tag{A.6}$$

Appendix B. Calculating the distance between point and ellipsoid surface

The distance between a point and the surface of an ellipsoid can be expresses as the length of the normal vector dropped from the given point onto the ellipsoidal surface. The surface of the ellipsoid in Cartesian coordinates (x, y, z) is defined be the equation:

$$\left(\frac{x}{a_1}\right)^2 + \left(\frac{y}{a_2}\right)^2 + \left(\frac{z}{a_3}\right)^2 = 1\ , \tag{B.1}$$

where a_1, a_2, a_3 are the semi-axes of the ellipsoid.

We first discuss the problem of determining the position of some point along the normal vector to ellipsoid's surface. Let this point be located at a given distance δ to a point on the ellipsoid's surface represented by the position vector $\mathbf{r} = x\mathbf{e}_1 + y\mathbf{e}_2 + z\mathbf{e}_3$. The unit external normal vector $\mathbf{n}$ to the ellipsoid's surface at the point $\mathbf{r}$ can be defined as:

$$\mathbf{n} = \frac{\frac{x}{a_1^2}}{\sqrt{\left(\frac{x}{a_1^2}\right)^2 + \left(\frac{y}{a_2^2}\right)^2 + \left(\frac{z}{a_3^2}\right)^2}}\mathbf{e}_1 + \frac{\frac{y}{b_1^2}}{\sqrt{\left(\frac{x}{a_1^2}\right)^2 + \left(\frac{y}{a_2^2}\right)^2 + \left(\frac{z}{a_3^2}\right)^2}}\mathbf{e}_2 + \frac{\frac{z}{c_1^2}}{\sqrt{\left(\frac{x}{a_1^2}\right)^2 + \left(\frac{y}{a_2^2}\right)^2 + \left(\frac{z}{a_3^2}\right)^2}}\mathbf{e}_3. \tag{B.2}$$

Let $\mathbf{r}_0 = x_0\mathbf{e}_1 + y_0\mathbf{e}_2 + z_0\mathbf{e}_3$ be the sought-for position-vector. Its coordinates can be determined from the following equations:

$$
\begin{aligned}
x_0 &= x + \frac{\frac{x}{a_1^2}}{\sqrt{\left(\frac{x}{a_1^2}\right)^2+\left(\frac{y}{a_2^2}\right)^2+\left(\frac{z}{a_3^2}\right)^2}}\delta \\
y_0 &= y + \frac{\frac{y}{b_1^2}}{\sqrt{\left(\frac{x}{a_1^2}\right)^2+\left(\frac{y}{a_2^2}\right)^2+\left(\frac{z}{a_3^2}\right)^2}}\delta. \\
z_0 &= z + \frac{\frac{z}{c_1^2}}{\sqrt{\left(\frac{x}{a_1^2}\right)^2+\left(\frac{y}{a_2^2}\right)^2+\left(\frac{z}{a_3^2}\right)^2}}\delta
\end{aligned}
\qquad \text{(B.3)}
$$

Returning to the problem of calculating the distance between a specified point and the surface of the ellipsoid, both the distance δ and the coordinates *x, y, z* are initially unknown. To find these values, we must solve an inverse problem described by the following system of equations:

$$
\begin{aligned}
&x_0 - \left(1 + \frac{\mathrm{h}}{a_1^2\sqrt{\left(\frac{x}{a_1^2}\right)^2+\left(\frac{y}{a_2^2}\right)^2+\left(\frac{z}{a_3^2}\right)^2}}\right)x = 0 \\
&y_0 - \left(1 + \frac{\mathrm{y}}{b_1^2\sqrt{\left(\frac{x}{a_1^2}\right)^2+\left(\frac{y}{a_2^2}\right)^2+\left(\frac{z}{a_3^2}\right)^2}}h\right)y = 0 \\
&z_0 - \left(1 + \frac{\mathrm{z}}{c_1^2\sqrt{\left(\frac{x}{a_1^2}\right)^2+\left(\frac{y}{a_2^2}\right)^2+\left(\frac{z}{a_3^2}\right)^2}}h\right)z = 0 \\
&\left(\frac{x}{a_1}\right)^2 + \left(\frac{y}{a_2}\right)^2 + \left(\frac{z}{a_3}\right)^2 - 1 = 0
\end{aligned}
\qquad . \qquad \text{(B.4)}
$$

Solution of the system of Eqs. (B.4) was found in the present research numerically.

MATERIALS PHYSICS AND MECHANICS RESEARCH ARTICLE

Submitted: August 13, 2024 Revised: September 8, 2024 Accepted: September 29, 2024

Influence of latent heat and heat exchange conditions on tension behavior of shape memory alloy specimen

F.S. Belyaev [1,2], **A.E. Volkov** [1], **E.A.Vukolov** [1], **M.E. Evard** [1] ✉,

K.V. Kudrina [1], **M.S. Starodubova** [1]

[1] St. Petersburg State University, St. Petersburg, Russia

[2] Institute for Problems in Mechanical Engineering of the Russian Academy of Sciences, St. Petersburg, Russia

✉ m.evard@spbu.ru

ABSTRACT

A microstructural model of functional behavior of shape memory alloys has been used for modeling of the pseudo-elasticity effect taking into account the influence of latent heat of the martensitic transformations, heat exchange conditions and strain rate. A completely coupled boundary value problem on tension of a cylindrical rod under conditions of heat exchange with the environment and heat diffusion along the radius has been solved. The obtained results are in good agreement with the available experimental data. The Fourier and Biot criteria were used to evaluate the critical radius, for which it is necessary to solve a fully coupled boundary value problem at given material parameters, deformation rate and heat exchange conditions. It has been shown that the microstructural model taking into account the latent heat release and adsorption is an adequate tool for describing the strain rate dependence of the pseudo-elastic behavior for shape memory alloys.

KEYWORDS

heat exchange conditions • latent heat • microstructural modeling • shape memory alloys • TiNi • tension boundary value problem • Fourier number • Biot number

Acknowledgements. *This work has been supported by the grant of the Russian Science Foundation, RSF 23-21-00167.*

Citation: Belyaev FS, Volkov AE, Vukolov EA, Evard ME, Kudrina KV, Starodubova MS. Influence of latent heat and heat exchange conditions on tension behavior of shape memory alloy specimen. *Materials Physics and Mechanics*. 2024;52(5): 18–28.

http://dx.doi.org/10.18149/MPM.5252024_2

Introduction

Nowadays the ability of shape memory alloy (SMA) parts to restore the original shape at heating after preliminary deformation (shape memory effect), as well as pseudoelastic behavior consisting in the recovery of significant deformations during isothermal unloading, has found wide application. These materials are used as active working elements of actuators and sensors [1,2], passive and semi-active vibration protection devices [3], medical devices [4,5]. The functional properties of SMAs are caused by martensitic transformations - reversible change of the crystal lattice from a high-temperature austenitic structure to a low-temperature martensitic one. Martensitic transformations in SMAs are usually controlled by temperature kinetics, so that the volume fraction of martensite smoothly increases at cooling through the temperature interval of the direct transformation and decreases at heating through the interval of the reverse transformation [6]. The finite rate of heat diffusion and the processes of release (or absorption) of the latent heat of the transformation can have a significant influence

Publisher: Peter the Great St. Petersburg Polytechnic University

on functional characteristics of a particular device [7–9]. For example, cyclic temperature variations of SMA samples associated with the release and absorption of the latent heat of transformation were revealed during cyclic loading at constant ambient temperature. Moreover, the oscillation amplitude increases with the loading rate [10,11]. Heat exchange with the environment leads to an attenuation of the influence of internal heat sources [12], but sometimes the heat exchange can be difficult, especially when an SMA element has a coating [13,14]. At some conditions, a loaded sample may develop deformation in time due to a delay of the martensitic transformation caused by the presence of two simultaneous processes: the release of the latent heat of transformation and heat flux to the environment [15].

Simulation, which takes into account the presence of internal heat sources in SMA elements and heat exchange conditions becomes especially important for devices that are required to operate at a given temperature and/or within a given time interval. For modelling of SMA element deformation different theoretical approaches can be used. For solving boundary value problems to find the stress and strain fields usually a macroscopic (phenomenological) model is used for calculation of the SMA deformation. In such models the volume fraction of the martensitic phase and the transformation strain are considered as internal variables, and the relationships that determine their evolution are based either directly on the results of experiments [16], or on a combination of experimental constitutive relations with basic thermodynamic principles [17–21]. When it is necessary to describe the reorientation of martensite, phenomenological models either introduce two types of martensite – chaotic and oriented, or consider the existence of several orientational variants or martensite plates and formulate criteria for reorientation [22,23]. Unfortunately, the ability of macroscopic models to describe the entire set of functional properties of SMA at changing thermal and mechanical regimes are greatly limited due to the lack of direct consideration of the structure of martensite and the details of the mechanisms of transformation and reorientation. Microstructural models of the behavior of SMAs [24–26], based on accounting for the structure of these materials and the specific features of the deformation mechanisms, have greater capabilities. Although a large number of internal variables as well as the complexity of determining the material constants are the obstacles for using such models, there are a few successful examples of solving boundary value problems for SMA elements based on a microstructural model [27–29]. In the present work, the simulation of pseudoelastic behavior of an SMA cylinder at different strain rates accounting the influence of heat release/absorption during martensitic transformations as well as heat exchange conditions have been performed. Two approaches within the frames of the microstructural model were used. The first one did not involve solving a boundary value problem in the classical sense and could be considered as a zero-dimensional problem for a cylinder with a uniform temperature field. The second one is the completely coupled boundary value problem. Since solving the connected boundary value problems for SMA bodies is associated with a number of difficulties, a theoretical estimate of the critical radius for the cylinder at which the temperature field can be considered homogeneous at a given loading rate and heat transfer conditions was made. It could reduce the cost of time and computational resources

Microstructural model

The microstructural model used in this work is described in detail in [15,29], so here we will only briefly present its basic assumptions. An SMA representative volume consists of grains characterized by the orientation ω of the crystallographic axes relative to the selected laboratory basis. The grains consist of a high-temperature phase austenite and orientation variants of martensite formed from austenite by one of *N* crystallographically equivalent variants of transformation of the crystal lattice. The internal variables Φ_n are such that the volume fraction of the *n*-th variant of martensite equals Reuss' averaging scheme is used, so that the strain of a representative volume is calculated by averaging the strains over all grains. The strain of a grain is found as the sum of elastic, thermal, phase, and micro-plastic deformation associated with accommodation of martensite. Active plastic deformation is not taken into account in this work. Elastic and thermal strain of austenite martensite variants are calculated with the Duhamel-Neumann law. The phase strain of the *n*-th variant of martensite is proportional to the Bain strain D_n realizing the transformation of the crystal lattice and to the volume fraction of the *n*-th martensitic variant. Due to the Reuss' hypothesis, the phase strain of the grain is calculated by averaging the phase strains over all orientational variants of martensite:

$$\varepsilon^{gr\ Ph} = \frac{1}{N}\sum_{n=1}^{N} \Phi_n D_n. \quad (1)$$

For calculation of the micro-plastic strain another set of internal variables ε_n^{mp} , that are related to martensitic variants, are introduced. It is assumed that the micro-plastic strain of the grain can be calculated by the relation similar to Eq. (1):

$$\varepsilon^{gr\ mp} = \frac{1}{N}\sum_{n=1}^{N} \kappa\varepsilon_n^{mp}\mathrm{dev}(D_n), \quad (2)$$

where κ is the scaling factor (the material constant), "dev" means the deviator.

Constitutive equations for calculation the evolution of variables Φ_n and $\varepsilon_n^{mp}$are formulated in terms of thermodynamic forces that are the derivatives of the Gibbs thermodynamic potential *G* with respect to these variables. These equations are described in detail in [29].

The condition for the martensitic transformation expresses the equality of the thermodynamic driving force $F_n = -\frac{\partial G}{\partial \Phi_n}$ to some dissipative force F^{fr} caused by the resistance to the growth of martensitic crystals and responsible for the existence of the transformation hysteresis:

$$F_n = \pm F^{fr}, \quad (3)$$

where a sign "+" is taken for the direct and "−" for the reverse transformation. The material constant F^{fr} is calculated through the values of the characteristic temperatures and latent heat of the transformation. When the driving force changes due to variation of temperature and stress, increments of internal variables also change so that condition (3) remains satisfied.

Modeling of pseudo-elastic effect at different strain rates

Simulation of loading and unloading of the cylindrical specimen made of a NiTi SMA at temperature 290 K, when the alloy demonstrates pseudo-elastic behavior, was performed. According to the experimental procedure presented in [20], the cylinder radius is 2.5 mm, the strain rate varied from $3.3\cdot10^{-4}$ to $3.3\cdot10^{-2}$ s^{-1}, maximum value of achieved strain is 9 %. Material constants for SMA and characteristics of the vibrating system are presented in Table 1.

Table 1. Material constants used for modeling

Material constant	Value
Characteristic temperatures *Mf*, *Ms*, *As*, *Af*, K	224, 227, 262, 265
Latent heat q_0, MJ/m^3	-150
Number of martensite variants *N*	12
Lattice deformation matrix *D*	$\begin{pmatrix} 0.025 & 0.059 & 0.0456 \\ 0.059 & 0.025 & 0.0456 \\ 0.0456 & 0.0456 & -0.042 \end{pmatrix}$
Elastic modulus of austenite E_A, GPa	80
Elastic modulus of martensite E_M, GPa	25
Poisson's ratio of austenite ν_A	0.33
Poisson's ratio of martensite ν_M	0.45
Density of austenite ρ_A, density of martensite ρ_M ,kg/m^3	6500
Thermal-expansion coefficient of martensite, K^{-1}	$6.6 \cdot 10^{-6}$
Specific heat of austenite C_A, J/(kg K)	550
Specific heat of austenite C_M, J/(kg K)	500

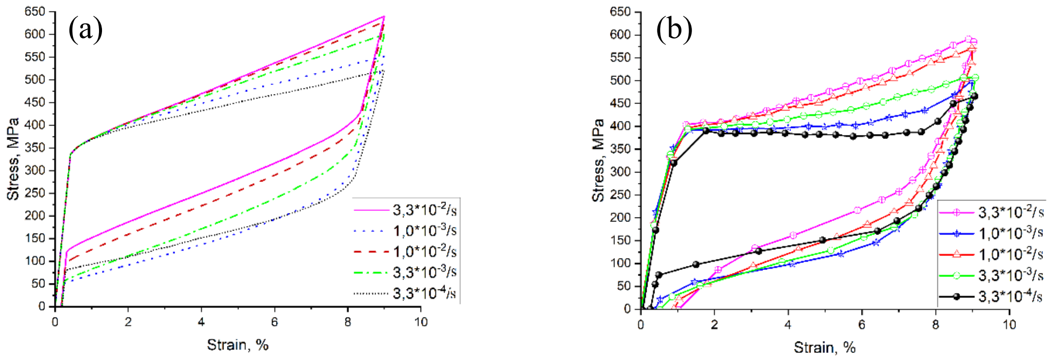

Fig. 1. Stress-strain diagrams for tension of SMA rod at different strain rates: (a) modeling with the microstructural model, (b) experiment [30]

In the first set of numerical experiments it is assumed for simplicity that the temperature in the SMA rod is uniform and the heat exchange is carried out through its surface in accordance with Newton's law. In this case one can write the thermal balance equation:

$$-(\rho_M\Phi_M + \rho_A(1-\Phi_M))(C_M\Phi_M + C_A(1-\Phi_M))\dot{T} + h_{conv}\frac{A_{SMA}}{V_{SMA}}(T - T_{amb}) = q_0\dot{\Phi}_M, \quad (4)$$

where ρ_M, ρ_A are the densities and C_M, C_A are the specific heats of martensite and austenite; Φ_M is the total volume fraction of martensite, T_{amb} is the ambient temperature, h_{conv} is the heat transfer coefficient, A_{SMA} and V_{SMA} are the area and volume of the SMA cylinder, dot means the time derivative. The value of h_{conv} was chosen as 80 W/(m^2 K) to be corresponding to a metal-air heat exchange [31].

The calculated stress-strain diagrams and the experimental results of Kan et al. [20] are presented on Fig. 1. One can see good agreement between the model curves and the experimental data. Deformation at higher strain rates causes greater heating of the specimen due to the release of latent heat of the direct martensitic transformation. This leads to increase of the maximum stress while the value of the phase yield limit (stress at which the elastic mechanism of deformation gives way to a phase one) does not change. As a result, the slope of the pseudo-elastic "flag" becomes steeper.

During unloading such a direct connection between the strain rate and cooling due to the reverse martensitic transformation is not observed. At a high strain rate, the sample does not have time to cool much more than the initial temperature. At a very slow strain rate, the sample does not cool much due to slow heat exchange with the environment. When the strain rate belongs to some medium range, the model specimen manages to cool down due to heat absorption caused by the endothermal reverse martensitic transformation.

Coupled boundary value problem

The results described in the previous section can be considered as the results of solving zero-dimension boundary value problem for the cylinder with the uniform temperature field. This seems acceptable for relatively thin samples and for characteristic deformation duration that assume temperature equalization along the radius of the cylinder. Otherwise, to calculate the deformation of the rod and distribution of temperature along the radius it is necessary to solve a connected boundary-value thermomechanical problem that takes into account heat exchange with the environment, thermal conductivity, the release of latent heat of transformation and the dependence of the change in phase state and deformation on the temperature and stress.

The cylindrical model element of the radius *R* that is in thermal contact with the environment has been considered. An axial force *F* acting along the axis *z* is supposed to be applied to the end of the cylinder (Fig. 2).

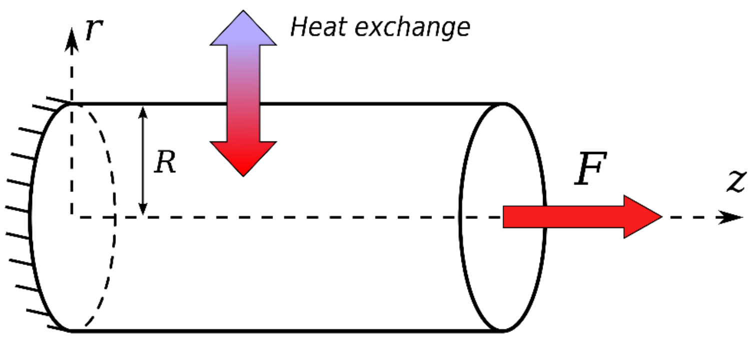

Fig. 2. Tension of a cylindrical rod, which is in thermal contact with the environment through the side surface (scheme)

It was assumed, that the cylinder was long enough so that the peculiarities of the force distribution at the end could be neglected and the cross-sections could be considered to remain flat. As a result, the longitudinal fibers' strain $\varepsilon_{zz} = \varepsilon$ does not depend on the radial coordinate *r*. In the cylindrical coordinate system *r*, φ, *z* non-zero can be strain components $\varepsilon_{rr}(r)$ and $\varepsilon_{\varphi\varphi}(r)$.

Conditions of static equilibrium of a rod under consideration are:

$$\int_S \sigma_{zz} dS = F, \quad (5)$$

where the integration is carried out over the entire cross section of the cylinder.

Let us assume that the constitutive relations of the material allow us to additively divide the total strain ε into elastic ε^{el} and non-elastic ε^{ne}components, so that $\varepsilon = \varepsilon^{el} + \varepsilon^{ne}$. Then, according to Hooke's law:

$$\sigma = E(\varepsilon - \varepsilon^{ne}), \tag{6}$$

where E is the effective Young's modulus, determined in this work by the "mixture rule" for elastic compliances:

$$E^{-1} = \Phi_M E_M^{-1} + (1 - \Phi_M) E_A^{-1}. \tag{7}$$

Increments of phase strain and internal variables were determined by the microstructural model described in the previous section. Formally, they can be written as:

$$\begin{aligned} \Delta\varepsilon^{ne}(r) &= F_1\big(\Delta T(r), \Delta\sigma(r), X(r)\big), \\ \Delta X(r) &= F_2\big(\Delta T(r), \Delta\sigma(r), X(r)\big), \end{aligned} \tag{8}$$

where the functions F_1 and F_2 are determined by the microstructural model and the symbol X denotes the set of internal variables $\Phi_n(\omega)$ and $\varepsilon_n^{mp}(\omega)$ for each of the n variants in each grain ω, correspondingly.

The variation of temperature over time was calculated by solving the heat conduction equation:

$$c\rho \frac{\partial T}{\partial t} = \frac{\partial}{\partial r}\left(\lambda \frac{\partial T}{\partial y}\right) + \dot{Q}, \tag{9}$$

where c is the specific heat capacity, ρ is the density and λ is the thermal conductivity. All these parameters were determined for mixture of martensite and austenite by the same way as it was previously done for the effective elastic compliance (7). The intensity of heat sources is determined by the latent heat of transformation of an SMA q_0 and the growth rate of the total volume fraction of martensite Φ_{M}, so that $\dot{Q} = -q_0 \dot{\Phi}_{\mathrm{M}}$.

It is assumed, that heat exchange with the environment occurs according to Newton's law:

$$\mp \lambda \frac{\partial T}{\partial y}\bigg|_{y=\pm\frac{h}{2}} = h_{conv}(T - T_{env}), \tag{10}$$

where h_{conv} is the heat transfer coefficient, T_{env} is the ambient temperature.

To solve the axis-symmetric problem, a discrete scheme was used. The radius R of the cylinder was divided into K equal segments, thereby determining the nodes of the spatial grid with coordinates $r_j = jR/K,\ j = 1, \dots K$. The stress, deformation and temperature fields at different points of the body were specified as a set of values at the grid nodes. During the calculation, at each loading step, the problem is divided into sub-problems with their own operators:

1. the mechanical equilibrium problem (an operator $\bar{M}$) – finding of the grid function $\sigma(r)$ for a given value of the applied force F and values $\varepsilon^{ne}(r_j)$ of inelastic deformation at the nodes using relations (5)–(7);
2. the "rheological" problem of finding inelastic deformation and density of heat sources (as well as internal variables) using the microstructural model (8) (an operator $\bar{F}$);
3. the thermal (heat diffusion) problem (an operator $\bar{T}$) – finding of the grid function $T(r_j)$ using the heat conductivity Eq. (9) under given heat exchange conditions (10) and known internal variables.

The search for such stress and temperature fields that satisfied simultaneously equations of equilibrium, thermal conductivity and boundary conditions changing during the step can be reduced to the problem of a fixed point of the operator $\bar{A}$:

$$\begin{pmatrix}\sigma(y)\\ T(y)\end{pmatrix} = \bar{A}\begin{pmatrix}\sigma(y)\\ T(y)\end{pmatrix}. \tag{11}$$

Here the operator $\bar{A}$ is a composition of operators $\bar{M}$, $\bar{F}$ and $\bar{T}$:

$$\begin{pmatrix}\sigma(r)\\ T(r)\end{pmatrix} = \begin{pmatrix}\bar{M}\left(\varepsilon^{ne}(r)\right)\\ \bar{T}\left(\dot{Q}(r)\right)\end{pmatrix}, \qquad \begin{pmatrix}\varepsilon^{ne}(r)\\ \dot{Q}(r)\end{pmatrix} = \bar{F}\begin{pmatrix}\sigma(r)\\ T(r)\end{pmatrix}. \tag{12}$$

In this work, this problem was solved by reducing it to finding the minimum of a functional of many variables [32]. The result of the solution were grid functions for stress, strain, temperature and internal variables of the microstructural model.

Boundary value problem: simulation of pseudo-elastic effect at different strain rates

The computational experiments described in the previous section were carried out by solving of the boundary value problem. The calculated stress-strain diagrams for a cylindrical sample with the radius 2.5 mm are presented on Fig. 3.

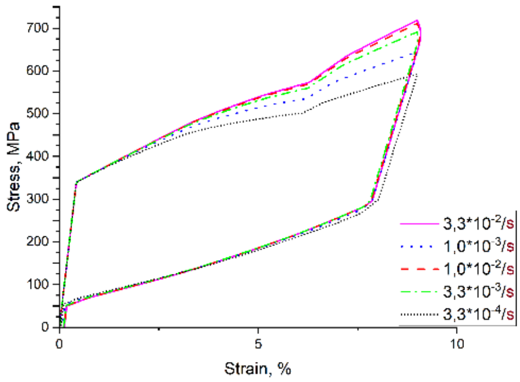

Fig. 3. Stress-strain diagrams for tension of SMA rod at different strain rates – calculated by solving coupled boundary-value problems

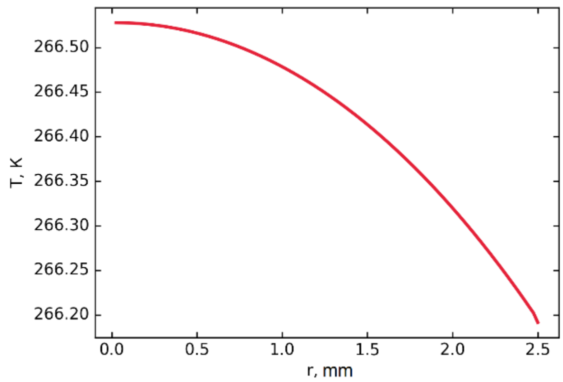

Fig. 4. Temperature distributions along the cylinder radius during deformation up to 9 % at strain rate $3.3{\cdot}10^{-2}$ s^{-1} at the end point of deformation

Although there are some peculiarities on the stress-strain curves in comparison with ones from Fig. 1(a), we can conclude that they are in a good qualitative and quantitative agreement with the results obtained previously. Apparently, at given deformation rates and heat exchange conditions, the temperature field in the sample under consideration does not differ much from the uniform one. The calculation results confirm this fact. Figure 4 shows the temperature distribution along the radius of the sample when the deformation achieved its maximum value of 9 % for the strain rate $3.3{\cdot}10^{-2}$ s^{-1}. The temperature difference in the center and on the surface does not exceed 0.3 K. The less deformation rate, the smaller is this difference.

Criteria for the need to solve the heat conduction equation

Considering the difficulties arising at solving coupled boundary value problems for SMA, the question emerges when it is possible to consider the temperature field to be uniform at given material constants, deformation rate and heat exchange conditions, and thus to avoid solving the heat conduction equation.

To calculate thermal conductivity in non-stationary modes, the Fourier and Biot criteria (numbers) are most often used. Initially, they were formulated for problems that did not imply the presence of internal heat sources. However, at present they are successfully used, for example, for calculating fuel rods of nuclear power plants [33].

The Biot number is the ratio of the internal thermal resistance of a body R/λ (a cylinder with the radius R in our case) to the external thermal resistance (resistance to heat transfer) $1/h_{conv}$:

$$Bi = \frac{h_{conv}R}{\lambda}. \quad (13)$$

This ratio indicates whether the temperature inside a body varies significantly in space when the body is heated or cooled over time by a heat flux at its surface. If the Biot number is small (much smaller than 1), the temperature field inside the body can be considered as nearly uniform. Requiring that Bi must not exceed 0.1, we obtain, for the material parameters presented in Table 1, that $R \leq 12.5$ mm. Therefore, the cylinder under consideration with the radius 2.5 mm satisfies this condition. The Biot number for this radius is 0.02.

The Fourier number characterizes the relationship between the rate of change of thermal conditions in the environment and the rate of redistributing of the temperature field inside the body under consideration. It depends on the characteristic size L of the body and its thermal diffusivity $\chi = \lambda/(\rho C)$:

$$Fo = \frac{\chi t_c}{L^2}, \quad (14)$$

where t_c is the characteristic time of change of external conditions. If we take the total deformation time to a given strain of 9 % as the characteristic time of the process, then for $L = R = 2.5$ mm and the strain rate $3.3 \cdot 10^{-2}$ s^{-1} we obtain $t_c \approx 2{,}7$ s and $Fo \approx 1{,}5$. It is known, that for the Fourier number significantly greater than 1.0 it can be assumed that there is enough time to establish the uniform temperature field across the entire characteristic length of the specimen.

Of course, 1.5 is not much greater than 1.0, nevertheless the model sample shows rather uniform temperature field at the chosen strain rate (Fig. 4). This may be due to the choice of the characteristic time for the characteristic length of the process.

One can try to evaluate the characteristic time and the Fourier number directly from the solution of the boundary value problem of heat conduction theory in dimensionless form with boundary conditions of the third kind. It is known [33] that application of the Fourier method gives the following solution for the cylinder:

$$\theta(x, Fo) = \theta_0 \cdot \sum_{k=1}^{\infty} A_k J_0(\mu_k x) \exp(-\mu_k^2 Fo), \quad (15)$$

$$A_k = \frac{2\, J_1(\mu_k)}{\mu_k \cdot \left(J_0^2(\mu_k) + J_1^2(\mu_k)\right)}, \quad (16)$$

where $x = r/R$ is dimensionless coordinate, $\theta(x,\tau) = T(x,t) - T_{amb}$ is the relative dimensionless temperature at time instant t, $\theta_0 = T_0 - T_{amb}$ is the relative dimensionless temperature at the initial moment of time, μ_k are positive roots of the equation:

$$\mu_k J_1(\mu_k) = Bi\, J_0(\mu_k), \tag{17}$$

(in ascending order). Here $J_\nu(x)$ are Bessel functions of the 1st kind of order ν.

Keeping only the first term of the series in Eq. (15) one can obtain for the cylinder

$$\theta(x, Fo) = \theta_0 A_1 J_0(\mu_1 x)\exp(-\mu_1^2 Fo), \tag{18}$$

$$A_1 = \frac{2Bi}{Bi^2 + \mu_1^2}. \tag{19}$$

Assuming that the permitted temperature difference on the surface (x = 1) and in the center (x = 0) is 1 K, for a given Bi = 0.02 it is possible to estimate the characteristic time. It occurred to be equal about 12 s. The corresponding $Fo \approx 8$ satisfies the condition of uniform temperature distribution. The values of the characteristic times and Fourier numbers for some other radii R are given in Table 2.

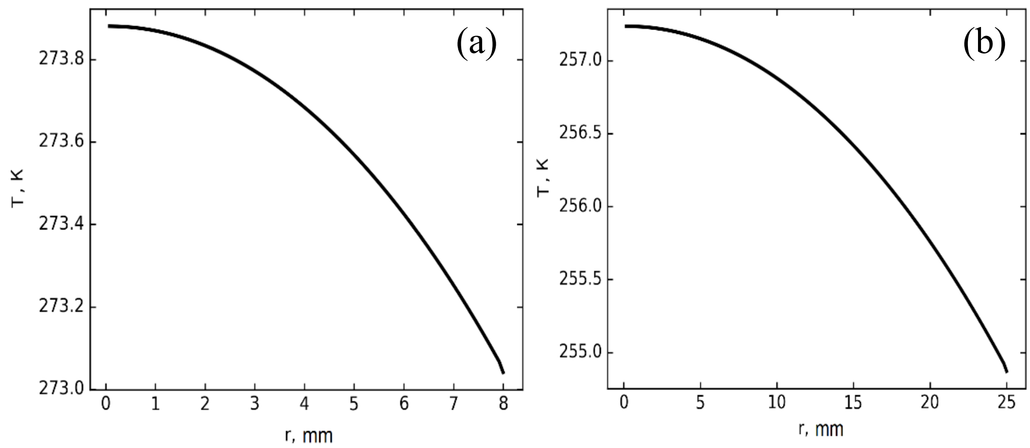

Fig. 5. Temperature distribution along the cylinder radius for R = 8 mm (a), R = 25 mm (b) at the final point of deformation. The strain rate $3.3{\cdot}10^{-2}$ s^{-1}

Figure 5 shows the calculated temperature distributing along the radius for R = 8 mm and R = 25 mm when the strain was 9 %. The maximum temperature difference in the center and on the surface of the sample ΔT in the first case was 0.8 K and in the second 2 K. The results for different radii are also presented in Table 2. One can note that for the permissible value ΔT = 1 K for the given strain rate and heat exchange conditions, the radius should not exceed 8 mm. This value seems to be quite large but although the strain rate $3.3{\cdot}10^{-2}$ s^{-1} is not extremely high, the deformation process takes only 2.7 s and the rod does not have enough time to cool significantly due to heat exchange with the environment.

Table 2. Characteristic times, Fourier numbers and maximum temperature difference

R, mm	2.5	3.0	8.0	9.0	25.0
t_c, s	12	15	49	–	259
Fo	8.0	5.5	2.5	2.3	1.4
ΔT, K	0.2	0.3	0.8	1	2

It should also be noted that the temperature fields obtained by solving the connected boundary value problem taking into account heat release and heat absorption demonstrates fairly good agreement with simple evaluations obtained using Fourier and Biot numbers excluding these processes.

Conclusions

1. The microstructural model, taking into account the release and absorption of the latent heat of martensitic transformations, is an adequate tool for describing the strain rate dependence of the pseudo-elastic behavior for SMAs. The strain rate growth forces an increase in the maximum achieved stress and the slope of the pseudo-elastic "flag". The obtained results are in good agreement with the available experimental data.
2. The microstructural model allows solving the boundary value problem of tension of an SMA cylinder in a fully coupled thermomechanical formulation, taking into account the heat exchange with the environment, the release of latent heat of transformation and thermal conductivity. It allowed simulating the pseudo-elastic stress-strain diagrams for different strain rates.
3. The Fourier and Biot criteria can be used to evaluate the critical radius of the cylinder for which, at a given strain rate and given heat exchange conditions, it is necessary to solve a fully coupled boundary value problem taking into account the thermal conductivity of the sample. The obtained estimates were confirmed by solving boundary value problems for cylinders of different radii.

References

1. Duerig TW, Melton KN, Stöckel D. (eds.) *Engineering Aspects of Shape Memory Alloys*. Butterworth-Heinemann; 1990.
2. Wanhill RJH, Ashok B. Shape Memory Alloys (SMAs) for Aerospace Applications. In: Prasad N, Wanhill R. (eds.) *Aerospace Materials and Material Technologies*. Singapore: Springer; 2017.
3. Tabrizikahou A, Kuczma M, Łasecka-Plura M, Farsangi EN, Noori M, Gardoni P, Li S. Application and modelling of Shape-Memory Alloys for structural vibration control: State-of-the-art review. *Constr. Build. Mater.* 2022;342(B): 127975.
4. Zhang W, Zhang Y, Zheng G, Zhang R, Wang Y. A Biomechanical Research of Growth Control of Spine by Shape Memory Alloy Staples. In: *BioMed Research International*. 2013. p.384894.
5. Petrini L, Bertini A, Berti F, Pennati G, Migliavacca F. The role of inelastic deformations in the mechanical response of endovascular shape memory alloy devices. *J. of Engineering in Medicine*. 2017;231(5): 391–404.
6. Otsuka K, Wayman CM. (eds.) *Shape memory materials*. Cambridge: Cambridge University Press; 1998.
7. Pieczyska EA, Tobushi H, Kulasinski K. Development of transformation bands in TiNi SMA for various stress and strain rates studied by a fast and sensitive infrared camera. *Smart Mater. Struct.* 2013;22: 035007.
8. Kato H. Latent heat storage capacity of NiTi shape memory alloy. *J. Mater. Sci.* 2021;56(13): 8243–8250.
9. Louia F, Michaelis N, Schütze A, Seelecke S, Motzki P. A unified approach to thermo-mechano-caloric characterization of elastocaloric materials. *J. Phys. Energy*. 2023:5(4): 045014.
10. He YJ, Sun QP. Frequency-dependent temperature evolution in NiTi shape memory alloy under cyclic loading. *Smart Mater. Struct.* 2010;19(11): 115014.
11. Yin H, He Y, Sun Q. Effect of deformation frequency on temperature and stress oscillations in cyclic phase transition of NiTi shape memory alloy. *J. Mech. Phys. Solids*. 2014;67: 100–128.
12. McCormick P, Liu Y, Miyazaki S. Intrinsic thermal-mechanical behaviour associated with the stress-induced martensitic transformation in NiTi. *Mater. Sci. Eng.: A.* 1993;167(1-2): 51–56.
13. Qiu C, Gong Z, Peng C, Li H. Seismic vibration control of an innovative self-centering damper using confined SMA core. *Smart Struct. Syst., Int. J.* 2020;25(2): 241–254.
14. Jin F, Zhao C, Xu P, Lin J. Nonlinear vibration of SMA hybrid composite beams actuated by embedded pre-stretched SMA wires with tension-bending coupling effect. *J. Sound Vib.* 2024;568: 117964.
15. Vukolov EA, Volkov AE, Evard ME, Belyaev FS. Simulation of bending for a shape memory alloy plate accounting influence of latent heat of transformation and heat exchange with an environment. *Mechanics of Composite Materials and Structures*. 2024;30(2): 198–221. (In-Russian)
16. Brinson L. One-dimensional constitutive behavior of shape memory alloys: Thermomechanical derivation with non-constant material functions and redefined martensite internal variable. *J. Intel. Mater. Syst. Struct.* 1993;4(2): 229–242.
17. Qidwai MA, Lagoudas DC. Numerical implementation of a shape memory alloy thermomechanical constitutive model using return mapping algorithms. *Int. J. Num. Methods in Engineering*. 2000;47(6): 1123–1168.

18. Boyd J, Lagoudas DC. A thermodynamical constitutive model for shape memory materials. Part I. The monolithic shape memory alloy. *Int. J. Plast.* 1996;12(6): 805–842.
19. Panico M, Brinson L. A three-dimensional phenomenological model for martensite reorientation in shape memory alloys. *J. Mech. Phys. Solids.* 2007;55(11): 2491–2511.
20. Chemisky Y, Duval A, Patoor E, Zineb TB. Constitutive model for shape memory alloys including phase transformation, martensitic reorientation and twins accommodation. *Mech. Mater.* 2011;43(7): 361–376.
21. Patoor E, Lagoudas DC, Entchev PB, Brinson LC, Gao X. Shape memory alloys, part I: General properties and modeling of single crystals. *Mech. Mater.* 2006;38(5–6): 391–429.
22. Oliveira SA, Savi MA, Kalamkarov AL. A three-dimensional constitutive model for shape memory alloys. *Arch. Appl. Mech.* 2010;80(10): 1163–1175.
23. Auricchio F, Bonetti E, Scalet G, Ubertini F. Theoretical and numerical modeling of shape memory alloys accounting for multiple phase transformations and martensite reorientation. *Int. J. Plast.* 2014;59: 30–54.
24. Patoor E, Eberhardt A, Berveiller M. Micromechanical modelling of superelasticity in shape memory alloys. *J. de Physique IV, C1.* 1996;6: 277–292.
25. Sun QP, Lexcellent C. On the unified micromechanics constitutive description of one-way and two-way shape memory effects. *J. de Physique IV, C1.* 1996;6: 367–375.
26. Huang M, Brinson LC. A multivariant model for single crystal shape memory alloy behavior. *J. Mech. Phys. Solids.* 1998;46(8): 1379–1409.
27. Volkov AE, Kukhareva AS. Calculation of the stress-strain state of a TiNi cylinder subjected to cooling under axial force and unloading. *Bulletin of the Russian Academy of Sciences: Physics.* 2008;72(9): 1267–1270.
28. Kukhareva A, Kozminskaia O, Volkov A. Calculation of the transformation plasticity strain in the shape memory cylinder. *E3S Web of Conferences.* 2020;157: 06016.
29. Volkov AE, Evard ME, Volkova NA, Vukolov EA. Microstructural modeling of a TiNi beam bending. *Materials Physics and Mechanics.* 2023;51(2): 177–186.
30. Kan Q, Yu C, Kang G, Li J, Yan W. Experimental observations on rate-dependent cyclic deformation of super-elastic NiTi shape memory alloy. *Mechanics of Materials.* 2016;97: 48–58.
31. Belyaev FS, Evard ME., Volkov AE, Starodubova MS. Modeling of vibration protection by shape memory alloy parts with an account of latent heat. *Smart Structures and Systems.* 2024;33(3): 243–251.
32. Ortega JM, Rheinboldt WC. *Iterative Solution of Nonlinear Equations in Several Variables.* Academic Press; 2014.
33. Lienhard JHV, Lienhard JHIV. *A Heat Transfer Textbook.* 5th ed. Cambridge MA: Phlogiston Press; 2020.

About Authors

Fedor S. Belyaev Sc
Candidate of Physical and Mathematical Sciences
Senior Researcher (St. Petersburg State University, St. Petersburg, Russia); Senior Researcher (Institute for Problems in Mechanical Engineering of the Russian Academy of Sciences, St. Petersburg, Russia)

Aleksandr E. Volkov Sc
Doctor of Physical and Mathematical Sciences
Professor (St. Petersburg State University, St. Petersburg, Russia)

Egor A. Vukolov
PhD Student (St. Petersburg State University, St. Petersburg, Russia)

Margarita E. Evard Sc
Candidate of Physical and Mathematical Sciences
Associate Professor (St. Petersburg State University, St. Petersburg, Russia)

Kristina V. Kudrina
Student (St. Petersburg State University, St. Petersburg, Russia)

Mariya S. Starodubova
Student (St. Petersburg State University, St. Petersburg, Russia)

MATERIALS PHYSICS AND MECHANICS RESEARCH ARTICLE

Submitted: September 4, 2024 Revised: November 4, 2024 Accepted: November 25, 2024

Copper-clad thermally stable Al-Zr wire, produced via copper electrodeposition

A.E. Medvedev[1]✉, K.E. Kiryanova[1], E.B. Medvedev[1], M.V. Gorbatkov[2], O.O. Zhukova[1], M.Yu. Murashkin[1]

[1]Ufa University of Science and Technology, Ufa, Russia

[2]LLC Krus-Zapad, Ufa, Russia

✉ medvedevandreyrf@gmail.com

ABSTRACT

Producing of the copper-clad aluminium wire made of Al-0.4Zr alloy via electrodeposition was studied. In order to ensure the adhesion of the copper after deposition, the intermediate Ni layer was applied to the aluminium wire surface. Formation of the composite wire with aluminium alloy core and copper sheath resulted in the increase of the ultimate tensile strength from 175 to 233 MPa, while also slightly decreasing electrical conductivity and notably decreasing ductility from 6 to 3 %. Annealing at 300 °C for 1 hour was performed to the composite wire to increase its ductility. Annealing resulted in the recovery of the mechanical properties back to the level of initial aluminium alloy wire, while electrical conductivity increased by 3.5 % IACS, allowing the newly produced composite wire to compete with the commercially produced copper-clad aluminium wires.

KEYWORDS

aluminium alloys • Al-Zr • copper-clad aluminium • copper-clad aluminium wire • electrodeposition mechanical strength • electrical conductivity • ductility

Acknowledgements. *M.Yu.M. acknowledges the support from the Russian Ministry of Science and Higher Education (state assignment FEUE-2023-0007).*

The authors express special gratitude to the Center for Collective Use "Nanotech" of the Federal State Budgetary Educational Institution of Higher Education "Ufa University of Science and Technology".

Citation: Medvedev AE, Kiryanova KE, Medvedev EB, Gorbatkov MV, Zhukova OO, Murashkin MYu. Copper-clad thermally stable Al-Zr wire, produced via copper electrodeposition. *Materials Physics and Mechanics*. 2024;52(5): 29–39.

http://dx.doi.org/10.18149/MPM.5252024_3

Introduction

Currently, the search for cheaper alternatives to copper as a material for electrical applications is a pressing issue in electrical and energy industries. The main disadvantage of copper is its high cost and high relative weight [1]. In order to avoid such complications, the choice of a substitute material is sometimes preferable.

Among the commercially available materials for the electrical purposes the aluminium and its alloys are close seconds after the copper [2–4]. The lower density and thus, lower weight of the products make aluminium attractive in terms of relative electrical conductivity being higher than that of copper alloys [5,6]. Unfortunately, aluminium is also characterized by significantly lower mechanical strength than copper, which limits the area of its application.

Attempts to increase the strength of aluminum by creating alloys based on it or by plastic deformation methods usually lead to a decrease in its electrical conductivity [7–9], and generally don't provide the level of mechanical strength similar to one of copper.

The other way to substitute the full-copper conductors is the use of layered metal composites, consisting of two or more different alloys [10–12]. Layered materials are attractive to researchers and developers since they are able to combine required properties of different alloys without their disadvantages. Layered materials can demonstrate simultaneously low density, high thermal and electrical conductivity, unique mechanical properties compare to monomaterials [13–15]. Implementing such approach to aluminium-copper composites allows to create a material with the reduced by 35–50% weight compared to copper while achieving electrical conductivity and mechanical strength surpassing even the best aluminium alloys [15,16].

Traditionally, materials with aluminum core and copper sheath are called copper-clad aluminium. They have found application in number of devices that require the use of high-frequency electrical currencies, since the main advantage of the copper-clad aluminium is the ability to navigate the electrical current along the thin copper layer, simulating the full-copper conductor with much lighter product [17–19].

The production of bimetallic aluminum-copper wires is associated with a number of difficulties, such as different thermal expansion coefficient, drastically different melting point, inclination towards both the formation of intermetallic of the contact areas and contact corrosion. One of the biggest concerns is the formation of the intermetallic Al-Cu particles that leads to a sharp decrease in the ductility and electrical conductivity of the composite. Annealing that is usually applied to cold-formed copper-clad wires to reduce the level of residual stress can amplify the negative effects mentioned above. Thus, the choice of temperature treatment is an important issue in the production of such materials [15,20].

The most common way of production the copper-clad aluminium wires (CCAW) is the joint deformation of the composite billet [21]. However, this method provides a few complications: necessity of keeping the aluminium-copper interface oxygen-free, the necessity of controlling the thickness and chemical composition of copper layer, the necessity of post-deformation annealing [18–20].

Another, a relatively new approach to obtaining copper-aluminum bimetallic wires can be the electrochemical deposition of copper onto an aluminum wire. Despite presenting a few old patents, the scientific literature is very scarce on this method of producing copper-clad aluminium wires. However, such approach may in theory provide more accurate control of the thickness of both the copper layer and the diffusion layer, as well as the purity of the copper layer.

In this study, an attempt was made to obtain a copper-clad aluminium wire by an electrochemical deposition of a copper onto aluminum alloy core. Usually, the technically pure aluminum is usually used base material [18], but in this work conductive and thermally-stable aluminum alloy Al-0.4Zr was used [22].

Materials and Methods

The Al-0.4 wt. % Zr alloy samples in a form of the rod with a diameter of 11 mm were cold-drawn to a diameter of 3.2 mm at room temperature. Before drawing, the rods were annealed at 375 °C for 120 h. Chemical composition of the aluminium alloy is presented in Table 1.

Table 1. Chemical composition of the Al-0.4Zr alloy

Element	Zr	Si	Fe	Mg	Cu	Zn	Mn	Cr	Ti	V	Al
Composition, wt. %	0.344	0.054	0.169	0.003	<0.002	0.033	0.010	0.001	0.0017	0.0145	99.37

The electrodeposition of the copper onto aluminium was performed in four steps: (i) surface preparation, (ii) surface clarification, (iii) Ni plating and (iv) Cu plating [23].

Surface preparation (i) included chemical degreasing in an alkali solution, subsequent washing in hot and then cold water. Surface clarification (ii) was carried out in 10 % nitric acid solution, also functioning as activation process. The Ni plating (iii) was performed at 40 °C in a sulfuric acid electrolyte ($NiSO_4$) for 3 min at a current density of 5 A/dm^2. The Cu plating (iv) was performed at room temperature in a sulfuric acid electrolyte ($CuSO_4$) for 2 h at a current density of 5 A/dm^2 until the copper layer obtained 90 ± 10 μm thickness. The control of the Cu layer thickness was performed by optical microscopy analysis of cross-sections at different electrodeposition time.

The choice of copper sheath thickness was based on the minimum current frequency that provides the skin effect at such skin depth. According to the skin depth calculations, the 100 μm of copper provides the skin effect at current frequences from 400 kHz and higher, which is the frequency range for the audio cables, audio equipment, high frequency current equipment, wireless charging devices etc. The introduction of the nickel layer is a necessary stage of electrochemical copper deposition onto aluminum. Copper cladding of aluminium without transition layers is possible but complicated by the reasonably high difference in the electronegativity of Cu and Al, causing corrosion on their interface [1]. The thickness of the nickel layer in the state after copper cladding was measured to be around 20–25 μm.

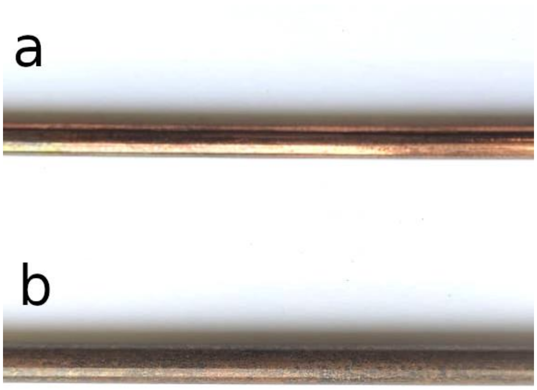

Fig. 1. Appearance of the Al-0.4Zr alloy wire after copper deposition (a) and subsequent annealing (b)

Optical microscopy was performed on an Olympus Q15OR light microscope. Scanning electron microscopy (SEM) was performed on a Tescan MIRA V microscope at an accelerating voltage of 15 kV.

Annealing was performed in atmosphere furnace Nabertherm B180 at 300 °C for 1 h. The choice of time and temperature was based on the study [21]. The samples after annealing were cooled into water to remove the dross from the surface. The appearance of the sample's surface is presented in Fig. 1.

Tensile tests were carried out on an Instron 5589 testing machine at room temperature. At least 3 samples were tested for each condition.

The specific electrical resistance of the material under study was measured in accordance with IEC 60468:1974 [24]. Straightened samples of at least 1 m in length were selected. The electrical resistivity of the studied material was measured in accordance with the IEC 62641:2023 standard [22]. The electrical conductivity value of the samples relative to annealed copper (International Annealed Copper Standard) was calculated using equation:

$$IACS = \omega_{Al} / \omega_{Cu} * 100\ [\%], \quad (1)$$

where ω_{Al} is the experimentally determined value of the electrical conductivity of the aluminum alloy sample, ω_{Cu} is the electrical conductivity of annealed copper, equal to 58 MSm/m. Electrical conductivity measurements were taken with an instrument operating at a single frequency of 50 Hz, while skin effect measurements require an instrument operating at varying current frequencies. In addition, the skin effect at a copper layer thickness of about 100 μm begins to appear at current frequencies from 400 kHz [25]. Thus, in this study, the conductivity of the entire wire was measured; the skin effect was not directly measured.

Results and Discussion

Figure 2(a) shows the results of optical metallography of bimetallic wire before and after annealing. According to Fig. 2(a), electrochemical deposition of nickel and copper onto aluminum alloy wire is characterized by the absence of pores, large intermetallic particles or other undesirable defects at both Al-Ni and Ni-Cu interfaces. The Al-Ni interface is characterized by the flake-like particles seemingly protruding into Ni layer, while the Ni-Cu interface appears smooth and continuous.

Annealing (Fig. 2(b)) results in the overall thinning of the copper-nickel shell. Two simultaneous processes occur: Ni-Cu interdiffusion and Cu layer thinning. Ni-Cu interdiffusion is resulted in visible thickening of the Ni layer, while Cu thinning occurs due to the surface oxidation and subsequent dross removal after heat treatment. While total width of Cu+Ni layer decreases from 90.5 ± 2.5 to 73.0 ± 2.5 μm and the thickness of copper layer decreases from 73.0 ± 2.5 to 52.0 ± 2.5 μm, the thickness of the Ni layer seemingly increases from 17.5±2.5 to 21.0 ± 2.5 μm indicating the interdiffusion between Ni and Cu layers.

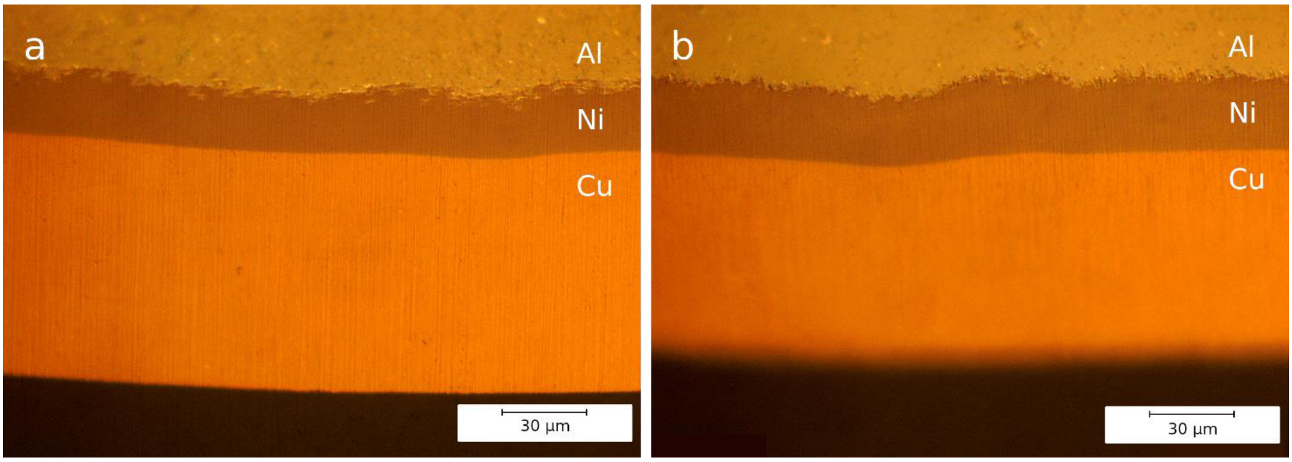

Fig. 2. Optical metallography of the cross-section of an copper-clad Al-0.4Zr alloy wire before (a) and after annealing (b)

The recommended fraction of the copper in aluminum-copper wires lies within the interval of 10–15 % [13,26]. In current study, the copper fraction are 8.4 and 6.1 % before and after annealing respectively (Table 2). The decrease in the copper content due to thinning of the copper layer occurs due to oxidation of the outer layer of the wire during annealing and the formation of carbon/scale on the copper surface. As a result of rapid cooling in water, the scale is removed from the surface, taking with it a certain amount of the copper that has entered the reaction. This effect is well known and described in literature.

Table 2. Changes in the Ni-Cu layer thickness during the annealing

State	Layer thickness, µm			Fraction in the cross-section, %		
	Ni+Cu	Ni	Cu	Ni+Cu	Ni	Cu
Al-0.4Zr copper-clad	90.5±2.5	17.5±2.5	73.0±2.5	10.3±0.3	1.9±0.3	8.4±0.3
Al-0.4Zr copper-clad and annealed	73.0±2.5	21.0±2.5	52.0±2.5	8.6±0.3	2.5±0.3	6.1±0.3

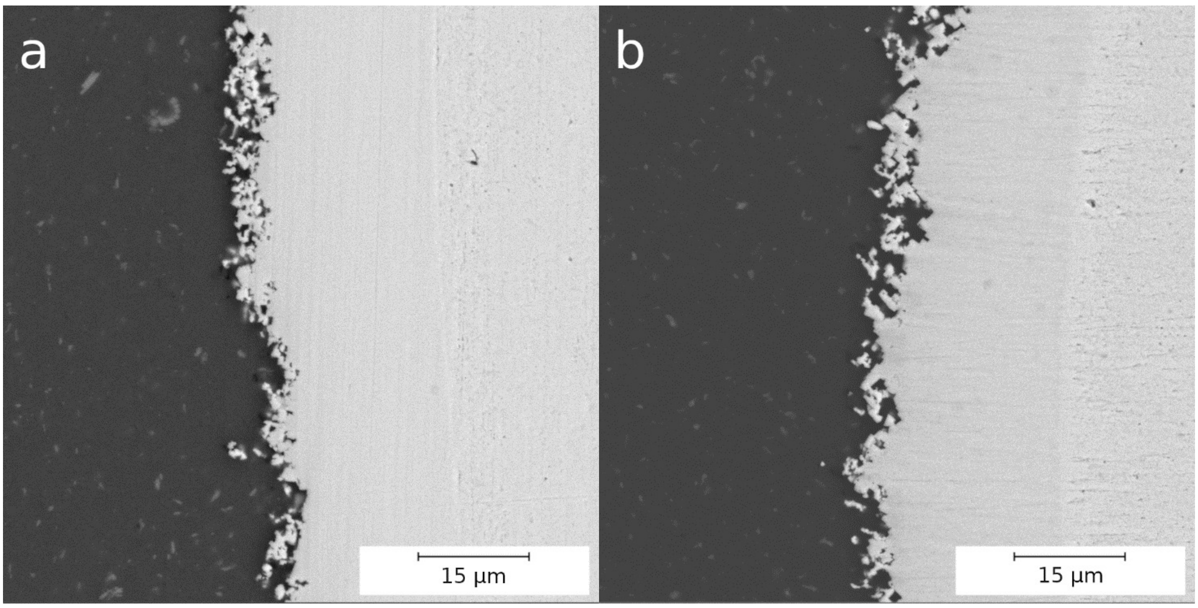

Fig. 3. Al-Ni-Cu interface in the wire after copper electrodeposition (a) and subsequent annealing (b), SEM

The results of the SEM examination of the wires' cross-section are presented in Fig. 3. The Al-Ni interface is characterized by the distinct flakes of Ni or Ni-based phase particles. The interface is also uneven which can be attributed to the initial surface of the Al alloy wire, that was not subjected to any addition surface treatment after cold drawing. Within the Al alloy wire volume intermetallic particles are clearly seen. The nature of these particles is most probable. Al_3Fe, $Al_{12}Fe3Si$ or $Al_9Fe_2Si_2$, forming in 1xxx series and Al-Zr system alloys, that conventionally have certain amount of Fe and Si in their chemical composition [4], just like in this study (Table 1). Since it was not the subject of this study, the exact phase composition of the Al wire was not established. The Ni-Cu interface is smooth and only distinguishable by the fact that copper, being softer material, was more roughly polished rather than Ni.

Annealing at 300 °C for 1 hour resulted in coagulation of the flakes at the Al-Ni interface, as well as in increased porosity of the Cu layer (Fig. 3(b)).

Table 3 presents the properties of Al-0.4Zr wire samples before and after copper deposition. The ultimate tensile strength (UTS) of Al-0.4Zr alloy wire is 175 MPa, level of electrical conductivity is 58.9 %IACS. Such combination while quite high in both parameters is not unique for aluminium alloys. The relative elongation before failure of Al-0.4Zr wire is decent – 6.1 %, allowing this composite wire to be recommended for practical applications. The formation of the Ni+Cu layer resulted in the moderate electrical conductivity decrease down to 57.1 %IACS with simultaneous increase in UTS up to 233 MPa, also significantly reducing the composite's ductility down to 3.1 %. The introducing of copper into composite material led to increase in mechanical and electrical properties, while either introducing the Ni or Al-Ni intermetallic particles resulted in the drop of ductility. In order to increase the ductility level, the annealing of the copper-clad aluminium alloy wire was performed.

As a result of thermal treatment, the ductility and the UTS of the material increased to the initial level (6.3 % and 176 MPa, respectively), electrical conductivity exceeded the original wire level (62.6 % IACS). The tensile strength of the composite wire after annealing has decreased, though remaining within the error limits relative to the original uncoated Al-0.4Zr wire.

The most probable reason for the decrease in electrical conductivity is the presence of a nickel layer between the copper and aluminum layers. In addition to the fact that the electrical conductivity of nickel itself is very low, nickel forms a number of continuous solid solutions with copper, on the one hand, and a number of intermetallic phases with aluminum, on the other. Both the solid solution and the intermetallic phases are characterized by reduced electrical conductivity relative to the base material. All of the above reasons could, both together and separately, negatively affect the electrical conductivity of copper-plated wire. The increase in electrical conductivity due to annealing occurred, most likely, due to the processes of recovery and recrystallization in the aluminum alloy, and the processes of recovery in the copper layer. Annealing at such parameters, as shown in the literature, is insufficient for noticeable changes to occur at the interface of materials, therefore, a potential decrease in electrical conductivity due to these processes was not recorded.

Similar method of copper deposition was applied to the Al-0.5 wt. % Fe alloy, produced by electromagnetic casting [27]. While having almost the same level of electrical and mechanical properties in the initial state (cold-drawn wire), Al-Zr based bimetallic wire demonstrates both higher electrical conductivity and ductility in the annealed state (Table 3).

Table 3. Physical and mechanical properties of copper-clad Al-0.4Zr alloy wires

Sample	Electrical properties		Mechanical properties		
	RER, $\Omega \cdot mm^2/m$	IACS, %	σ_{YS}, MPa	σ_{UTS}, MPa	δ, %
Al-0.4Zr wire	0.02929	58.9±0.4	157±3	175±4	6.1±0.5
Al-0.4Zr (copper-clad)	0.03020	57.1±0.5	167±19	233±11	3.0±0.5
Al-0.4Zr (copper-clad) annealed	0.02754	62.6±0.6	153±3	176±6	6.3±0.3
AW [29]	0.02952	58.4±0,4	170±12	204±14	5.3±0.2
CCAW [27]	0.02996	57.5±0.5	185±6	187±7	1.5±0.1
CCAW-A [27]	0.02831	60.9±0.3	135±5	184±6	4.3±0.6
Al-10%Cu hard-drawn [28]	-	>62.9	-	110−205	>1
Al-10%Cu annealed [28]	-	>62.9	-	135−170	>5-15
Al-15%Cu hard-drawn [28]	-	>64.4	-	110−205	>1
Al-15%Cu annealed [28]	-	>64.4	-	135−170	>5−15

According to the commercial prospects the requirements for the copper-clad aluminium wires are as follows: electrical conductivity is 62.9...64.4 %, tensile strength is 110...205 MPa, and for ductility is 1...15 % [28], depending on the state (hard-drawn or annealed) and copper content.

The copper-clad Al-0.4Zr alloy wire after annealing demonstrates the combination of UTS, electrical conductivity and ductility on par with the commercially produced Al-10 %Cu copper-clad wire in the annealed state while having almost twice as low copper content (6.1 %) (Table 3).

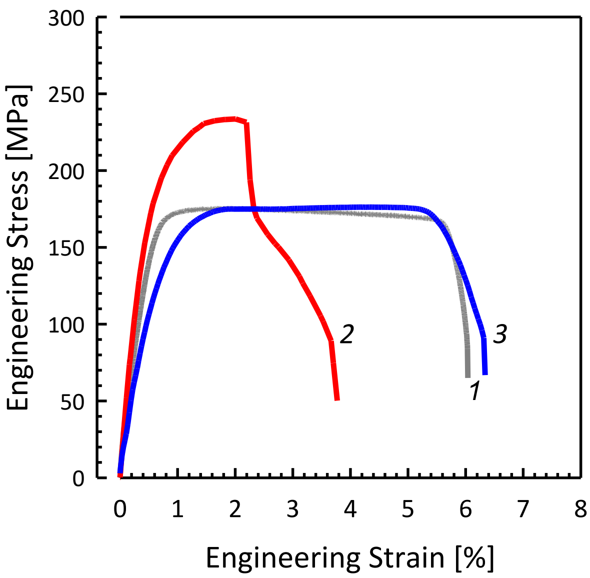

Fig. 4. Engineering stress-strain curves of initial Al-0.4Zr wire (1), copper-clad wire before (2) and after annealing (3)

Figure 4 shows the engineering stress-strain curves of copper-clad Al-0.4Zr wire samples before and after annealing, as well as the data for the original cold-drawn wire. The tensile test for the uncoated wire is represented by the curve characteristic for the aluminium alloys. Samples obtained by the electrodeposition method are characterized by the higher ultimate tensile strength and two-stage fracture – one being caused by the Cu-Ni layer fracture, and the latter by the fracture of aluminium wire itself. Such behavior during tensile tests contributed to the decrease of the elongation to failure.

Annealing at 300 °C for 1 h results in the staged character of the tensile test curve, meaning that the fracture of the wire occurs as a whole. The level of ultimate tensile strength and elongation to failure of the CCAW-A returns to the levels of initial wire, with only exception being lower level of yield stress.

The results of fractographic analysis are presented in Fig. 5. Peeling of the Ni+Cu layer from the Al alloy core could be observed in the as-deposited state. The Ni+Cu layer doesn't function as a whole having seemingly brittle cracks. Such cracks are not observed in the annealed stste (Fig. 5(b)) although the disjoinment of the Ni+Cu and Al alloy layer occurs as well.

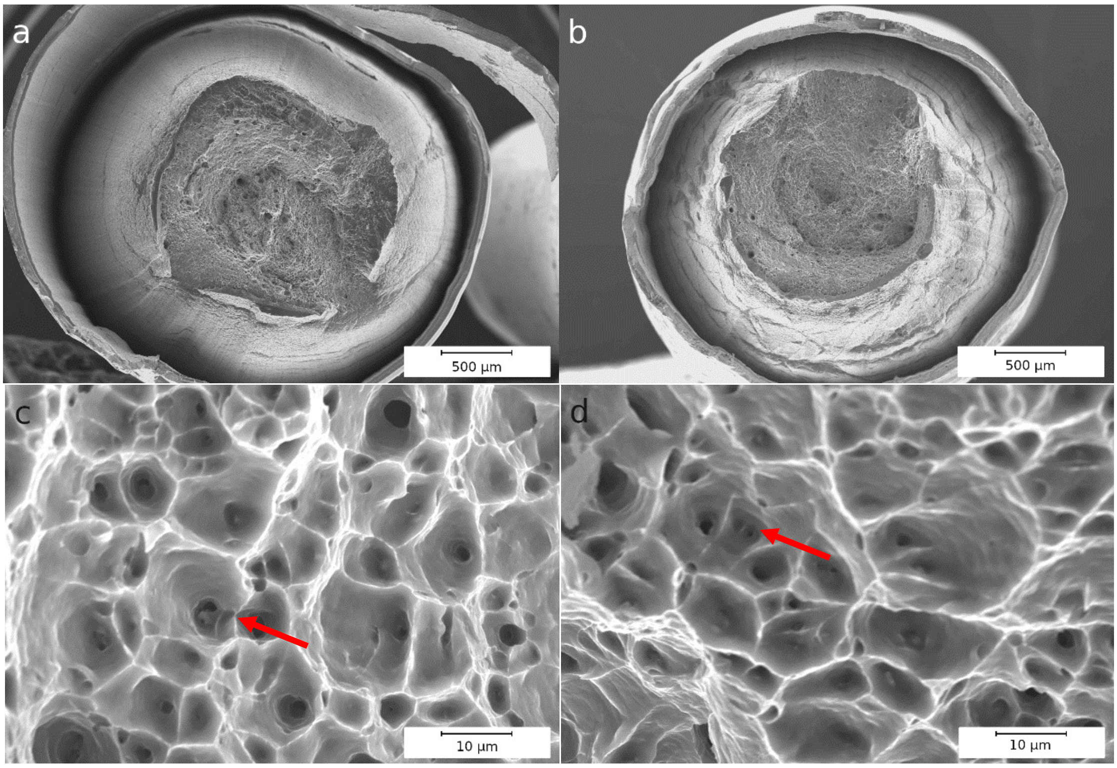

Fig. 5. Fractographic images of the copper-clad wire before (a,c) and after annealing (b,d), SEM

The detailed study of the aluminium alloy wire core demonstrats characteristic dimple fracture both in samples before (Fig. 5(c)) and after annealing (Fig. 5(d)), which along with the evidence presented before allows to establish the ductile nature of the aluminium alloy wire core fracture.

Figure 5(d) demonstrates the presence of the coarse particles in the root of the certain dimples, meaning that the fracture starts at them.

The fractographic images of the Cu-Ni alyer in the samples before and after annealing are presentyed in Fig. 6. Ni layer in sample before annealing demonstrates the clean, flat surface, indicating brittle character of the layer fracture. Cu layer fracture surface is characterized by the presence of so-called "river patterns" which also indicate the brittle nature of the fracture [30]. At the same time Cu layer is also characterized by the wave-like patterns on the fracture surface. Since Cu layer has multiple pit-like lines along the surface, it would be safe to assume that the fracrure started in the Ni layer and the transferred to the Cu layer, in which the fracture occurred in semi-brittle way.

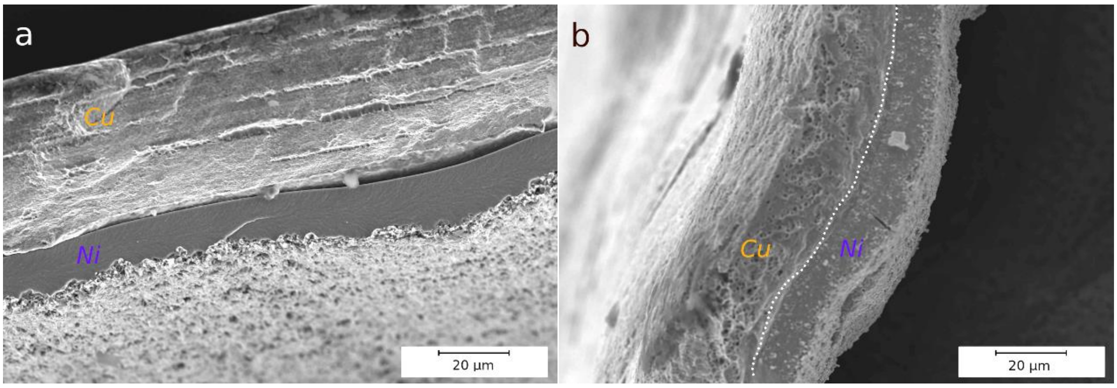

Fig. 6. Fractographic images of the Cu-Ni layer in the copper-clad wire before (a) and after annealing (b), SEM

Fracture surface of the Cu-Ni layer after annealing is presented in Fig. 6(b). Surface of both Ni and Cu layer looks spongy, most likely due to the porosity that was formed during the annealing – no protective atmosphere or vacuum was applied, thus the oxygen migration into Cu and Ni layers occurred. Despite Ni layer having flakes on the fracture surface, it also posesses the fracture, demonstrating the semi-brittle type of the fracture [31].

Conclusions

This paper studies the novel method of obtaining copper-clad aluminium wires via electrodeposition. The thermally stable Al-Zr alloy was used as a base material for the copper electrodeposition. The choice of the Al alloy was dictated by the necessity of increasing the overall strength and thermal stability of the composite wire. The proposed method is promising for producing copper-coated aluminum wires due to ability to precisely control the copper layer thickness down to tens of microns, as well as the chemical composition of this layer.

1. Samples of a copper-clad wire based on Al-0.4Zr alloy wire coated with copper using the electrodeposition method were obtained. The Ni layer was applied between aluminium and copper layers in order to eliminate electrochemical corrosion between aluminium and copper. The copper content in the cross-section is about 8 %, and there are no visible defects/intermetallic particles at the metal interfaces.

2. Electrochemical copper deposition onto Al-0.4Zr aluminum wire while having positive effect on mechanical strength and electrical conductivity, significantly (twofold) reduced the ductility of the composite wire, as well as causing the brittle nature of the

samples fracture. Annealing of composite wire at 300 °C for 1 h resulted in an increase in electrical conductivity up to 62.6 % IACS, while relative elongation before failure and UTS values recovered to the initial wire level – 6.3 % and 176 MPa, respectively.

3. The studied composite wire demonstrates the combination of UTS, electrical conductivity and ductility on par with the commercially produced Al-10%Cu copper-clad wire in the annealed state. Change of the core material from commercially pure Al to thermally stable Al-Zr alloy allowed to achieve this with almost twice as low copper content (6.1 %). Moreover, due to the use of Al-Zr alloy, the resulting wire will retain its strength properties stable even at elevated temperatures, at least up to 150 °C.

References

1. Weisenberger L, Durkin B. *Copper Plating, Surface Engineering*. ASM International; 1996.
2. Draissia M, Debili MY. *Study of solid-solution hardening in binary aluminium-based alloys*. 2005.
3. Dursun T, Soutis C. Recent developments in advanced aircraft aluminium alloys. *Mater Des.* 2014;56: 862–871.
4. Polmear I, StJohn D, Nie JF, Qian M. *Light Alloys: Metallurgy of the Light Metals*. 5th ed. Butterworth-Heinemann; 2017.
5. Shikagawa T, Itoh G, Suzuki S, Kuroda H, Horikoshi T. Effect of Small Additions of Fe on the Tensile Properties and Electrical Conductivity of Aluminium Wires. *Materials Science Forum*. 2006;519–521: 515–518.
6. Matveeva I, Dovzhenko N, Sidelnikov S, Trifonenkov L, Baranov V, Lopatina E. Development and Research of New Aluminium Alloys with Transition and Rare-Earth Metals and Equipment for Production of Wire for Electrotechnical Applications by Methods of Combined Processing. In: Sadler BA. (eds) *Light Metals 2013*. Cham: Springer; 2016. p.443–447.
7. Valiev RZ, Murashkin M, Sabirov I. A nanostructural design to produce high-strength Al alloys with enhanced electrical conductivity. *Scr Mater.* 2014;76: 13–16.
8. Medvedev AE, Murashkin MYu, Enikeev NA, Ovid'ko IA, Valiev RZ. Strength and electrical conductivity of ultrafine-grained aluminum alloy Al-2Fe subjected to annealing and straining. *Materials Physics and Mechanics*. 2015;24(3): 297–307. (In Russian)
9. Sabirov I, Murashkin MY, Valiev RZ. Nanostructured aluminium alloys produced by severe plastic deformation: New horizons in development. *Materials Science and Engineering A*. 2013;560: 1–24.
10. Qi Y, Lapovok R, Estrin Y. Microstructure and electrical conductivity of aluminium/steel bimetallic rods processed by severe plastic deformation. *J Mater Sci*. 2016;51: 6860–6875.
11. Pambhar AC, Valaki JB. Experimental studies of formability in single point incremental forming of Cu-Al bimetallic sheets. To be published in *Mater Today Proc*. [Preprint] 2023. Available from: doi.org/10.1016/j.matpr.2023.07.158.
12. Lapovok R, Ng HP, Tomus D, Estrin Y. Bimetallic copper-aluminium tube by severe plastic deformation, *Scr Mater*. 2012;66: 1081–1084.
13. Sasaki TT, Morris RA, Thompson GB, Syarif Y, Fox D. Formation of ultra-fine copper grains in copper-clad aluminum wire. *Scr Mater*. 2010;63: 488–491.
14. Eivani AR, Mirzakoochakshirazi HR, Jafarian HR. Investigation of joint interface and cracking mechanism of thick cladding of copper on aluminum by equal channel angular pressing (ECAP). *Journal of Materials Research and Technology*. 2020;9: 3394–3405.
15. Hug E, Bellido N. Brittleness study of intermetallic (Cu, Al) layers in copper-clad aluminium thin wires, *Materials Science and Engineering A*. 2011;528: 7103–7106.
16. Gueydan A, Hug E. Secondary creep stage behavior of copper-clad aluminum thin wires submitted to a moderate temperature level. *Materials Science and Engineering A*. 2018;709: 134–138.
17. Li K, Liu X, Zhao Y. Research status and prospect of friction stir processing technology. *Coatings*. 2019;9(2): 129
18. Cho YR. Clad Metals: Fabrication, Properties, and Applications. *Metals*. 2021;11(8): 1186.
19. Lee JE, Bae DH, Chung WS, Kim KH, Lee JH, Cho YR. Effects of annealing on the mechanical and interface properties of stainless steel/aluminum/copper clad-metal sheets. *J Mater Process Technol*. 2007;187–188: 546–549.
20. Gueydan A, Domengès B, Hug E. Study of the intermetallic growth in copper-clad aluminum wires after thermal aging. *Intermetallics*. 2014;50: 34–42.

21. Fu X, Wang R, Zhu Q, Wang P, Zuo Y. Effect of Annealing on the Interface and Mechanical Properties of Cu-Al-Cu Laminated Composite Prepared with Cold Rolling. *Materials*. 2020;13(2): 369.
22. International Standard. SIST EN IEC 62641:2023. *Conductors for overhead lines - Aluminium and aluminium alloy wires for concentric lay stranded conductors*. 2023.
23. Kravchenko DV, Kozlov IA, Nikiforov AA. Methods for preparing the surface of aluminium alloys for electroplating (review). *Proceedings of VIAM*. 2021;6: 82–99. (In Russian)
24. *International Standard*. IEC 60468:1974. *Method of measurement of resistivity of metallic materials*. 1974.
25. Hayt WH, Buck JA. *Engineering Electromagnetics*. 8th ed. McGraw-Hill Education; 2011.
26. Chu D, Zhang J, Yao J, Han Y, Wu C. Cu–Al interfacial compounds and formation mechanism of copper cladding aluminum composites. *Transactions of Nonferrous Metals Society of China*. 2017;27: 2521–2528.
27. Medvedev AE, Kiryanova KE, Medvedev EB, Gorbatkov MV, Motkov MM. Microstructure and properties of the Al-0,5 wt.% Fe alloy wire, copper-clad by electrochemical deposition. To be published in *International Journal of Lightweight Materials and Manufacture*. [Preprint] (2024). Available from: doi.org/https://doi.org/10.1016/j.ijlmm.2024.08.001.
28. *MWS Wire Industries*. *Copper Clad Aluminium*. Available from: https://mwswire.com/copper-clad-aluminum/ [Accessed 17th October 2023].
29. Medvedev AE, Zhukova OO, Fedotova DD, Murashkin MYu. The mechanical properties, electrical conductivity, and thermal stability of a wire made of Al–Fe alloys produced by casting into an electromagnetic crystallizer. *Frontier Materials & Technologies*. 2022;3: 96–105. (In Russian)
30. François D. Fracture mechanisms of metals. In: *Statistical Models for the Fracture of Disordered Media*, Elsevier; 1990. p.59–65.
31. Ardebili H, Zhang J, Pecht MG. Encapsulation defects and failures. In: *Encapsulation Technologies for Electronic Applications*. Elsevier; 2018. p.259–315.

About Authors

Andrey E. Medvedev Sc
Candidate of Physical and Mathematical Sciences
Senior Researcher (Ufa University of Science and Technology, Ufa, Russia)

Kristina E. Kiryanova
Master Student (Ufa University of Science and Technology, Ufa, Russia)

Evgenii B. Medvedev
Candidate of Technical Sciences
Associate Professor (Ufa University of Science and Technology, Ufa, Russia)

Mikhail V. Gorbatkov
Engineer (LLC Krus-Zapad, Ufa, Russia)

Olga O. Zhukova Sc
Engineer (Ufa University of Science and Technology, Ufa, Russia)

Maxim Yu. Murashkin Sc
Candidate of Technical Sciences
Senior Researcher (Ufa University of Science and Technology, Ufa, Russia)

MATERIALS PHYSICS AND MECHANICS RESEARCH ARTICLE

Submitted: August 1, 2024 Revised: September 5, 2024 Accepted: September 30, 2024

The heat treatment effect on the spectral and luminescent properties of sodium-germanate glass with CdS

A.N. Babkina ✉, **R.D. Kharisova**, **V. G. Sheremet, O.S. Barbash**, **K.A. Zhikov**, **K.S. Zyryanova**

ITMO University, St. Petersburg, Russia

✉ babkina.anastasya@bk.ru

ABSTRACT

The nucleation of CdS quantum dots in a sodium germanate glass matrix by means of isothermal treatment is demonstrated. It is shown that a sufficiently high concentration of cadmium ions in the initial glass results in nucleation of fairly big quantum dots. The luminescence of CdS is mainly of a trap nature and is localized in the region of 600–900 nm. Excess cadmium ions and nucleation of quantum dots in oxide glass lead to the defect nature of the luminescence bands: mainly associated with interstitial cadmium ions (ICd), the donor-acceptor pairs [V_{Cd}–V_S], and deep trap levels created by volume cadmium vacancies. The luminescence quantum yield of CdS quantum dots is less than 1 %, indicating that nonradiative recombination of charge carriers is the dominant process.

KEYWORDS

cadmium sulfate • germanate glass • heat-induced crystallization • trap luminescence

Acknowledgements. *The research was carried out at the expense of a grant from the Russian Science Foundation, No. Russian Science Foundation (Grant No. 24-43-20020).*

Citation: Babkina AN, Kharisova RD, Sheremet VG, Barbash OS, Zhikov KA, Zyryanova KS. The heat treatment effect on the spectral and luminescent properties of sodium-germanate glass with CdS. *Materials Physics and Mechanics*. 2024;52(5): 40–47.

http://dx.doi.org/10.18149/MPM.5252024_4

Introduction

CdS quantum dots (QDs) have attracted much attention as a special class of nanoparticles due to their luminescent and semiconducting properties [1–3]. Due to the intense luminescence, continuous excitation spectrum, controllable emission band location, and ease of functionalization for tissue labeling, CdS QDs have been becoming promising for medical imaging and disease treatment [4–6]. Since CdS has a wide band gap, it is used as a window material for heterojunction solar cells, avoiding the recombination of photogenerated charge carriers and improving the efficiency of solar cells [7]. Due to its high photostability, CdS can be a basis for light-emitting diodes, photodetectors, and sensors [8,9].

The photoluminescence of QDs is very intense and occurs with a fairly narrow spectral profile: the full width at half maximum (FWHM) is usually less than 40 nm [10]. By choosing the chemical composition (i.e. the band gap of the bulk material) and the size of the nanocrystals, it is possible to tune the radiation energy so that it falls in the spectral region from UV to IR. Optical and electronic processes in a semiconductor nanocrystal include radiative and nonradiative recombination of excitons; radiative and nonradiative recombination of surface defect states, which in turn can be an oxidizing surface trap (electron trap) and a reducing surface trap (hole trap) [11].

A surface passivation procedure is used to reduce the influence of defects on the optical and spectral properties of QDs and to reduce the probability of nonradiative relaxation of photoexcitation. Quite a few methods of surface passivation have been considered to date. In this paper, we will focus on the nucleation of quantum dots in an inorganic glass matrix [12,13], which was initially intended as protection of the QD surface from interaction with an oxygen-containing atmosphere and stabilization of the quantum dot structure [14–16].

As off today, only three works have been devoted to the nucleation of cadmium chalcogenide quantum dots in germanate glass [17–19], but none of them demonstrate the luminescent and optical properties of the resulting nanocrystals. Alkali metal oxides are usually added to pure GeO_2 [20–22] to improve the crystallization ability of the germanate glassy matrix. Since glass synthesis is usually carried out in a reducing atmosphere to decrease sulfur volatility, the use of lithium ions in large quantities is contraindicated. Therefore, sodium oxide was used in the germanate matrix to nucleate cadmium chalcogenide nanocrystals [17].

Here, the influence of the isothermal treatment mode on the spectral and luminescent properties of CdS nanocrystals nucleated in a sodium germanate glass matrix is demonstrated.

Methods

The chemical composition of initial sodium-germanate glass matrix was: 20 Na_2O – 80 GeO_2 mol. %, 7.4 mol. % CdS were introduced as activating additives over 100 % of the matrix. Chemicals Na_2CO_3, GeO_2, CdS of reagent grade were used for synthesis of 100 g glass bulk. Glasses were synthesized in a Gero laboratory high-temperature furnace at 1150 °C for 30 min in closed quartz crucible by standard melt-quenching technique in argon atmosphere. In two articles devoted to the nucleation of CdS and CdSe in sodium germanate glass, the authors took either 8 Na_2O – 92 GeO_2 (mol. %) composition with subsequent heat treatment (HT) at a temperature of 500–550 °C [18], or 40 Na_2O – 60 GeO_2 (mol. %) composition with heat treatment at 580–620 °C [17]. Since in this work an intermediate composition in terms of Na_2O content was chosen, subsequent single-stage heat treatment was conducted in the Nabertherm muffle furnace at 560 °C.

Absorption spectra were measured on a double-beam Lambda 650 PerkinElmer spectrophotometer in the wavelength range 200–800 nm with 1 nm resolution. For these measurements polished plane samples of 0.8–1.0 mm thick were prepared.

Photoexcitation and photoluminescence spectra were obtained by spectrofluorometer LS-55 (Perkin Elmer) in the 200–900 nm region with 1 nm step. The luminescence decay kinetics were obtained using a pulse mode of a built-in Xenon lamp and by varying the time delay from the exciting pulse with a step of 0.01 μs. Based on this, the time dependence of the luminescence intensity was plotted and mathematically processed by the Origin Pro software.

The actual chemical composition of the glass-ceramics was determined by X-ray fluorescence spectroscopy (XRF) using an X-ray fluorescence spectrometer ARL

PERFORM'X by Thermo Scientific with Rh tube, 4.2 kW/60kV generator, FPC and Sc detectors (chemical elements: from oxygen to uranium). The study was done at ambient temperature in the vacuum atmosphere. The chemical composition was averaged over a sample area of 20 mm^2. The resulting composition of the glass under study was: 7.4 Na_2O – 84.8 GeO_2 – 7.5 CdO – 0.3 S wt. %. Despite the use of a closed crucible and an inert atmosphere, the sulfur content decreased by 4 times due to high volatilization. According to the phase equilibrium diagram of the Na_2O-GeO_2 system [23], in the region of high GeO_2 content, the compounds $Na_2O{\cdot}4GeO_2$ or $2Na_2O{\cdot}9GeO_2$ should crystallize. The eutectic point between first compound and GeO_2 accounted for 94.5 wt. % GeO_2 having a melt temperature of 950 °C. Since in our case the actual Na_2O/GeO_2 ratio was close to this numbers, we should expect the corresponding phase separation.

Results and Discussion

Figure 1 shows the absorption spectra of the initial glass and glass-ceramics after the heat treatment at a temperature of 560 °C for different durations. The heat treatment temperature was chosen according to the literature and below the exothermic peak on the differential scanning calorimetry curve for the glass matrix under study [24]. Nevertheless, even a duration of 1 hour led to intensive release of CdS nanocrystals in the glass matrix (Fig. 1(a)). This was confirmed by the fact that the absorption edge of the initial glass located in the region of 400 nm (3.1 eV), and the absorption boundary of the heat-treated glass was in the region of 512 nm (2.42 eV). The band gap of bulk CdS in the form of zinc blende is 2.42 eV [25]. Thus, after the heat treatment, rather large crystals were immediately released in the glasses under study. With an increase in the heat treatment duration, the amount of the crystalline phase increased, which was confirmed by an increase in the absorption intensity of nanocrystals. As well as the scattering level was increased which was associated with phase separation and partial crystallization of the glass matrix. In this case, the absorption edge location remained practically unchanged, which indicated that the mean crystal size remained the same.

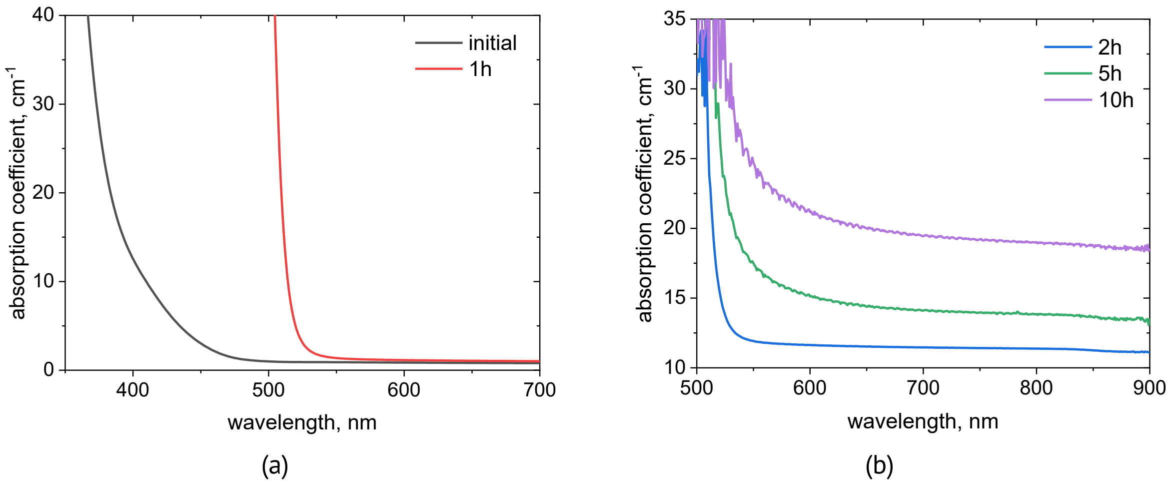

Fig. 1. Absorption spectra of the glass under study: initial and after heat treatment at a temperature of 560 °C with different durations

It is worth noting that the location of the band gap edge on the absorption spectrum is directly related to the size of the quantum dot [26–28]. If the position of the absorption edge is close to the band gap of the macrocrystal (E_{ex} = 2.4 ÷ 2.5 eV), then quantum dots have grown so that they are either related to the weak size quantization regime [29,30] or no longer obey the rules of strong size quantization [31,32] (in case of exceeding the Bohr exciton radius a_{ex}=2.5 Å [33,34] by two times).

For the exciton photoluminescence band of CdS QDs, the Stokes shift was in the range of 0.01–0.15 eV with a band maximum at 350–480 nm for QDs with an average size of 1.5–5 nm [25,35,36]. For the luminescence band associated with radiative recombination involving defects, the Stokes shift was significantly larger and varied from 0.2 to 1.2 eV for different defects [25,35,36]. The presence of defects leads to the appearance of localized levels within the band gap. Even though at low concentrations of defects these levels are practically not distinguished in the absorption spectra, their contribution to luminescence can be significant, as in our case (Fig. 2).

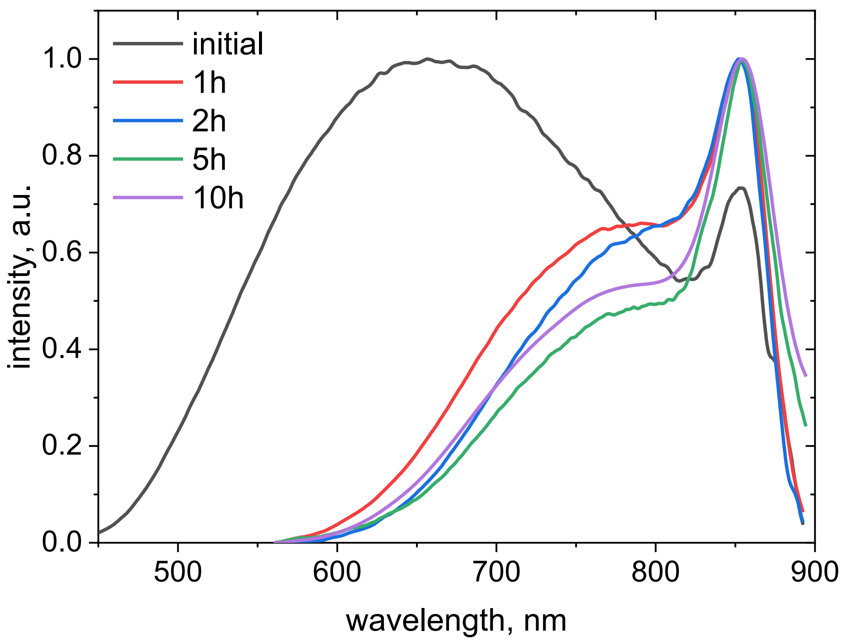

Fig. 2. Luminescence spectra of the studied glass: initial and after heat treatment at a temperature of 560 °C with different durations (λ_{ex} = 390 nm)

The luminescence of CdS QDs in the long-wavelength region is determined by the local states associated with intrinsic defects of the crystal structure. Such defects are surface states, interstitial cadmium and sulfur ions (I_{Cd}, I_S), sulfur vacancies (V_S), cadmium vacancies (single V_{Cd}, paired with a sulfur vacancy [V_{Cd}–V_S] or oxygen in the sulfur position [V_{Cd}-O_S]) [16,25,37–39]. According to these papers, in single crystals cadmium vacancies V_{Cd} led to the luminescence at 1.2 eV, the complex of a cadmium vacancy with oxygen [V_{Cd}-O_S] – 1.51 eV, the donor-acceptor pair [V_{Cd}–V_S] – 1.72 eV, the interstitial cadmium atom I_{Cd} – 2.05 eV, the interstitial sulfur atom I_S – 2.38 eV and sulfur vacancies V_S – in the region of 1.77–1.85 eV.

Due to the presence of several factors, namely: the quantum-size effect, size dispersion, and the allocation of quantum dots in the oxide glass matrix, in our case the location of the corresponding bands will differ slightly from those indicated above. A wide structureless band, which dominated the luminescence spectrum (Fig. 2) with a maximum at 650 nm was a superposition of at least three bands with maxima at 610, 700, and 765 nm. These bands can be attributed to transitions to levels associated with interstitial cadmium ions (I_{Cd}), and the donor-acceptor pair [V_{Cd}–V_S]. A separate band with a maximum at 855 nm can be associated with a radiative transition involving the states of the cadmium vacancy with oxygen [V_{Cd}-O_S]. An increase in the intensity of this band after isothermal treatment confirmed its oxygen nature, since the heat treatment was carried out in an oxygen-containing atmosphere. According to the analysis of the chemical composition, an excess of cadmium ions over sulfur was found in the glass under study, thus the probability of the presence of many cadmium vacancies and interstitial cadmium ions was quite high; therefore, most of the radiative transitions were attributed to these types of structural defects.

The luminescence quantum yield in the studied glasses was less than 1 %. Low QY is usually taken as a sign that nonradiative recombination of charge carriers is the dominant process. Since in our case the luminescence spectra demonstrate a large number of bands associated with structural defects, the probability of nonradiative recombination on them can be quite high.

The multi-exponential luminescence decay observed for cadmium chalcogenide nanocrystals also indicates the distribution of both the size and shape of the nanoparticles, the presence of radiative states with different lifetimes, as well as the release of traps and the redistribution of charge carriers at different energies [40–42].

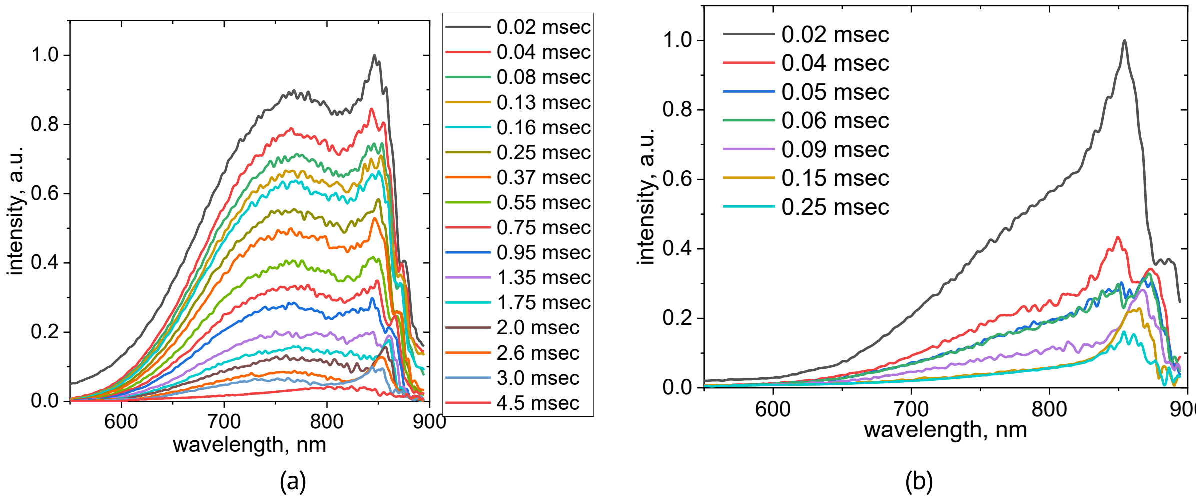

Fig. 3. Time-resolved luminescence spectra of the initial glass (a) and glass after heat treatment for 2 hours (b) with different delays after the exciting pulse (λ_{ex} = 390 nm)

The time-resolved luminescence spectra for the initial and heat-treated glass are shown in Fig. 3. The luminescence decay kinetics of the heat-treated sample was described by a single-exponential function with a lifetime of 17 μsec, which corresponded to the decay of a Xenon flash lamp used in the registration method. This suggests that the decay kinetics of CdS in this case was probably quite fast: on the order of hundreds of nanoseconds, which is quite consistent with the literature [43,44] and which is not resolvable in this method. However, the luminescence decay kinetics of the initial glass with CdS was significantly more protracted and the single-exponential lifetime was 850 μsec at 760 nm and 662 μsec at 845 nm. The nature of such a long lifetime requires additional research. In both graphs (Fig. 3), after a certain delay, a luminescence band with a maximum at 875 nm appeared in the spectra, which can be attributed to transitions to deep trap levels created by cadmium vacancies in the volume of nanocrystals.

Conclusions

The article demonstrated the nucleation of CdS quantum dots in a sodium germanate glass matrix by means of isothermal treatment, as well as the dependence of the luminescent properties of quantum dots on the treatment mode. It was shown that due to a sufficiently high concentration of cadmium ions in the initial glass components, the resulting quantum dots were quite large. The luminescence of CdS was mainly of a trap nature and was localized in the region of 600–900 nm. Excess cadmium ions and nucleation of quantum dots in oxide glass led to the fact that the nature of the luminescence bands was mainly associated with such crystal structure defects as interstitial cadmium ions (I_{Cd}), the donor-acceptor pairs [V_{Cd}–V_S], and deep trap levels created by volume cadmium vacancies. The luminescence quantum yield of CdS quantum dots was less than 1 %, indicating that nonradiative recombination of charge carriers was the dominant process.

References

1. Liz-Marzán LM, Artzi N, Bals S, Buriak JM, Chan WCW, Chen X, Hersam MC, Kim ID, Millstone JE, Mulvaney P, Parak WJ, Rogach A, Schaak RE. Celebrating a Nobel Prize to the "Discovery of Quantum Dots, an Essential Milestone in Nanoscience." *ACS Nano*. 2023;17(20): 19474–19475.

2. Montanarella F, Kovalenko MV. Three Millennia of Nanocrystals. *ACS Nano*. 2022;16(4): 5085–5102.

3. Rempel AA, Ovchinnikov OV, Weinstein IA, Rempel SV, Kuznetsova YV, Naumov AV, Smirnov MS, Eremchev IY, Vokhmintsev AS, Savchenko SS. Quantum dots: modern methods of synthesis and optical properties. *Russ Chem Rev*. 2024;93(4): RCR5114.

4. Goris T, Langley DP, Stoddart PR, Rosal B del. Nanoscale optical voltage sensing in biological systems. *J Lumin*. 2021;230: 117719.

5. Pandey S, Mukherjee D, Kshirsagar P, Patra C, Bodas D. Multiplexed bio-imaging using cadmium telluride quantum dots synthesized by mathematically derived process parameters in a continuous flow active microreactor. *Mater Today Bio*. 2021;11: 100123.

6. Dhas N, Pastagia M, Sharma A, Khera A, Kudarha R, Kulkarni S, Soman S, Mutalik S, Barnwal RP, Singh G, Patel M. Organic quantum dots: An ultrasmall nanoplatform for cancer theranostics. *J Control Release*. 2022;348: 798–824.

7. Kumar S, Prakash R, Maiti P. Redox mediation through integrating chain extenders in active ionomer polyurethane hard segments in CdS quantum dot sensitized solar cell. *Sol Energy*. 2022;231): 985–1001.

8. Sadeghi S, Olieaei S. Capped cadmium sulfide quantum dots with a new ionic liquid as a fluorescent probe for sensitive detection of florfenicol in meat samples. *Spectrochim Acta - Part A Mol Biomol Spectrosc*. 2019;223: 117349.

9. Mohammed IMS, Gubari GMM, Sonawane ME, Kasar RR, Patil SA, Mishra MK, Kutwade VV, Sharma R. Influence of pH on the physical properties of CdS thin film and its photosensor application. *Appl Phys A Mater Sci Process.* 2021;127(8): 1–10.
10. Dabbousi BO, Rodriguez-Viejo J, Mikulec F V., Heine JR, Mattoussi H, Ober R, Jensen KF, Bawendi MG. (CdSe)ZnS core-shell quantum dots: Synthesis and characterization of a size series of highly luminescent nanocrystallites. *J Phys Chem B.* 1997;101(46): 9463–9475.
11. Silvi S, Credi A. Luminescent sensors based on quantum dot-molecule conjugates. *Chem Soc Rev.* 2015;44(13): 4275–4289.
12. Shirshnev PS, Snezhnaia ZG, Shirshneva-Vaschenko EV, Romanov AE, Bougrov VE. Relation of the optical properties of boron copper-containing glasses on the concentration of lithium. *Materials Physics and Mechanics.* 2018;40(1): 78–83.
13. Shirshnev PS, Spiridonov VA, Panov DI, Shirshneva-Vaschenko EV, Gafarova AR, Eremina RM, Romanov AE, Bougrov VE. The influence of gamma rays radiation on optically induced luminescence of copper-containing potassium-lithium-borate glass. *Materials Physics and Mechanics.* 2019;42(2): 198–203.
14. Losin AL, Babkina AN, Kharisova RD, Zyryanova KS, Dolgopolov AD, Sergeev MM. Effect of femtosecond irradiation on the luminescence of CsPbI 3 perovskite crystals in borogermanate glass. *Materials Physics and Mechanics.* 2024;52(2): 76–81.
15. Kolobkova EV, Lipovskii AA, Nikonorov NV, Sitnikova AA. Phosphate glass doped with CdS nanocrystals. *Phys Status Solidi.* 1995;147(2): K65–K68.
16. Kuznetsova YV, Popov ID. Design and technological aspects of novel CdS quantum dots doped glass–ceramics. *Ceram Int.* 2022;48(13): 18972–18982.
17. El-Rabaie S, Taha TA, Higazy AA. Synthesis and characterization of CdS nanocrystals embedded in germanate glasses. *Appl Nanosci.* 2014;4(2): 219–226.
18. Tanaka A, Onari S, Arai T. Raman scattering from CdSe microcrystals embedded in a germanate glass matrix. *Phys Rev B.* 1992;45(12): 6587–6592.
19. Hwang YN, Shin S, Park HL, Park SH, Kim U, Jeong HS, Shin E, Kim D. Raman shifts of CdSe quantum dots in glass matrices. *Conf Proc - Lasers Electro-Optics Soc Annu Meet.* 1996;54(21): 285.
20. Marcondes LM, Evangelista RO, Gonçalves RR, de Camargo ASS, Manzani D, Nalin M, Cassanjes AC, Poirier GY. Er3+-doped niobium alkali germanate glasses and glass-ceramics: NIR and visible luminescence properties. *J Non Cryst Solids.* 2019;521): 119492.
21. Nascimento Guedes LF, Marcondes LM, Evangelista RO, Batista G, Mendoza VG, Cassanjes FC, Poirier GY. Effect of alkaline modifiers on the structural, optical and crystallization properties of niobium germanate glasses and glass-ceramics. *Opt Mater.* 2020;105: 109866.
22. De Pietro GM, Pereira C, Gonçalves RR, Ribeiro SJL, Freschi CD, Cassanjes FC, Poirier G. Thermal, Structural, and Crystallization Properties of New Tantalum Alkali-Germanate Glasses. *J Am Ceram Soc.* 2015;98(7): 2086–2093.
23. Murthy MK, Aguayo J. Studies in Germanium Oxide Systems: II, Phase Equilibria in the System Na2O—GeO2. *J Am Ceram Soc.* 1964;47(9): 444–447.
24. Babkina A, Valiev D, Kulpina E, Pavliuk A, Zyryanova K, Monogarova A, Ignatiev A, Kuzmenko N, Zhizhin E, Koroleva A. Intense red emission of mixed-alkali rare-earth free germanate glass-ceramics with Mn ions. *Opt Mater Express.* 2022;12(5): 2072.
25. Veamatahau A, Jiang B, Seifert T, Makuta S, Latham K, Kanehara M, Teranishi T, Tachibana Y. Origin of surface trap states in CdS quantum dots: Relationship between size dependent photoluminescence and sulfur vacancy trap states. *Phys Chem Chem Phys.* 2015;17(4): 2850–2858.
26. Efros AL, Efros AL. Interband absorption of light in a semiconductor sphere. *Sov Physics Semicond.* 1982;16(7): 772–775.
27. Ekimov AI, Efros AL, Onushchenko AA. Quantum Size Effect in Semiconductor Mircrocrystals. *Solid State Commun.* 1985;56(11): 921–924.
28. Brus LE. Electron-electron and electron-hole interactions in small semiconductor crystallites: The size dependence of the lowest excited electronic state. *J Chem Phys.* 1984;80(9): 4403–4409.
29. Wang Y, Herron N. Nanometer-sized semiconductor clusters: Materials synthesis, quantum size effects, and photophysical properties. *J Phys Chem.* 1991;95(2): 525–532.
30. Marín JL, Riera R, Cruz SA. Confinement of excitons in spherical quantum dots. *J Phys Condens Matter.* 1998;10(6): 1349–1361.

31. Schmidt HM, Weller H. Quantum size effects in semiconductor crystallites: Calculation of the energy spectrum for the confined exciton. *Chem Phys Lett.* 1986;129(6): 615–618.
32. Lipatova ZO, Kolobkova E, Babkina AN. Luminescent properties of cadmium selenide quantum dots in fluorophosphate glasses. *Opt Spectrosc.* 2016;121(5): 761–769.
33. Gaponenko SV. *Optical properties of semiconductor nanocrystal.* Cambridge University Press; 1998.
34. Woggon U, Gaponenko S V. Excitons in Quantum Dots. *Phys Status Solidi.* 1995;189(2): 285–343.
35. Yu Z, Li J, O'Connor DB, Wang LW, Barbara PF. Large resonant Stokes shift in CdS nanocrystals. *J Phys Chem B.* 2003;107(24): 5670–5674.
36. Yu WW, Peng X. Formation of high-quality CdS and other II-VI semiconductor nanocrystals in noncoordinating solvents: Tunable reactivity of monomers. *Angew Chemie - Int Ed.* 2002;41(13): 2368–2371.
37. Davydyuk HY, Kevshyn AH, Bozhko V V., Halyan V V. Special features of the mechanism of defect formation in CdS single crystals subjected to irradiation with high doses of fast reactor neutrons. *Semiconductors.* 2009;43(11): 1401–1406.
38. Kulp BA. Displacement of the cadmium atom in single crystal CdS by electron bombardment. *Phys Rev.* 1962;125(6): 1865–1869.
39. Ramsden JJ, Grätzel M. Photoluminescence of small cadmium sulphide particles. *J Chem Soc Faraday Trans 1 Phys Chem Condens Phases.* 1984;80(4): 919–933.
40. Shea-Rohwer LE, Martin JE. Luminescence decay of broadband emission from CdS quantum dots. *J Lumin.* 2007;127(2): 499–507.
41. Ovchinnikov OV, Smirnov MS, Korolev NV, Golovinski PA, Vitukhnovsky AG. The size dependence recombination luminescence of hydrophilic colloidal CdS quantum dots in gelatin. *J Lumin.* 2016;179: 413–419.
42. Brus L. Electronic wave functions in semiconductor clusters: Experiment and theory. *J Phys Chem.* 1986;90(12): 2555–2560.
43. Kuznetsova YV, Letofsky-Papst I, Sochor B, Schummer B, Sergeev AA, Hofer F, Rempel AA. Greatly enhanced luminescence efficiency of CdS nanoparticles in aqueous solution. *Colloids Surfaces A Physicochem Eng Asp.* 2019;581: 123814.
44. Califano M, Franceschetti A, Zunger A. Temperature dependence of excitonic radiative decay in CdSe quantum dots: The role of surface hole traps. *Nano Lett.* 2005;5(12): 2360–2364.

About Authors

Anastasiia N. Babkina Sc
Candidate of Physico-Mathematical Sciences
Associate Professor (ITMO University, St. Petersburg, Russia)

Rufina D. Kharisova Sc
PhD Student (ITMO University, St. Petersburg, Russia)

Varvara G. Sheremet
Student (ITMO University, St. Petersburg, Russia)

Olesia S. Barbash
Student (ITMO University, St. Petersburg, Russia)

Konstantin A. Zhikov
Student (ITMO University, St. Petersburg, Russia)

Ksenia S. Zyryanova Sc
Leading Engineer (ITMO University, St. Petersburg, Russia)

MATERIALS PHYSICS AND MECHANICS RESEARCH ARTICLE

Submitted: October 1, 2024 Revised: October 19, 2024 Accepted: November 22, 2024

Effect of high-temperature annealing on the internal friction and optical transmittance of single crystal gallium oxide

V.V. Kaminskii [1], **D.Yu. Panov** [1], **V.A. Spiridonov** [1], **D.A. Bauman** [1], **D.A. Kalganov** [2]✉, **M.P. Scheglov** [2], **A.E. Romanov** [1]

[1] ITMO University, St. Petersburg, Russia

[2] Ioffe Institute, St. Petersburg, Russia

✉ kalganov@itmo.ru

ABSTRACT

The effect of high-temperature annealing on the structure and properties of single crystal β-phase gallium oxide is reported in this work. The investigated sample obtained by cleaving from a bulk β-Ga_2O_3 ingot grown by the edge-defined film-fed growth method. Some of the samples were annealed in an oxygen-containing atmosphere at temperatures up to T = 1673 K. The temperature dependences of internal friction and dynamic modulus of elasticity were obtained by the composite oscillator method at a frequency of 100 kHz. Optical absorption spectra were investigated in the wavelength range from 200 nm to 2 μm. It was found that annealing and redistribution of gallium vacancies in beta-phase gallium oxide crystals is accompanied by simultaneous changes in the internal friction in the temperature region around 290 K and in the optical spectrum in the infrared region.

KEYWORDS

Young's modulus • internal friction • optical transmittance • vacancies • single crystal • gallium oxide

Acknowledgements. *This research is supported by the grant of Russian Science Foundation № 24-12-00229. https://rscf.ru/project/24-12-00229/*

Citation: Kaminskii VV, Panov DYu, Spiridonov VA, Bauman DA, Kalganov DA, Scheglov MP, Romanov AE. Effect of high-temperature annealing on the internal friction and optical transmittance of single crystal gallium oxide. *Materials Physics and Mechanics*. 2024;52(5): 48–54.
http://dx.doi.org/10.18149/MPM.5252024_5

Introduction

The design of new devices for power electronics and energy converters is essential for improving the energy efficiency of production and maintaining ecological balance. In modern devices, efficiency improvements are provided by technologies based on wide bandgap semiconductors such as silicon carbide and gallium nitride. The use of ultrawide bandgap semiconductors such as gallium oxide, aluminum nitride, and diamond should lead to the next round of technological development due to their unique electrical characteristics and high temperature stability. Various applications of these materials in power electronics [1], ultraviolet [2] and X-ray detectors [3] have been predicted. The availability of methods to produce single crystals of beta-phase gallium oxide (β-Ga_2O_3) from melt [4] allows the creation of bulk elements and substrates for homoepitaxy, which provides a technological advantage in the use of this semiconductor [5]. High-temperature growth and prevention of thermal decomposition of other Ga_2O_3 polymorphs are possible only for epitaxial layers [6] and small particles.

Publisher: Peter the Great St. Petersburg Polytechnic University

Gallium oxide is an ultrawide bandgap semiconductor with an optical band edge near 250 nm (~4.9 eV) [2,4,5]. Most of β-Ga_2O_3 crystals available today are n-type due to the unintentional doping by silicon. At the same time, varying the dopant content during growth implies achieving and controlling the desired crystal properties [7]. The mechanisms of the influence of oxygen and gallium vacancies on the electrical conductivity and other characteristics of gallium oxide are also still not studied in detail. Studies of different types of vacancies are important to clarify the redistribution of charge carriers localized near the corresponding sites of the crystal lattice. Variations of different types of vacancies should apparently change the number of stable hole centers and anisotropic electrical properties in the β-Ga_2O_3 [8,9]. In the same way, the electrical properties of β-Ga_2O_3 are related to the migration energy of vacancies. Relevant questions in view of the complexity of organizing direct experiments and interpreting indirect measurements were solved earlier mostly numerically by density functional theory (DFT) calculations [10–16] with some rare exceptions [8,9,17–19]. Structure-dependent mechanical properties were determined previously on epitaxial layers and single crystals of β-Ga_2O_3 by nanoindentation [20], which is important from the point of view of their application. However, such measurements did not allow us to draw conclusions about the fine effects associated with impurities in this material.

In this work, we study the internal friction, dynamic modulus of elasticity (Young's modulus) and optical transmittance of gallium oxide single crystals before and after high-temperature annealing in an oxygen atmosphere.

Materials and Methods

Gallium oxide single crystal samples were obtained from a melt using edge-defined film-fed growth (Stepanov) method similar to reported in [4].

To exclude defects introduced by processing, the investigated sample plates with thickness about 1 mm were prepared by cleaving along the (100) crystallographic plane. The procedure for preparing samples by this method is described in detail in [21]. The length of the studied specimens was about 33 mm, their dimensions in rectangular cross-section did not exceed 3 mm. For strain amplitudes in the range of $10^{-8} \leqslant \varepsilon \leqslant 10^{-3}$ considered in this paper, the use of the dislocation theory of anisotropic internal friction is appropriate. In the framework of this theory, the deformation of a crystal under the action of elastic waves is composed of the deformation of the ideal crystal lattice and additional deformation due to the motion of dislocations. The main contribution to the internal friction comes from the motion of dislocations distributed on slip systems in the sample volume. In this case, the role of surface topology is less significant than the possible influence of the disturbed layer during processing, since later correlates with the stress distribution in the standing ultrasonic wave. Also due to the straightforward delamination and absence of a disturbed surface layer, these samples were used to evaluate the crystalline quality using X-ray. The area of measurement of optical characteristics and maximum mechanical stress during ultrasonic vibrations was located at the geometric center of the plate (100). X-ray diffraction of this region was obtained to confirm the crystalline quality of the samples. The rocking curve were obtained by two-crystal X-ray diffractometry under condition of symmetric 800 (CuKα_1) reflection. Analysis of Bragg peaks and determination of the exact lattice parameter were carried out with the high precision three-crystal X-ray spectrometer.

The samples were annealed in a muffle furnace with air atmosphere at 1673 K. The annealing time was 9 h. After annealing, the temperature was slowly reduced to room conditions for 20 h. We chose the annealing mode based on the high migration energy of gallium and oxygen atoms inside the bulk sample in the corresponding vacancy positions [22,23].

To determine the internal friction and dynamic modulus of elasticity (effective Young's modulus), we used the method of composite piezoelectric oscillator with an excitation frequency about of 100 kHz. This method, first presented by Quimby [24], is based on the transfer of elastic vibration energy between the quartz crystal and the cemented sample. To measure the vibration damping, a second quartz crystal is also used, thus forming a three-component oscillator which vibrates as a single body [25]. Effective Young's modulus E was calculated according to the first longitudinal mode of standing waves condition as:

$$E = 4\rho l^2 {f_s}^2, \tag{1}$$

where ρ is the density of the material under study, l is the length of the sample, f_s is the frequency of oscillations in the sample. The oscillation attenuation in the sample δ_s corresponds to internal friction (IF). This value δ_s and the oscillation frequency f_s are determined according to the equations of motion and constants [25,26]. Previously, we have shown the possibility of using this method to study microplasticity and structure-dependent internal friction in gallium oxide [27].

Optical transmittance studies were performed on a LAMBDA 1050 (PerkinElmer) with a 2D detector module. The same samples before and after annealing, obtained by chipping of the crystal along the cleavage plane (100) without further processing, were used. Relative change of transmittance ΔT was determined according to equation:

$$\Delta T = \frac{T_a - T_0}{T_0}, \tag{2}$$

where T_0 is the absorption before annealing and T_a is the absorption after annealing.

Results and Discussion

The full width at half-maximum of rocking curves was no more than 50" for all the samples studied. A shift in the parameter *a* from 12.2255 to 12.2272 Å was observed in the samples before and after annealing, correspondingly.

The temperature dependences of effective Young's modulus and internal friction for β-Ga_2O_3 were obtained by composite oscillator studies. In Fig. 1, it can be seen that the internal friction both before and after annealing decreases with decreasing temperature while Young's modulus increases. Measurements of E and IF of samples after annealing in a wider temperature range were hampered by the peculiarities of equipment operation. The Young's modulus of Ga_2O_3 on the pre-annealed samples increased by 20 GPa (or 4 %) from 257 GPa at room temperature to 267 GPa at 120 K. An increase in the E values from 264 GPa at room temperature to 275 GPa at 120 K was observed on the samples after annealing. The steepness of the E curve is generally preserved, and insignificant changes are explained by the peculiarity of the measurement method itself.

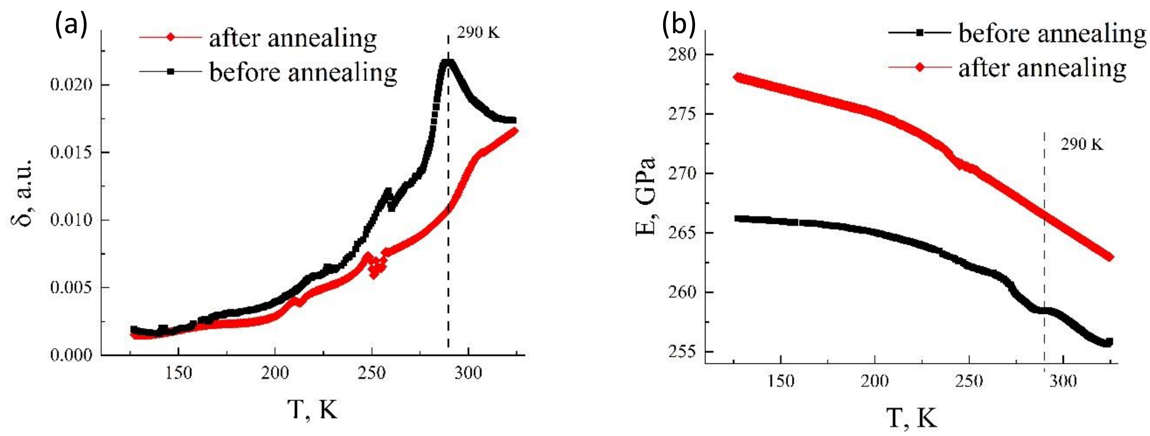

Fig. 1. Temperature dependences of (a) internal friction *δ* and (b) Young's modulus *E* of beta-phase Ga_2O_3 samples before and after annealing. The dotted line shows the temperature at which relaxation occurs

The increase in internal friction and decrease in *E* with temperature in semiconductor materials is primarily due to the larger amplitude of vibrations of atoms in the lattice and greater scattering of phonons (elastic waves) on them. After annealing, there was an increase in Young's modulus and a decrease in internal friction associated with the relaxation of residual stresses in the crystal lattice due to a decrease in the density of defects (vacancies) and their redistribution.

At a temperature of about 290 K one can observe a relaxation peak of internal friction marked in Fig. 1(b) by a dashed line. This peak corresponds to a bend in the Young's modulus curve. This relaxation peak in gallium oxide seems to be associated with point defects such as vacancies. The energetically most suitable mechanism for this process is the Hashiguchi relaxation, which is associated with the interaction of dislocations (kinks) with intrinsic defects: vacancies and their complexes.

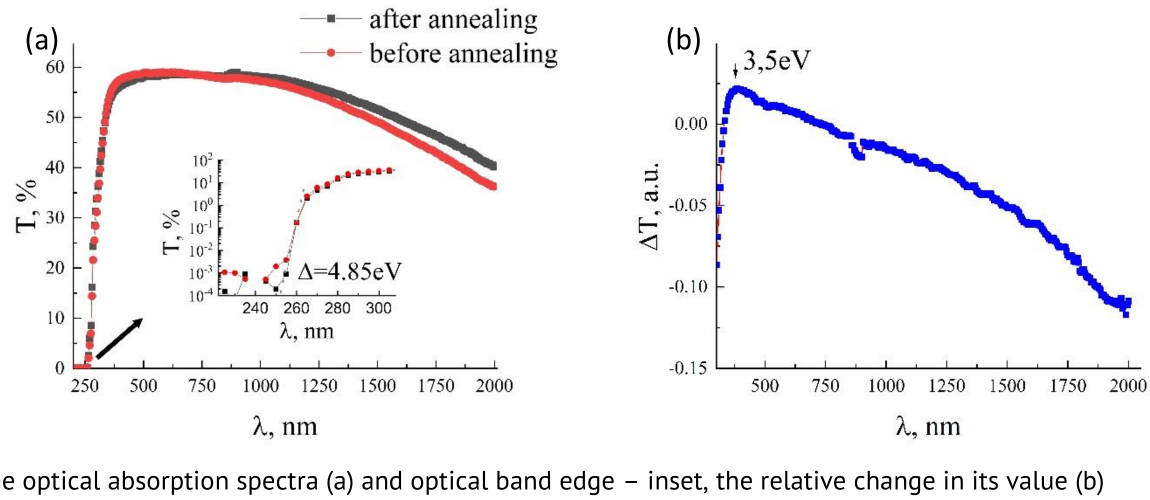

Fig. 2. The optical absorption spectra (a) and optical band edge – inset, the relative change in its value (b) for samples of single crystal gallium oxide before and after annealing for 12 h at 1673 K

The optical transmission edge is located around 269 nm, which corresponds to a band gap energy of about 4.85 eV (Fig. 2(a) – inset). The smooth decrease in transmission with increasing wavelength (Fig. 2) is associated with absorption by free electrons [9,28]. Additional absorption in the high-energy region around 3.5 eV (Fig. 2(b)) can be caused by defects like gallium vacancies [29]. Thus, the decrease of transmittance in the high-energy part and its simultaneous increase in the long-wave part can be related to the redistribution of gallium vacancies of different types. At the same time, the change of energy in the longwave region may be intrinsically correspond to various transitions from the valence bands to the conduction band caused by residual strain and impurities [30].

Conclusions

In this paper, the effect of high-temperature annealing on the structure and properties of single-crystalline beta-phase gallium oxide is investigated. Data on internal friction and optical absorption are presented. It is found that annealing is accompanied by simultaneous changes in the internal friction in the temperature region around 290 K and in the optical spectrum in the infrared region, which is associated with the redistribution of gallium vacancies of different types with a general decrease in their number. This is consistent with the hypothesis of the effect of high-temperature annealing on gallium vacancies, which leads to an increase in the crystalline quality of the material. The presented results are also in agreement with known experimental [17,28–30] and theoretical [9,12] works.

References

1. Rozhkov MA, Kolodeznyi ES, Smirnov AM, Bougrov VE, Romanov AE. Comparison of characteristics of Schottky diodes based on β-Ga2O3 and other wide bandgap semiconductors. *Materials Physics and Mechanics.* 2015;24(2): 194–200.
2. Kaur D, Kumar M. A strategic review on gallium oxide based deep-ultraviolet photodetectors: recent progress and future prospects. *Advanced Optical Materials.* 2021;9(9): 2002160.
3. Li Z, Tang H, Li Y, Gu M, Xu J, Chen L, Liu J, Ouyang X, Liu B. Enhanced scintillation performance of β-Ga2O3 single crystals by Al3+ doping and its physical mechanism. *Applied Physics Letters.* 2022;121(10): 102102.
4. Bauman DA, Panov DI, Spiridonov VA, Kremleva AV, Romanov AE. On the successful growth of bulk gallium oxide crystals by the EFG (Stepanov) method. *Functional Materials Letters.* 2023;16(7): 2340026.
5. Galazka Z, Ganschow S, Seyidov P. Irmscher K, Pietsch M, Chou TS, Anooz SB, Grueneberg R, Popp A, Dittmar A, Kwasniewski A, Suendermann M, Klimm D, Straubinger T, Schroeder T, Bickermann M. Two inch diameter, highly conducting bulk β-Ga2O3 single crystals grown by the Czochralski method. *Applied Physics Letters.* 2022;120(15): 152101.
6. Nikolaev VI, Polyakov AY, Stepanov SI, Pechnikov AI, Guzilova LI, Scheglov MP, Chikiryaka AV. Epitaxial stabilization of α-Ga2O3 layers grown on r-plane sapphire. *Materials Physics and Mechanics.* 2023;51(1): 1–9.
7. Butenko PN, Panov DI, Kremleva AV, Zakgeim DA, Nashchekin AV, Smirnova IG, Bauman DA, Romanov AE, Bougrov VE. Czochralski grown (AlxGa1-x)2O3 crystals with variable Al content. *Materials Physics and Mechanics.* 2019;42(6): 802–807.
8. Van Bardeleben HJ, Zhou S, Gerstmann U, Skachkov D, Lambrecht WR, Ho QD, Deák P. Proton irradiation induced defects in β-Ga2O3: A combined EPR and theory study. *APL Materials.* 2019;7(2): 022521.
9. Wang Z, Chen X, Ren FF, Gu S, Ye J. Deep-level defects in gallium oxide. *Journal of Physics D: Applied Physics.* 2020;54(4): 043002.
10. Varley JB, Weber JR, Janotti A, Van de Walle CG. Oxygen vacancies and donor impurities in β-Ga2O3. *Applied Physics Letters.* 2010;97(14): 142106.
11. Varley JB, Peelaers H, Janotti A, Van de Walle CG. Hydrogenated cation vacancies in semiconducting oxides. *Journal of Physics: Condensed Matter.* 2011;23(33): 334212.
12. Zacherle T, Schmidt PC, Martin M. Ab initio calculations on the defect structure of β-Ga2O3. *Physical Review B—Condensed Matter and Materials Physics.* 2013;87(23): 235206.
13. Dong L, Jia R, Xin B, Peng B, Zhang Y. Effects of oxygen vacancies on the structural and optical properties of β-Ga2O3. *Scientific Reports.* 2017;7(1): 40160.
14. Deák P, Duy Ho Q, Seemann F, Aradi B, Lorke M, Frauenheim T. Choosing the correct hybrid for defect calculations: A case study on intrinsic carrier trapping in β-Ga2O3. *Physical Review B.* 2017;95(7): 075208.

15. Ingebrigtsen ME, Kuznetsov AY, Svensson BG, Alfieri G, Mihaila A, Badstübner U, Perron A, Vines L, Varley JB. Impact of proton irradiation on conductivity and deep level defects in β-Ga2O3. *APL Materials.* 2019;7(2): 022510.

16. Yao J, Liu T, Wang B. Optical properties for the oxygen vacancies in β-Ga2O3 based on first-principles calculations. *Materials Research Express.* 2019;6(7): 075913.

17. Galazka Z, Irmscher K, Uecker R, Bertram R, Pietsch M, Kwasniewski A, Bickermann M. On the bulk β-Ga2O3 single crystals grown by the Czochralski method. *Journal of Crystal Growth.* 2014;404: 184–191.

18. Kananen BE, Halliburton LE, Stevens KT, Foundos GK, Giles NC. Gallium vacancies in β-Ga2O3 crystals. *Applied Physics Letters.* 2017;110(20): 202104.

19. Frodason YK, Varley JB, Johansen KMH, Vines L, Van de Walle CG. Migration of Ga vacancies and interstitials in β-Ga2O3. *Physical Review B.* 2023;107(2): 024109.

20. Guzilova LI, Grashchenko AS, Pechnikov AI, Maslov VN, Zav'yalov DV, Abdrachmanov VL, Romanov AE, Nikolaev VI. Study of β-Ga2O3 epitaxial layers and single crystals by nanoindentation technique. *Materials Physics and Mechanics.* 2016;51(2): 166–171. (In Russian)

21. Bauman DA, Panov DI, Zakgeim DA, Spiridonov VA, Kremleva AV, Petrenko AA, Brunkov PN, Prasolov ND, Nashchekin AV, Smirnov AM, Odnoblyudov MA, Bougrov VE, Romanov AE. High-Quality Bulk β-Ga2O3 and β-(AlxGa1−x)2O3 Crystals: Growth and Properties. *Physica Status Solidi (a).* 2021;218(20): 2100335.

22. Kuramata A, Koshi K, Watanabe S, Yamaoka Y, Masui T, Yamakoshi S. High-quality β-Ga2O3 single crystals grown by edge-defined film-fed growth. *Japanese Journal of Applied Physics.* 2016;55(12): 1202A2.

23. Yuan Y, Hao W, Mu W, Wang Z, Chen X, Liu Q, Hao Y. Toward emerging gallium oxide semiconductors: A roadmap. *Fundamental Research.* 2021;1(6): 697–716.

24. Quimby SL. On the experimental determination of the viscosity of vibrating solids. *Phys. Rev.* 1925;25(4): 558–573.

25. Marx J. Use of the Piezoelectric Gauge for Internal Friction Measurements. *Review of Scientific Instruments.* 1951;22(7): 503–509.

26. Kustov S, Golyandin S, Ichino A, Gremaud G. A new design of automated piezoelectric composite oscillator technique. *Materials Science and Engineering: A.* 2006;442(1-2): 532–537.

27. Kaminskii VV, Kalganov DA, Panov DI, Spiridonov VA, Ivanov AI, Rozaeva MV, Bauman DA, Romanov AE. A study of gallium oxide by using the piezoelectric composite oscillator technique at a frequency of 100 kHz. *Condensed Matter and Interphases.* 2023;25(4): 548–556.

28. Okada A, Nakatani M, Chen L, Ferreyra RA, Kadono K. Effect of annealing conditions on the optical properties and surface morphologies of (-201)-oriented β-Ga2O3 crystals. *Applied Surface Science.* 2022;574: 151651.

29. Jesenovec J, Weber MH, Pansegrau C, McCluskey MD, Lynn KG, McCloy JS. Gallium vacancy formation in oxygen annealed β-Ga2O3. *Journal of Applied Physics.* 2021;129(24): 245701.

30. Onuma T. Optical Properties. Fundamental Absorption Edge and Emission Properties of β-Ga2O3. In: Higashiwaki M, Fujita Sh. (eds) *Gallium Oxide: Materials Properties, Crystal Growth, and Devices.* Cham: Springer; 2020. p.475–500.

About Authors

Vladimir V. Kaminskii Sc

Candidate of Physical and Mathematical Sciences
Head of Laboratory (ITMO University, St. Petersburg, Russia)

Dmitrii Yu. Panov Sc

Candidate of Physical and Mathematical Sciences
Head of Laboratory (ITMO University, St. Petersburg, Russia)

Vladislav A. Spiridonov Sc

PhD Student (ITMO University, St. Petersburg, Russia)

Dmitrii A. Bauman Sc
Candidate of Physical and Mathematical Sciences
Leading Researcher (ITMO University, St. Petersburg, Russia)

Dmitrii A. Kalganov Sc
Junior Researcher (Ioffe Institute, St. Petersburg, Russia)

Mikhail P. Shcheglov Sc
Candidate of Physical and Mathematical Sciences
Leading Researcher (Ioffe Institute, St. Petersburg, Russia)

Alexey E. Romanov Sc
Doctor of Physical and Mathematical Sciences, Professor
Principal Researcher (ITMO University, St. Petersburg, Russia)

MATERIALS PHYSICS AND MECHANICS RESEARCH ARTICLE

Submitted: October 21, 2024 Revised: November 13, 2024 Accepted: December 2, 2024

Spalling-induced β-Ga_2O_3 lift-off protocol

P.N. Butenko ✉, A.V. Chikiryaka, M.E. Boiko, L.I. Guzilova, V.M. Krymov, B.A. Obidov, R.B. Timashov, S.V. Shapenkov, M.D. Sharkov, V.I. Nikolaev

Ioffe Institute, St. Petersburg, Russia

✉ pavel.butenko@mail.ioffe.ru

ABSTRACT

Fabrication of gallium oxide 1–100 μm-thick layers by exfoliation them from single crystals opens up the way to provide good thermal management in high-power Ga_2O_3 devices. Here we propose a lift-off protocol based on spalling of homoepitaxial layers from (100) β-Ga_2O_3 bulk crystal. The process includes sputtering of Ni sacrificial mask on β-Ga_2O_3 substrate and its modification by annealing, prior to epitaxial layer deposition in mist-CVD reactor. The separated 4 μm-thick β-Ga_2O_3 layers have been studied. It is shown that implementation of the lift-off protocol allows obtaining high-quality free-standing layers.

KEYWORDS

gallium oxide • thick layers • single crystals • exfoliation • lift-off • mist-CVD • free-standing layers

Acknowledgements. *P.N. Butenko and L.I. Guzilova gratefully appreciate the Russian Science Foundation for financial support project No. 23-29-10196.*

Citation: Butenko PN, Chikiryaka AV, Boiko ME, Guzilova LI, Krymov VM, Obidov BA, Timashov RB, Shapenkov SV, Sharkov MD, Nikolaev VI. Spalling-induced β-Ga_2O_3 lift-off protocol. *Materials Physics and Mechanics*. 2024;52(5): 55–63.

http://dx.doi.org/10.18149/MPM.5252024_6

Introduction

Growth of the bulk β-Ga_2O_3 crystals is still a complex task, which only a few research groups in the world have successfully accomplished to some extent. This is evidenced by the fact that the only company that has achieved a commercial result to date is Tamura Corp. [1], whose substrates remain extremely expensive. In fact, bulk Ga_2O_3 crystals are grown exclusively from-melt techniques, which in this case have a number of drawbacks. First of all, the temperature distribution in both the crystallization zone and the melt region is unstable due to the multifactorial nature of the process, which is difficult to model. One of these factors is the step-by-step dissociation of gallium oxide into lower oxides and ultimately into O_2 and Ga, which is noticeable already at 1200 °C [2]. In addition, oxygen released during the decomposition of Ga_2O_3 deteriorates the growth zone equipment during chemical interaction, and free gallium forms an intermetallic compound with iridium. For this reason, the extremely expensive iridium used in the Czochralski process [3] (CZ) or Stepanov edge-defined film-fed growth (EFG) [4] techniques become a consumable. To fabricate *epi-ready* substrates, expensive bulk crystals must be subjected to post-growth processing (cutting, grinding, polishing), during which the material is underwent to mechanical and thermal effects. It has been experimentally established [5] that the structure of the subsurface layers of *epi-ready* substrates has a lower degree of crystal perfection than the bulk and contains defects, for example, in the form of threading dislocations due to post-growth processing. In addition to being highly anisotropic material in its physical properties, gallium oxide suffers from low thermal conductivity that emerges for substrate thicknesses of 500 μm and more [4]. These are the thicknesses of the substrates cut from the grown ones (in the form of boules), which is limited by the cutting capabilities. Obviously, this limits the scope of application of the material in power electronic devices.

Ground on this, an idea of development of bulk free-standing gallium oxide layers looks highly attractive. One of the most effective approaches from the collection of lift-off techniques is the use of a sacrificial interlayer. The main challenge of this layer is to form a weakened interface to accomplish detachment. There are number examples are known among such semiconductor materials as: GaAs [6,7], InP [8], GaN [9–23]. The majority of authors employ epitaxial growth to obtain the upper layer that will be subjected for exfoliation. The novel mist chemical-vapor-deposition is one of the few techniques that allows growth of the thick gallium oxide layers at high growth rates [24–26]. This method is cost-effective and provides flexible doping schemes, precise layer thickness control and high crystal perfection.

In this paper, we report the lift-off procedure by spalling (100) β-Ga_2O_3 homoepitaxial layers grown by mist-CVD for the first time. A modified Ni film was used as a sacrificial interlayer. Fabrication of a such a Ni-droplet mask pursues two goals: to provide further growth process according epitaxial lateral overgrowth (ELOG) technique and to employ it as a sacrifice layer that weakens the following exfoliation spalling.

Materials and Methods

(100) oriented β-Ga_2O_3 plates were used as the host-substrates. Previously the cylindric boule was grown in our lab by Czochralski process (Cz). The setup and the process parameters can be found in our recent publications [27–30]. Since (100) is a gallium oxide perfect cleavage plane, blocks splitting occurs precisely along it. Thus, the boule was cleaved manually into close-to-rectangular plates measuring approximately to 2 × 1 cm^2 and 2 mm thick. The plates that had plane surfaces without chip outs were selected. It is known that (100) β-Ga_2O_3 surface inherent interlaced patchwork morphology with 20–200 mm size regions that are highly smooth [27]. Therefore, such regions are adapted for epitaxial growth.

Vacuum thermal evaporation (VTE) at VUP-2KU4.2 was applied to sputter Ni sacrifice layer prior to homoepitaxy process. The Ni foil (99.8 % purity) divided into 0.0034 g portions per one sputtering process was used. The Ni portion weight was measured with a help of a Radwag WAS 220/C/2 analytical balance to provide Ni layer thickness of ~200 nm. The correspondence between film thickness and film weight was determined experimentally in advance. The evaporation process was performed at partial pressure of 10^{-5} Pa and a voltage of 60 V applied to the W-filament. To form self-ordered droplet-like island arrays, the subsequent thermal annealing was used. The improved Granat vacuum chamber was utilized. The annealing was performed at 1200 °C for 30 min in Ar ambient (at $2{\cdot}10^4$ Pa). The verification of the Ni layer thickness proceeded by registration the difference in the contrast of the grown layer from the base in the scanning electron microscope (SEM) on a scratch. It was mechanically applied to the sputtered layer using a needle, the depth of which was registered by a microscope relative to the top surface of the layer.

The epitaxial growth was developed on the (100) Ni/β-Ga_2O_3 substrate by the mist-CVD technique. The home-made mist-CVD reactor employed a process based on acetylacetonate (acac). The growth temperature and duration were 950 °C and 3 h, correspondingly. The detailed process parameters can be found in our previous paper [31].

The thicknesses of the homoepitaxial layers were measured by defining a difference in weights (recalculated through the layer volume and β-Ga_2O_3 density) of the Ni/β-Ga_2O_3 wafer and this sample (β-Ga_2O_3/Ni/β-Ga_2O_3) after growth. The Snoll 4/1300 muffle furnace was employed for sample annealing to weaken the Ni interface and impel epitaxial layer exfoliation. The annealing mode was set as 30 min at 700 °C on air. Directly for the exfoliation process the 3M Scotch double-sided tape was utilized. To get read of the rest of the Ni interlayer the sample was etched with HNO_3 for 10 min at 30 °C [32]. The complete scheme of (100) β-Ga_2O_3 the lift-off is shown in Fig. 1.

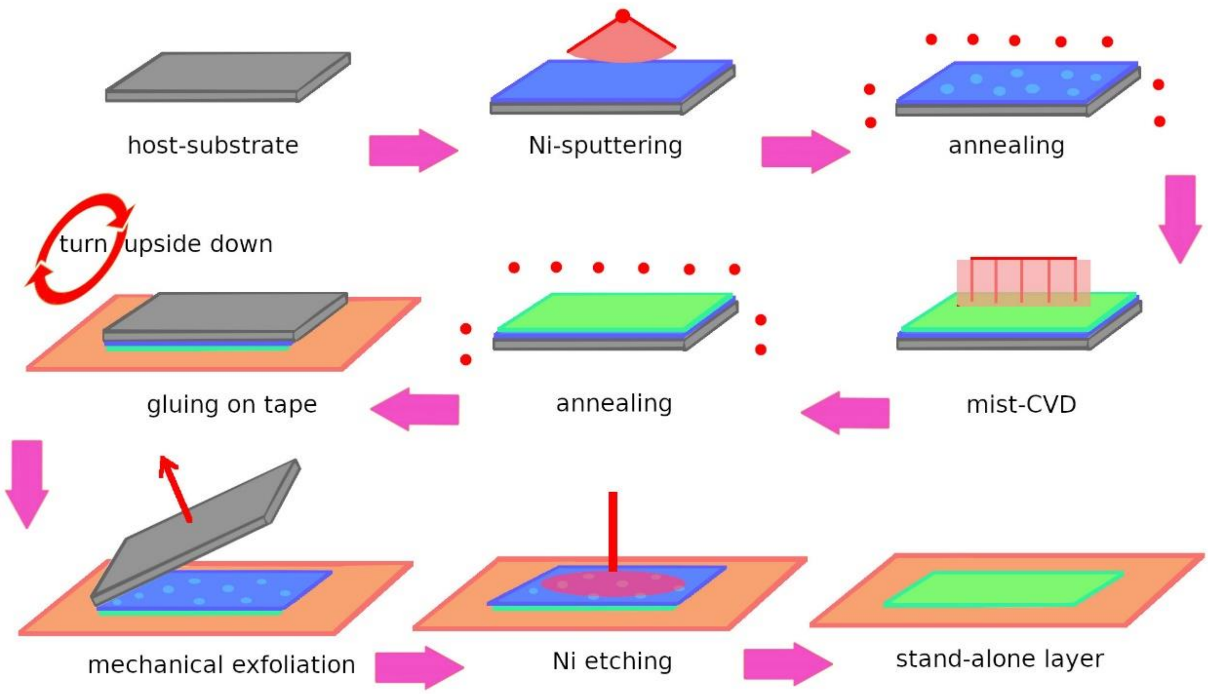

Fig. 1. The complete scheme of (100) β-Ga_2O_3 the lift-off

The surface morphology of the grown gallium oxide layer was analyzed using a Phenom ProX SEM operating in secondary electron (SE) mode at 10 kV. Energy dispersive spectroscopy (EDS) implemented in SEM was applied for chemical characterization. The phase composition and the crystallinity of the homoepitaxial layers were analyzed by X-ray diffraction (XRD) at Bourevestnik DRON-7 setup utilizing equipped with Ge (111) monochromator crystal on doublet Cu $K_{\alpha 1,2}$ radiation, the wavelets 1.5406 Å ($K_{\alpha 1}$) and 1.5444 Å ($K_{\alpha 2}$).

Results and Discussion

The Ni sacrificial layer was sputtered on the (100) surface of the β-Ga_2O_3 substrate. The estimation ground on scratch measurement (see Fig. 2) gave a value of 230 nm which is very close to the experimental evaluation.

At the next step the sample was annealed with an aim to form separate droplets. The surface contains Ni self-organized droplets of 0.5–1 μm in diameter is shown in Fig. 3(a). The chemical composition measured within a droplet region was Ga:Ni:O ≈ 28:29:43 at. %, at the same time in the rest region the Ni concentration appeared to be as below 1 at. % and the chemical formula corresponded to trivalent gallium oxide.

The surface of the sample upon mist-CVD epitaxy is depicted in Fig. 3(b). One can see, that it has relatively homogeneous morphology that consists of facetted crystals of various shapes with sizes of 1–2 μm. The thickness of the grown layer was estimated as 4 μm by weighting based on the β-Ga_2O_3 density ρ = 5.95 g/cm^3 [33].

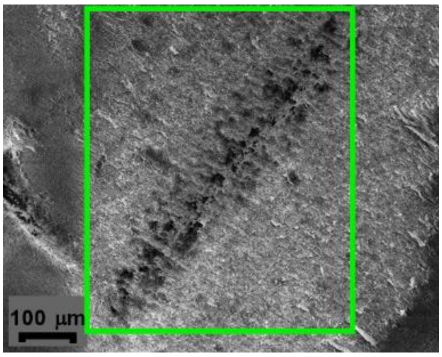

Fig. 2. SEM plan-view image of the Ni layer with a scratch in green square

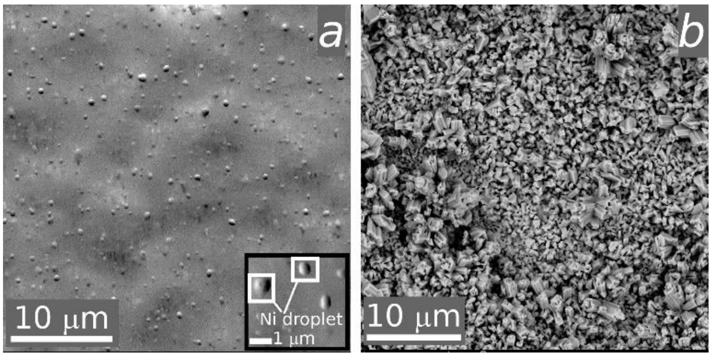

Fig. 3. SEM plan-view images of the (100) β-Ga_2O_3 layer: after Ni sputtering and annealing (a) and after mist-CVD growth (b). The inset the (a) shows the average droplet size of 0.5–1 μm

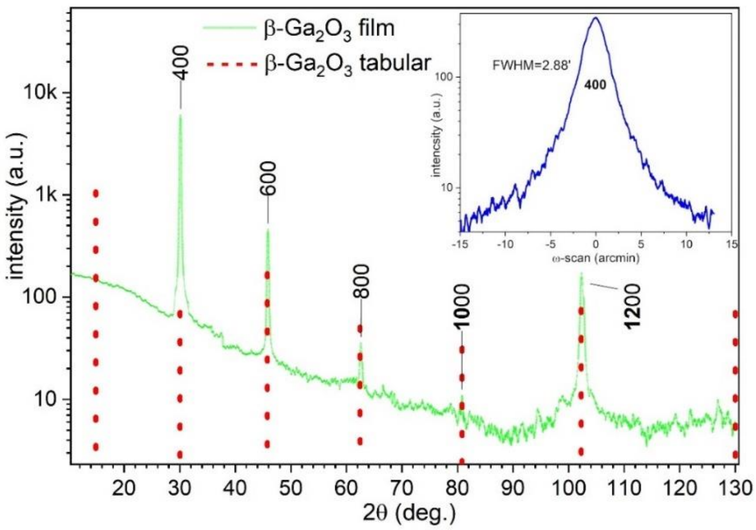

Fig. 4. XRD pattern and ω-scan (the inset) for the (100) β-Ga_2O_3 homoepitaxial layer

The phase composition and the crystal perfection were estimated via θ-2θ curve and the ω-scan, respectively. Figure 4 illustrates a single-crystal structured homoepitaxial [100] oriented β-Ga_2O_3 layer. No additional peaks indicating the presence of other phases or polycrystalline inclusions were detected. Perfection of the grown layer is confirmed by the successive series of even reflection orders from 400 up to 12 0 0 observed on the X-ray diffraction pattern obtained in the θ-2θ scanning mode (ICDD #00-041-1103). 200 and 14 0 0 reflections are not registered since their intensities are very low themselves as it is shown by pattern modeling [34].

An ω-scan of the 400-peak shown in the inset demonstrated that the rocking curve peak can be effectively fitted via a Gaussian function with the FWHM (full-width-of-half maximum) of less than 3 arcmin. I.e., the crystallinity of the layer can be thus estimated as 2.88 arcmin (see inset of the Fig. 4) which is highly acceptable value for the epitaxial layer. The absence of additional peaks within the incident beam area of 0.1 × 1.0 mm^2 indicates the presence of a coherent β-Ga_2O_3 mosaic of high perfection for this field of study.

Prior to lift-off process, the samples were undergoing annealing for initiating the exfoliating procedure. The exfoliation process was carried out using double-sided tape. The sample was glued to the tape with the epitaxial layer surface (see Fig. 5(a)). The substrate was then pulled upwards to peel off the epitaxial layer (see Fig. 5(b–d)). The most of epitaxial layers were successfully detached using this approach.

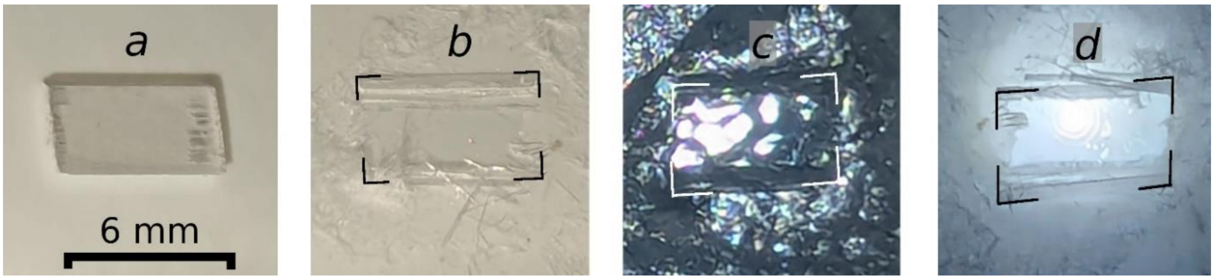

Fig. 5. Exfoliation process: the sample glued to the tape with the epitaxial layer surface (a), the peeled off epitaxial layer (b), the same in reflected light (c), the same in transmitted light (d). The silhouette of the epitaxial layer is indicated by the frame. The scale of all images is the same

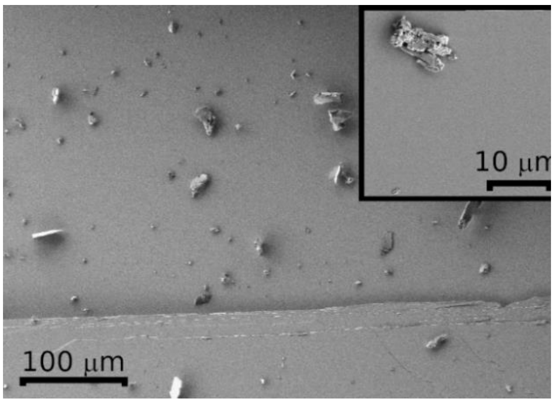

Fig. 6. SEM plan-view images of the (100) β-Ga_2O_3 stand-alone layer with particularities. A zoomed region is depicted in the inset

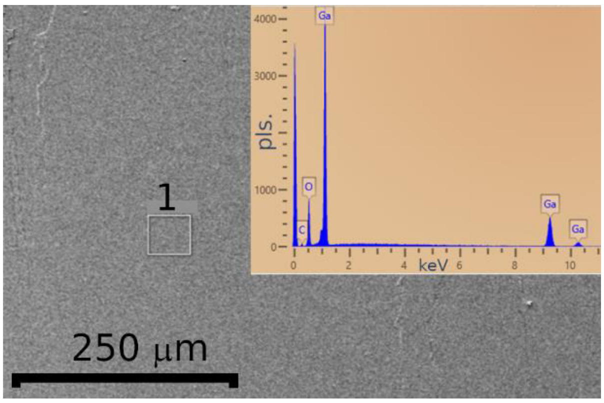

Fig. 7. SEM plan-view images of the (100) β-Ga_2O_3 stand-alone layer upon etching. EDS measurements were registered in the box marked as "1". The inset shows an energy spectrum contains Ga and O peaks only

SEM showed (see Fig. 6) that the contact surface of the exfoliated layer is suffered from uneven morphology, since it may include parts of the sacrificial Ni layer and fragments of gallium oxide itself which is capable of splitting along the cleavage plane. As soon as HNO_3 at room temperature does not affect gallium oxide substrate (unless it is in the form of thin films), but able to dissolve Ni, it was utilized as the etchant.

Upon etching the surface contained no particularities as well as no Ni has been found. This was approved by EDS measurements. The inset in Fig. 7 shows identification of Ga and O only while the white box indicates the scanning area.

The diffraction pattern registered for the spalled layer is depicted in Fig. 8. It shows split (due to the doublet nature of the radiation) reflections 400, 600, 800, 12 0 0, and also 10 0 0, which has the form of a separate peak (probably from the $K_{\alpha 1}$ line) with a satellite of reduced intensity (which can be interpreted as a contribution from the $K_{\alpha 2}$ component). Processing of the reflections set caused by the $K_{\alpha 1}$ radiation component yields the interplanar distance d_{200} (i.e. between adjacent (200) crystallographic planes) of about 11.865 Å. The similar value obtained on treating the reflections formed due to the $K_{\alpha 2}$ beam component turned out to be approximately 11.864 Å. The coherent-domain-size (CDS) value happened to be about 170 nm in both cases with a microstrain of no more than 10^{-4}. The set of the peaks in the range of ~ 13–28 deg. obviously belongs to tape material. Profile analysis of the ω-scan curve from the homoepitaxial β-Ga_2O_3 film of thickness 4 μm separated from a single-crystal substrate showed that its perfection (3.77 arcmin for the ω-scan curve FWHM) is close to the one of the unseparated layer (2.88 arcmin, see Fig. 4, the inset). Somewhat broadening and formation of symmetrical steps on both slopes of the ω-scan peak can be associated with its mechanical destruction in separating from the substrate.

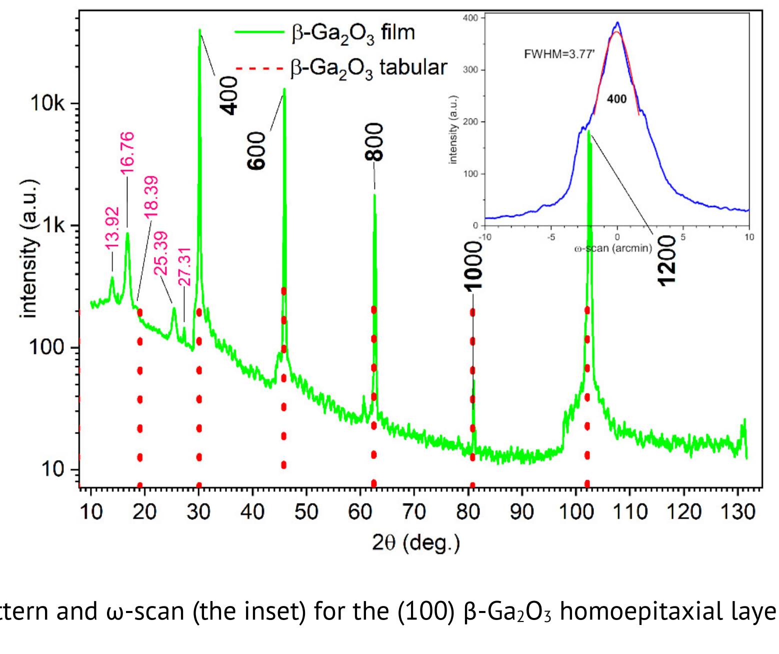

Fig. 8. XRD pattern and ω-scan (the inset) for the (100) β-Ga_2O_3 homoepitaxial layer after spalling

Conclusion

The fabrication of free-standing homoepitaxial (100) β-Ga_2O_3 layer by spalling from the native host-substrate is developed. It includes: 200-nm-thick sacrificial Ni film sputtering by vacuum thermal evaporation; formation of nickel micron scale drop-like mask by high temperature annealing and homoepitaxial growth of 4-μm-thick layer by mist-CVD. The mechanical exfoliation itself was carried out with preliminary annealing. The exfoliated layer is characterized as a coherent β-Ga_2O_3 mosaic structure with high perfection. The measured value of the coherent-domain-size is about 170 nm with a microstrain of no more than 10^{-4}. The full-width-of-a-half-maxima value is amounted as 3.77 arcmin, which is broadened compared to as-grown non-spalled layer (FWHM = 2.88 arcmin) presumably due to mechanically induced destruction. The exfoliated layers have smooth surface, and relatively high crystal quality. We propose that such approach is cost-effective for production of high power devices based on gallium oxide single crystals.

References

1. *World's first successful epitaxial deposition of gallium oxide on a 6-inch wafer using the HVPE method*. Available from: https://www.novelcrystal.co.jp/eng/2022/1107/ [Accessed 10th October 2024].
2. Ueda N, Hosono H, Waseda R, Kawazoe H. Synthesis and control of conductivity of ultraviolet transmitting β-Ga_2O_3 single crystals. *Appl. Phys. Lett.* 1997;70: 3561–3563.
3. Ritter JR, Lynn KG, McCluskey MD. Iridium-related complexes in Czochralski-grown β-Ga_2O_3. *J. Appl. Phys.* 2019;126: 225705.
4. Heinselman KN, Haven D, Zakutayev A, Reese SB. Projected Cost of Gallium Oxide Wafers from Edge-Defined Film-Fed Crystal Growth. *Crystal Growth & Design.* 2022;22(8): 4854–4863.
5. Butenko PN, Guzilova LI, Chikiryaka AV, Boiko ME, Sharkov MD, Almaev AV, Nikolaev VI. Impact on the subsurface layers of the single-crystal β-Ga2O3 wafers induced by a mechanical wear. *Materials Science in Semiconductor Processing*. 2022;143: 106520.
6. McClelland RW, Bozler CO, Fan JCC. A technique for producing epitaxial films on reuseable substrates. *Appl. Phys. Lett.* 1980;37(6): 560-562.
7. Cheng CW, Shiu KT, Li N, Han SJ, Shi L, Sadana DK. Epitaxial lift-off process for gallium arsenide substrate reuse and flexible electronics. *Nature Communications.* 2012;4: 1577.
8. Park H, Won H, Lim C, Zhang Y, Han WS, Bae SB, Lee CJ, Noh Y, Lee J, Lee J, Jung S, Choi M, Lee S, Park H. Layer-resolved release of epitaxial layers in III-V heterostructure via a buffer-free mechanical separation technique. *Sci. Adv.* 2022;8(3): eabl6406.
9. Hu H, Zhang B, Liu L, Xu D, Shao Y, Wu Y, Hao X. Growth of Freestanding Gallium Nitride (GaN) Through Polyporous Interlayer Formed Directly During Successive Hydride Vapor Phase Epitaxy (HVPE) Process. *Crystals.* 2020;10: 141.
10. Badokas K, Kadys A, Augulis D, Mickevicius J, Ignatjev I, Skapas M, Šebeka B, Juška G, Malinauskas T. MOVPE Growth of GaN via Graphene Layers on GaN/Sapphire Templates. *Nanomaterials.* 2022;12: 785.
11. Fujii K, Lee S, Ha JS, Lee HJ, Lee HJ, Lee SH. Leakage current improvement of nitride-based light emitting diodes using CrN buffer layer and its vertical type application by chemical lift-off process. *Appl. Phys. Lett.* 2009;94(24): 722–747.
12. Horng RH, Pan CT, Tsai TY, Wuu DS. Transferring Thin Film GaN LED Epi-Structure to the Cu Substrate by Chemical Lift-Off Technology. *Electrochem. Solid-State Lett.* 2011;14(7): H281.
13. Víllora EG, Shimamura K, Kitamura K, Aoki K, Ujiie T. Epitaxial relationship between wurtzite GaN and β-Ga_2O_3. *Appl. Phys. Lett.* 2007;90(23): 234102.
14. Wei T, Yang J, Wei Y, Huo Z, Ji X, Zhang Y, Wang J, Li J, Fan S. Cross-stacked carbon nanotubes assisted self-separation of free-standing GaN substrates by hydride vapor phase epitaxy. *Sci. Rep.* 2016;6: 28620.
15. Rogers DJ, Hosseini Teherani F, Ougazzaden A, Gautier S, Divay L, Lusson A. Use of ZnO thin films as sacrificial templates for metal organic vapor phase epitaxy and chemical lift-off of GaN. *Appl. Phys. Lett.* 2007;91(7): 71120.

16. Liu HF, Liu W, Chua SJ. Epitaxial growth and chemical lift-off of GaInN/GaN heterostructures on c- and r-sapphire substrates employing ZnO sacrificial templates. *J. Vac. Sci. Technol. A.* 2010;28(4): 590–594.
17. Tsai TY, Horng RH, Wuu DS, Ou SL, Hung MT, Hsueh HH. GaN Epilayer Grown on Ga_2O_3 Sacrificial Layer for Chemical Lift-Off Application. *Electrochem. Solid. ST.* 2011;14(11): H434–H437.
18. Tsai TY, Ou SL, Hung MT, Wuu DS, Horng RH. MOCVD growth of GaN on sapphire using a Ga_2O_3 interlayer. *J. Electrochem. Soc.* 2011;158(11): H1172–H1178.
19. Park J, Song KM, Jeon SR, Baek JH, Ryu SW. Doping selective lateral electrochemical etching of GaN for chemical lift-off. *Appl. Phys. Lett.* 2009;94: 221907.
20. Lin CF, Dai JJ, Wang GM, Lin MS. Chemical lift-off process for blue light-emitting diodes. *Appl. Phys. Express.* 2010;3(9): 2101.
21. Lin CF, Dai JJ, Lin MS, Chen KT, Huang WC, Lin CM, Jiang RH, Huang YC. An AlN sacrificial buffer layer inserted into the GaN/patterned sapphire substrate for a chemical lift-off process. *Appl. Phys. Express.* 2014;3(3): 031001.
22. Horng RH, Hsueh HH, Ou SL, Tsai CT, Tsai TY, Wuu DS. Chemical lift-off process for nitride LEDs from an Eco-GaN template using an AlN/strip-patterned-SiO_2 sacrificial layer. *Phys. Stat. Sol.* 2017;214(3): 1600657.
23. Hsueh HH, Ou SL, Wuu DS, Horng RH. InGaN LED fabricated on Eco-GaN template with a Ga_2O_3 sacrificial layer for chemical lift-off application. *Vacuum.* 2015;118: 8–12.
24. Zuo Y, Feng Q, Zhang T, Tian X, Li W, Li J, Zhang C, Zhang J, Hao Y. A Novel Method for Growing α-Ga2O3 Films Using Mist-CVD Face-to-face Heating Plates. *Nanomaterials.* 2023;13(1): 72.
25. Zhang Z, Yan P, Song Q, Chen H, Zhang W, Yuan H, Du F, Liu D, Chen D, Zhang Y. Recent progress of Ga2O3 materials and devices based on the low-cost, vacuum-free Mist-CVD epitaxial growth method. *Fundamental Research.* 2024;4(5): 1292-1305.
26. Vasin AV, Yatskiv R, Černohorský O, Bašinová N, Grym J, Korchovyi A, Nazarov AN, Maixner J. Challenges and solutions in Mist-CVD of Ga2O3 heteroepitaxial films. *Materials Science in Semiconductor Processing.* 2025;186; 109063.
27. Butenko PN, Boiko ME, Guzilova LI, Krymov VM, Shapenkov SV Sharkov MD, Verbitskii VN, Zarichny AA, Nikolaev VI. Enhancing the perfection of bulk (100) β-Ga2O3 crystals grown by Czochralski method. *J. Cryst. Growth.* 2024;630: 127597.
28. Butenko PN, Boiko ME, Sharkov MD, Almaev AV, Kitsay AA, Krymov VM, Zarichny AA, Nikolaev VI. High-temperature annealing of (201) β-Ga2O3 substrates for reducing structural defects after diamond sawing, *J. Semiconductors.* 2023;44: 122801,
29. Zarichny AA, Butenko PN, Boiko ME, Sharkov MD, Nikolaev VI. The analysis of the etch pits parameters in the (201) plane of the β-Ga2O3 substrate crystals. *Materials Physics Mechanics.* 2023;51(3): 46–51.
30. Butenko PN, Timashov RB, Boiko ME, Guzilova LI, Shapenkov SV, Sharkov MD, Sergienko ES, Stepanov AI, Nikolaev VI. Thick β-Ga2O3 homoepitaxial films grown on (201) substrate by mist-CVD. *Materials Today Communications.* 2024;41: 110970.
31. Butenko PN, Timashov RB, Stepanov AI, Pechnikov AI, Chikiryaka AV, Guzilova LI, Stepanov SI, Nikolaev VI. *Condensed Matter and Interphases.* 2023;25(4): 542.
32. *Metallographic Products for Sample Preparation and Analysis.* Available from: https://www.metallographic.com/ [Accessed 10th October 2024].
33. Stepanov SI, Nikolaev VI, Bougrov VE, Romanov AE. Gallium oxide: Properties and applications: a review. *Rev. Adv. Mater. Sci.* 2016;44(1): 63–86.
34. Persson K. *Materials Data on Ga_2O_3 (SG:12) by Materials Project.* Available from: https://doi.org/10.17188/1312771 [Accessed 10th October 2024].

About Authors

Pavel N. Butenko
Candidate of Technical Sciences
Senior Researcher (Ioffe Institute, St Petersburg, Russia)

Andrew V. Chikiryaka
Researcher (Ioffe Institute, St Petersburg, Russia)

Michael E. Boiko Sc
Candidate of Physical and Mathematical Sciences
Senior Researcher (Ioffe Institute, St Petersburg, Russia)

Liubov I. Guzilova Sc
Candidate of Physical and Mathematical Sciences
Researcher (Ioffe Institute, St Petersburg, Russia)

Vladimir M. Krymov Sc
Candidate of Physical and Mathematical Sciences
Senior Researcher (Ioffe Institute, St Petersburg, Russia)

Barzu A. Obidov Sc
Candidate of Physical and Mathematical Sciences
Researcher (Ioffe Institute, St Petersburg, Russia)

Roman B. Timashov Sc
Researcher (Ioffe Institute, St Petersburg, Russia)

Sevastian V. Shapenkov Sc
Candidate of Physical and Mathematical Sciences
Researcher (Ioffe Institute, St Petersburg, Russia)

Michael D. Sharkov Sc
Candidate of Physical and Mathematical Sciences
Senior Researcher (Ioffe Institute, St Petersburg, Russia)

Vladimir I. Nikolaev Sc
Candidate of Physical and Mathematical Sciences
Head of laboratory, Leading Researcher (Ioffe Institute, St Petersburg, Russia)

MATERIALS PHYSICS AND MECHANICS RESEARCH ARTICLE

Submitted: October 9, 2024 **Revised: October 9, 2024** **Accepted: December 4, 2024**

Surface study by x-ray scattering technique and phase contrast imaging: the examples of graphene and sapphire

T.S. Argunova [1]✉, V.G. Kohn [2], B.S. Roshchin [2], A.D. Nuzhdin [2], J.H. Lim [3], S.P. Lebedev [1], A.V. Ankudinov [1]

[1] Ioffe Institute, Saint-Petersburg, Russia

[2] National Research Centre "Kurchatov Institute", Moscow, Russia

[3] Pohang Accelerator Laboratory, Pohang, South Korea

✉ argunova2002@mail.ru

ABSTRACT

Nano-roughness evaluation for the surface of epitaxial graphene and height measurement are considered for a microstep on as-grown surface of sapphire in order to provide homogeneous graphene films on large areas of silicon carbide or sapphire substrates. To investigate dissimilar surface properties, different approaches have been used: off-specular grazing incidence X-ray scattering and in-line phase contrast imaging with synchrotron radiation. Statistical and local parameters of two types of surface morphology are measured. For the graphene surface, the dependence of the root-mean-square roughness of terrace-step nanostructure on the direction of the steps is estimated. For the vicinal face of sapphire, a surface step height of about one micron is determined directly from a phase contrast image, proving for the first time that the phase contrast imaging resolves surface morphology on a micrometer scale. Atomic force microscopy confirmed the obtained results.

KEYWORDS

graphene • epitaxial • SiC • sapphire ribbons • X-ray scattering • phase contrast imaging • synchrotron radiation

Acknowledgements. *The work of T.S. Argunova and S.P. Lebedev was carried out with the support of the Ministry of Science and Higher Education of the Russian Federation (agreement No 075-15-2021-1349). The work of V.G. Kohn was carried out within the state assignment of National Research Centre "Kurchatov Institute".*

Citation: Argunova TS, Kohn VG, Roshchin BS, Nuzhdin AD, Lim JH, Lebedev SP, Ankudinov AV. Surface study by x-ray scattering technique and phase contrast imaging: the examples of graphene and sapphire. *Materials Physics and Mechanics*. 2024;52(5): 64–73.
http://dx.doi.org/10.18149/MPM.5252024_7

Introduction

Silicon carbide (SiC) and sapphire (Al_2O_3) substrates are widely used for epitaxial films and thin coatings. Substrate production requires the use of complex processing to obtain a smooth surface with standard roughness parameters (root mean square roughness, RMS; mean height of peaks; mean depth of valleys, etc.). Nevertheless, a residual damage layer remains on the substrate surface and its removal leads to the formation of terrace-step nanostructures (TSN). Thus, both flat and TSN surfaces are specific to SiC and Al_2O_3 depending on their processing. The fabrication of high-quality graphene by the thermal decomposition of SiC meets requirements on cleaning and annealing of substrate. The removal of the residual damaged layer results in TSN. The formation of a continuous graphene sheet on such a substrate may be a serious problem [1]. Chemical vapor

Publisher: Peter the Great St. Petersburg Polytechnic University

deposition (CVD) offers an alternative possibility to synthesize graphite films on Al_2O_3 substrates at elevated temperature. According to some authors [2], CVD films demonstrate improved electrical parameters compared to epitaxial graphene on SiC.

When making single-layer graphene on a substrate containing TSN, one should consider the minimum step height and maximum terrace width at the lowest surface roughness values. During thermal processing, the graphene sheet partly repeats the TSN pattern on the substrate. Moreover, single- and few-layer graphene grow on the same substrate leading to the formation of regions with different values of surface potential [3]. Increasing roughness, in turn, results in a spread in the electrical resistance of electronic devices (see, e.g., [4]). For example, in sensor chips that detect viruses, harmful gases, chemicals, etc., the conducting graphene channel is located between contact pads whose orientation does not correspond to that of the TSN. At the same time, the correlation between the root-mean-square roughness and the direction of steps is not yet clear.

Various methods can be suitable for the fabrication of graphene, each with its own advantages and substrate requirements. For instance, the synthesis of graphene on sapphire reduces the cost of purchasing substrates. The main benefit of the Stepanov–LaBelle technology over those for growing large sapphire crystals is the production of finished substrates. In particular, basal-faceted sapphire ribbons do not require the use of machining and finishing processes. The ribbons can serve as substrates for GaN, Ga_2O_3 or graphene. Wide and thin ribbons which can be used to epitaxially grow these materials still have structural defects. The defects include microsteps arising due to small differences in the ribbon thickness or deflection of its surface from the basal face.

In this work, grazing-incidence X-ray scattering (GIXS) measurements and phase contrast imaging (PCI) using Synchrotron Radiation (SR) have been employed to investigate the nano- and microscale morphology of graphene and sapphire. Specular reflectometry and off-specular X-ray scattering technique allow roughness, density and thickness determination in extremely thin surface layers. Spectral data processing and inverse problem solution are based on the theories of grazing incidence X-ray methods (see, e.g., [5–10]). Particularly, off-specular GIXS provides an opportunity to determine Power Spectral Density (PSD) function, which is directly associated with the statistical parameters of roughnes [10–13].

X-ray phase contrast imaging has become widespread due to the construction of 3rd–generation SR sources [14,15] and to upgrades of existing ones. In the setup of PCI, SR propagates through the sample and illuminates the volume within the field of view. When a local phase shift caused by small changes in electron density is variable over the beam cross-section, the corresponding intensity variation can be detected through the phenomenon of refraction. Though this method was used to quantitatively analyze micro-inhomogeneities in crystals [16,17], its feasibility for quantitative surface imaging has not been demonstrated yet. It has recently been shown that PCI is applicable to thin composite layers [18] that may contain microcracks [19]; however, this method has only been employed for qualitative observations.

We emphasize that the quantitative aspects of using PCI for characterization of surface morphology have not been previously considered, but will now be addressed in this paper. In the next sections, two different experimental methods are briefly described. X-ray scattering measurements near the critical angle for total external reflection of epitaxial graphene are discussed. The results of imaging experiments on sapphire ribbons conducted at Pohang Light Source-II (PLS-II) are analyzed.

Materials and Methods

Semi-insulating SiC (0001) substrates purchased from different commercial channels had off-axis miscut angles, typically of the order of ⩽ 0.2 – 2°. The residual damaged layer was eliminated by high vacuum annealing in a closed tantalum cell in the temperature range of 1400 – 1500 °C at a residual gas pressure of 10^{-4} Pa [20,21]. As a result, a fairly regular pattern of terraces separated by steps formed on the polar silicon (Si) face of SiC. A further increase in temperature to 1725 °C allowed us to obtain a graphene sheet in an area of ~ 1 cm^2. Graphene was formed under an argon (Ar) atmosphere at a pressure of ~ 10^5 Pa. The specific properties of graphene were confirmed by Raman spectroscopy.

Figure 1(a) shows a cross-section view of a typical multilayer graphene on 4H-SiC substrate obtained by high resolution transmission electron microscopy (HRTEM). An electron-transparent lamella was prepared by cutting the substrate, with the cutting line lay perpendicular to the step direction. It can be seen that the graphene is not uniform. A white line encircles the step on the substrate surface. The image shows a distinct feature located at the interface between the film and substrate, but we cannot distinguish a gap from a step on the film. Both types of these defects increase the surface roughness.

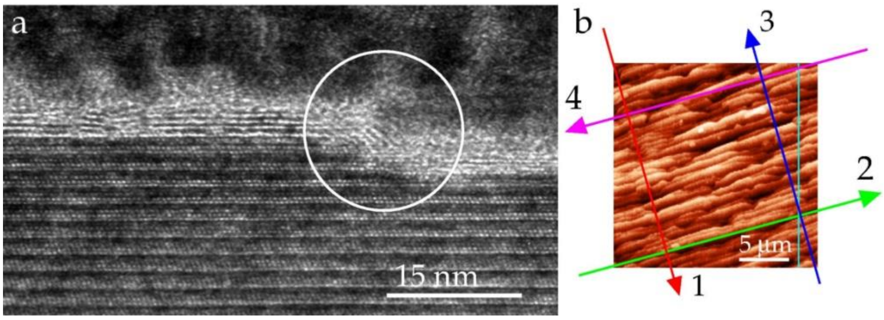

Fig. 1. (a) High resolution TEM image of the interface between Si-face 4H-SiC and multilayer graphene. White line encircles a step on the SiC surface; (b) AFM image of graphene surface. Arrows represent the X-ray scan directions, selected parallel (green, magenta) and perpendicular (red, blue) to the steps

The X-ray measurements were performed on a laboratory diffractometer [22]. A conventional X-ray tube with a Cu-anode served as a source. Radiation with wavelength λ = 0.154 nm reflected in a monochromator Si (111) within a passband of $\Delta\lambda/\lambda \approx 10^{-5}$. A vacuum collimator was placed between the sample and the detector to reduce parasitic scattering by air molecules. The collimated beam had a width of ~ 0.2 mm, a divergence of ~ 10^{-4} rad and an intensity of $I \approx 3{\cdot}10^6$ c^{-1}. The initial position of the sample surface was horizontal and parallel to the direction of the incident beam. During X-ray measurements, the source and detector rotated around a stationary sample. A scintillation detector SCSD-4 (Radicon Ltd., St. Petersburg, Russia) was used in conjunction with a position-sensitive strip Dectris MYTHEN 2R (Dectris AG, Baden-Dättwil, Switzerland). The detectors provided good linearity and made it possible to measure the intensities of specularly reflected and scattered radiation in one process. Angular scanning varied between 0° and

3°; the direction of incidence was fixed by the angle 0.236°; the scattering transfer vector and spatial frequency were in the range of 0–0.42 $Å^{-1}$ and 0.05–10 μm^{-1}, respectively. When the direct beam width in the plane of detector was 20 μm, the beam spot width on the sample was 5 mm at a grazing angle of 0.236°. The GIXS methodology for estimating TSN parameters was previously developed using Al_2O_3 and SiC substrates [23–25].

Compared to GIXS, PCI setup is very simple. Apart from the SR source, sample and detector, nothing else is required, provided that the spatial coherence of the incoming beam is sufficient. PCI is an appropriate technique to use, when a surface step entails a detectable phase shift. Since only intensities are measured, analytical means are needed to regain the phase-related information. Several efficient phase retrieval algorithms were produced.

The PCI experiments were carried out at the PLS-II operating at an electron energy of 3.0 GeV. At the BL6C beamline, a wiggler with a strong magnetic field (2.0 T) provides SR in the spectral range E = 23–50 keV. At a given energy of E = 23 keV, the double crystal monochromator selected a bandwidth $\Delta E/E = 2.9 \cdot 10^{-4}$. To obtain X-ray images, a sapphire ribbon was placed in the beam with its basal face perpendicular to the beam direction at a distance of r_s = 36 m from the wiggler source. Images were recorded with a scintillator screen coupled to a digital detector [26] located at a distance of r_d = 8 mm or 20 cm from the sample. Magnifying light optics projected a luminescent image onto the pixelated detector, and high image resolution was ensured by the small pixel size. In particular, the detector was equipped with a CCD matrix PCO Edge (PCO AG, Kelheim, Germany). Each chip had a resolution of 2560 × 2160 pixels and a size of 6.5 × 6.5 μm^2. The combination of ×20 objective lense with the PCO matrix led to an effective pixel size of 0.325 μm and a view field of 832 × 702 μm^2. For each pixel, a 16 bit analogue digital conversion was available.

Statistical parameters of roughness of epitaxial graphene on SiC

A characteristic feature within our approach is the computation of PSD function from angular distribution of scattered X-ray radiation [11–13]. The integral of the PSD function gives the effective roughness height σ_{eff}. The σ_{eff} is determined in the region of spatial frequencies limited by the width of the X-ray beam on one side and by the beam intensity on the other. In our case, the frequency range is limited by values $\nu_{min} = 0.05\ \mu m^{-1}$ and $\nu_{max} = 10\ \mu m^{-1}$.

X-rays illuminate large surface areas; actually, the entire sample area (up to 25–30 mm, when the width of the direct beam in the detector plane is ~ 100 μm), therefore GIXS technique can detect high σ_{eff} values. An increase in the average roughness height leads to a significant increase in the PSD-function values. Atomic force microscopy (AFM) scan size is usually lower than 100 × 100 μm^2. Nevertheless, AFM has higher resolution, therefore this method can image finer roughness scales. With this approach, a probed area is approximately three orders of magnitude smaller. One can characterize the roughness scales by comparing the values of the PSD functions calculated from GIXS and AFM data.

Figure 1(b) is an AFM image of TSN on the surface of a multilayer graphene film. The image shows X-ray scan directions relative to the step edges. Colored lines numbered 1 and 3 indicate two parallel scans located perpendicular to the step edges. In Fig. 2 the red (1) and blue (3) markers represent the PSD-curves plotted against frequency for scans 1 and 3, respectively. In the same diagram, the PSD-plots 2 and 4, shaped by green and magenta markers, refer to directions 2 and 4, which are parallel to the step edges. Note a peak in functions 1 and 3 that occurs when the beam scan is directed perpendicular to the steps. The position of the peak on the abscissa axis corresponds to the spatial frequency of the average TSN period. The peak shape is approximated by a Gaussian. The spread of periods and uneven edges of the terraces increase the peak width. The period value estimated from the GIXS data is 2.96 μm, but it should be noted that this result is obtained by averaging over a surface area of ~ 1 cm^2 illuminated by the beam. Scanning with a 90° rotation results in smoothing of the peak, as in the case of functions 2 and 4.

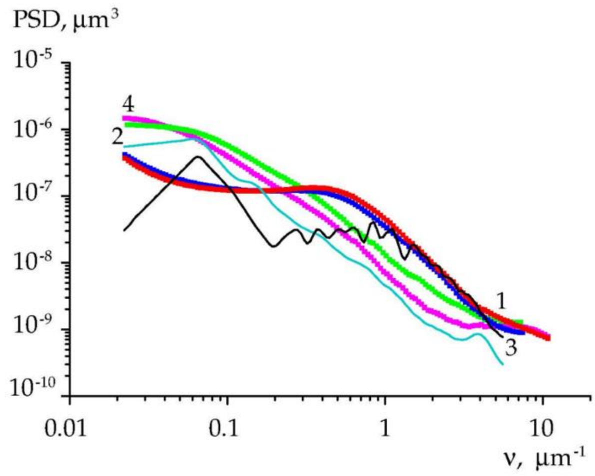

Fig. 2. Roughness PSD functions for multilayer graphene on Si face of 4H SiC. Plots corresponding to different scan directions are represented by markers of different colors: green, magenta (parallel) and red, blue (perpendicular) to the steps of TSN, respectively. PSD functions derived from AFM scans across (black) and along (cyan) the steps are indicated by curves without markers

In Fig. 2, solid lines (without markers) correspond to AFM scans directed along (cyan) or across (black) the steps, respectively. The behaviors of these PSD curves depending on the calculation direction are similar to those obtained with GIXS. Particularly, calculations across or along the steps result in a broad peak or monotonic decline, respectively. The discrepancy is seen in the low frequency region. The reason for the discrepancy relates to the decrease in AFM resolution that occurs when the roughness period is close to the AFM scan size. It should be stressed that in case of SiC substrates, a better match was obtained between the GIXS and AFM curves [25].

The effective roughness height σ_{eff} can be determined by the equation: $\sigma_{eff} = \sqrt{\int_{\nu_{min}}^{\nu_{max}} PSD\,(\nu)d\nu}.$

The value of σ_{eff} extracted from PSD curves I–IV for directions 1–4 is: $\sigma_{eff}^{(1)}$ = 0.37 nm, $\sigma_{eff}^{(2)}$ = 0.35 nm, $\sigma_{eff}^{(3)}$ = 0.35 nm, $\sigma_{eff}^{(4)}$ = 0.31 nm. Thus, we see that the deviation (calculated as the arithmetic mean of the absolute values of the deviations) does not exceed 17 %. According to various researchers who have measured the root-mean-square roughness of graphene, these values are unlikely to result in a noticeable variation in electrical resistance.

Local step height on as-grown surface of sapphire

As described in the previous section, spatially averaged X-ray scattering gives the root-mean-square roughness of the entire sample area (e.g. ~ 1 cm^2). In this section we have again used the interaction of X-rays with matter, but in a different approach, which has the essential advantage of ensuring locality of measurements. The ensemble of local measurements constitutes an image. The image shows contrast due to changes in absorption, phase, or Bragg diffraction. Here we present X-ray phase contrast. The PCI setup provides a relatively limited field of view – from a few square millimeters to fractions of a millimeter. Nevertheless, the method combines localization and a fairly large area by moving the sample in front of the detector and recording images [27]. Since PCI cannot display morphology in a way similar to AFM, the latter is used in this work to obtain additional information about a surface structure.

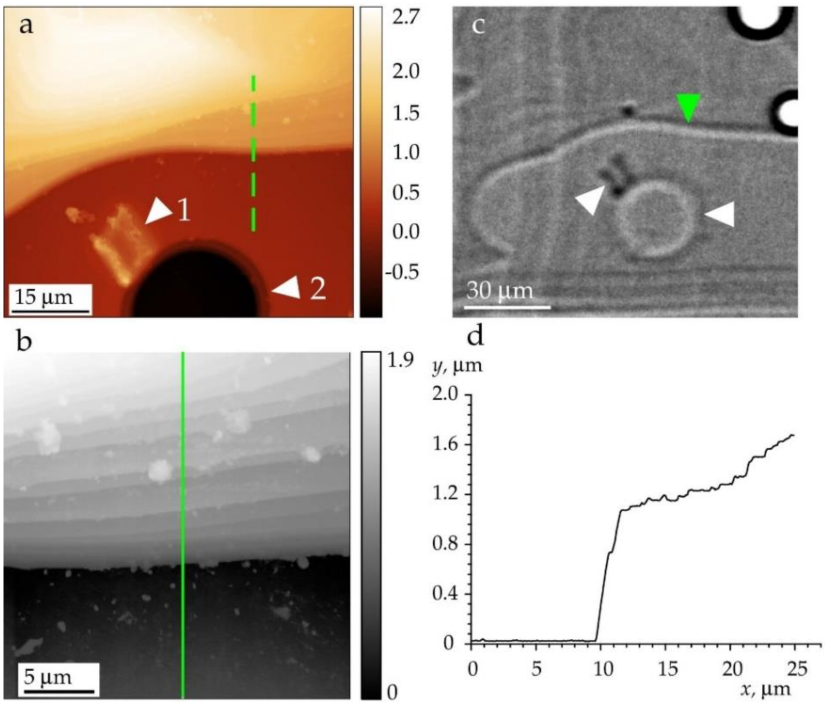

Fig. 3. (a) 2D representation of AFM data showing various defects in the sample. White arrows point to a particle (1) and a pit (2). The green dashed line indicates the AFM probing direction across the surface step. (b) AFM map of the step location. The solid line stands for the probing direction, identical to that shown in (a). In the phase contrast image (c), the green arrow points to the step region probbed by AFM. White arrows point to the same features as in (a). Profile (d) of the step height (y, µm) vs. the distance across the step (x, µm)

Figure 3 contains AFM and PCI images of the sapphire ribbon grown from the melt using Stepanov's method at a growth rate of 1 mm/min up to a size of 10 × 0.4 × 100 (W×H×L) mm^3. The misorientation of the ribbon surface relative to the basal facet was only a few arc minutes. Figure 3(a) shows several defects imaged by AFM. At the bottom of the figure, one can see a rounded pit and an irregularly shaped defect in the vicinity of the pit. In the 3D representation of the AFM data, this defect appears as a particle (data not shown). The wavy line dividing the light and dark areas defines a step on the surface of the ribbon. Green dashed line is for AFM scan across the step. The same scan is shown by the solid line in Fig. 3 (b), which displays a large-scale AFM map of the step location. At the top of the map, the light contrast corresponds to the step, and the dark contrast at the bottom comes from the material underneath the step. Furthermore, in the phase image (Fig. 3(c)) the same surface step is represented by a wavy line of black and white contrast. The green arrow indicates the position of the AFM scan on the sample surface. Note that the same location was chosen for the contrast evaluation on the phase image.

The pit and particle indicated above are present inside the region of interest. They were used as markers to localize both AFM and PCI measurements. We assume the following scenario for their formation. When a ribbon is pulled out, the metallic shaper heats up to a high temperature. A molten droplet can fall on the ribbon at some distance from the crystallization front, and overheating of the surface will lead to the formation of a pit.

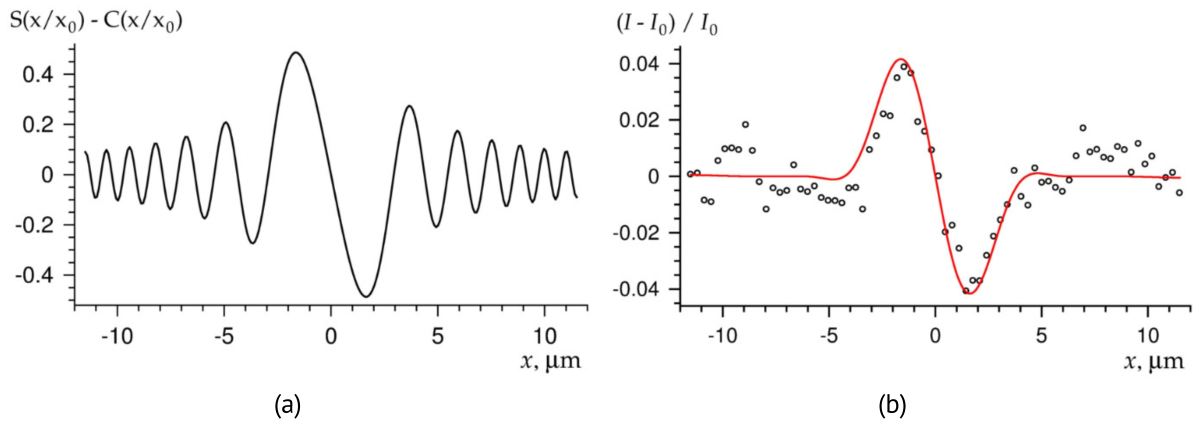

Fig. 4. Intensity profiles vs. the distance across the surface step. (a) Theoretical profile calculated for coherent radiation from a point source. x_0 = 2.32 μm. (b) Experimental (open circles) and theoretical (smooth red curve) relative intensity distributions. The red curve is obtained by averaging the profile in (a) after convolution with a Gaussian function (FWHM is 3 μm)

To evaluate theoretical intensity distribution for the step we employed X-Ray Wave Propagation (XRWP) computer program [28]. The result obtained for a point source and fully coherent radiation is shown in Fig. 4(a), where the maximum is located on the side of the smaller sample thickness. We note that many Fresnel fringes are formed besides the maximum and minimum.

The experimental profile was obtained by measuring the contrast of the phase image recorded in a CCD (Fig. 3(c)). The image was stored in TIFF format, 16-bit. TIFF file was converted into a matrix. In the course of further processing, the matrix was used to produce the image of the step with highest possible contrast. The intensity was measured perpendicular to the step section. Here we want to emphasize again that the section was located within the region of the AFM scan (Fig. 3(a)). In Fig. 4(b) open circles stand for the experimental data. One can see that the Fresnel fringes are simply not detected.

The theoretical and experimental intensity distributions were compared. Prior to the comparison, averaging on the fringes was performed. As an averaging method we propose to employ the standard convolution with a Gaussian function. The method is successful in cases when the factors responsible for the reduction in spatial coherence are unspecified. The full width at half maximum (FWHM) of Gaussian can be determined from preliminary experiments on test objects [29,30]. Finally, the smoothed theoretical profile is drawn by the red line in Fig. 4(b) (FWHM of the Gaussian is 3 μm).

Analytical solution gives the same results in a much more simple way. When the phase shift ϕ introduced by a surface step is small compared to unity, the intensity profile can be calculated as a power series of ϕ. Retaining only the first dominant contribution, we conclude that the contrast is proportional to ϕ, and the intensity profile is calculated analytically using an equation:

$$I/I_0 = 1 + \phi[S(x/x_0) - C(x/x_0)],\ \phi = K\delta t,\ x_0 = (\lambda r_d/2)^{1/2}, \quad (1)$$

where *S(x)* and *C(x)* are the sine and cosine Fresnel integrals, r_d is the distance from the object to the detector, ϕ is the local phase shift introduced by the step; $\phi \ll 1$. The contrast of the step determined from the plot is 0.2ϕ. Using the estimation of phase $\phi = 0.2$, obtained from the comparison of the experimental and simulated contrasts, and the decrement of the refractive index of sapphire $\delta = 1.532 \cdot 10^{-6}$, we find the step height t from the Eq. (1): $t = 1.12$ μm. This value is confirmed by the AFM data. The AFM analysis, whose graphical result is presented in Fig. 3(d), gives the step height versus the distance across the step. One can see that the step height changes slightly from 1 to 1.5 μm.

Conclusions

The present study is an example of the application of grazing-incidence X-ray scattering technique and phase contrast imaging to graphene and sapphire. The quality of graphene surface was estimated by statistical parameters of roughness. The surface of sapphire was investigated by in-line PCI method, which did not yet deal with solid surfaces and crystal faces. The novelty in the PCI experiment is that the microstep height has been determined directly from an image with fairly good accuracy (~ 1 μm), despite the relatively large decrease in spatial coherence. Our experimental design involves techniques that are not feasible in the same setup. Nevertheless, the combination of X-ray-matter interactions, namely scattering and refraction, which are commonly used for different purposes, has led to a better interpretation of surface morphology.

References

1. Yakimova R, Virojanadara C, Gogova D, Syväjärvi M, Siche D, Larsson K, Johansson LI. Analysis of the formation conditions for large area epitaxial graphene on SiC substrates. *Materials Science Forum.* 2010;645–648: 565–568.

2. Shan J, Sun J, Liu Z. Chemical vapor deposition synthesis of graphene over sapphire substrates. *ChemNanoMat.* 2021;7(5): 515–525.

3. Mammadov S, Ristein J, Krone J, Raidel C, Wanke M, Wiesmann V, Speck F, Seyller T. Work function of graphene multilayers on SiC(0001). *2D Mater.* 2017;4(1): 015043.

4. Shmidt NM, Shabunina EI, Gushchina EV, Petrov VN, Eliseyev IA, Lebedev SP, Priobrazhenskii SI, Tanklevskaya EM, Puzyk MV, Roenkov AD, Usikov AS, Lebedev AA. Quality assessment of processed graphene chips for biosensor application. *Materials.* 2023;16(16): 5628(1–10).

5. Vinogradov AV, Zorev NN, Kozhevnikov IV, Yakushkin IG. Phenomenon of total external reflection of X–rays. *Sov. Phys. JETP.* 1985;62(6): 1225–1229.

6. Kozhevnikov IV, Asadchikov VE, Alaudinov BM, Karabekov AYu, Vinogradov AV. X-ray investigations of supersmooth surfaces. In: *Proceedings of X-ray Optics and Surface Science.* 1995. p. 141–153.

7. Stoev KN, Sakurai K. Review on grazing incidence X-ray spectrometry and reflectometry. *Spectrochimica Acta Part B.* 1999;54(1): 41–82.

8. Zhou X-L, Chen S-H. Theoretical foundation of X-ray and neutron reflectometry. *Physics Reports.* 1995;257(4–5): 223–348.
9. Andreev AV. Theory of X-ray scattering by rough surfaces without distorted wave approximation. *Phys. Lett. A.* 1996;219(5–6): 349–354.
10. Kozhevnikov, IV, Pyatakhin MV. Use of DWBA and perturbation theory in X-ray control of the surface roughness. *J. X-Ray Sci. Technol.* 1998;8(4): 253–275.
11. Kozhevnikov IV. Physical analysis of the inverse problem of X-ray reflectometry. *Nucl. Instrum. Methods Phys. Res. A.* 2003;508(3): 519–541.
12. Asadchikov VE, Kozhevnikov IV, Krivonosov YS, Mercier R, Metzger TH, Morawe C, Ziegler E. Application of X-ray scattering technique to the study of supersmooth surfaces. *Nucl. Instrum. Meth. Phys. Res. A.* 2004;530(3): 575–595.
13. Kozhevnikov IV. General laws of x-ray reflection from rough surfaces: II. Conformal roughness. *Crystallogr. Rep.* 2012;57: 490–498.
14. Snigirev A, Snigireva I, Kohn V, Kuznetsov S, Schelokov I. On the possibilities of x-ray phase contrast microimaging by coherent high-energy synchrotron radiation. *Rev. Sci. Instrum.* 1995;66(12): 5486–5492.
15. Cloetens P, Barrett R, Baruchel J, Guigay JP, Schlenker M. Phase objects in synchrotron radiation hard x-ray imaging. *Journal of Physics D.* 1996;29(1): 133–146.
16. Kohn VG, Argunova TS, Je JH. Study of micropipe structure in SiC by x-ray phase contrast imaging. *Appl. Phys. Lett.* 2007:91(17); 171901.
17. Argunova TS, Kohn VG. Study of micropores in single crystals by in-line phase contrast imaging with synchrotron radiation. *Physics-Uspekhi.* 2019;62(6): 602–616.
18. Yeager JD, Luo SN, Jensen BJ, Fezzaa K, Montgomery DS, Hooks DE. High-speed synchrotron X-ray phase contrast imaging for analysis of low-Z composite microstructure. *Composites Part A.* 2012;43(6): 885–892.
19. Ignateva EV, Krasnitckii SA, Sheinerman AG, Gutkin MYu. The finite element analysis of crack tolerance in composite ceramics. *Materials Physics and Mechanics.* 2023;51(2): 21–26.
20. Dunaevskii MS, Makarenko IV, Petrov VN, Lebedev AA, Lebedev SP, Titkov AN. Using atomic-step-structured 6H-SiC(0001) surfaces for the calibration of nanotranslations in scanning probe microscopy. *Tech. Phys. Lett.* 2009;35(1): 47–49.
21. Lebedev SP, Petrov VN, Kotousova IS, Lavrentev AA, Dementev PA, Lebedev AA, Titkov AN. Formation of periodic steps on 6H-SiC (0001) surface by annealing in a high vacuum. *Mater. Sci. Forum.* 2011;679–680: 437–440.
22. Asadchikov VE, Babak VG, Buzmakov AV, Dorokhin YP, Glagolev IP, Zanevskii YV, Zryuev VN, Krivonosov YS, Mamich VF, Moseiko LA, Moseiko NI, Mchedlishvili BV, Savel'ev SV, Senin RA, Smykov LP, Tudosi GA, Fateev VD, Chernenko SP, Cheremukhina GA, Cheremukhin EA, Chulichkov AI, Shilin YuN, Shishkov VA. An X-ray diffractometer with a mobile emitter-detector system. *Instrum. Exp. Technol.* 2002;48(3): 364–372.
23. Butashin AV, Muslimov AE, Kanevsky VM, Deryabin AN, Pavlov VA, Asadchikov VE. Structural contribution to the roughness of supersmooth crystal surface. *Cryst. Rep.* 2013:58(3): 483–487.
24. Asadchikov VE, Blagov AE, Butashin AV, Volkov YO, Deryabin AN, Kanevskii VM, Muslimov AE, Protsenko AI, Roshchin BS, Targonskii AV, Chukhovskii FN. Lateral inhomogeneities of sapphire plates determined with the aid of x-ray and probe methods. *Technical Physics.* 2020;65(3): 400–406.
25. Roschin BS, Argunova TS, Lebedev SP, Asadchikov VE, Lebedev AA, Volkov YO, Nuzhdin AD. Application of grazing-incidence X-ray methods to study terrace-stepped SiC surface for graphene growth. *Materials.* 2022;15(21): 7669(1–13).
26. Bonse U, Busch F. X-ray computed microtomography using synchrotron radiation. *Prog. Biophys. Mol. Biol.* 1996;65(1–2): 133–169.
27. Argunova TS, Kohn VG, Lim J-H, Krymov VM, Gutkin MYu. Large-area mapping of voids and dislocations in basal-faceted sapphire ribbons by synchrotron radiation imaging. *Materials.* 2023;16(19): 6589.
28. Kohn VG. Available online: https://xray-optics.ucoz.ru/XR/xrwpe.htm (accessed on 08 October 2024).
29. Kohn V, Snigireva I, Snigirev A. Interferometric characterization of spatial coherence of high energy synchrotron X-rays. *Optics Communications.* 2001;198(4-6); 293–309.
30. Argunova TS, Kohn VG, Lim J-H, Krymov VM, Ankudinov AV. Imaging of micro-steps on as-grown surface of sapphire with X-ray phase contrast technique. *Physics Letters A.* 2024;525: 129901(1–4).

About Authors

Tatiana S. Argunova Sc
Doctor of Physical and Mathematical Sciences
Chief Researcher (Ioffe Institute, Saint-Petersburg, Russia)

Victor G. Kohn Sc
Doctor of Physical and Mathematical Sciences
Chief Researcher (National Research Centre "Kurchatov Institute", Moscow, Russia)

Boris S. Roshchin Sc
Candidate of Physical and Mathematical Sciences
Researcher (National Research Centre "Kurchatov Institute", Moscow, Russia)

Alexander D. Nuzhdin Sc
Junior Researcher (National Research Centre "Kurchatov Institute", Moscow, Russia)

Jae-Hong Lim Sc
Beamline Scientist (Pohang Accelerator Laboratory, Pohang, South Korea)

Sergey P. Lebedev Sc
Candidate of Physical and Mathematical Sciences
Senior Researcher (Ioffe Institute, Saint-Petersburg, Russia)

Alexander V. Ankudinov Sc
Candidate of Physical and Mathematical Sciences
Senior Researcher (Ioffe Institute, Saint-Petersburg, Russia)

MATERIALS PHYSICS AND MECHANICS RESEARCH ARTICLE

Submitted: July 4, 2024 **Revised: October 7, 2024** **Accepted: October 21, 2024**

S-parameters of flexible electromagnetic radiation shields with Fe-Ni system coating

A.D. Gladinov ✉, **O.V. Boiprav**, **V.A. Bogush**

Belarusian State University of Informatics and Radioelectronics, Minsk, Belarus

✉ mr.gladinov@mail.ru

ABSTRACT

The results of studies of 2.0–17.0 GHz frequency responses of S11 and S21 values of flexible electromagnetic radiation shields made of metallized polymer film, on the surface of which a coating of the Fe–Ni system is applied by electron beam evaporation, are presented. It has been experimentally established that an alloy in the Fe–Ni system containing 56 wt. % (~ 57 at. %) Fe and 44 wt. % (~ 43 at. %) Ni is azeotropic one. Such composition corresponds to the minimum temperature at which the total vapor pressure reaches 10 Pa. It has been determined that by applying of the Fe–Ni system coating with the specified content of components to the surface of a metallized polymer film, it is possible to reduce S11 value by a maximum of 5.0 dB and S21 value by a maximum of 6.7 dB in the frequency range of 2.0–17.0 GHz of this film.

KEYWORDS

flexible shield • electromagnetic radiation • Fe–Ni system • electron beam evaporation

Citation: Gladinov AD, Boiprav OV, Bogush VA. S-parameters of flexible electromagnetic radiation shields with Fe-Ni system coating. *Materials Physics and Mechanics*. 2024;52(5): 74–82.
http://dx.doi.org/10.18149/MPM.5252024_8

Introduction

Electromagnetic radiation (EMR) shielding is currently a pressing chronic problem due to the continuous development of radio-electronic devices, especially with wireless power supplies, which has necessitated the constant improvement of means of protection against negative electromagnetic interference. In recent years, employees of Belarusian State University of Informatics and Radioelectronics, based on the results of their research, have developed various devices for EMR shielding.

Thus, at the research laboratory "Materials, Technologies and Equipment for Safety" of Belarusian State University of Informatics and Radioelectronics, the following main kinds of EMR shields have been developed:

1. non-flammable shields based on aluminum oxide and magnetic powder [1];
2. shields based on fabric materials [2,3].

One of the current directions of the research work conducted in the indicated laboratory is development of EMR shields based on foil and foiled film materials [4,5]. EMR shields based on foil, or foiled (metallized) film materials are also direction of the work conducted by the other researchers [6–10]. The main advantage of such materials is their thinness and flexibility. Due to this advantage it’s possible to modify the shape of the shields based on these materials. Such materials are widely used nowadays for obtaining EMR shields with frequency selective surface (metasurface) [11–19]. Moreover, origami technic is widely used nowadays to create EMR shields based on such materials [20–29].

Publisher: Peter the Great St. Petersburg Polytechnic University

All of the above shields are composite structures that provide a high degree of EMR shielding. At the same time, the use of thin-film vacuum coatings for EMR shielding systems, combining metal layers with high values of electrical conductivity (Al, Cu) and relative magnetic permeability (Ni, Fe), is one of the little-studied and promising areas. The choice of the electron beam evaporation method for the Fe–Ni system films obtaining is primarily due to the impossibility of using magnetron sputtering methods due to the shielding of the magnetron cathode unit magnetic field by targets. Since electron beam evaporation causes alloy fractionation, the azeotropic composition of the alloy was calculated for the Fe–Ni system. The relevance of the work is due to the ever-increasing requirements for noise immunity of electronic devices.

This article discusses the results of studies of the protective properties of flexible EMR screens made of metallized polymer film with coatings of the Fe–Ni system formed on their surface by electron beam evaporation.

Justification of the composition of Fe–Ni system coating

As follows from the phase diagram (Fig. 1), Fe–Ni system alloys are unlimited solid solutions, therefore, during their electron beam evaporation, the liquid → vapor phase transition obeys Raoult's law. The sizes of the elements radii near their melting temperatures, R_{Fe} = 0.1290 nm, R_{Ni} = 0.1246 nm. Therefore, Fe and Ni activities ratio in accordance with [30] is equal to:

$$\frac{f_{Fe}}{f_{Ni}} = \left(\frac{R_{Fe}}{R_{Ni}}\right)^3 = \left(\frac{0.1290}{0.1246}\right)^3 = 1.11. \quad (1)$$

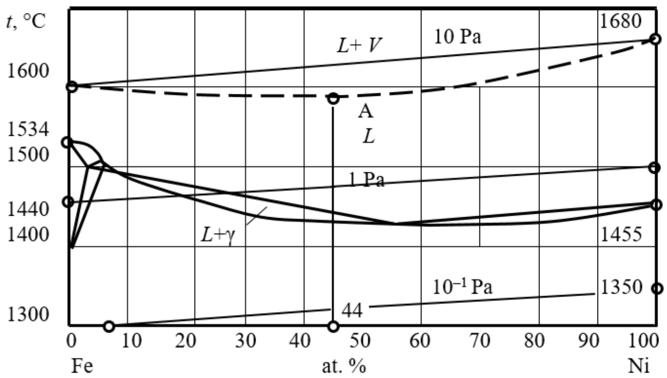

Fig. 1. State diagram of the Fe–Ni system (L – liquid; V – vapor; γ – γ-phase)

The required rate of deposition of Fe–Ni systems coatings with a thickness of 150 nm is ensured at a Ni and Fe vapor pressure ranging from 1 to 20 Pa. According to Fig. 1, the evaporation temperatures of Ni–Fe system alloys should be in the range from 1500 to 1650 °C. The average pressure of Fe vapor in this temperature range is 13 Pa, and that of Ni vapor is 11 Pa [30]. The atomic masses of the elements Ni and Fe are 58.71 and 55.85 amu. respectively.

Substituting all the indicated values into Eq. (1), for the Fe–Ni system we obtain:

$$\frac{n_{Ni}}{n_{Fe}} = \frac{f_{Ni} x_{Ni} P_{Ni}}{f_{Fe} x_{Fe} P_{Fe}} \left(\frac{A_{Fe}}{A_{Ni}}\right)^{1/2} \text{at } \frac{n_{Ni}}{n_{Fe}} = 1, \text{ we get } x_{Fe} = 1.11 \cdot \left(\frac{13}{11}\right) \cdot \left(\frac{58.71}{55.85}\right)^{1/2} \cdot x_{Ni} = 1.345 \cdot x_{Ni}. \quad (2)$$

From equation $x_{Fe} + x_{Ni} = 1$ we find that $x_{Fe} = 0.574$; $x_{Ni} = 0.426$. Thus, according to the carried calculations out, it was established that Fe–Ni system alloy containing 56 wt. % (~57 at. %) Fe and 44 wt. % (~ 43 at. %) Ni is azeotropec one. Such composition corresponds to the minimum temperature value at which the total vapor pressure reaches 10 Pa (Fig. 1, point A on the isobar).

The reproducibility of the composition of layers of Ni–Fe system alloys obtained by electron beam evaporation was judged by the results of an analysis of their elemental composition. Nickel grade NP2 and iron 005ZhR were used as starting materials. Five samples of alloys were prepared from these materials. The compositions of the alloys, as well as the average content of elements in coatings 150 nm thick, are given in Table. 1. Each value was obtained from elemental analysis data of at least 3 samples.

Table 1. Compositions of the Fe–Ni system alloys and average element contents in 150 nm thick coatings obtained by electron beam evaporation

Alloy number	Alloy composition, at. %		150 nm thick coatings composition, at. %		
	Fe	Ni	Fe	Ni	Others
1	30	70	51.5	45.4	3.1
2	40	60	38.8	58	3.2
3	55	45	51	47.6	1.4
4	60	40	58.7	38.8	2.5
5	70	30	68.5	28.7	2.8

It can be seen that the elemental composition of the films is preserved upon evaporation of the $Fe_{55}Ni_{45}$ alloy, i.e. its congruent evaporation occurs. At the same time, as follows from Table 1, due to the very similar values of vapor pressure, molecular weights, parameters of the crystal lattices of Fe and Ni, as well as the unlimited solubility of these elements in melts, the elemental composition of films of the Fe–Ni system is quite close to all the compositions of evaporated alloys that we have studied.

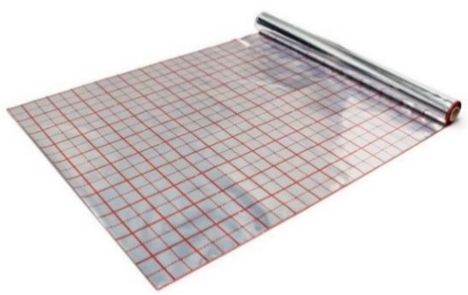

Fig. 2. The appearance of the film Kotar IZOFOLIX

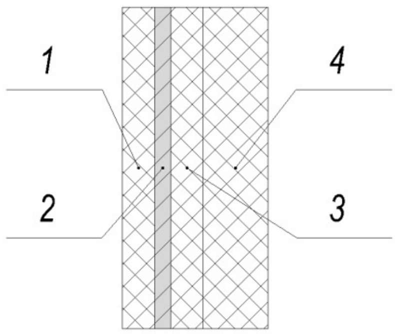

Fig. 3. Layers' layout of the film Kotar IZOFOLIX: 1, 3 – polypropylene film; 2 – aluminum layer; 4 – polyethylene layer

Kotar IZOFOLIX film was chosen as a polymer base for the coating [31]. This film has a thickness of 105 μm. It has multilayer structure, one of the layers of which is aluminum with a thickness of 150 nm. The appearance of this film is shown in Fig. 2, and its layers' layout is shown in Fig. 3.

An alloy of composition $Fe_{55}Ni_{45}$ was used as material for applying coatings by electron beam evaporation. Coatings were applied to the polymer substrate using a VU-1A installation according to the following regime:

1. the residual gas pressure in the chamber was no more than $5 \cdot 10^{-2}$ Pa;
2. the substrate temperature was no more than 40 °C;
3. the application time was 150 s;
4. the application speed was 1 nm/s;
5. the distance from the crucible to the polymer substrate was 400 mm;
6. the weight of the sample was 20 g.

In this case, the thickness of the applied Fe–Ni system coating was 150 nm. The choice of this thickness value is due to the low heat resistance of the polymer substrate. At a coating application rate of 1 nm/s and a process duration of more than 150 s, the substrate is destroyed. The layers' layout of the EMR shield obtained according to the presented method is shown in Fig. 4.

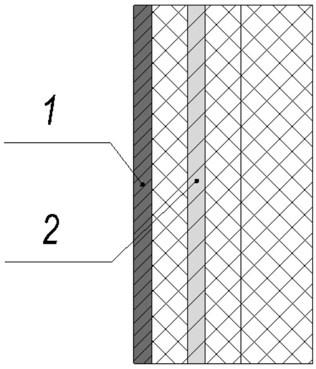

Fig. 4. Layers' layout of the EMR shield:
1 – coating of the Fe–Ni system; 2 – the film Kotar IZOFOLIX

Methods

The measurements of the EMR reflection and transmission coefficients the shields (S11 and S21 values, respectively) were carried out in the frequency range of 2.0–17 GHz. The panoramic meter of transmission and reflection coefficients SNA 0.01–18 was used for the measurements. The measurements were carried out in accordance with Standard 20271.1–91 "Microwave electronic products. Methods for measuring electrical parameters". The modulus of the measurements relative error of EMR reflection and transmission coefficients doesn't exceed 10.0 %. The connection diagrams of the modules of this meter are shown in Fig. 5.

The dimensions of the studied EMR shields samples were 300 × 400 mm. The following EMR shields samples were studied:

1. single-layer EMR shield sample based on Kotar IZOFOLIX film (Fig. 3), sample 1.1;
2. double-layer EMR shield sample based on Kotar IZOFOLIX film (Fig. 6), sample 1.2;
3. single-layer EMR shield sample based on Kotar IZOFOLIX film, on the surface of which a 150 nm coating from $Fe_{55}Ni_{45}$ alloy was applied (Fig. 4), sample 2.1;

4. double-layer EMR shield sample based on Kotar IZOFOLIX film, on the surface of which 150 nm coating from $Fe_{55}Ni_{45}$ alloy was applied (Figs. 7,8), samples 2.2 and 2.3, respectively.

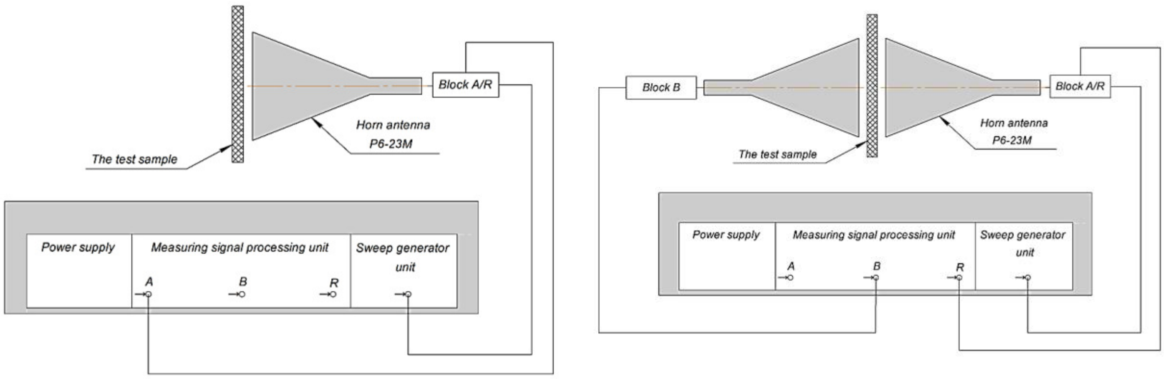

Fig. 5. The connection diagrams of the modules of panoramic meter of transmission and reflection coefficients SNA 0.01–18 for S11 value (a) and S21 value (b) measuring

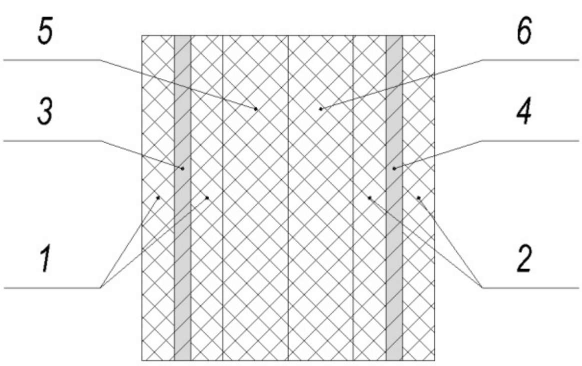

Fig. 6. Layers layout of the sample 1.2:
1, 2 – polypropylene film; 3, 4 – aluminum layer;
5, 6 – polyethylene layer

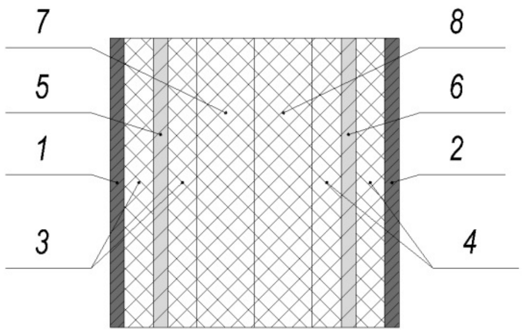

Fig. 7. Layers' layout of the sample 2.2:
1, 2 – coating of the Fe–Ni system;
3, 4 – polypropylene film; 5, 6 – aluminum layer; 7, 8 – polyethylene layer

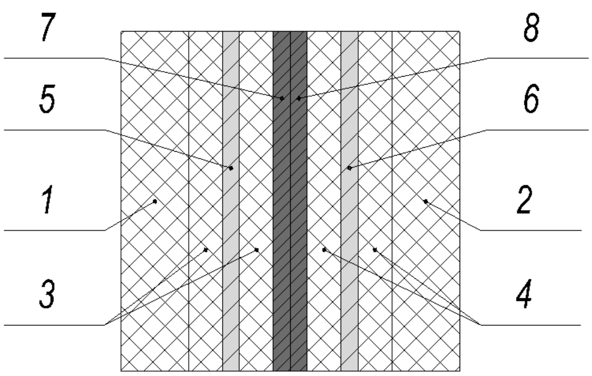

Fig. 8. Layers' layout of the sample 2.3: 1, 2 – polyethylene layer; 3, 4 – polypropylene film;
5, 6 – aluminum layer; 7, 8 – coating from $Fe_{55}Ni_{45}$ alloy

Fig. 9. External view of the measuring unit IUS-3 with an installed sample

Measurement of the surface resistance of the sample 2.1 was performed. The measuring unit IUS-3 was used for this (Fig. 9).

The surface resistance (ρ_s) of the indicated sample was measured using the four-probe method under the following conditions: the probes were arranged in a row at five points; the distance between the probes was 1 mm; slides measuring 75×25×2 mm^3 were used as substrates.

Based on the results of such measurements, the specific surface resistance (ρ) of the sample was calculated according to the following equation:

$$\rho = \rho_s \cdot t, \quad (3)$$

where t is the sample thickness.

Results and Discussion

2–17 GHz frequency responses of S11 values of the samples 1.1 and 1.2 are presented on Fig. 10.

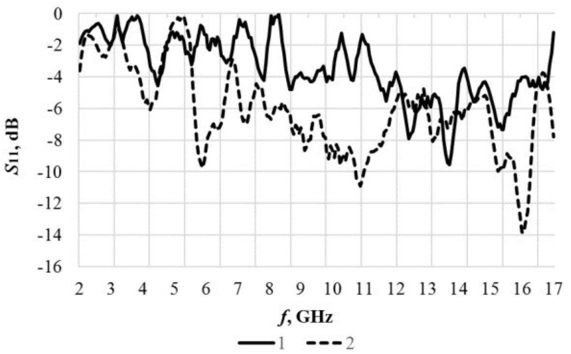

Fig. 10. 2–17 GHz frequency responses of S11 values of the samples 1.1 (curve 1) and 1.2 (curve 2)

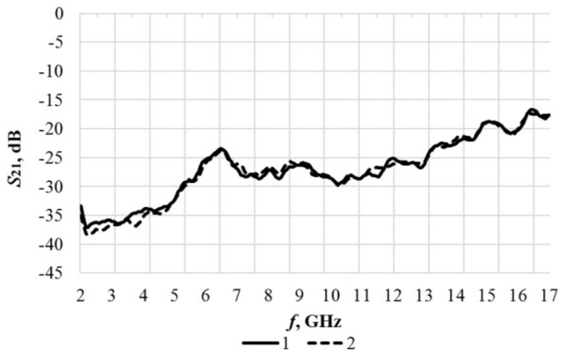

Fig. 11. 2–17 GHz frequency responses of S21 values of the samples 1.1 (curve 1) and 1.2 (curve 2)

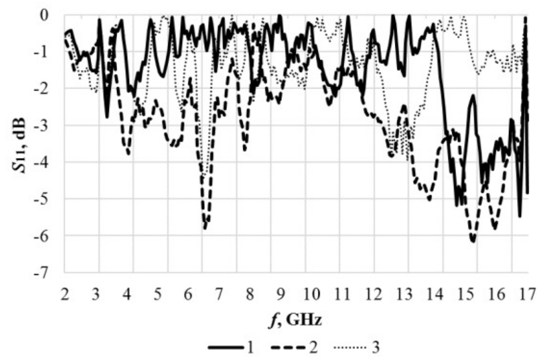

Fig. 12. 2–17 GHz frequency responses of S11 values of the samples 2.1 (curve 1), 2.2 (curve 2) and 2.3 (curve 3)

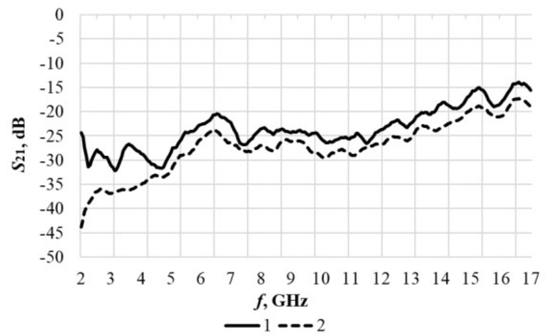

Fig. 13. 2–17 GHz frequency responses of S21 values of the samples 2.1 (curve 1), 2.2 and 2.3 (curve 2)

In the frequency range 2–17 GHz, S11 values change from -9.4 to -0.04 dB and from -13.8 to -0.14 dB for the samples 1.1 and 1.2 respectively. It should be noted that when the number of layers in the shield based on the film Kotar IZOFOLIX increases from one to two, the energy of the EMR reflected from it decreases. This phenomenon is most clearly observed in the frequency ranges of 5–7, 10–12 and 15–16 GHz. This phenomenon is associated with the resonant interaction in antiphase of the EMR of the listed frequency ranges. 2–17 GHz frequency responses of S21 values of the samples 1.1 and 1.2 are presented on Fig. 11.

In the frequency range of 2–17 GHz, S21 values change from -36.5 to -16.6 dB and from -38.2 to -17.4 dB for of the samples 1.1 and 1.2 respectively. Thus, increasing the number of layers in shields based on film Kotar IZOFOLIX doesn't have a significant effect on their S21 values. 2–17 GHz frequency responses of S11 values of the samples 2.1, 2.2 and 2.3 are presented on Fig. 12.

In the frequency range of 2–17 GHz, S11 values vary from -5.5 to -0.017 dB for the sample 2.1, from -6.2 to -0.25 dB for the sample 2.2, and from -4.4 to -0.006 dB for the sample 2.3. 2–17 GHz frequency response of S11 value of the sample 2.2 is characterized by a resonant decrease in the frequency ranges of 5–7 and 14–16 GHz. 2–17 GHz frequency responses of S21 values of the samples 2.1, 2.2 and 2.3 are presented on Fig. 13.

S21 values vary from -33.0 to -14.2 dB for the sample 2.1 and 2.2 and from -43.7 to -17.3 dB for the samples 2.3. Thus, an increase from one to two layers in the shield based on film Kotar IZOFOLIX, on the surface of which a 150 nm coating of $Fe_{55}Ni_{45}$ alloy is applied, leads to a decrease by 3–18 dB in the S21 value of this shield.

The relative measurement error of the surface resistance of coatings using the four-probe method doesn't exceed 5.0 %. To reduce the measurement error, the results of five measurements of the specified parameter for each sample were averaged.

The results of surface resistance measurements of the sample 2.1 are presented in Table 2.

Table 2. The results of surface resistance measurements of the sample 2.1

Area No. 1, Ω/ square	Area No. 2, Ω/ square	Area No. 3, Ω/ square	Area No. 4, Ω/ square	Area No. 5, Ω/ square
39.3	47.9	42.3	53.1	58.8

Based on the results of calculations carried out using Eq. (3), it was determined that the specific surface resistance of a 150 nm coating of $Fe_{55}Ni_{45}$ alloy is $7.242 \cdot 10^{-6}$ Ω·m: $\left(\frac{39.3+47.9+42.3+53.1+58.8}{5}\right) \cdot 150 \cdot 10^{-9} = 48.28\ \Omega/\text{square}\ \cdot 150 \cdot 10^{-9}\ \text{m} = 7.242 \cdot 10^{-6} \Omega \cdot \text{m}.$

Conclusions

Calculations of the parameters of the compositions a coating of Fe–Ni alloys were carried out. Based on the results of such calculations, it was found that the $Fe_{55}Ni_{45}$ alloy is azeotropic one. The mode of applying a 150 nm coating of this alloy onto a substrate in the form of a foil-clad polypropylene film (film Kotar IZOFOLIX) was developed.

It was found that applying a 150 nm coatings of $Fe_{55}Ni_{45}$ alloy onto film Kotar IZOFOLIX allows to reduce its S11 value by a maximum of 5 dB, and S21 value by a maximum of 6.7 dB. When increasing the number of layers in the shield based on film Kotar IZOFOLIX from one to two, its S11 value decreases by a maximum of 10 dB. S21 value remains virtually unchanged. Increasing the number of layers in the shield based on film Kotar IZOFOLIX, on the surface of which a 150 nm coating of $Fe_{55}Ni_{45}$ alloy is applied, from one to two leads to a decrease by a maximum of 5 dB in the S11 value of such shield. It's S21 value decreases by 3–18 dB in such case. It was determined that the specific surface resistance of a 150 nm coating of $Fe_{55}Ni_{45}$ alloy is $7.242{\times}10^{-6}$ Ω·m.

References

1. Penialosa Ovalies DI, Boiprav OV, Tumilovich MV, Lynkou LM. Electromagnetic Radiation Shielding Composite Coatings Based on Powdered Alumina and Iron Oxides. *Doklady BGUIR*. 2021;19(3): 104–109.
2. Boiprav OV, Ahmed AAA, Lynkou LM. Electromagnetic Radiation Reflection and Transmission Characteristics of Shielding Polyester Fabric with Nanostructured Ferromagnetic Microwire, Containing Copper Clusters. *Doklady BGUIR*. 2015;3(89): 49–52. (In Russian)
3. Abdulhadi HA, Almashat EA, Boiprav OV, Bogush VA, Prudnik AM. Electromagnetic and Sound Insulation Properties of Combined Shields Based on the Needle-Punching Material and Fragments of Aluminum Foil. *Doklady BGUIR*. 2020;18(1): 89–95. (In Russian)
4. Boiprav OV, Lynkou LM, Mukhurov NI, Al-Mashat EAA. Electromagnetic Radiation Shields Based on Anodic Aluminum Oxide. *Doklady BSUIR*. 2018;7(117): 159–161.
5. Boiprav O, Hasanov M, Bogush V, Lynkou L. Flexible Double-Layered Microwave Absorbers Based on Foiled Materials with Mechanically Treated Surface. *New Materials, Compounds and Applications*. 2023;7(2): 100–110.
6. Rambung E, Kalanjati VP, Abdurachman. Aluminum Foil Shield Diminishes the Electromagnetic Radiation of Mobile Phones in the Cerebellum of Adult Male Rats. In: *Proceedings of Surabaya International Physiology Seminar (SIPS 2017)*. 2017: 97–100.
7. Li W, Jin H, Zeng Z, Zhang L, Zhang H, Zhang Z. Flexible and easy-to-tune broadband electromagnetic wave absorber based on carbon resistive film sandwiched by silicon rubber/multi-walled carbon nanotube composites. *Carbon*. 2017;121: 544–551.
8. Kim T, Wan Do H, Choi KJ, Kim S, Lee M, Kim T, Yu BK, Cheon J, Min BW, Shim W. Layered Aluminum for Electromagnetic Wave Absorber with Near-Zero Reflection. *Nano Letters*. 2021; 21(2): 1132–1140.
9. Hwang U, Kim J, Seol M, Lee B, Park IK, Suhr J, Nam JD. Quantitative Interpretation of Electromagnetic Interference Shielding Efficiency: Is It Really a Wave Absorber or a Reflector? *ACS Omega*. 2022;7(5): 4135–4139.
10. Lu Z, Zhang Y, Wang H, Xia C, Liu Y, Dou S, Li Y, Tan J. Transparent Thermally Tunable Microwave Absorber Prototype Based on Patterned VO_2 Film. *Engineering*. 2023;29: 198–206.
11. Hussein MN, Zhou J, Huang Y, Kod M, Sohrab AP. A Miniaturized Low-Profile Multilayer Frequency-Selective Surface Insensitive to Surrounding Dielectric Materials. *IEEE Transactions on Microwave Theory and Techniques*. 2017;65(12): 4851–4860.
12. Zhou Z, Chen K, Zhao J, Chen P, Jiang T, Zhu B, Feng Y, Li Y. Metasurface Salisbury screen: achieving ultra-wideband microwave absorption. *Optics Express*. 2017;24(24): 30241–30252.
13. Wang P, Zhang Y, Chen H, Zhou Y, Jin F, Fan H. Broadband radar absorption and mechanical behaviors of bendable over-expanded honeycomb panels. *Composites Science and Technology*. 2018;162: 33–48.
14. Chakradhary VK, Baskey HB, Roshan R, Pathik A, Akhtar MJ. Design of Frequency Selective Surface-Based Hybrid Nanocomposite Absorber for Stealth Applications. *IEEE Transactions on Microwave Theory and Techniques*. 2018;66(11): 4737–4744.
15. Xu Y, He M. Design of Multilayer Frequency-Selective Surfaces by Equivalent Circuit Method and Basic Building Blocks. *International Journal of Antennas and Propagation*. 2019: 9582564.
16. Dutta R, Mitra D, Ghosh J. Dual-band multifunctional metasurface for absorption and polarization conversion. *International Journal of RF and Microwave Computer-Aided Engineering*. 2020;30: e22200.
17. Qian J, Gou P, Pan H, Zhu L, Gui YS, Hu CM, An Z. Hybrid Perfect Metamaterial Absorber for Microwave Spin Rectification Applications. *Scientific Reports*. 2020;10: 19240.
18. Zhang Z, Zhao Y, Fan G, Zhang W, Liu Y, Liu J, Fan R. Paper-Based Flexible Metamaterial for Microwave Applications. *EPJ Applied Metamaterials*. 2021;8: 6.
19. Shen Y, Pang Y, Wang J, Ma H, Pei Z, Qu S. Origami-inspired metamaterial absorbers for improving the larger-incident angle absorption. *Journal of Physics D: Applied Physics*. 2015;48(44): 445008.
20. Zhang J, Liu S, Zhang L, Wang C. Origami-Based Metasurfaces: Design and Radar Cross Section Reduction. *AIAA Journal*. 2020;58(12): 5478–5482.

21. Chen X, Li W, Wu Z, Zhang Z, Zou Y. Origami-based microwave absorber with a reconfigurable bandwidth. *Optics Letters*. 2021;46(6); 1349–1352.
22. Fan X, Pan Z, Chen S, Li Y, Zhao Z, Xin Y, Pan T. Design and fabrication of a reconfigurable and flexible frequency selective surface with a buckling dipole via mechanical stretching. *Soft Science*. 2021;1(13).
23. Biswas A, Zekios CL, Ynchausti C, Howell LL, Magleby SP, Georgakopoulos SV. An ultra-wideband origami microwave absorber. *Scientific Reports*. 2022;12(1): 13449.
24. Zhu Z, Wang H, Li Y, Meng Y, Wang W, Zheng L, Wang J, Zhang J, Qu S. Origami-Based Metamaterials for Dynamic Control of Wide-Angle Absorption in a Reconfigurable Manner. *IEEE Transactions on Antennas and Propagation*. 2022;70(6): 4558–4568.
25. Yao J, Gui D, Zhang D, Zhang H. Ultra-Broadband Origami Absorber with Large Angle Stability in the THz Region. *Journal of the Optical Society of America B.* 2022; 39(10); 2603–2609.
26. Sun Y, Gao C, Chen L, Han L. A Design Method for Rectangular Waveguide-Typed Microwave Devices Based on a Novel Origami Process. *Materials*. 2023;16(24): 7625.
27. Zhang Z, Lei H, Duan S, Zhao Z, Chen M, Wang C, Fang D. Bioinspired Double-Broadband Switchable Microwave Absorbing Grid Structures with Inflatable Kresling Origami Actuators. *Advanced Science*. 2024;11(4): 2306119.
28. Song Z, Zhu JF, Wang X, Zhang R, Min P, Cao W, He Y, Han J, Wang T, Zhu J, Wu L, Qiu CW. Origami metamaterials for ultra-wideband and large-depth reflection modulation. *Nature Communications.* 2024;15: 3181.
29. Zhu Z, Li Y, Qin Z, Jiang L, Wang W, Chen H, Wang J, Zheng L, Qu S. Miura-Ori Based Reconfigurable Multilayer Absorber for High-Efficiency Wide-Angle Absorption. *Optics Express*. 2024;32(14): 24091–24106.
30. Zelenin VA, Narushko EO, Gladinov AD. Formation of Films of Alloys of Cr–Ni, Cr–Ni–Si and Fe–Ni Systems by Sublimation and Evaporation Methods for Electronic Products. *Doklady BGUIR*. 2023;21(5): 5–12. (In Russian)
31. *Insulating foil IZOFOLIX*. URL: https://www.kotar.pl/ru/oferta/folie-izolacyjne/108-folia-izolacyjna-izofolix-rus (In Russian)

About Authors

Anton D. Gladinov
Junior Researcher (Belarusian State University of Informatics and Radioelectronics, Minsk, Belarus)

Olga V. Boiprav Sc
Candidate of Technical Sciences
Associate Professor (Belarusian State University of Informatics and Radioelectronics, Minsk, Belarus)

Vadim A. Bogush Sc
Doctor of Physical and Mathematical Sciences
Rector (Belarusian State University of Informatics and Radioelectronics, Minsk, Belarus)

MATERIALS PHYSICS AND MECHANICS RESEARCH ARTICLE

Submitted: February 15, 2024 **Revised: September 23, 2024** **Accepted: October 10, 2024**

Numerical and experimental study of the effect of adhesive quality on the repair efficiency of corroded and cracked aluminum plate under mechanical loading

M. Berrahou [1] ✉, M. Zahraoui [1,2], S. Djabbar [1], H. Kamel [1], H. Benzinab [1]

[1] University of Relizane, Relizane, Algeria

[2] Université Oran, Oran, Algeria

✉ berrahou22@yahoo.com

ABSTRACT

A corroded aluminum plate with an inclined crack at the corrosion end was repaired by boron/epoxy composite patches, bonded with various adhesive types under mechanical loads. The aim of this study was to discover which glue types are better for the composite patch adhesive and the most efficient in transferring stresses from the aluminum plate to the patch, so in this study three-dimensional finite element analysis was used to study the changes in the damaged area of the adhesive (DR) and the stress factor (SIF) in the two modes (mode I K_{I} and mode II K_{II}), then compare them. To confirm the analytical results, we conducted a laboratory experiment using corroded aluminum plate 2024 with random cracks that were repaired with a composite patch affixed with several adhesive types, and then we calculated the ultimate tensile strength. The obtained results, both on the analytical and experimental side, showed that the adhesive type FM73 is more efficient in fixing the composite patch and more effective in transferring stress from the damaged plate towards the patch compared to the other materials used in this study (araldite, adekit and redux).

KEYWORDS

composite • corrosion • mixed mode • stress intensity factor • SIF • damaged area ratio • DR • ultimate tensile strength

Acknowledgements. *The authors extend their sincere thanks to the staff of the Materials Laboratory of Sidi Bel Abbes University for their assistance in carrying out the laboratory experiments for the preparation of this manuscript.*

Citation: Berrahou M, Zahraoui M, Djabbar S, Kamel H, Benzinab H. Numerical and experimental study of the effect of adhesive quality on the repair efficiency of corroded and cracked aluminum plate under mechanical loading. *Materials Physics and Mechanics*. 2024;52(5): 83–100.
http://dx.doi.org/10.18149/MPM.5252024_9

Introduction

The appearance of cracks in a metal structure in any field such as aviation structures and marine structures is a major concern for maintenance operators and a real threat of structural damage [1].

Composite patches have become widely used to repair metal structures that have been damaged due to fatigue or external stresses whether mechanical or thermal. These patches make it possible to delay the spread of cracks and thereby increase the life of structures repaired in this way. The mechanical properties of these repaired structures have been studied in several articles. The influence of several parameters on crack propagation behavior has been carefully studied by several researchers. For example, the effect of composite patch size [2,3], number of layers [4], asymmetry of the repaired structure [5], component tension before bonding of the composite patch [6], incomplete bonding of the composite patch [7] or residual stresses [8], have been examined in recent literature.

The adhesive plays an important role in the process of repairing damaged structures, it is the mediator between the patch and the plate, and it is responsible for transferring stress from the plate to the patch. The damaged area criterion was proposed by [9,10] for the analysis of damage in the adhesive. This standard assumes that the material will fail once the measured stress exceeds the ultimate strength of the material. Sheppard and colleagues [10] introduced the idea of a damaged area of an aluminum plate repaired with a single and double composite. This area is determined by a surface, where the von-Mises deformations exceed the maximum permissible deformation, and the fracture load of glue joints was determined experimentally. Damage to the adhesive layer occurs when the strains or stresses in the adhesive are greater than the material properties. Failure in the adhesive is not caused by crack propagation in the substrate, but rather by initiation and propagation of the damaged area in the layer containing defects such as microcracks or voids [11]. The percentage of damaged area has been suggested to predict the load of glue joint failure. For FM73 epoxy adhesive, it has been shown that this adhesive fails when the damaged area ratio reaches the D_{RC} = 0.247. In the damaged area theory, it is assumed that the glue joint is non-adherent when the damaged area reaches a certain critical value. The affected area can be determined by either pressure or deformation criterion. The deformation criterion is more appropriate when the adhesive exhibits significant non-linearity. There are two ways for adhesive joints to fail: interface failure and cohesion. In the interfacial mode, the critical failure load of the glue joint is related to the interfacial pressure between the adhesive and the part to be glued [12].

There are several works carried out by M. Berrahou [13–19] to study the repair of plates, whether metal such as aluminum or composite plates using the composite patching technique, and these studies were numerical analytical research and laboratory experiments. In [20–22], it was also showed that the determination of the stress intensity factor on the crack tip is one of the possible ways to analyze the repair performance associated with these composite materials, using the three-dimensional finite element method.

In this work, we place ourselves in the context of a numerical analytical study using the 3D finite element method to assess the damaged area ratio of the adhesive and the intensity of the stress factor at the crack tip, in addition to laboratory experiments to find out the ultimate tensile strength value for each sample. These samples were corroded aluminum plates of type 2024 with random cracks, originally made by boron / epoxy resin bonded with different types of adhesives (FM73, araldite, adekit and redux). The aim of this study was to determine which of these adhesives are more efficient in stress transfer and reduce the risk of repair damage and thus enhance the corrosion resistance properties.

Geometrical model

The geometry of the structure considered in this study is shown in Fig. 1. For a rectangular elastic thin plate of 2024-T3 aluminum with random shaped corrosion, with the following dimensions: H_{pl} = 254 mm, W_{pl} = 254 mm and e_{pl} = 5mm, with an inclined crack of length a = 15 mm. The plate was repaired with a single boron/epoxy patch of different shapes

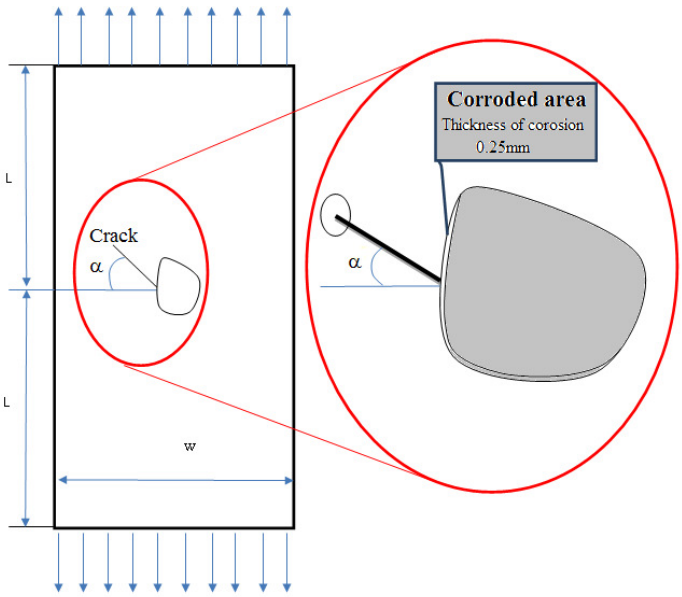

Fig. 1 Geometry of the damaged plate

and constant thickness e_{pat} = 1.5 mm, the layers in the patch have a unidirectional stacking where the fibers are oriented along the length direction of the specimen (parallel to the load direction). In order to analyze the effect of the type of adhesive, four types of adhesives were chosen in this study: (FM73, adekit A140, redux and araldite). We used four patch shapes in this study: rectangular, trapezoidal, circular and elliptical, having the same surface A = 9750 mm^2. The sizes of these patches are given in Fig. 2. The patch is bonded with 0.15 mm thick adhesive. The plate is subjected to a uniaxial tensile load of amplitude σ = 100 MPa and with an ambient temperature T = 20 °C.

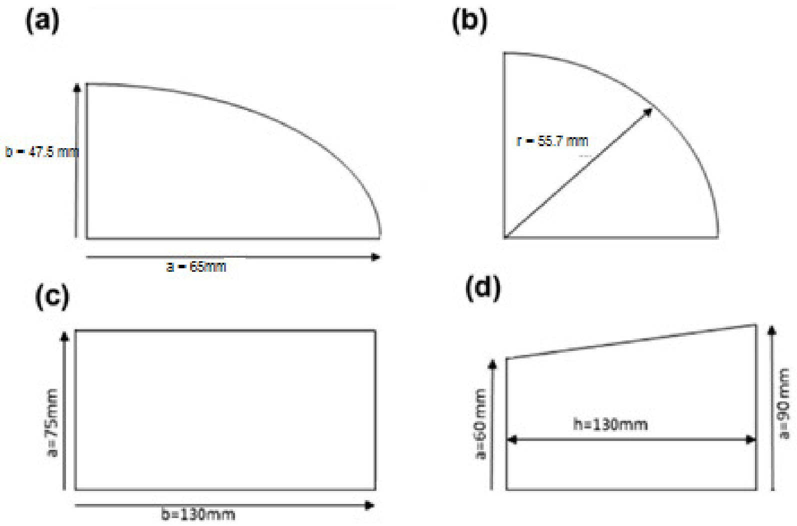

Fig. 2. Patch dimensions: (a) elliptical, (b) circular, (c) rectangular, (d) trapezoidal

The mechanical properties of (the plate, patch and of the adhesive) are shown in Table 1. The geometric shape of the corrosion used is randomly in 3D with a thickness 0.25 mm, before repairing the structure, the corroded area is cleaned to remove the Corrosion film and keep the same mechanical properties.

Table 1. Elastic property of different materials [23]

	Boron/ep	AL 2024	FM 73	Adekit	Redux	Araldite
E_1, GPa	200	72				
E_2, GPa	2.5					
E_3, GPa	2.5					
υ_{12}	0.21	0.33	0.32	0.3	0.36	0.36
υ_{13}	0.21					
υ_{23}	0.21					
G_{12}, GPa	7.2		4.2	2.69	3.808	2.448
G_{13}, GPa	5.5					
G_{23}, GPa	5.5					

Finite element modeling

The analysis involved a three-dimensional finite element method to supplement and analyze the experiments by using a commercially available finite element code ABAQUS [24]. The finite element model consisted of three subsections to model the cracked plate, the adhesive, and the composite. The *J* integral values were extracted using a domain integral method within ABAQUS. This method provides high accuracy with rather coarse models in three- dimensions. The *J* integral values were extracted using a domain integral method within ABAQUS. This method provides high accuracy with rather coarse models in three dimensions. To generate crack front some brick elements are replaced by "crack block". These crack-blocks are meshes of brick elements which are mapped into the original element space and merged with surrounding mesh. Boundary conditions and loads are transferred to the crack-block elements. The mesh was refined near the crack-tip area with an element dimension of 0.067 mm using at least 15 such fine elements in the front and back of the crack tip. The finite element mesh was generated using brick elements with 20 nodes. The number of elements used in this analysis is 50000 and number of degrees of freedom DOF is 322016. Figure 3 shows the overall mesh of the specimen and mesh refinement in the crack-tip region.

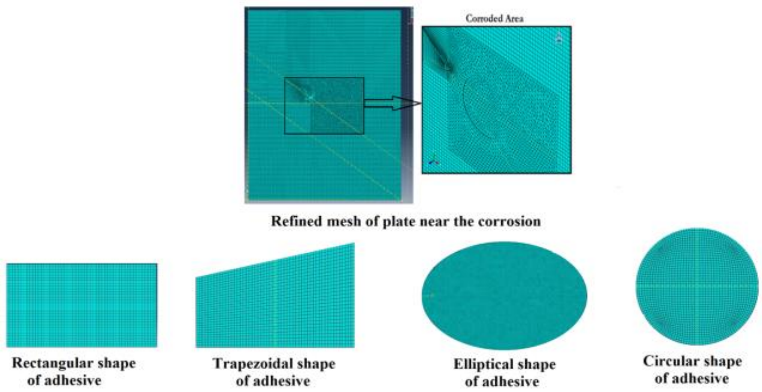

Fig. 3. Typical mesh model of the plate and the patch

Results and Discussions

The von-Mises Failure criterion was introduced by von-Mises (1913) and has been used since as one of the most reliable failure criteria for engineering materials. It relies on the second deviatoric invariant and the effective average stress. Assuming a triaxial test condition where $\sigma_1>\sigma_2=\sigma_3$.

$$\sqrt{J_2} = 1/3(\sigma_1 - \sigma_3). \quad (1)$$

The effective average stress can be expressed by the following equation:

$$\sigma_m - P_0 = 1/3(\sigma_1 + 2\sigma_3) - P_0, \quad (2)$$

where P_0 formation pore pressure and the effective average stress is defined as the average stress minus the pore pressure.

In the von-Mises shear criterion, the second deviatoric invariant is plotted against the effective average stress for various axial loads σ_1 and confining pressures σ_3. The resulting curve, known as the failure curve, specifies two regions, one below the curve as being safe and stable and the other above the curve as being unstable and failed as shown in Fig. 4.

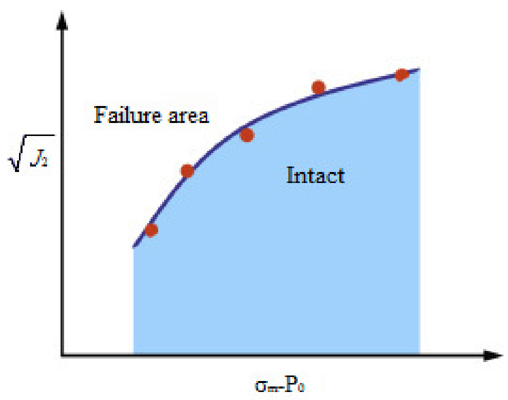

Fig. 4. Von-Mises failure model from triaxial test data

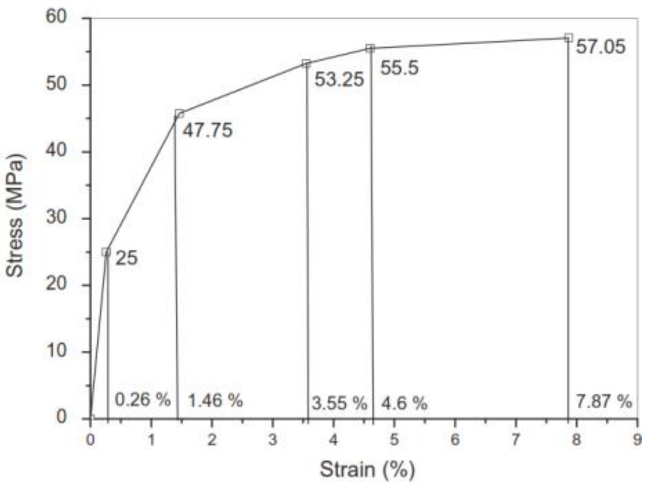

Fig. 5. Stress-strain curve of eoxy adhesive FM73

The theory's Main assumption of is that the adhesive and crack initiation in the bonded patch occurs after a damaged area develops. Under low amplitude of load, the localized damage arrives at the edges of patch. This damage occurs because the material is locally subjected to strains higher than the ultimate material strain. Under medium load amplitude, the damaged zones grow in size and the concentration of points of the damaged areas increases. As the failure load is reached, the damaged area in the adhesive grows to a critical size and the individual components of the damage coalesce and form a crack. Numerically, the damaged area is identified by marking items for which a failure criterion is exceeded. The adhesive tested is a toughened ductile adhesive which is expected to fail in performance. Consequently, the failure criterion used for the cohesive damage of the adhesive layer is the equivalent von-Mises strain criterion:

$$\varepsilon_{equiv} = \frac{1}{\sqrt{2(1+\vartheta)}} X \sqrt{(\varepsilon_{p1} - \varepsilon_{p2})^2 + (\varepsilon_{p2} - \varepsilon_{p3})^2 + (\varepsilon_{p3} - \varepsilon_{p2})^2}, \quad (3)$$

where ε_{equiv} is the equivalent patches, ε_{pi} are the plastic strains in the different directions and ϑ is the Poisson ratio.

This criterion is satisfied when the maximum principal strain in the material reaches the ultimate principal strain. For each failure criterion an ultimate strain will be defined and the corresponding damage zone size at failure is determined. The damaged area theory is based on the principle that the adhesive joint is assumed to fails when the damaged area reaches a certain critical value. The damaged zone can be determined by either stress or a strain criterion. Therefore, the adhesive fails to perform its functions when the cohesive failure criterion is satisfied with the adhesive joint. Since adhesive failure occurs at the adhesive joint, the adhesive failure criterion for the damaged area should be used. For isotropic materials, failure criteria such as the von-Mises and Tresca criteria can be used to better understand the adhesive failure. Chang-Su Ban [12] proved that the area where the equivalent strain of the adhesive exceeds the ultimate strain of 7.87 %. After conducting studies on the FM-73 adhesive they concluded that this adhesive fails when the D_R (damaged area ratio) reaches a percentage exceeding 0.24 which is considered critical [25] (Fig. 4). The value of the damaged area ratio is calculated according to the following relationship:

$$\boldsymbol{D_R} = \frac{\text{sum of damaged areas}}{\text{total adhesive area}} \qquad (4)$$

In our work, the evaluation of the breaking stress of the FM73 adhesive is calculated from the curve in Fig. 5.

This study was carried out to determine the evolution of the damaged area in the adhesive layer which ensures the adhesion of the composite patch to the cracked plate with randomly shaped corrosion. The area of the damaged zone was calculated for different parameters such as the following effects, patch shapes (rectangular, trapezoidal, and circular), patch types (boron/epoxy, graphite/epoxy and glass/epoxy) and crack inclination under thermo-mechanical loading. The damaged area theory was used to evaluate the progression of damage in the adhesive layer during the analysis. The color of the damaged area can be seen in gray.

The criterion of von-Mises is used as criterion of plasticity. The theory of additional plasticity is introduced to model the non-linearity of the adhesive material. The stress intensity factors at the crack tip are calculated using the virtual crack closure technique (VCCT) based on the energy balance. In this technique, the stress intensity factors are obtained for the three failure modes according to the equation:

$$G_\mathrm{i} = \frac{K_\mathrm{i}^2}{E}, \qquad (5)$$

where G_i is the Fracture energy for mode I, K_I is the stress intensity factor for mode i and E is the modulus of elasticity.

The model referred to above is called the linear elastic fracture mechanics model and has found wide acceptance as a method for determining the resistance of a material to below-yield strength fractures. The model is based on the use of linear elastic stress analysis; therefore, in using model one implicitly assumes that at the initiation of fracture any localized plastic deformation is small and considered within the surrounding elastic stress field.

$$\begin{cases} \sigma_x = \frac{K}{\sqrt{2\pi r}}\cos\frac{\theta}{2}\left[1-\sin\frac{\theta}{2}\sin\frac{3\theta}{2}\right] \\ \sigma_y = \frac{K}{\sqrt{2\pi r}}\cos\frac{\theta}{2}\left[1+\sin\frac{\theta}{2}\sin\frac{3\theta}{2}\right]. \\ \sigma_{xy} = \frac{K}{\sqrt{2\pi r}}\sin\frac{\theta}{2}\left[\cos\frac{\theta}{2}\cos\frac{3\theta}{2}\right] \end{cases} \quad (6)$$

The stress in the third direction are given by $\sigma_z = \sigma_{xz} = \sigma_{yz} = 0$ for the plane stress problem, and when the third directional strains are zero (plane strain problem), the out of plane stresses become $\sigma_{xz} = \sigma_{yz} = 0$ and$\sigma_z = \vartheta(\sigma_x + \sigma_y)$. While the geometry and loading of a component may change, as long as the crack opens in a direction normal to the crack path, the crack tip stresses are found to be as given by Eq. 6.

The stress intensity factor (*K*) is used in fracture mechanics to predict the stress state "stress intensity" near the tip of a crack or notch caused by a remote load or residual stresses. It is a theoretical construct usually applied to a homogeneous, linear elastic material and is useful for providing a failure criterion for brittle materials, and is a critical technique in the discipline of damage tolerance. The concept can also be applied to materials that exhibit small-scale yielding at a crack tip.

The magnitude of *K* depends on specimen geometry, the size and location of the crack or notch, and the magnitude and the distribution of loads on the material. It can be written as [26,27]:

$$K = \sigma\sqrt{\pi a} f\left(\frac{a}{W}\right), \quad (7)$$

where: $f(\frac{a}{W})$ is a specimen geometry dependent function of the crack length *a*, the specimen width *W*, and σ is the applied stress.

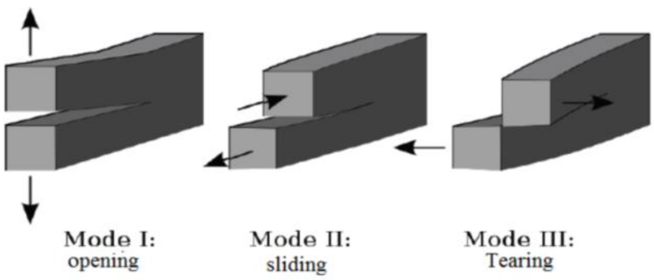

Fig. 6 Mode I, mode II, and mode III crack loading

In 1957, G. Irwin [28] found that the stresses around a crack could be expressed in terms of a scaling factor called the stress intensity factor. He found that a crack subjected to any arbitrary loading could be resolved into three types of linearly independent cracking modes. These load types are categorized as Mode I, II, or III as shown in Fig. 6. Mode I is an opening (tensile) mode where the crack surfaces move directly apart. Mode II is a sliding (in-plane shear) mode where the crack surfaces slide over one another in a direction perpendicular to the leading edge of the crack. Mode III is a tearing (antiplane shear) mode where the crack surfaces move relative to one another and parallel to the leading edge of the crack. Mode I is the most common load type encountered in engineering design.

Different subscripts are used to designate the stress intensity factor for the three different modes. The stress intensity factor for mode I is designated K_I and applied to the crack opening mode. The mode II stress intensity factor K_{II}, applies to the crack sliding mode and the mode III stress intensity factor K_{III} applies to the tearing mode. These factors are formally defined as [29]:

$$
\begin{aligned}
K_I &= \lim_{r\to 0}\sqrt{2\pi r}\,\sigma_{yy}(r,0),\\
K_{II} &= \lim_{r\to 0}\sqrt{2\pi r}\,\sigma_{yx}(r,0),\\
K_{III} &= \lim_{r\to 0}\sqrt{2\pi r}\,\sigma_{yz}(r,0).
\end{aligned}
\qquad (8)
$$

Effect of crack inclination on adhesive damage

This part was carried out in order to determine the development of the damaged area in the adhesive layer due to corrosion. The damaged area theory was used to achieve the objectives of the analysis. The surface of the damaged area was calculated from the adhesive used to repair the damaged plate with random corrosion with a inclined crack at an angle θ for the effects of different types of adhesives and with different patch shapes (rectangular, trapezoidal, circular and elliptical). Where, using the damage area theory, the surface of the damaged areas appears in gray. By calculating the surface of this gray area, the development of damage in the adhesive layer during mechanical loading can be assessed.

This effect is shown on the images in Fig. 7, 9 and 11. This shows the differences in the damaged area of the adhesive as a function of the crack inclination (θ) for a fixed length a = 15 mm repaired with a single boron/epoxy patch. We fixed the adhesive thickness e_{ad} = 0.15 mm and the thickness of the ep_{at} = 1.5 mm, for different patch shapes (rectangle, trapezoid, circle, ellipse) and for an equal applied load at 100 MPa. We changed the crack inclination at angles θ = 15, 45, 75°, after defining the different graphs of the proportion of the damaged area and the curves of variation of the intensity modulus, a comparison can be made between the different types of different adhesives and determine the effect of the crack inclination.

Rectangular Patch

Figure 7 shows the pictorial results that allowed us to follow the development of the damaged area according to the crack inclination. In general, we find that the higher the crack inclination, the smaller the damaged area surface for all adhesive types. In the cases of θ = 15° and θ = 75° one notices a damaged area only at the patch periphery. As for the inclination θ = 15°, we notice the appearance of the damaged area around the corrosion and crack.

Figure 8 shows the variance of D_R as a function of the crack inclination θ for different adhesives (araldite, redux, adekit and FM73). All curves have the same behavior, because D_R decreases with the increase in the value of the inclination θ. By comparing the performance through the curves obtained, it can be seen that FM73 adhesive is the most efficient as it gives the lowest D_R values. The least effective for repair is redux adhesive.

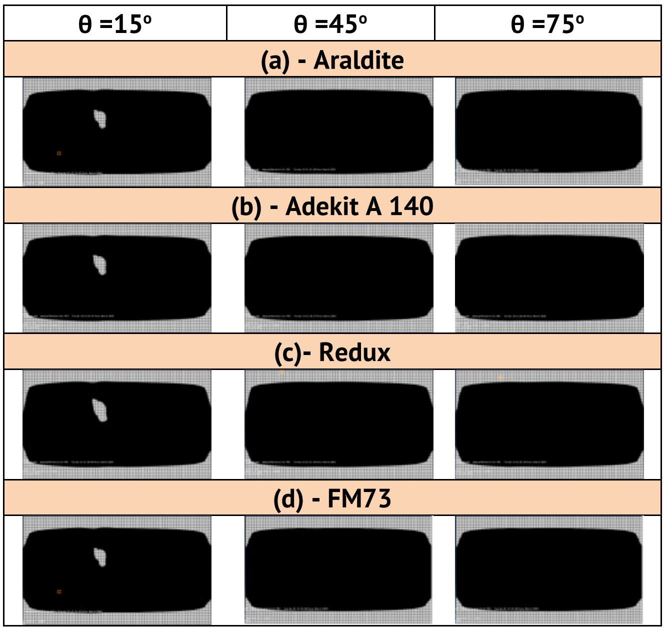

Fig. 7 Damaged area for a patch of rectangular shape and glue (a) araldite, (b) adekit A 140, (c) redux and (d) FM73

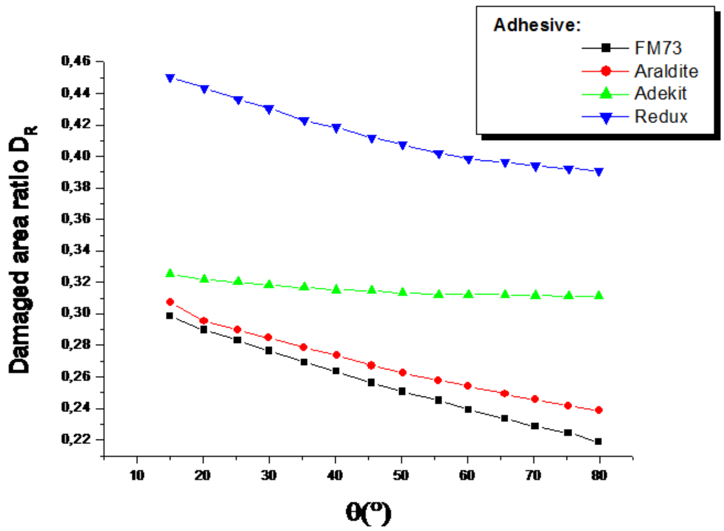

Fig. 8 Variation of D_R ratio for rectangular shape for different adhesives

Trapezoidal patch

Figure 9 represents the results that make it possible to observe the evolution of the surface of the damaged area of the adhesive according to the crack inclination. In general, we find a direct proportion between crack inclination and the damaged area of the adhesive, the greater the crack inclination, the greater this damaged area for all types of glue. In all cases, we also note the presence of a damaged area in the patch vicinity only, and the absence of any damage in the vicinity of the corrosion and crack.

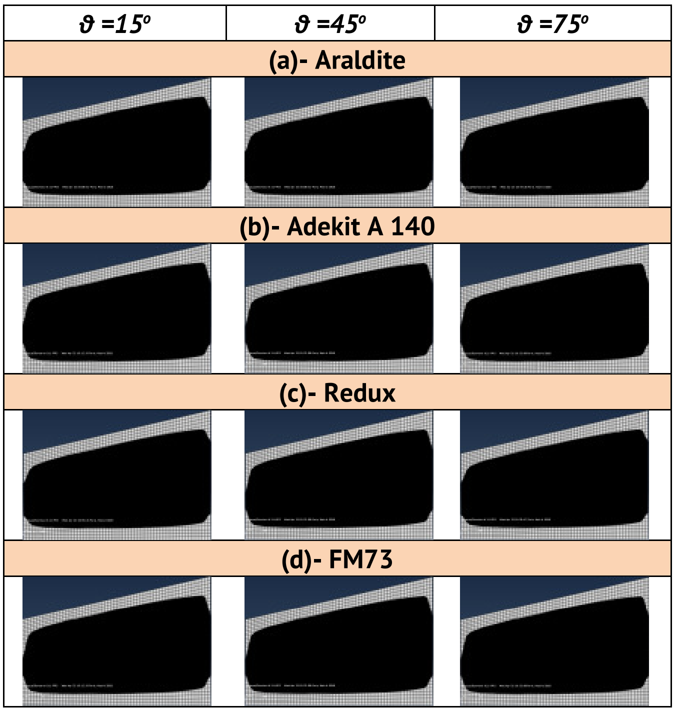

Fig. 9 Damaged area for a patch of trapezoidal shape and glue (a) Araldite, (b) Adekit A 140, (c) Redux and (d) FM73

Figure 10 shows the variance of D_R as a function of the crack inclination θ of the different adhesives (araldite, reduxe, adekite and FM73). The damaged area of the adhesive (araldite, reduxe and adekit) passes a minimum of θ=55° and then gradually stabilizes after this inclination. Redux glue is the worst among these adhesives because it gives the greatest values for the damaged area ratio. The variance in D_R increases for the FM73 adhesive but with a much lower inclination than for the other three adhesives and at a very small interval of values 0.26 until D_R = 0.24 for θ=80° is reached. It can be concluded that the FM73 adhesive is the most efficient because it gives the lowest D_R values.

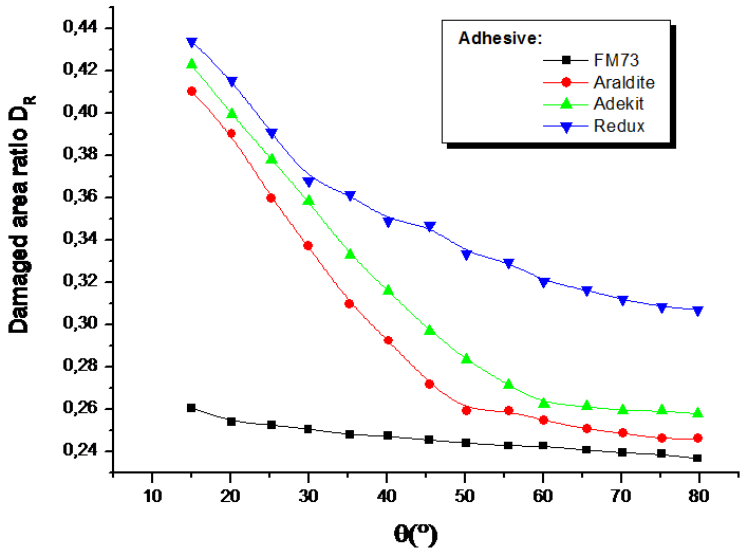

Fig. 10 Variation of D_R ratio for trapezoidal shape for different adhesives

Circular Patch

Figure 11 represents the results that make it possible to follow the development of the damaged area according to the crack inclination in the case of circular patching. In general, we find that the increase in the crack inclination leads to a decrease in the surface of the damaged area of the adhesive. In all cases, we note a damaged area in the patch vicinity. In addition, we observe the appearance of small damaged areas in the corrosion vicinity and crack in this case of araldite, adekit and FM73 for the inclination angle θ = 15°.

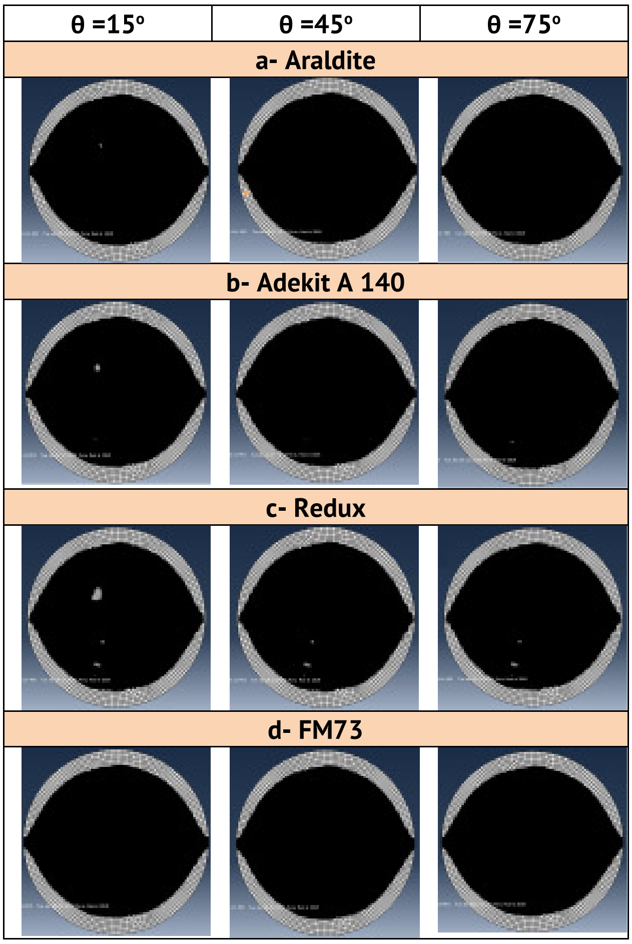

Fig. 11 Damaged area for a patch of circular shape and glue (a) araldite, (b) adekit A 140, (c) redux and (d) FM73

One notes in Fig. 12 the differences in D_R according to the crack inclination θ of different adhesives (araldite, redux, adekit and FM73). The damaged areas of the adhesives (redux and adekit) are noticeably the same for all angles inclinations. The variance of the D_R for the FM73 adhesive decreases but with values much lower than those of the other three adhesives and in an interval of values ranging from 0.21 until reaching D_R = 0.12 which is always less than D_{RC} = 0.247. We can conclude that FM73 adhesive is the most effective because it gives the lowest D_R values. Araldite is more efficient than adekit and redux.

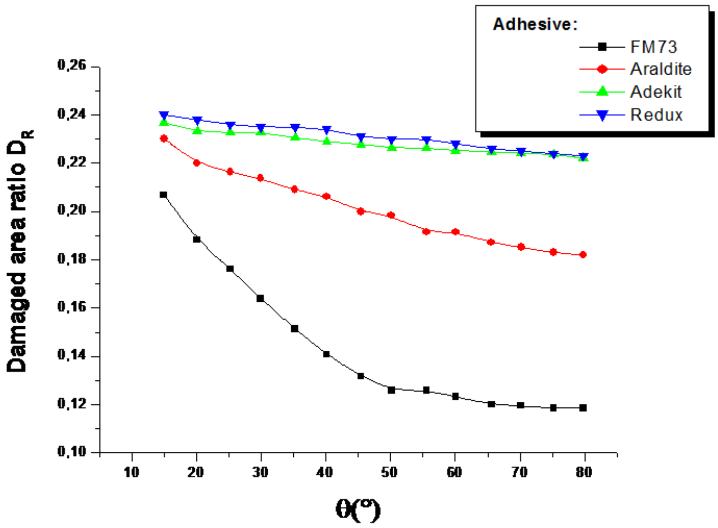

Fig. 12. Variation of D_R ratio for circular shape for different adhesives

Elliptical patch

Figure 13 represents the results that make it possible to follow the development of the damaged area according to the crack inclination in the case of an elliptical patch. In general, we find that as the crack inclination increases, the area of the damaged area of the adhesive decreases. In all cases, we note the presence of a damaged area in the patch vicinity, and the absence of any damage in the vicinity of the corrosion and crack.

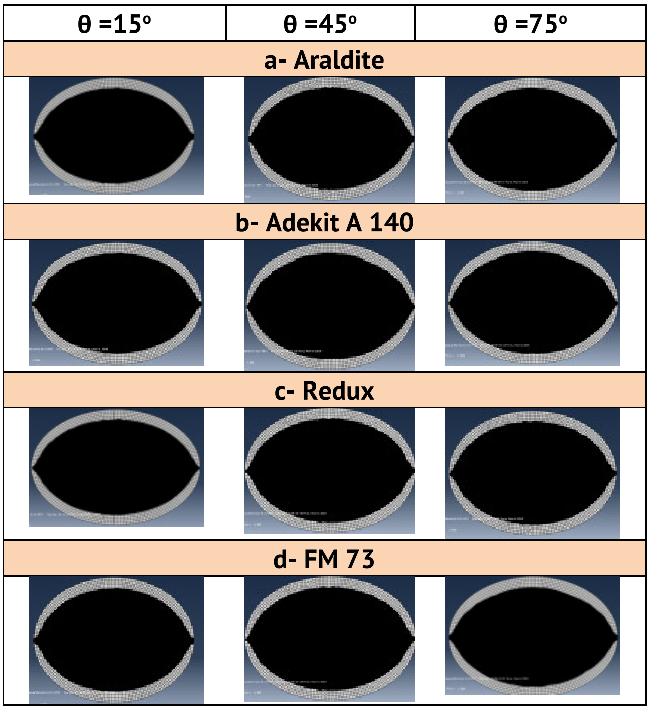

Fig. 13. Damaged area for a patch of elliptical shape and glue (a) araldite, (b) adekit A 140, (c) redux and (d) FM73

We observed in Fig. 14 the variation of D_R according to the crack inclination θ of the different adhesives (araldite, redux, adekit and FM73). The damaged area ratio of adhesives (FM73) is better than that of (adekit, redux and araldite) because their values are the smallest. On the other hand, we conclude for elliptical patch that FM73 glue is the most efficient than other adhesives.

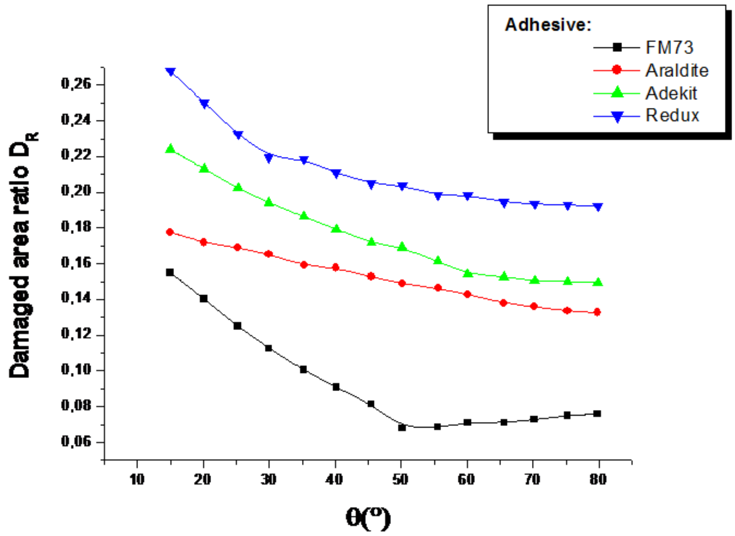

Fig. 14. Variation of D_R ratio for elliptical shape for different adhesives

Stress intensity factor Calculation according to the crack inclination θ

Figures 15-17 present, respectively, the variations of the SIFs in modes I, II and mixed mode (I+II) according to the crack inclination θ for the length crack of 15 mm. We have used in this part of the study the Elliptical-shaped patch, because from the results obtained in the part dedicated to the damaged area of the adhesive or in previous studies we carried out [13,15,17,19], we have confirmed that the elliptical shape gives the best results compared to other shapes (rectangular, trapezoidal and circular).

For mode I

The curves in Fig. 15 present the variations of SIFs according to the crack inclination θ, for a crack with a size a = 15 mm in mode I. SIF "K_I" is calculated for four different types of adhesives (araldite, redux, adekit and FM73) used in the installation of the boron/composite patch epoxy and with four shapes (rectangular, trapezoidal, circular and elliptical) according to the crack inclination θ of the crack, Under pressure σ = 100 MPa and temperature Δt = 20 °C. The curves presented in Fig. 15 have almost the same behavior, where the decrease in SIF values is related to the increase in the crack inclination for all types of composites used in this study.

As it is clear to us according to all shapes and types of adhesives used that the stress intensity factor is at its maximum when the cracks are perpendicular to the stress, which leads to the largest crack opening at the angle θ = 0°, this behavior is due to the fact that for θ = 0°, The pure mode I exists and therefore the stress absorption by the patch is maximum which increases the patch performance.

The difference in SIF between FM73 and araldite is about 36 % for θ = 0° and 17 % for adekit and 15 % for redux, this difference tends towards 0 for θ = 90°.

After comparing the results of all curves, it becomes clear to us that the FM73 type adhesive is the most efficient compared to the other adhesives, because it gives the lowest values for the stress intensity factor in all patch shapes.

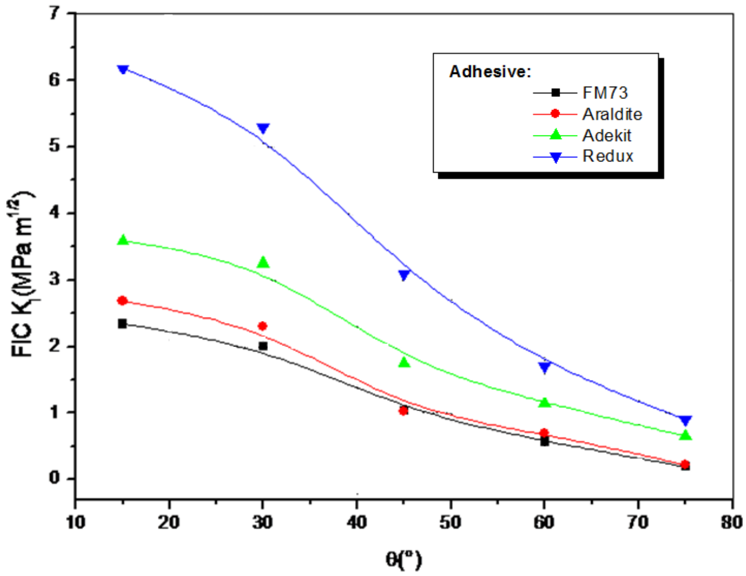

Fig. 15 SIF vs the crack inclination θ of mode I for elliptical shape patch

For mode II

Figure 16 shows that the SIF (K_{II}) differences in Mode II are affected by the crack inclination θ and with a size a = 15 mm. It can be seen that the K_{II} values increase starting from 0 reaching the maximum at the inclination value about θ ≈ 45°. Then, these curves start decreasing differently once the angular value exceeds 45° (θ >45°), it all depends on the properties of adhesive and shapes of the patches.

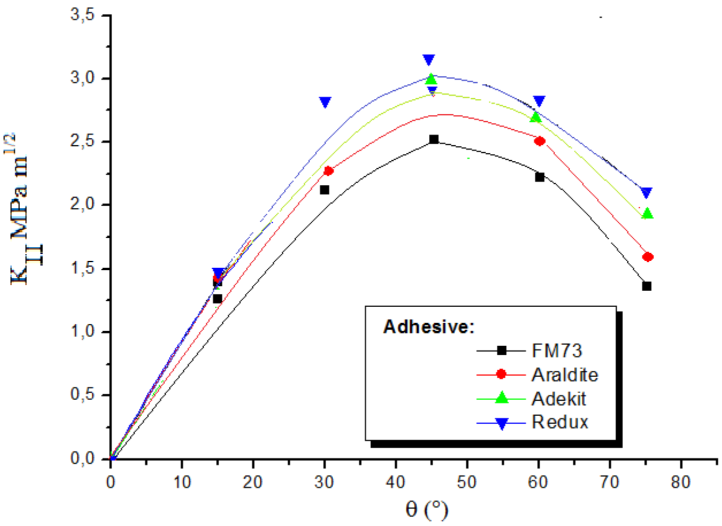

Fig. 16 SIF vs the crack inclination θ of mode II for elliptical shape patch

The curves are almost the same for all adhesives types, after studying the curves we note that the K_{II} values are close, except that the FM73 adhesive gives the lowest values of SIF (K_{II}), and this clearly indicates that this adhesive relieves stresses at the crack level better, thus presenting the energy gain which equals 16 % for adekit and 15 % for redux, this difference tends towards 0 for θ = 90° and θ = 0°.

Variation of stress intensity factor SIF (K_I+K_{II}) according to the crack inclination *θ* for different adhesive types

The stress intensity factor study of the sum of SIFs (K_I + K_{II}) was presented as a function of the crack inclination θ in Fig. 3, it is evident that (K_I + K_{II}) values decrease with increasing crack inclination, regardless of the composite shape or the type of adhesive. We note that the (araldite, redux and adekit) curves have the same behavior, because the difference in the values of the SIFs (K_I + K_{II}) is very small compared to FM73 adhesive. The energy gain of these results is returned: (θ = 0°) 29 % and (θ = 75°) 37 % on average compared to the other three types of adhesives.

The redux glue was the worst compared to all other types of adhesives used in this study, with the (K_I + K_{II}) values being very high. SIF varies between (10 to 7.5 MPa m). The curves of Fig. 17 show that FM73 glue gives the lowest values of $K_I + K_{II} = 3.5$ MPa·m$^{1/2}$, indicating its effectiveness. From it we conclude that FM73 glue is the most efficient in this study.

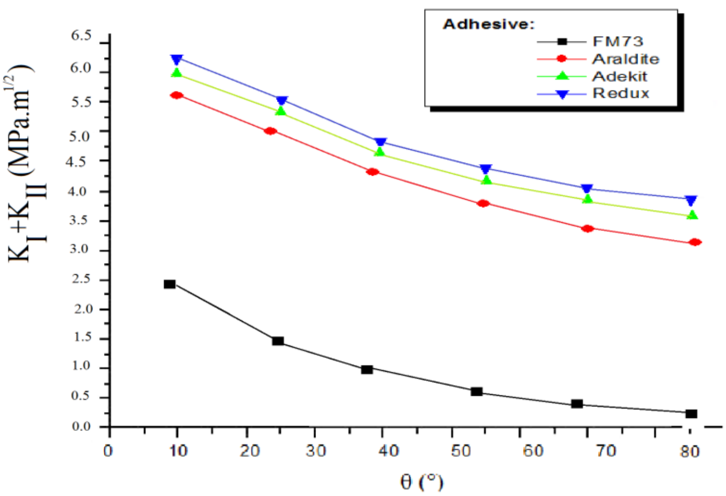

Fig. 17. K_I and K_{II} vs the crack inclination θ for different adhesive type

Ultimate strength and stiffness depending on the patch type

In this experimental study we used AL 2024 aluminum alloy. To obtain the appropriate samples for the experiment, we accelerate the corrosion using water + salt basins, and then immerse these plates in this solution, and then we cut the AL2024 alloy into several samples. These samples have a rectangular shape with dimensions (200 × 150 × 3) mm^3.

Aluminum is naturally covered with a layer of oxide, which often protects it from corrosion. In neutral aqueous solutions (4 < pH < 9), this oxide film is 50 Å thick and protects the metal (passivation), but chloride (Cl) ions have a very destabilizing effect on this oxide layer, then a rupture of the oxide layer occurs, which leads to corrosion.

Figures 18 and 19 show the completed stages in which we obtained corroded aluminum plates. To confirm the results obtained in the analytical study, we conducted an experimental study on AL 2024 aluminum alloy. To obtain the appropriate corroded samples for the experiment, we accelerate the corrosion using water + salt basins, and then immerse these plates in this solution, and then we cut the AL2024 alloy into several samples. These samples have a rectangular shape with dimensions (200 × 150 × 3) mm^3 (Fig. 20).

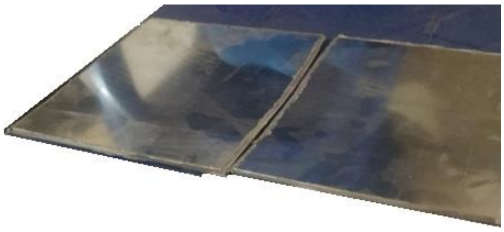

Fig. 18 Before the process

Fig. 19 Three weeks after the operation

Fig. 20 Geometry of the repaired specimens

Aluminum is naturally covered with a layer of oxide, which often protects it from corrosion. In neutral aqueous solutions ($4 < pH < 9$), this oxide film is 50 Å thick and protects the metal (passivation), but chloride (Cl) ions have a very destabilizing effect on this oxide layer, leading to corrosion.

According to the ASTM D3039-76 [30], ultimate strength is obtained. The ASTM D3039 tensile test is used to measure the force required to break a composite sample and how far the sample stretches or elongates to that breaking point. Tensile testing produces a stress–strain diagram which is used to determine the tensile modulus.

The objective of this pilot study was to analyze the absolute strength as a function of the types of adhesives (FM73, redux, araldite and adekit) for fixing the rectangular-shaped boron/epoxy patch used to repair the corroded aluminum plate.

This study proved that the use of composite materials increases the value of the absolute strength of the aluminum plate so that the untreated corroded plate fails with a value of only 100 MPa, while using composite materials, this value increased to reach the value of 150 MPa when using the graphite / epoxy adhesive, 188 MPa for redux, 190 for araldite and 220 MPa for boron/epoxy adhesive.

After observing the obtained values, it can be concluded that FM73 adhesive has effective effect and high stress transfer efficiency compared to other materials (redux, araldite and adekit) with an increase of 16 % compared to araldite, 30 % redux and 45 % graphite which allows us to say that The FM73 adhesive is the best type of adhesive compared to other materials used in this work (Fig. 21).

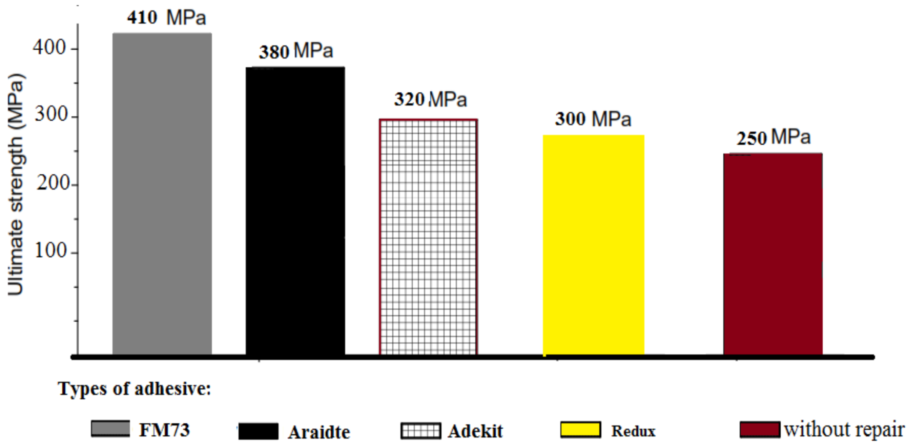

Fig. 21. Ultimate strength depending the type of adhesive for Al2024 aluminum plate on T = 20 °C

Conclusions

This study made it possible to understand the corrosion behavior of 2000 series aluminum alloy under mechanical influence. This work focused in particular on aluminum alloy 2024-T4 with inclined crack, consists of two parts: a numerical analytical part and an experimental part. The analytical part, using the finite element method focused on evaluating the damaged area of several adhesives (FM73, araldite, adekit and redux) used in patch fixation, determining the stress intensity factor and then comparing the results for the different adhesive types. In the experimental part, we compared the ultimate tensile strength of the damage of corroded aluminum sheets that were repaired by boron / epoxy patch with several adhesive types.

This study allowed us, both on the analytical and experimental side, to conclude that FM73 adhesive is more efficient and effective compared to other adhesives (araldite, adekit and redux), because in the analytical study it gives the lowest values of the damaged area ratio of adhesive, the stress intensity factor, yither in mode I or mode II. As for the experimental study, it gives greater resistance to tensile strength and longer life compared to other adhesives.

References

1. Baker AA, Chester RJ. Recent advances in bonded composite repair technology for metallic aircraft components. In: *Proceeding of the International Conference on Advanced Composite Materials*. 1993. p.45-49.
2. Toudeshky HH. Effects of composite patches on fatigue crack propagation of single-side repaired aluminum panels. *Composite Structures*. 2006;76(3): 243–251.
3. Chung KH, Yang WH. A study of the fatigue crack growth behaviour of thick aluminium panels repaired with a composite patch. *Composite Structures*. 2003;60(1): 1–7.

4. Toudeshky HH, Sadeghi G, Daghyani HR. Experimental fatigue crack growth and crack-front shape analysis of assymetric repaired aluminium panels with glass-époxy composite patches. *Composite Structures.* 2005;71(3): 401–406.
5. Seo DC, Lee JJ, Daghyani HR. Fatigue crack growth behaviour of cracked aluminium plate repaired with composite patch. *Composite Structures*. 2003;57(1); 323–330.
6. Bassetti A. *Lamelles précontraintes en fibres de carbone pour le renforcement de ponts rivetés endommagés par fatigue*. Lausanne, Switzerland: EPFL; 2001.
7. Naboulsi S, Mall S. Fatigue growth of adhesively repaired panel using perfectly and imperfectly composite patches. *Theoretical and Applied Fracture Mechanics*. 1997;28(1): 13–28.
8. Sabelkin V, Mall S, Hansen MA, Vanderwaker RM, Derriso M. Investigation into cracked aluminium plate repaired with bonded composite patch. *Composite Structures*. 2007;79(1): 55–66.
9. Crocombe A, Richardson G. A unified approach for predicting the strength of cracked and non-cracked adhesive joints. *Int J Adhes.* 1995;49(3-4): 211–244.
10. Sheppard A, Kelly D, Tong L. A damage zone model for the failure analysis of adhesively bonded joints. *International Journal of Adhesion and Adhesives*. 1998;18(6): 385–400.
11. Kemal Apalak M, Gulapalak Z, Gunes R. Thermal and geometrically nonlinear stress analyses of an adhesively bonded composite, tee joint with double support. *J Thermoplast Compos Mater*. 2004;17(1): 103–36.
12. Ban CS, Lee YH, Choi JH, Kweon JH. Strength prediction of adhesive joints using the modified damage zone theory. *Composite Structure*. 2008;86(1-3): 96–100.
13. Berrahou M, Bachir Bouiadjra B. Analysis of the adhesive damage for different patch shapes in bonded composite repair of corroded aluminum plate. *Structural Engineering and Mechanics*. 2016;59(1): 123-132.
14. Berrahou M, Salem M, Mechab B, Bouiadjra BB. Effect of the corrosion of plate with double cracks in bonded composite repair. *Techno. Press.* 2017;64(3): 323-328.
15. Salem M, Berrahou M, Mechab B, Bouiadjra BB. Effect of the angles of the cracks of corroded plate in bonded composite repair. *Frattura ed Integrità Strutturale*. 2018;46(46): 113-123.
16. Berrahou M, Salem M, Belaïd M. Analysis of the plate failure repaired by composite patch and reinforced by stiffeners. In: *1st Conference on Renewable Energies & Advanced Materials ERMA'19 – Relizane, Algeria*. 2019; 276-280.
17. Salem M, Berrahou M, Mechab B, Bachir Bouiadjra B. Analysis of the adhesive damage for different patch shapes in bonded composite repair of corroded aluminum plate under thermo-mechanical loading. *Journal of Failure Analysis and Prevention*. 2021;21: 1274–1282.
18. Amari K, Berrahou M. Experimental and Numerical Study of the Effect of Patch Shape for Notched Cracked Composite Structure Repaired by Composite Patching. *Journal of Failure Analysis and Prevention.* 2022;22: 1040–1049.
19. Benzineb H, Berrahou M, Serier, M. Analysis of the adhesive damage for different shapes and types patch's in corroded plates with an inclined crack. *Frattura ed Integrità Strutturale*. 2022;16(60): 331-345.
20. M'hamdia R, Bachir Bouiadjra B, Serier B, Ouddad W, Feaugas X, Touzain S. Stress intensity factor for repaired crack with bonded composite patch under thermo-mechanical loading. *J Reinf Plast Compos*. 2011;30(5): 416–424.
21. Cetisli F, Kaman M. Numerical analysis of interface crack problem in composite plates jointed with composite patch. *Steel Compos Struct*. 2014;16(2): 203–220.
22. Bachir Bouiadjra B, Fari Bouanani M, Albedah A, Benyahia F, Es-Saheb M. Comparison between rectangular and trapezoidal bonded composite repairs in aircraft structures. *Mater Des*. 2011;32: 3161–3166.
23. Ruoyuliu T, Lingzhen L, Kazuo T. A parctial stress intensity factor formula for CFRP repaired steel plates with a central crack. *Journal of Constructional Steel Research.* 2019;152: 105755.
24. *ABAQUS standard/user's manual, version 6.5.* Pawtucket, RI, USA: Hibbit Karlsson & Sorensen, Inc.; 2007.
25. Soboyejo WO. *Mechanical Properties of Engineered Materials.* Marcel Dekker; 2003.
26. Janssen M, Zuidema J, Wanhill R. *Fracture Mechanics: Fundamentals and Applications.* London; CRC Press; 2014.
27. Suresh S. *Fatigue of Materials*. Cambridge University Press; 2004.
28. Rooke DP, Cartwright DJ. *Compendium of stress intensity factors*. HMSO Ministry of Defence. Procurement Executive; 1976.
29. Sih GC, Paris PC, Erdogan F. Crack-tip stress intensity factors for the plane extension and plate bending problem. *Journal of Applied Mechanics.* 1962;29: 306–312.
30. ASTM Standard. *Standard test method for tensile properties of fiberresin composites D 3039-76.* Philadelphia: American Society for Testing and Materials; 1990.

MATERIALS PHYSICS AND MECHANICS RESEARCH ARTICLE

Submitted: July 08, 2024 **Revised: September 13, 2024** **Accepted: October 9, 2024**

Resistance of alloys in seawater

A.K. Leonov ✉, M.A. Skotnikova

Peter the Great St. Petersburg Polytechnic University, St. Petersburg, Russia

✉ leonov_anton@bk.ru

ABSTRACT

Using the methods of optical metallography and scanning electron microscopy, a systematic study of the features of destruction of structurally and crystallographically textured titanium blanks after low-cycle tests in synthetic seawater containing 3.5 % NaCl was carried out. It is shown that corrosion-resistant structurally and crystallographically isolated regions with a basic orientation of the interface and a width of 20–30 μm, which periodically lay over the entire thickness of the workpiece in increments of 100–170 μm, are responsible for reducing fatigue life. The main types of corrosion of steels in sea water are considered. It is shown that for austenitic steels there is a duality regarding the presence of chlorine in seawater: it reduces the activity of microbiological corrosion but increases the risk of pitting and crevice corrosion.

KEYWORDS

corrosion • seawater • microbiological • pitting • crevice corrosion and corrosion cracking

Acknowledgements. *The research was carried out at the expense of a grant from the Russian Science Foundation, No. Russian Science Foundation (Grant No. 22-19-00178).*

Citation: Leonov AK, Skotnikova MA. Resistance of alloys in seawater. *Materials Physics and Mechanics*. 2024;52(5): 101–111.
http://dx.doi.org/10.18149/MPM.5252024_10

Introduction

Currently, the Government of the Russian Federation has focused on the development of the Northern Sea Route. The plan includes over 150 projects, including the construction of marine facilities and terminals for the production, storage and transportation of liquefied natural gas, gas condensate.

In accordance with the above, the issue of selecting essential materials resistant to corrosive wear for the manufacture of both primary and auxiliary equipment, applicable under conditions of simultaneous exposure to seawater, atmosphere, and low-cycle vibrations of the floating vessel's hull, is becoming crucial.

The main types of metal and alloy corrosion in seawater are microbiologically influenced corrosion (MIC), crevice corrosion, pitting corrosion, and stress corrosion cracking. Seawater contains a 3.5 % NaCl solution, where the chloride ion shifts the potential of metal atoms towards a lower electronegativity, thereby increasing the corrosion rate. Chlorine ions are easily adsorbed by oxide films on metal surfaces and displace oxygen (passivator) from them, dissolving the passivating films and forming soluble metal chlorides in the process [1].

Stainless high-chromium steels and titanium- and aluminum-based alloys have high resistance to general corrosion. However, in environments with increased chlorine ion content, such as seawater, they can be susceptible to microbiologically influenced corrosion, pitting corrosion, and stress corrosion cracking.

Corrosion in seawater

The primary component determining the corrosive aggressiveness of seawater is halide ions, whose concentration reaches 30 g/L. Testing in seawater exhibits more localized corrosion development and results in greater depth of damage with lower overall mass losses. Moreover, the aggressiveness of seawater is significantly influenced by the oxygen content, the concentration of which depends on the salinity of the water, flow rate, and depth of immersion, and may vary across a wide range.

Previous studies [2–6] have shown that the degradation of materials, such as austenitic stainless steel AISI 316, follows a cumulative effect primarily determined by environmental parameters. These parameters include temperature, chlorine ion (Cl-) concentration, pH level, and flow velocity [7–10].

In addition to environmental factors, the surface and subsurface structures of the material play a crucial role in the onset of mechanical and corrosive degradation. Below, the main types of corrosion characteristic of marine environments are discussed.

Microbial corrosion

Microbiologically influenced corrosion (MIC) is a type of corrosion caused by bacteria or microorganisms (Fig. 1) [11].

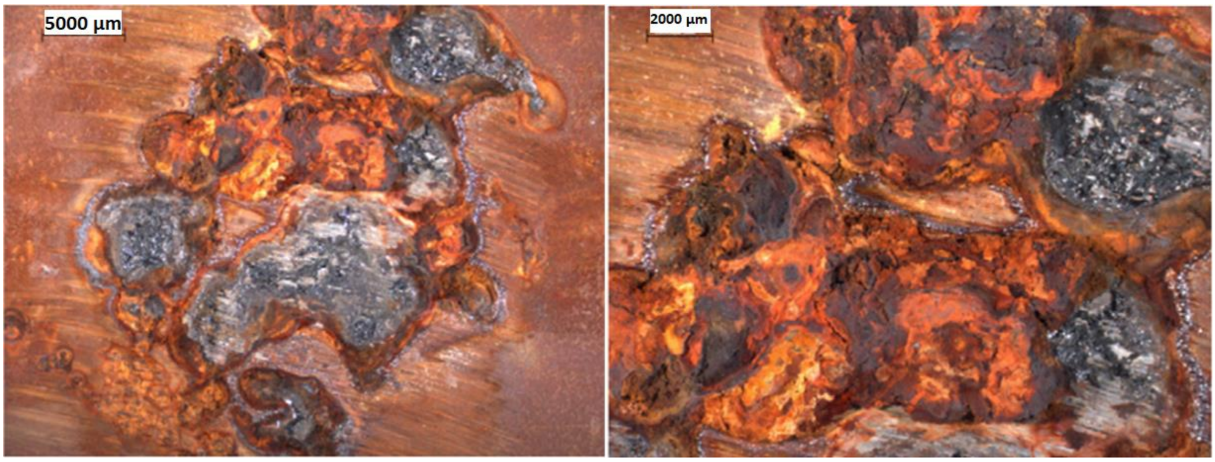

(a) (b)

Fig. 1. Corrosion products on the metal surface:
(a) general view (×5); (b) detailed view of corrosion wear (×10)

Biological fouling of submerged floating objects results from the development of natural marine biota. Each organism selects ideal conditions for its existence; therefore, the vertical distribution of fouling organisms on both mobile and stationary surfaces is determined by various factors such as light availability, water flow rate, depth, and others. The attachment points of biofoulers are primarily determined by the hydrophilicity and adsorption capacity of the material, and secondarily by the nature and speed of water flow along the surface, as well as micro-turbulence at points where this flow is disrupted [12]. The most studied type of microbiologically influenced corrosion is bacterial corrosion [13].

The term "microbiologically influenced corrosion" does not describe a single corrosion mechanism but rather serves as an umbrella term for various mechanisms through which microorganisms alter the kinetics of corrosion reactions by their presence or activity. The occurrence of MIC requires the specific interaction of three components: microorganisms, the environment, and the metal. The combination of these components determines different mechanisms that can directly or indirectly change the rate of metal degradation [14].

Pitting corrosion

Pitting corrosion (Fig. 2) is the most destructive form of corrosion, as cavities ("pits") form on local, difficult-to-detect areas of the surface. The causes of the initiation and propagation of pitting corrosion wear are heterogeneous inclusions, local defects in the protective corrosion-resistant film such as cracks, scratches, abrasions, etc.

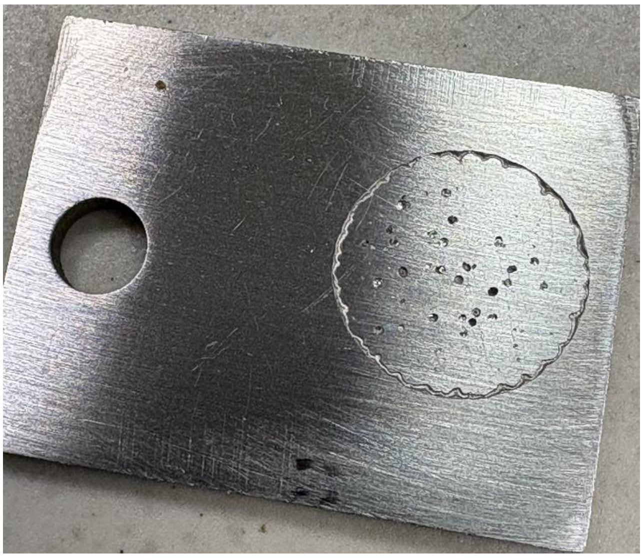

Fig. 2. Pitting and crevice corrosion on the metal surface

The mechanism of pitting corrosion is electrochemical in nature: during its formation, the "pit" becomes the anode, and the base metal becomes the cathode (Fig. 2).

The influences of various factors on corrosion in seawater are complex and, in some cases, contradictory due to their interactions and the dominance of one factor over others. The high salt content in seawater leads to high electrical conductivity, which causes an increase in the rate of corrosion. The impact of seawater salinity on corrosion is maximized when the concentration of NaCl exceeds 10 % [15]. The catalysts (accelerators) of pitting corrosion include: chlorides that contaminate the metal surface and hinder surface passivation; oxygen that accelerates the cathodic reaction; and residual chlorine, which is a strong oxidizer and, when entering the "pitting", locally lowers the pH of the environment within the cavity.

Crevice corrosion

Crevice corrosion is a type of localized corrosion that occurs within "crevices" formed by metal-metal and metal-nonmetal pairs. In terms of the destruction mechanism, crevice corrosion is identical to pitting destruction. The primary difference lies in the mechanism of the initiation of destruction.

The initiators of destruction are small cavities or "crevices" where localized corrosion occurs [16]. These crevices can be formed due to the geometric characteristics of the structure, such as in the areas of welded, riveted, and threaded joints; the contact of metal with non-metallic solid bodies, such as plastics, rubber, and glass; or the deposition of sand, dirt, or corrosion products on the metal surface.

Such crevices can allow fluid to penetrate, creating a stagnant zone and, at the same time, restricting the access of oxygen from the outside necessary to maintain the integrity of the metal's passive layer. This leads to the weakening of the metal's passive layer, accumulation of dissolved metal ions inside the crevice, and consequently, a decrease in the pH of the environment within the crevice. Subsequently, the destruction process proceeds according to the pitting corrosion scenario.

Especially sensitive to crevice corrosion are certain metals whose passive state on the surface is maintained through the access of oxidizing agents. These metals primarily include stainless steels, aluminum, and titanium alloys, which are crucial structural materials.

Selection of stainless steels and control of service conditions

The main method of preventing corrosion damage is the correct selection of steel grades based on the content of alloying elements. With an increase in the content of chromium, molybdenum, and nitrogen in the steel, its corrosion resistance increases. For instance, steel grades such as 10Cr17Ni3Mo2Ti and 12Cr18Ni12Mo3TiL exhibit high corrosion resistance in seawater.

Another common method of preventive protection against corrosion damage is the control of external and internal operating conditions. Control of external conditions, such as air humidity, and internal ones, such as restricting water exposure, ambient temperature, regulation of the pH level of the environment, concentration of chlorides, and residual chlorine. For example, temperature control allows avoiding critical temperatures for pitting formation; reducing chloride concentration decreases the intensity of the cathodic reaction on the steel surface; control of residual chlorine (chlorines) creates an unfavorable environment for the activity of microorganisms [17]. Inhibitors, when added in small quantities, slow down corrosion and differ in their mechanisms and nature of action [18]: passivating and adsorptive; by the chemical nature of types of media: acidic corrosive, hydrogen sulfide, petroleum, neutral, atmospheric; by the degree of metal surface blockage [19].

Stress corrosion cracking

Steels and alloys are also susceptible to brittle corrosion cracking (SCC) under stress [20,21]. Depending on the material and the aggressiveness of the environment, fractures can be either intergranular or transgranular in nature [22] and may be one of the main causes of product failures [23,24]. Stress corrosion cracking occurs under the influence of constant or cyclic mechanical loads in a corrosive environment (3.5 % NaCl). Stress corrosion cracking is one of the most unpredictable and dangerous types of destruction, occurring during the operation of high-strength steels and alloys in seawater.

In [25], it was shown that the entire stress corrosion cracking process can be divided in three stages: initiation of crack, propagation of crack and, as the result, fracture.

The process of stress corrosion cracking has the following characteristics: brittle crack propagation in the direction perpendicular to tensile stresses; formation of branching intergranular, transgranular, or mixed cracks; dependency of steel and alloy susceptibility to SCC on relative humidity [26] and the level of externally applied tensile stresses [27,28].

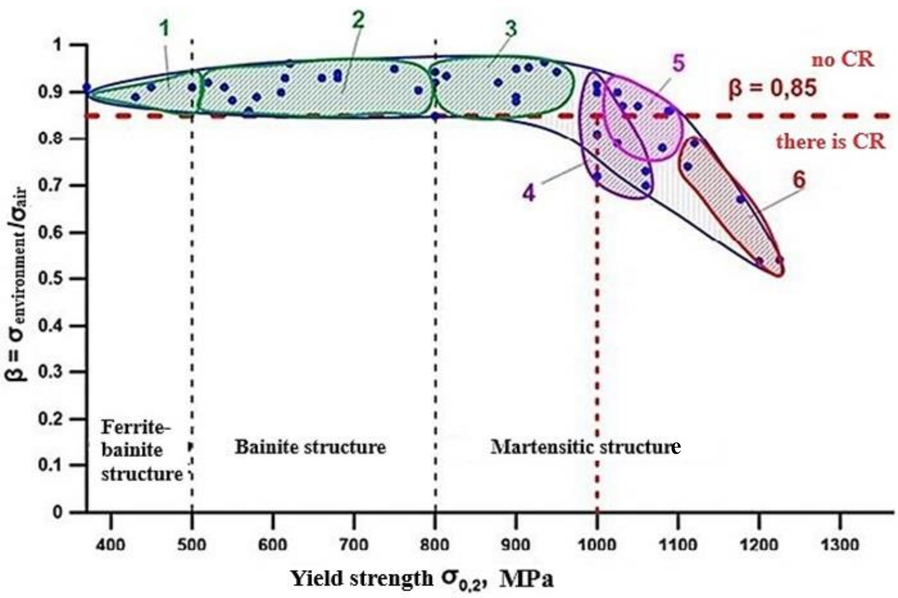

Fig. 3. The dependence of the coefficient of inclination to CR, β, obtained during the 3.5 % NaCl test by the stepwise cantilever bending method, on the yield strength: 1 – ferrite-bainite low–alloy steels; 2 – bainite-martensitic medium-alloy steels; 3 and 6 – martensitic alloy steels; 4 – low carbon martensitic steels; 5 – medium carbon martensitic steels

Figure 3 shows the testing results of high-strength steels with different structural and phase composition obtained on the basis of [29] using the cantilever bending method for SCC in seawater under stepwise increasing loads. It was found that steels with ferrite-bainite, bainite-martensite, and martensite structures and corresponding yield strength values in the range of 370 to 1000 MPa do not show susceptibility (β) to SCC under general corrosion conditions (regions 1–3, Fig. 3). The highest susceptibility to SCC was shown by martensitic low and medium carbon alloy steels with a yield strength of 1200 MPa (region 6, Fig. 3).

Corrosion damage prevention of stainless steels

The primary method for preventing corrosion damage is the rational selection of steel grades based on their chemical composition, where corrosion resistance increases with the content of the alloying element chromium. For instance, grades such as 10Cr17Ni3Mo2Ti and 12Cr18Ni12Mo3TiL, containing 17–18 % Cr, exhibit high corrosion resistance in seawater. The simplest and most common method for assessing the corrosion resistance of a steel in specific conditions is the pitting resistance equivalent number (PREn). The value of PREn depends on the percentage content of alloying elements in the steel and is calculated by:

$$PREn = \%\,Cr + 3.3 \cdot \%\,Mo + 16 \cdot \%\,N. \quad (1)$$

It is evident that the main alloying elements that increase corrosion resistance are chromium, molybdenum, and nitrogen. Table 1 presents some of the most widely used steel grades, in order of increasing corrosion resistance. Chemical compositions are taken from [30].

Table 1. Steel grades and PREn

Steel grade	PREn value	Steel type
304	19	Austenitic
316	24	
317	30	
904L	34	
2205	38	Duplex
255	44	Superduplex
2507	48	
6Mo / 254 SMO	46	Superaustenitic

Another common method for preventive protection against corrosion damage is the control of external and internal operating conditions, such as air humidity and exposure control. Internal condition control is conducted, for example, by limiting the influence of water or environmental temperature, regulating the pH level, or controlling chloride and residual chlorine concentrations. For instance, temperature control helps to avoid critical pitting temperature; reducing chloride concentration decreases the intensity of the cathodic reaction on the steel surface; controlling the residual chlorine (chloramines) creates an unfavorable environment for microbial activity. Inhibitors, or corrosion retarders, are substances used to slow down or prevent corrosion when added in small amounts to an aggressive environment.

Corrosion inhibitors vary in their mechanisms and nature: passivating and adsorptive; by chemical nature in different environments: acidic corrosive, hydrogen sulfide, oil, neutral, atmospheric; by the degree of surface blocking of the metal.

However, as evidenced by the aforementioned, these methods cannot be applied indiscriminately because reducing the risk of one type of corrosion might increase the risk of another. For example, in preventing microbiological corrosion by introducing so-called biocides, the activity of microorganisms is significantly reduced or entirely stopped, which in turn leads to a substantial decrease in the overall pH of the environment, hence increasing risks of pitting and crevice corrosion.

In [30], it was found that maximum operational temperatures as well as maximum residual chlorine values for certain cases. For instance, for pipelines, pumps, vessels, and other equipment operating in seawater conditions, the maximum residual chlorine value is 0.7 mg/L. This value is to be considered as a guideline rather than a strict standard requirement.

Materials and Methods

Tests were conducted on low-cycle specimens from the PT-5V titanium alloy with an annular notch, cut from the surface layer of billets so that their axis was parallel to the rolling direction (Fig. 4(a)). Testing was carried out with tension-compression fatigue testing machine in accordance with standard test methods defined in [31]. The colored electrochemical staining was conducted for surface preparation prior fractography inspection.

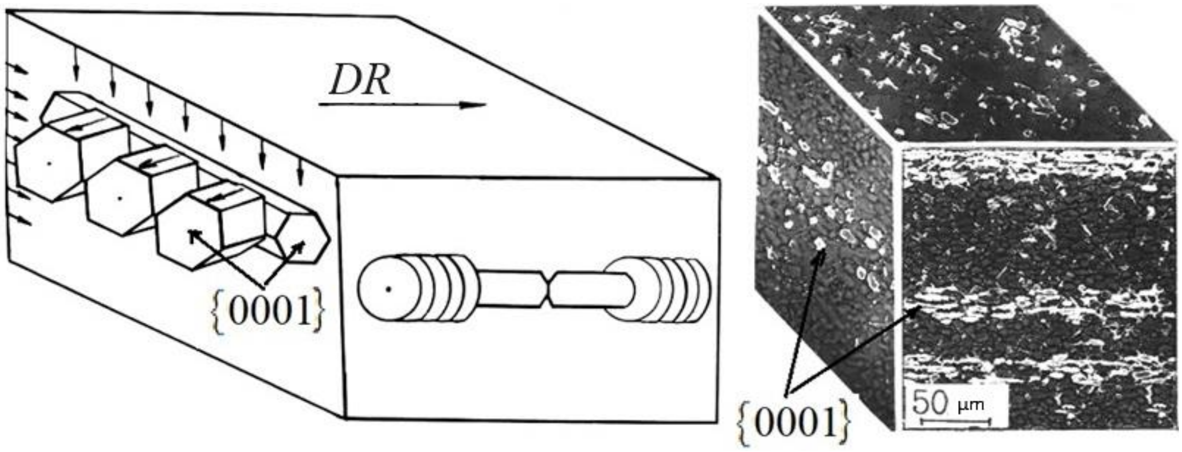

(a) (b)

Fig. 4. Sample cutting scheme for low-cycle fatigue tests (a) and structurally-crystallographically isolated areas with the basic orientation of the separation boundaries, revealed by colored electrochemical staining of the workpiece (b)

The structural texture of the studied materials was expressed in the preferential orientation of large-angle grain boundaries of flattened and elongated α-phase particles (Fig. 4(b)). Crystallographic texture was observed in the preferential orientation of the elementary hexagonal cells of the α-titanium crystal lattice (Fig. 4(a)). The texture of the material had a layered structure.

These layers with a basic {0001} orientation of structurally and crystallographically distinct regions with a width of 20–30 μm periodically with a step of 100–170 μm were distributed throughout the thickness of the billets. The presence of such regions in the material altered the failure mechanism and increased the scatter in values of low-cycle fatigue resistance in specimens from two-phase titanium alloys.

Results and Discussion

A total of 120 specimens were tested in a 3.5 % NaCl solution in a zero-tension mode with a pulsating loading cycle at a frequency of 2–3 cycles per minute with an applied stress amplitude of 0.8 and 0.7 of the average yield limits (Fig. 5).

The test results showed that at loads of 0.8 σ_y and 0.7 σ_y, the number of cycles to failure ranged from 200 to 1900 and from 700 to 3800 cycles, respectively. Thus, as the level of applied stress decreased, the scatter in the number of cycles to failure increased.

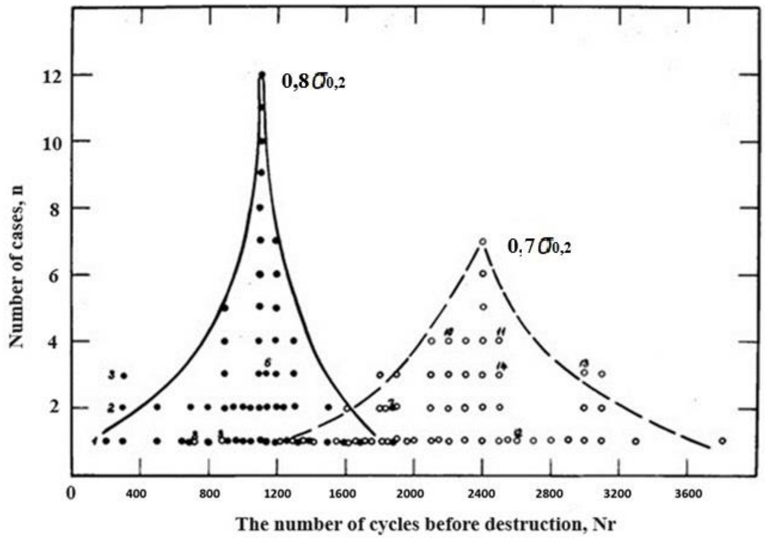

Fig. 5. Results of the low-cycle fatigue tests of the PT-5V alloy

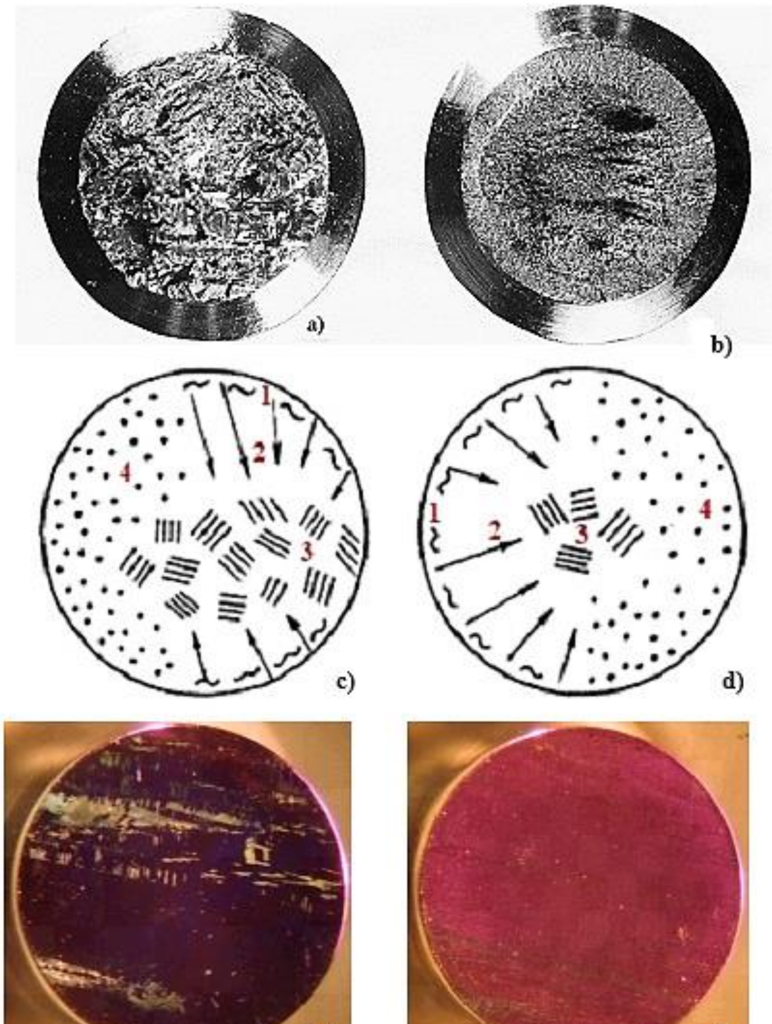

Fig. 6. Characteristic fractures (a,b), destruction schemes (c,d), and structurally-crystallographically isolated areas with the basic orientation of the separation boundaries, revealed by colored electrochemical staining of low-cycle samples (e,f), tested in a 3 % NaCl solution with low (N = 269) (a,c,e) and high (N = 1885) (b,d,f) numbers of cycles to failure

Fractographic analysis of the macro- and micro-topography of the fractures of the tested specimens (Fig. 6(a,b)) allowed the conclusion that as the main crack length increased and the live cross-section of the specimen decreased, four characteristic fracture zones formed on its surface (Fig. 6(c,d)). The initiation zone of the fatigue crack (zone 1) transitioned into an area of stable crack propagation with large fields of regular fatigue striations (zone 2). The accelerated crack growth area showed a mixed mechanism of fatigue rupture and single-event corrosion cracking (zone 3). Finally, the zone of final failure corresponded to rapid static fracture of the remaining cross-section (zone 4).

The micro-topography of zone 3, representing corrosion cracking, appeared as a mosaic of misoriented fracture facets "*G* (1010)" (Fig. 7(b)) and perpendicular macro-groove colonies "*K* (0001)" (Fig. 7(b)). In fractures of specimens tested in air, although macro-grooves were present, corrosion cracking facets were not observed (Fig. 7(b)).

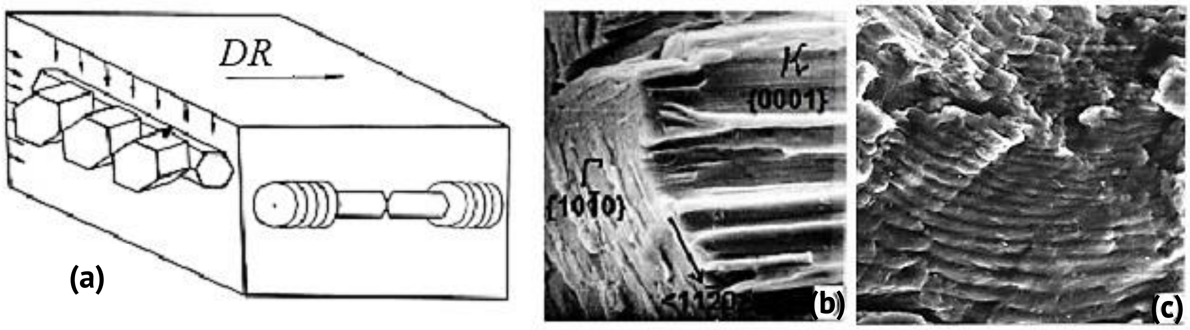

Fig. 7. Destruction scheme (a) and characteristic fracture appearance of low-cycle samples after testing in seawater (b) and in air (c)

In specimens with low cycle counts to failure, the corrosion embrittlement zone occupied most of the surface and reached the edge of the specimen. Color electrochemical staining of the metal directly below the fracture allowed the identification of structurally and crystallographically distinct regions with basic boundary orientations and widths of 20–30 μm, periodically layered with a step of 100–170 μm throughout the billet thickness (Fig. 6(d,e)).

In specimens with high cycle counts to failure, the corrosion cracking zone was either absent or located in the middle of the fracture. Electrochemical staining of these specimens revealed the absence of elongated α-phase particles with basic boundary orientations in the plane of main crack propagation.

Conclusions

In seawater, there is a risk of main types of corrosion: microbiological, crevice, pitting, and stress corrosion cracking. The dual nature of chlorine presence in seawater results in reducing microbial corrosion activity, but increases the risks of pitting, crevice corrosion, and stress corrosion cracking. It was shown that the reduction in low-cycle fatigue endurance is attributed to structurally and crystallographically distinct regions with basic boundary orientations and widths of 20–30 μm, periodically layered with a step of 100–170 μm across the billet thickness. The lower the level of applied stress during cyclic testing, the more significant the crack initiation stage is in the specimen's life time, emphasizing the importance of considering the quantity and geometry of such structurally and crystallographically distinct regions in flat billets, influencing the macro-mechanism of specimen failure.

References

1. Ajeel SA, Abdul-Hussein BA, Baker YM. Electrochemical measurements of anodizing stainless-steel type AISI 304. *International Journal of Mechanical Engineering and Technology*. 2013;4(3): 63–74.
2. Wyllie WE, Duquette DJ. Effect of dissolved ozone on corrosion behavior of stainless steels in artificial seawater. *Corrosion*. 1998;54(10): 781–799.
3. Malik AU, Ahmad S, Andijani I, Al-Fouzan S. Corrosion behavior of steels in Gulf seawater environment. *Desalination*. 1999;123(2-3): 205–213.
4. Sridhar N, Brossia CS, Dunn DS, Anderko A. Predicting localized corrosion in seawater. *Corrosion*. 2004;60(10): 915–936.
5. Malik AU, Siddiqi NA, Ahmad S, Andijani IN. The Effect of Dominant Alloy Additions on the Corrosion Behavior of Some Conventional and High-Alloy Stainless-Steels in Seawater. *Corros. Sci*. 1995;37(10): 1521–1535.
6. Scatigno GG, Ryan MP, Giuliani F, Wenman MR. The effect of prior cold work on the chloride stress corrosion cracking of 304L austenitic stainless steel under atmospheric conditions. *Mater. Sci. Eng. Struct. Mater. Prop. Microstruct. Process*. 2016;668: 20–29.
7. Nogara J, Sadig J, Zarrouk. Coorrosion in geothermal environment: Part 1: Fluids and their impact. *Renewable and Sustaionable Energy Reviews*. 2018;82(1): 1333–1346.
8. Kaidrikov RA, Vinigradova SS. Pitting corrosion of metals and multilayer systems (research, modeling, forecasting, monitoring). *Vestn. Kazan. Tekhnol. Univ*. 2010;4: 212–227.
9. Iversen A, Leffler B. Corrosion and Degradation of Engineering Materials. *Corrosion*. 2010;3: 1802–1878.
10. Varchenko EA, Kurs MG. Crevice corrosion of aluminum alloys and stainless steels in seawater. *Proceedings of VIAM*. 2018;7(67): 96–105.
11. Loto CA. Stress corrosion cracking: Characteristics, Mechanisms and Experimental study. *Mor. J. Chem*. 2017;5(4): 622–640
12. Varchenko EA, Kurs MG. Influence of the parameters of the corrosive environment on the properties of structural metal materials during testing in seawater (review). *Proceedings of VIAM*. 2019;9: 85. (In Russian)
13. Kablov EN, Startsev OV, Medvedev IM. Review of foreign experience in corrosion research and corrosion protection products. *Aviation Materials and Technologies*. 2015;2: 76–87.
14. Kaidrikov RA, Vinogradova SS. Pitting corrosion of metals and multilayer systems (research, modeling, forecasting, monitoring). *Technology of chemical production*. 2010;4: 212–227.
15. Ivanova OA, Rodkina AV. The influence of various factors on the corrosion of structural elements of floating structures in seawater. *Vestnik VGAVT*. 2018;56: 50–56. (In Russian)
16. Navid R, Seyed A. Crevice corrosion theory, mechanism and prevention methods. In: *3rd Annual GRASP Symposium. Wachita State University*. 2000. p.215–216.
17. McClements D, Paulsen G. *How to Prevent Pitting Corrosion*. Available from: https://dz6wltn9e7i51.cloudfront.net/resources/shop-tips/how-to-prevent-pitting-corrosion/ [Accessed 2nd December 2024].
18. Khudyakova LP, Flegentov IA, Kharisov RA, Zhvelev OY, Shestakov AA, Fakhretdinov IR. Investigation of the corrosion resistance of steels to the effects of seawater. In: *Problems of Collection, Preparation and Transport of Oil and Petroleum Products*. 2020. p.89.
19. Kozlova LS, Sibileva SV, Chesnokov DV, Kutyrev AE. Corrosion inhibitors (review). *Aviation Materials and Technologies*. 2015;35: 67–75. (In Russian)
20. Prosek T, Lieberzeit J, Jarvis A, Kiener L. Atmospheric stress corrosion cracking of stainless-steel rock-climbing anchors, part 2: laboratory experiments. *Corrosion*. 2019;75(11): 1371–1382.
21. Frankel GS. Pitting corrosion of metals. a review of the critical factors. *Electrochem. Soc*. 1998;145: 2186–2198.
22. Loto CA. Stress corrosion cracking: Characteristics, Mechanisms and Experimental study. *Int J Adv Manuf Technol*. 2017;93: 3567–3582.
23. Ghosh S, Kain V. Effect of surface machining and cold working on the ambient temperature chloride stress corrosion cracking susceptibility of AISI 304L stainless. *Mater. Sci. Eng. Struct. Mater. Prop. Microstruct. Process*. 2010;527(3): 679–683.

24. Zhang WQ, Fang KW, Hu YJ, Wang SU, Wang XL. Effect of machining-induced surface residual stress on initiation of stress corrosion cracking in 316 austenitic stainless steel. *Corros. Sci.* 2016;108: 173–184.
25. Kharkov AA, Alkhimentko AA, Spaposhnikov NO, Alekseeva EL. SSRT Method: Application to studying the mechanism of stress corrosion cracking in steels and alloys (overview). *Material Physics and Mechanics*. 2021;47(3): 483–492.
26. Katona RM, Taylor JM, McCready TA, Bryan CR, Schaller RF. Towards understanding stress corrosion cracking of austenitic stainless steels exposed to realistic sea salt brines. *Corrosion Science.* 2024;232: 111992.
27. Ren Z, Ernst F. Stress–Corrosion Cracking of AISI 316L Stainless Steel in Seawater Environments: Effect of Surface Machining. *Metals.* 2020;10(10): 1324.
28. International Standard. *BPVC.II.A - BPVC Section II-Materials-Part A-Ferrous Materials Specifications (2 Volumes)*. ASME; 2023.
29. Kostin SK. *Corrosion cracking in seawater of high-strength steels of various structural and phase composition. PhD Thesis.* St. Petersburg; 2018. (In Russian)
30. International Standard. ISO 21452. *Petroleum, petrochemical and natural gas industries — Materials selection and corrosion control for oil and gas production systems*. International Organization for Standardization; 2010.
31. International Standard. ASTM E606/E606M. *Standard Test Method for Strain-Controlled Fatigue Testing*. ASTM International; 2021.

About Authors

Anton K. Leonov
PhD Student (Peter the Great St. Petersburg Polytechnic University, Saint-Petersburg, Russia)

Margarita A. Skotnikova Sc
Doctor of Technical Sciences
Professor (Peter the Great St. Petersburg Polytechnic University, Saint-Petersburg, Russia)

MATERIALS PHYSICS AND MECHANICS RESEARCH ARTICLE

Submitted: March 29, 2024 **Revised: August 21, 2024** **Accepted: October 21, 2024**

The properties of rubber based on a combination of butadiene nitrile NBR 4045 and halobutyl CIIR and BIIR caoutchoucs

E.N. Egorov , N.I. Kol'tsov

I.N. Ulyanov Chuvash State University, Cheboksary, Russia

✉ enegorov@mail.ru

ABSTRACT

The influence of chlorinated butyl rubber (CIIR) and bromobutyl rubber (BIIR) in combination with nitrile butadiene rubber NBR 4045 on the rheometric characteristics of the rubber compound, physico-mechanical, performance and dynamic properties of rubber is examined. Along with rubber, the rubber compound contained a vulcanizing agent (sulfur), vulcanization accelerators (2,2′-dibenzthiazole disulfide, diphenylguanidine), vulcanization activators (zinc white, stearic acid), stabilizer (naphtham-2), softeners (rosin, SMPlast resin, bitumen petroleum, industrial oil I-12A), fillers (carbon blacks P 514 and P 803, natural chalk, trans-polynorbornene) and other ingredients. It has been established that the nature of halobutyl rubbers in combination with NBR 4045 rubber has virtually no effect on the maximum and minimum torques, and BIIR promotes a higher rate of vulcanization of the rubber mixture. Vulcanizates containing combinations of NBR 4045 rubber with halobutyl rubbers are characterized by almost identical physical and mechanical properties and, after exposure to sea water, their masses change slightly. Vulcanizate based on a combination of rubbers NBR 4045: BIIR = 75:25 parts per hundred parts of rubber (phr) has the least changes in physical and mechanical properties in sea water and advanced dynamic properties.

KEYWORDS

physico-mechanical performance and dynamic properties • butadiene-nitrile rubber • halobutyl rubber vulcanized rubber • rheometric •

Citation: Egorov EN, Kol'tsov NI. The properties of rubber based on a combination of butadiene nitrile NBR 4045 and halobutyl CIIR and BIIR caoutchoucs. *Materials Physics and Mechanics*. 2024;52(5): 112–118. http://dx.doi.org/10.18149/MPM.5252024_11

Introduction

It is known [1–6] that vulcanized rubber, due to its elastic elastic structure, has higher dynamic properties compared to other materials. To improve the dynamic (vibration damping) properties of rubbers, special ingredients are introduced into them (for example, diatomite [7], various grades of carbon black N 110, N 330, N 550, and N 990 [8], graphene nanoplatelets [9], zeolite [10], organic montmorillonite [11], silicon dioxide Silica Perkasil KS-408 [12], organically modified nanoclay Cloisite 30B as a nanoscale anisotropic additive in combination with carbon black [13]. In [14–16], *trans*-polynorbornene [14,15] and various dispersed fillers (diatomites NDP-D-400 and NDP-230, microquartz and magnesium hydrosilicate) [16] were used as such ingredients. In [14,15], it was shown the prospects of using *trans*-polynorbornene as a functional ingredient of targeted action for a rubber mixture based on general rubbers (butadiene-methylstyrene SKMS-30 ARK, butadiene SKD and isoprene SKI-3) and special (butadiene-nitrile NBR 6280) rubbers for the manufacture of gaskets for rail fastenings. Using the method of dynamic mechanical analysis, it was established that the introduction of trans-polynorbornene into the rubber mixture helps to improve the vibration-damping properties of vulcanizates. In [16], the influence of dispersed fillers on the dynamic characteristics of rubber based on general and special purpose rubbers for railway under-rail pads was studied. It has been shown that rubber containing diatomite NDP-D-400 has increased damping properties.

In [17–26], it was shown that the use of combinations of rubbers of different nature (nitrile butadiene [17], butadiene rubber and ethylene vinyl acetate [18], siloxane rubber [19], urethane rubber and epoxy resin [20], natural rubber and epoxidized natural rubber [21], natural and nitrile butadiene rubbers [22], nitrile butadiene rubber and polyvinyl chloride [23], natural and styrene butadiene rubbers [24], chlorobutyl rubber [25], ethylene propylene diene and epoxidized natural rubbers [26]) is one of the promising ways of creating rubbers with improved dynamic properties. In [27,28], it is shown that the use of a combination of rubbers of different polarities (polar butadiene-nitrile NBR 4065 and non-polar butadiene-methylstyrene SKMS-30ARK and butyl rubber BK-1675) with the addition of *trans*-polynorbornene, sevilene 11808-340 [27] and polyisobutylene P-200 or sevilene 11808-340 [28] leads to an increase in the dynamic parameters of rubbers for products operating under conditions of exposure to sea water. In this regard, the purpose of the work was to study the influence of a combination of halobutyl caoutchoucs (chlorinated butyl rubber (CIIR) and bromobutyl rubber (BIIR)) with butadiene-nitrile rubber NBR 4045 on the properties of rubber used to manufacture products used in sea water. To achieve this goal, the following tasks were solved: rheometric characteristics of a rubber compound containing different combinations of rubbers were studied, physico-mechanical, performance and dynamic properties of vulcanizates obtained on the basis of this rubber compound were determined and analyzed.

Materials and Method

The rubber compound based on CIIR and BIIR with a Mooney viscosity ML_{1+8} (125 °C) of 39 and 32, mass fraction of chlorine (bromine) of 1.20 and 1.74 %, respectively (Nizhnekamskneftekhim, Russia), in combination with nitrile butadiene rubber NBR 4045 with a mass fraction of acrylic acid nitrile 36-40 wt. %, Mooney viscosity ML_{1+4} (100 °C) 42–48 (Sibur, Russia) contained the following ingredients: vulcanizing agent (sulfur (Kaspiygaz, Russia)), vulcanization accelerators (2,2′-dibenzthiazole disulfide Vulkacit DM (Lanxess, Germany), diphenylguanidine (Khimprom, Russia)), vulcanization activators (zinc oxide (Empils-zinc, Russia), stearic acid (RossPolymer, Russia)), antioxidant (naphtham-2 (Bina Grupp, Russia)), softeners (rosin (Sibles, Russia), SMPlast resin (Region-NK, Russia), petroleum bitumen (TAIF-NK, Russia), factis (Alphaplastic, Russia) and industrial oil I-12A (Necton Sea, Russia)), fillers (carbon black P 514 (Ivanovskii Tekhuglerod i Rezina, Russia), carbon black P 803 (Ivanovskii Tekhuglerod i Rezina, Russia), natural chalk (Melstrom, Russia), trans-polynorbornene (Astron Industriebeteiligungs GmbH, Austria)). The rubber mixture was prepared on laboratory rollers LB 320 160/160 (Polimermash group, Russia) at a roller temperature of 60–70 °C for 25 min. The rheometric characteristics of the rubber compound were studied on a MDR 3000 Basic rheometer from Mon Tech (Buchen, Germany) at 150 °C for 30 min in accordance with ASTM D2084-79. Standard samples for determining physico-mechanical properties were vulcanized at a temperature of 150 °C for 30 min in a P-V-100-3RT-2-

PCD vulcanization press (Pan Stone Hydraulic Industries Co., Ltd., Taiwan). The main characteristics of vulcanizates were determined according to the standards in force in the rubber industry: elastic strength properties were determined according to Russian State Standard GOST 270-75 "Rubber. Method of the determination elastic and tensile stress-strain properties", Shore A hardness was measured in accordance with Russian State Standard GOST 263-75 "Rubber. Method for the determination of Shore A hardness", tear resistance was found according to Russian State Standard GOST 262-93 "Rubber, vulcanized. Determination of tear strength (trouser, angle and crescent test pieces)", the change in conditional tensile strength, relative elongation at break and hardness after exposure to sea water (8 % aqueous solution of sea salt) was determined according to Russian State Standard GOST 9.030-74 (method B) "Unified system of corrosion and ageing protection. Vulcanized rubbers. Method of testing resistance to attack by corrosive media in limp state", the change in mass after exposure to sea water was found according to Russian State Standard GOST 9.030-74 (method A) "Unified system of corrosion and ageing protection. Vulcanized rubbers. Method of testing resistance to attack by corrosive media in limp state". The dynamic parameters (mechanical loss tangent) of vulcanizates of various variants of the rubber compound were studied at a temperature of 30 °C on a Metravib VHF 104 dynamic mechanical analyzer (France) in the "tension-compression" deformation mode (degree of deformation 0.01%) and a frequency of 1000 Hz.

Results and Discussion

The effectiveness of using the combination of SKN-4045 with CIIR and BIIR was assessed by the rheometric properties of the rubber compound, physico-mechanical properties, and changes in these indicators after exposure to sea water, as well as the dynamic properties of vulcanizates. Variants of the studied rubber compound containing NBR 4045, CIIR and BIIR in various proportions are shown in Table 1. Figure 1 and Table 1 show the obtained vulcanization curves and the following values of the rheometric parameters of the rubber compound respectively.

Table 1. Variants and rheometric properties of the rubber compound

Caoutchoucs	Variants of the rubber compound						
	1	2	3	4	5	6	7
CIIR, phr*	25.0	–	20.0	–	–	100.0	–
BIIR, phr	–	25.0	–	20.0	–	–	100.0
NBR 4045, phr	75.0	75.0	80.0	80.0	100.0	–	–
Rheometric properties of the rubber compound at 150 °C							
M_H, dN·m	9.00	8.99	8.46	8.28	6.37	5.43	5.05
M_L, dN·m	0.83	0.87	0.78	0.80	0.70	1.01	0.94
t_s, min	3.15	2.76	3.24	2.87	5.37	8.09	5.78
t_{90}, min	20.04	18.11	19.79	18.31	22.39	22.94	15.64
Note: M_H is the maximum torque; M_L is the minimum torque; t_s is the curing scorch time; t_{90} is the optimum curing time. *phr (parts per hundred parts of rubber)							

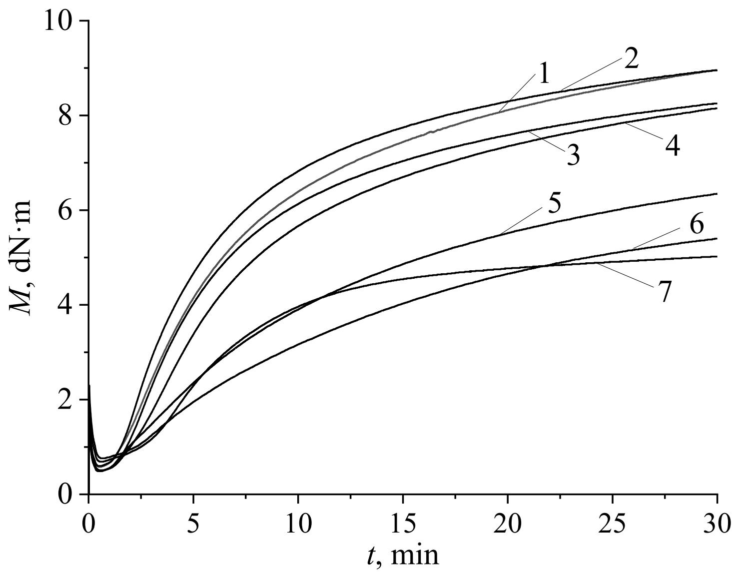

Fig. 1. Rubber compound vulcanization curves
(curve numbers correspond to rubber compound variant numbers)

As can be seen from Fig. 1 and Table 1, replacing CIIR with BIIR (variants 1–4) has virtually no effect on the maximum and minimum torques of the rubber compound. At the same time, BIIR helps to reduce the start and optimum times of vulcanization of the rubber compound. Such a change in the curing scorch time and optimum curing time is due to the increased reactivity of bromobutyl rubber due to the lower energy of the C–Br bond compared to the C–Cl bond and the higher rate of vulcanization of the rubber compound containing bromobutyl rubber [29–32]. Variants 5–7 of the rubber compound are characterized by lower values of the maximum torque and longer times for the onset and optimum of vulcanization compared to the rubber compound options containing combinations of nitrile-butadiene and halobutyl rubbers.

Table 2. Physico-mechanical and performance properties of vulcanizates

Indicators	Variants of the rubber compound						
	1	2	3	4	5	6	7
Physico-mechanical properties of vulcanizates							
f_p, MPa	5.4±0.2	5.6±0.2	4.2±0.2	4.4±0.2	3.8±0.2	4.0±0.2	3.7±0.1
ε_p, %	510±20	510±18	420±16	410±15	490±19	500±21	520±20
H, units Shore A	60±1	63±1	64±1	68±1	51±1	57±1	53±1
B, kN/m	29±2	30±2	28±2	26±2	24±2	22±2	22±2
Changes in the physical and mechanical properties of vulcanizates after exposure to sea water at 23 °C for 24							
Δf_p, %	+6.2±0.2	+4.9±0.2	+5.2±0.2	+5.4±0.2	+10.8±0.4	-14.4±0.6	-16.2±0.6
$\Delta\varepsilon_p$, %	-2.6±0.1	-1.9±0.1	-5.8±0.2	-6.3±0.2	-2.0±0.1	-10.2±0.4	-9.6±0.4
Δ*H*, units Shore A	+3±1	+2±1	+2±1	+3±1	+6±1	+6±1	+7±1
Change in the mass of vulcanizates after exposure to sea water at 23 °C for 7 days							
Δ*m*, %	0.68±0.01	0.64±0.01	0.62±0.01	0.59±0.01	0.15±0.01	0.43±0.01	0.39±0.01
Note: f_p is the tensile strength; ε_p is the elongation at break; *H* is the hardness; *B* is the tear resistance; Δf_p, $\Delta\varepsilon_p$, Δ*m* are relative changes in tensile strength, elongation at break and mass after exposure of rubber to sea water; ΔH is the difference in hardness after and before aging in sea water.							

The results of studies of physico-mechanical properties (Table 2) show that vulcanizates containing combinations of NBR 4045 rubber and halobutyl rubbers are characterized by almost identical elastic-strength properties, hardness and tear resistance (variants 1-4).

Moreover, an increase in the proportion of halobutyl rubbers in combination with NBR 4045 leads to an increase in the elastic-strength properties of rubber. Vulcanizates of variants 5–7, containing separately only each of the rubbers used, have lower physical and mechanical properties. It also follows from Table 2 that the smallest change in elastic-strength properties after daily exposure to sea water is characterized by rubber that includes the rubber combination SKN-4045: BIIR = 75:25 phr. The mass of vulcanizates based on a combination of nitrile butadiene and halobutyl rubbers changes slightly after a week's exposure to sea water.

Subsequently, the values of the mechanical loss tangent tanδ were determined for different variants of vulcanizates (see Fig. 2).

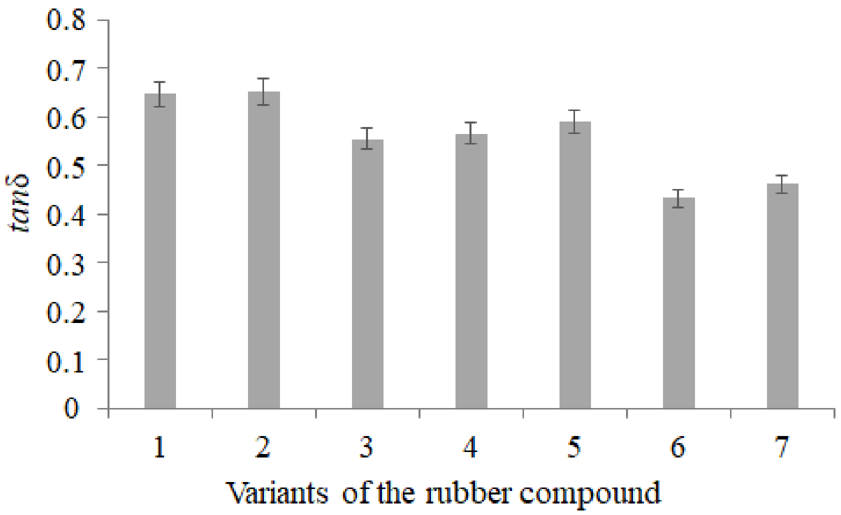

Fig. 2. The mechanical loss factor of vulcanizates

According to [33–36], materials (polymers) with high *tan*δ values have good dynamic properties. As can be seen from Fig. 2, an increase in the content of halobutyl rubbers leads to an increase in *tan*δ. Vulcanizates of options 1 and 2 have almost equally high *tan*δ values, and, therefore, they are characterized by better dynamic properties.

Conclusions

1. The effect of halobutyl rubbers (CIIR and BIIR) in combination with nitrile butadiene rubber NBR 4045 on the rheometric properties of the rubber compound, physico-mechanical, performance and dynamic properties of the vulcanizates was studied.
2. It was shown that equal-mass replacement of CIIR with BIIR has virtually no effect on the rheometric characteristics (maximum and minimum torques) of the rubber compound. At the same time, BIIR helps to reduce the onset and optimum times of vulcanization (higher vulcanization rate) of the rubber compound.

3. It was established that the vulcanizate of the rubber compound based on a combination of NBR 4045:BIIR rubbers at a ratio of 75:25 phr has increased physico-mechanical properties; their smallest changes after exposure to sea water; better dynamic properties (high value of the mechanical loss factor).

References

1. Schaefer RJ. Mechanical properties of rubber. In: *Harris' Shock and Vibration Handbook*. New York: McGraw-Hill; 2010. p.33–31.
2. Najib NN, Ariff ZM, Bakar AA, Sipaut CS. Correlation between the acoustic and dynamic mechanical properties of natural rubber foam: Effect of foaming temperature. *Materials and Design*. 2011;32(2): 505–511.
3. Nafeesa MS, Azura AR. The Influence of Different Types of Rubber on Curing Behaviour and Dynamic Properties of Rubber Compound. *Journal of Physics: Conference Series*. 2018;1082: 012010.
4. Cheng X, Chen Z, Gu T, Zeng L, Yao L, Chen Z, Huang K, Zhang Z, Zhang C, Liu K, Huang S. Study on the dynamic and static mechanical properties of microsphere rubber powder reinforced oil well cement composites. *Construction and Building Materials*. 2021;309: 125145.
5. Zhang D, Li H, Tu H, Weng Y. Investigation on the quasi-static mechanical properties and dynamic compressive behaviors of ultra-high performance concrete with crumbed rubber powders. *Materials and Structures*. 2022;55: 104.
6. Kang H, Tang Y, Yao L, Yang F, Fang Q, Hui D. Fabrication of graphene/natural rubber nanocomposites with high dynamic properties through convenient mechanical mixing. *Composites Part B: Engineering*. 2017;112: 1–7.
7. Sheng Z, Yang S, Wang J, Lu Y, Tang K, Song S. Preparation and Properties Analysis of Chlorinated Butyl Rubber (CIIR)/Organic Diatomite Damping Composites. *Materials*. 2018;11(11): 2172.
8. Pöschl M, Vašina M, Zádrapa P, Měřínská D, Žaludek M. Study of Carbon Black Types in SBR Rubber: Mechanical and Vibration Damping Properties. *Materials*. 2020;13(10): 2394.
9. Mohamad N, Yaakub J, Ab Maulod HE, Jeefferie AR, Yuhazri MY, Lau KT, Ahsan Q, Shueb MI, Othman R. Vibrational damping behaviors of graphene nanoplatelets reinforced NR/EPDM nanocomposites. *Journal of Mechanical Engineering and Sciences*. 2017;11(4): 3274–3287.
10. Murniati R, Rahmayanti HD, Utami FD, Cifriadi A, Iskandar F, Abdullah M. Effects of magnetically modified natural zeolite addition on the crosslink density, mechanical, morphological, and damping properties of SIR 20 natural rubber reinforced with nanosilica compounds. *Journal of Polymer Research*. 2020;27(2): 37.
11. Liu W, Lv L, Yang Z, Zheng Y, Wang H. The Effect of OMMT on the Properties of Vehicle Damping Carbon Black-Natural Rubber Composites. *Polymers*. 2020;12(9): 1983.
12. Pöschl M, Vašina M. Study of the Mechanical, Sound Absorption and Thermal Properties of Cellular Rubber Composites Filled with a Silica Nanofiller. *Materials*. 2021;14(23): 7450.
13. Praveen S, Bahadur J, Yadav R, Billa S, Umasankar Patro T, Rath SK, Ratna D, Patri M. Tunable viscoelastic and vibration damping properties of a segmented polyurethane synergistically reinforced with carbon black and anisotropic additives. *Applied Acoustics*. 2020;170: 107535.
14. Egorov EN, Ushmarin NF, Sandalov SI, Kol'tsov NI. Studying the Effect of *trans*-Polynorbornene on the Properties of a Rubber Mixture for Rail Fastener Pads. *Inorganic Materials: Applied Research*. 2022;13(4): 1019–1023.
15. Egorov EN, Salomatina EV, Vassilyev VR, Bannov AG, Sandalov SI. Effect of Polynorbornene on Physico-Mechanical, Dynamic, and Dielectric Properties of Vulcanizates Based on Isoprene, α-Methylstyrene-Butadiene, and Nitrile-Butadiene Rubbers for Rail Fasteners Pads. *Journal of Composites Science*. 2023;7(8): 334.
16. Egorov EN, Sandalov SI, Kol'tsov NI. Study of the influence of dispersed fillers on properties of rubber for gaskets of rail fastening. *Materials Physics and Mechanics*. 2023;51(6): 119-126.
17. Zhang J, Wang L, Zhao Y. Fabrication of novel hindered phenol/phenol resin/nitrile butadiene rubber hybrids and their long-period damping properties. *Polymer Composites*. 2012;33(12): 2125–2133.
18. Liu K, Lv Q, Hua J. Study on damping properties of HVBR/EVM blends prepared by in situ polymerization. *Polymer Testing*. 2017;60: 321–325.
19. Yu F, Lu A, Lu J, Wang Z, Zhang Q, Geng C, Li Z. Effect of phenyl content, sample thickness and compression on damping performances of silicone rubber: A study by dynamic mechanical analysis and impact damping test. *Polymer Testing*. 2019;80: 106101.

20. Hejna A, Korol J, Przybysz-Romatowska M, Zedler Ł, Chmielnicki B, Formela K. Waste tire rubber as low-cost and environmentally-friendly modifier in thermoset polymers – A review. *Waste Management*. 2020;108: 106–118.
21. Qin R, Huang R, Lu X. Use of gradient laminating to prepare NR/ENR composites with excellent damping performance. *Materials and Design*. 2018;149: 43–50.
22. Zhao X, Yang J, Zhao D, Lu Y, Wang W, Zhang L, Nishi T. Natural rubber/nitrile butadiene rubber/hindered phenol composites with high-damping properties. *International Journal of Smart and Nano Materials*. 2015;6(4): 239–250.
23. Dharmaraj MM, Chakraborty BC, Begum S. The effect of graphene and nanoclay on properties of nitrile rubber/polyvinyl chloride blend with a potential approach in shock and vibration damping applications. *Iranian Polymer Journal*. 2022;31: 1129–1145.
24. Akyüz S, Darı ME, Esiyok YE, Ermeydan MA. Effects of NR/SBR ratio on mechanical properties and artificial mechanical performance of anti-vibration bushings. *Iranian Polymer Journal*. 2021;30: 1317–1328.
25. Liu C, Fan J, Chen Y. Design of regulable chlorobutyl rubber damping materials with high-damping value for a wide temperature range. *Polymer Testing*. 2019;76: 106003.
26. Lu X, Huang R, Li H, Long J, Jiang Z. Preparation of an elastomer with broad damping temperature range based on EPDM/ENR blend. *Journal of Elastomers and Plastics*. 2017;49(8): 758–773.
27. Egorov EN, Ushmarin NF, Sandalov SI, Kol'tsov NI. Research of operational and dynamic properties of rubber for products working in sea water. *ChemChemTech*. 2020;63(11): 96–102. (In Russian)
28. Egorov EN, Ushmarin NF, Sandalov SI, Kol'tsov NI, Voronchikhin VD. Investigation of the dynamic properties of seawater-resistant rubber. *Journal of Siberian Federal University. Chemistry*. 2021;14(1): 38–44.
29. Chaikun AM, Alifanov EV, Naumov IS. Rubbers based on butyl rubber (review). *Novosti materialovedeniya. Nauka i tekhnika*. 2016;6(24): 49–59. (In Russian).
30. Cao R, Zhao X, Zhao X, Wu X, Li X, Zhang L. Bromination modification of butyl rubber and its structure, properties and application. *Industrial and Engineering Chemistry Research*. 2019;58(36): 16645–16653.
31. Scagliusi SR, Cardoso EC, Pozenato CA, Lugão AB. Degrading radiation effects on properties of bromobutyl rubber compounds. In: *Proc. of INAC 2013: International nuclear atlantic conference; Recife, PE (Brazil); 24-29 Nov 2013*. 2013. p.46004077.
32. Pazur RJ, Petrov I. The thermo-oxidation of chlorinated and brominated isobutylene-co-isoprene polymers: Activation energies and reactions from room temperature to 100 °C. *Polymer Degradation and Stability*. 2015;121: 311–320.
33. Egorov EN, Kol'tsov NI. Influence of glass fibers on the physico-mechanical and performance properties of rubber based on general and special purpose caoutchoucs. *Materials Physics and Mechanics*. 2024;52(1): 126–131.
34. Egorov EN, Ushmarin NF, Salomatina EV, Matyunin AN. The effect of polyisobutylene on physical-mechanical, operational, dielectric and dynamic properties of rubber for laying rail fasteners. *ChemChemTech*. 2022;65(5): 94–102. (In Russian)
35. Moradi G, Nassiri P, Ershad-Langroudi A, Monazzam MR. Acoustical, damping and thermal properties of polyurethane/poly(methylmethacrylate)-based semi-interpenetrating polymer network foams. *Plastics, Rubber and Composites*. 2018;47(5): 221–231.
36. Sujon MAS, Islam A, Nadimpalli VK. Damping and sound absorption properties of polymer matrix composites: A review. *Polymer Testing*. 2021;104: 107388.

About Authors

Evgeniy N. Egorov iD Sc
Candidate of Chemical Science
Associate Professor (I.N. Ulyanov Chuvash State University, Cheboksary, Russia)

Nikolay I. Kol'tsov iD Sc
Doctor of Chemical Science
Professor (I.N. Ulyanov Chuvash State University, Cheboksary, Russia)

MATERIALS PHYSICS AND MECHANICS RESEARCH ARTICLE

Submitted: July 24, 2024 Revised: August 20, 2024 Accepted: October 14, 2024

Development of the semi empirical approach on wormhole formation in carbonates

R.M. Ganopolskij [1] ✉, **K.M. Fedorov** [1], **B.R. Gilmutdinov** [2], **A.E. Folomeev** [2]

[1] University of Tyumen, Tyumen, Russia

[2] Irkusk Oil Company LLC, Irkutsk, Russia

✉ r.m.ganopolskij@utmn.ru

ABSTRACT

Carbonate acidizing is a technology of well productivity stimulation in oil recovery practice. The maximum effect of such a well treatment is connected with acidizing channels formation of several millimeters in diameter (wormholes). One of the approaches to predict the acidizing effect of wormholing is the semi empirical simulation based on the results of the experiments of core plug channeling by acid injection. It was established that maximum of permeability improvement corresponds to the minimum of injected volume and is defined by wormhole breakthrough. Presentation of such equation in the dimensionless form involves dimensionless criteria such as Damköhler, Peclet, etc, that are defined by the results of the calculation and with experiment data matching. The new approach to derivate of the main equation defining the acid wormholing process is developed in the present paper.

KEYWORDS

wormhole formation in carbonate core plug • dimensionless numbers by Damköhler and Peclet acidizing of carbonate reservoir

Citation: Ganopolskij RM, Fedorov KM, Gilmutdinov BR, Folomeev AE. Development of the semi empirical approach on wormhole formation in carbonates. *Materials Physics and Mechanics*. 2024;52(5): 119–126. http://dx.doi.org/10.18149/MPM.5252024_12

Introduction

Well's productivity stimulation in carbonate reservoirs by acid solutions had a practice history from the middle of the previous century [1–3]. The main target of carbonate formation acidizing is the permeability improvement in the near well bore zone. Application of different technologies was proposed for this purpose: from low-rate acid injection for cavity creation near a well to high velocity injection that leads to reservoir fracturing and fracture stabilization by etching of its side surfaces. The ideology of channeling or wormholing of an oil formation was developed in the works [4–7].

A lot of the studies analyzed the formation and structure of wormholes in carbonates with the radioscopy and computer tomography of a core plug during acid injection [8,9]. In [10,11], it was used the large, massive carbonates blocks with a cylindrical channel or the well bore model. Application of unprecedented experimental scale helps to understand the formation of wormhole net in the vicinity of a well, their structure including fractal form.

These investigations helped to develop the general semi empirical theory of wormhole growth. It was established that the injection rate defines the following modes of the stimulation process: frontal acidizing of carbonate matrix and cavity creation near

Publisher: Peter the Great St. Petersburg Polytechnic University

the inlet of core plug due to low-rate acid injection; wormhole growth with critical value of injection rate and volumetric acid reaction accompanied by high velocity acid flow. The maximum of well productivity increase occurs due to deep acid penetration to the matrix with formation of high permeability wormholes. The understanding of the mechanisms was achieved in the analysis of linear core plug experiments. The result of these studies established that wormhole formation is operated by injection rate through the Damköhler number or relation of reaction rate to acid flow velocity. The Peclet (or the ratio of convective to diffusive fluxes) and the acid capacity (defining the specific mass of matrix that can be dissolved by acid in pore space) numbers describe the influence of other parameters on the process. Its role in the reaction was considered in [12]. Note that the Peclet number is proportional to the injection rate but the Damköhler number is inverse proportional to the same parameter. Introducing the critical values of injection rate and volume of acid needed for wormhole breakthrough Fredd and Fogler [5] proposed new dimensionless parameters of the process: the ratio of injected acid volume and the rate to the critical values of these characteristics. Using these variables, they established the unique dependence: introduced specific acid volume from the Damköhler number. The physical meaning of the dependence is the connection of acid injection volume with the length of the created wormhole. Processing of the experiments by different investigators covered limestone and dolomite, various types of acid, their concentration, reaction and injection rates confirmed the unique dependence. The reservoir mineralogy of cause plays a definite role in the value of dimensionless numbers. Note that the heterogeneous reaction rate is defined from the experiments with the rotating disk apparatus [3] and by the volumetric method [13] and the definition of Damköhler number may involve internal wormhole parameters (radius, length) [4] and external characteristics (permeability, flow velocity) [14].

Acidizing experiments in a vuggy carbonate showed that specific acid volume to breakthrough is an order of magnitude lower than what has been observed with relatively homogeneous limestone [15]. Large-Scale Dual-Porosity Approach is developed for such reservoirs in [16].

The idea of the developing of the simulator including all acidizing modes attracts many investigators [8]. These approaches may be divided into several categories. Huang et al. [17] used the capillary tube approach to predict wormhole population density and calculate the volume of acid required to create wormholes of a certain density and length. Semi empirical models will be considered further in details. Wang et al. [18] developed transition pore theory to calculate the optimum flux to generate dominant wormholes during a matrix acid treatment. As a network model approach Fredd and Fogler [6] proposed the model to describe wormhole growth in 3D physically representative network where distribution of acid concentration is calculated due to transport and reaction with sphere grains. The last group uses Darcy scale models for acid transport in reacting matrix [19].

Further only semi empirical model group will be considered. This group [8] considers micromechanics of creation and growth of the main wormhole in a carbonate core plug. The underground of this model group is the laboratory investigation of wormhole creation and growth in a carbonate core plug and the study of heterogeneous reaction (in situ diffusion and reaction rate) on the rotating disk installation. As a result, these models involve the formulation of the main equation bonding pore volume of acid injection till its breakthrough to the outlet of core plug with the injection rate and also the influence of other parameters such as acid type and concentration [4], temperature [20] on the main equation. Note that it is difficult to find out the systematic study of reliable quality in the present studies, most researches give the 2–5 experimental points. Several investigators consider the main dimensionless characteristics of the process is the Damköhler number [6], other outline the Peclet number [20,21], Gong and El Rabaa [14] use mixed approach.

The impact of effective tortuosity of porous media of the Damkohler and Peclet dimensionless numbers is considered in [22]. Wang et.al analyzed the process of matrix acidizing in naturally fractured carbonate reservoirs [23]. The influence of acid type and combined acid systems on the process was studied experimentally in [24].

Summarizing the above considerations, the main equation bonding acid breakthrough pore volume (*PV*) and injection rate (*q*) has the following structure [14]:

$$PV = \frac{A}{q^2} + Bq^{\frac{1}{3}}, \tag{1}$$

where *A* and *B* are the constants depending on carbonate mineralogy, acid composition and concentration, in situ diffusion and some other factors. These constants are defined by matching calculation with the experimental data.

Gong and El Rabaa [14] integrated the approaches of Fredd and Fogler [4] and Daccord, Touboul and Lenormand [18] and proposed the following dimensionless version of the main Eq. (1). Their equation involves the Damköhler N_{Da}, the Peclet N_{Pe} and the acid capacity N_{ac}:

$$PV = f_1 \frac{N_{Da}}{N_{Pe}} + f_2 \frac{N_{Pe}^{\frac{1}{3}}}{N_{ac}}, \tag{2}$$

where f_1 and f_2 are the empirical constants defined from matching experimental data.

In [14], the dimensionless numbers are defined as the following:

$$N_{Pe} = \frac{q\sqrt{k}}{D} \quad N_{ac} = \frac{\emptyset \varkappa_R c \rho_w}{(1-\emptyset)\rho_R} \quad N_{Da} = \frac{D^{\frac{5}{3}}\sqrt{k}}{\nu^{\frac{2}{3}} q} \text{ (for dolomite)}, \; N_{Da} = \frac{K D^{\frac{2}{3}} k}{\nu^{\frac{2}{3}} q} \text{ (for limestone)}, \tag{3}$$

where *D* is the in-situ diffusion coefficient, *K* is the reaction kinetic constant, *k* and Ø are the permeability and porosity of a rock matrix, ρ_w/ρ_R is the ratio of acid solution and rock matrix densities, *ν* is the kinematic viscosity, $\varkappa_R$ is the solubility of matrix in acid, *c* is an acid concentration.

Further exactly these expressions of the dimensionless numbers will be used in the paper. Unfortunately, incorrect mathematical calculations hinder the application of the Gong and El Rabaa model for practical prediction of the process.

The main conclusion of the experimental studies is the establishment of the critical value of acid injection rate q_{cr} that accompanies wormhole formation and minimum pore volume injection till acid breakthrough PV_{cr}. The dependence of dimensionless variables $PV/PV_{cr} = f(q/q_{cr})$ is a universal function that is defined only by the Damköhler number.

Note that most of the models of other mentioned simulation approaches were verified by matching the calculations with the results of leaner experiments which are the framework the of semi empirical approach [25,26]. In a manner, the accuracy of these approaches is approximately the same as for semi-empirical models based on *PV* breakthrough curves from core scale experiments.

Formulation of the main theorems

Let's accept the main hypothesis about the dependence of breakthrough pore volume *PV* from the acid injection rate (1) by more general function:

$$PV = \frac{A}{q^m} + Bq^n. \tag{4}$$

The minimum of this function may be obtained by differentiating with respect to the injection rate and setting it to zero. The obtained equation may be rearranged to yield the expression of q_{cr}. Finally, the critical rate and the minimum/critical breakthrough pore volume are expressed as:

$$q_{cr} = \left(\frac{mA}{nB}\right)^{\frac{1}{m+n}}, \quad PV_{cr} = \frac{A^{\frac{n}{m+n}}B^{\frac{m}{m+n}}(m+n)}{m^{\frac{m}{m+n}}n^{\frac{n}{m+n}}}. \tag{5}$$

The first item. Let's prove the statement that Fredd's and Fogler's universal equation of wormhole growth is the consequence of the adoption of the equation in the form (1) and depends on only the values of exponents *m* and *n*. For this purpose, let's introduce the new dimensionless parameters PV/PV_{cr} and q/q_{cr} and rearrange the Eq. (4) to the following form:

$$P\frac{PV}{PV_{cr}} = \frac{1}{(m+n)}\left(n\left(\frac{q_{cr}}{q}\right)^m + m\left(\frac{q}{q_{cr}}\right)^n\right). \tag{6}$$

If we choose the inverse Damköhler number as the dimensionless injection rate than Eq. (6) will be defined by one universal constant *a*:

$$\frac{PV}{PV_{cr}} = \frac{1}{(m+n)}\left(n(aN_{Da})^m + \frac{m}{(aN_{Da})^n}\right). \tag{7}$$

Fredd and Fogler have determined this constant by matching calculations and experimental data and obtained the value 0.29. Consequently, the initial hypothesis (1) and (4) lead to the conclusion of the existence of universal dependence:

$$\frac{PV}{PV_{cr}} = f\left(\frac{1}{N_{Da}}\right). \tag{8}$$

The proved statement is true for various values of *m* and *n*.

Taking into account the dependence of introduced dimensionless numbers from injection rate (4) and Eq. (7) it is expedient to consider the following dimensionless numbers and their combination:

$$N_{ac};\ N_{Da};\ N_{FG} = N_{Pe}N_{Da}. \tag{9}$$

Here only Damköhler number depends on the injection rate that is why we can suppose that the critical value of parameters involve only N_{ac} and N_{FG} and breakthrough pore volume *PV* is defined by Eq. (4). The combination N_{FG} is applied in the theory of solutions separation by filters [27] and further will refer as the generalized Damköhler number. The authors propose the following expressions for the critical values:

$$PV_{cr} = \frac{g_1 {N_{FG}}^{\varepsilon}}{N_{ac}}, \quad q_{cr} = g_2 {N_{FG}}^{\theta}(N_{Da}q), \tag{1}$$

where ε and θ are arbitrary exponents defined by matching experimental and calculated data. The proposed expressions (10) are based on the physical considerations that critical breakthrough pore volume PV_{cr} is directly bonded with matrix pore volume that could react with acid injected volume or $1/N_{ac}$.

The second item. The proposed approach bases on the main postulate that the wormhole growth mechanisms is defined by introduced critical values but the Eqs. (1) or (4) matches the injection rate only in the narrow rate interval. The extension of the dependence in the modes of frontal or volumetric acidizing or mixed reaction modes is not correct. The common trends of the main equation in the regions of high and low injection rates tends to infinity, from the other hand the objectives of frontal and volumetric reaction modes have definite solutions with the finite values. For example, in the low rate region, the breakthrough pore volume is defined by $1/N_{ac}$.

Let's analyze the experimental data on breakthrough pore volume, for example gathered in [6], which are presented on Fig. 1. First of all, the majority of experimental point lays in the vicinity of the critical injection rate. The number of points far from the critical value is less and the deviation of them is much higher. If we adopted the universal dependence in the form (4) than we can restrict the experimental points by two curves with exponents values: 1) m = 2, n = 1/3 and 2) m = 5/2, n = 3/5. In order to get away from the details the coordinates of points were normalized on Fig. 1. Therefore, the main target of the model's equation is to describe the behavior of PR function near the critical point and to define the critical parameters with sufficient accuracy.

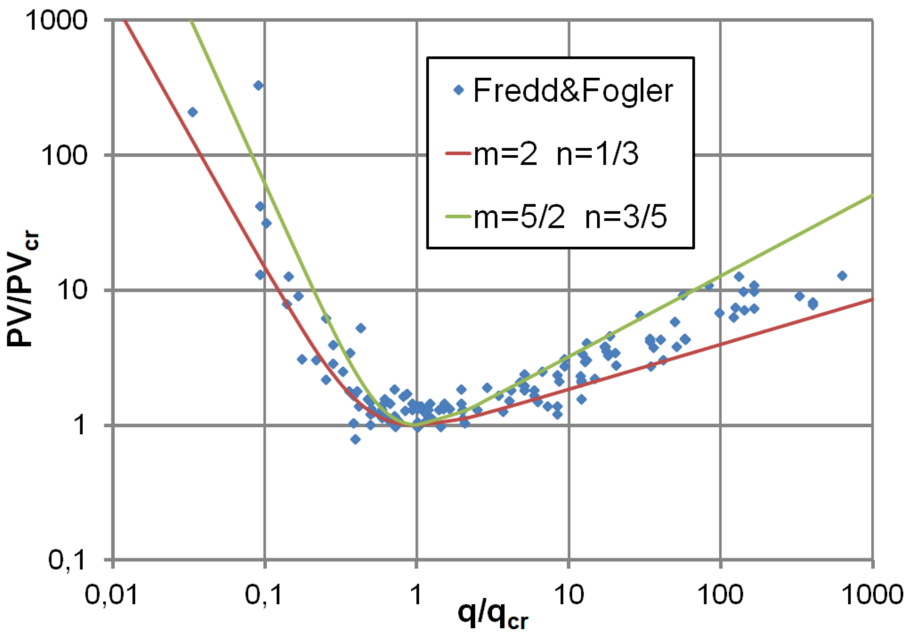

Fig. 1. Experimental data on normalized dependence of the breakthrough pore volume from dimensionless injection rate extracted from [6]

The third item. The proposed approach generalized the models presented by Fredd and Fogler [6], Gong and El Rabaa [14] and does not contradict the empirical results by Dong, Zhu and Hill [28], Pange, Ziauddin and Balakotaiah [29]. In the first item, it was established that the universal Fredd's and Fogler's equation (8) is defined by the assumptions about the structure of equations and could be arranged to the view (2) by simple mathematical calculations.

The main proposal of Gong and El Rabaa on the dimensionless numbers that operates the process is the same in the suggested approach. The equation (4) generalizes the Eq. (1) proposed by Gong and El Rabaa.

Dong, Zhu and Hill [28] analyzed experimental data executed by Wang et al. [18] and their own on temperature and acid concentration influence on the critical injection rate. They established the invariant that does not dependent from temperature and acid concentration. This invariant is defined as follows:

$$\frac{PV_{cr}D}{q_{cr}} = \text{const.} \tag{11}$$

After substitution the expressions of the critical parameters (10) to the invariant (11) one can obtain that the Dong's, Zhu's and Hill's conclusion is performed when ε and θ satisfy the condition: $\varepsilon = \theta + 1$.

This equation with Fredd and Fogler assumption lead to the following expression of critical parameters: $\varepsilon = 1, \quad \theta = 0, \quad PV_{cr} = \frac{g_1 N_{FG}}{N_{ac}}, \quad q_{cr} = g_2(N_{Da}q), \quad g_2 = a = 0.29.$

If we take into account the proposal of Pange, Ziauddin end Balakotaiah on the equation form than we shall come to the following conclusions: $\varepsilon = 0.5, \quad \theta = -0.5,$ $PV_{cr} = \frac{g_1\sqrt{N_{FG}}}{N_{ac}}, \quad q_{cr} = \frac{g_2(N_{Da}q)}{\sqrt{N_{FG}}}.$

At last, despite the mathematical claims to the work of Gong end El Rabaa we present the expressions of critical parameters in their model: $\varepsilon = \frac{1}{7}, \quad \theta = -\frac{4}{7},$ $PV_{cr} = \frac{g_1(N_{ac}N_{FG})^{\frac{1}{7}}}{N_{ac}}, \quad q_{cr} = \frac{g_2(N_{Da}q){N_{ac}}^{1/7}}{(N_{ac}N_{FG})^{4/7}}$ but instead of N_{FG} these expressions involve dimensionless constant N_{FG}, N_{ac} and critical injection rate includes excess N_{ac}.

Conclusions

Generalizing the conclusions of the proved items the following results can be declared:

1. The proposed approach integrates the main aspects of Fredd's and Fogler's theory on the influence of Damköhler number on the wormhole formation in carbonates, the proposal of Daccord, Gong et al. on the role of Damköhler, Peclet and acid capacity numbers in the acidizing process and the type of the equation bonding breakthrough pore volume with acid injection rate, established by Dong, Zhu end Hill invariant (10) is also being executed by Eq. (11).
2. The main purpose of the equation bonding breakthrough pore volume with acid injection rate is the precise determination of critical parameters. The key factors of the wormholing process are the critical parameter PV_{cr} and q_{cr}, which are dependent from Damkeler, Peclet and acid capacity numbers. The critical parameters do not dependent from exponents n and m, that is why the role of these parameters is limited by the approximation of breakthrough pore volume from injection rate and precise determination of critical parameters from experimental data.
3. The experiments on the influence of acid concentration, matrix permeability, in situ diffusion on critical parameters are of current interest. These experiments could help to select the most accurate models of wormholing growth in carbonates [30,31].

References

1. Pourabdollah K. Matrix acidizing: a fouling mitigation process in oil and gas wells. *Reviews in Chemical Engineering*. 2020;36(2): 311–331.
2. Krivoshchekov SN, Vyatkin KA, Ravelev KA, Kochnev AA. Influence of geological and technological parameters on effectiveness of hydrochloric acid treatment of carbonate reservoirs. *International Journal of Engineering*. 2020;33(10): 2113–2119.
3. Schechter RS. *Oil Well Stimulation*. Englewood Cliffs: Prentice Hall; 1993.
4. Fredd CN, Fogler HS. The kinetics of calcite dissolution in acetic acid solutions. *Chemical Engineering Science*. 1998;53(22): 3863–3874.
5. Fredd CN, Fogler HS. Influence of Transport and Reaction on Wormhole Formation in Porous Media. *AIChE Journal*. 1998;44(9): 1933–1949.
6. Fredd CN, Fogler HS. Optimum Conditions for Wormhole Formation in Carbonate Porous Media: Influence of Transport and Reaction. *SPE Journal*. 1999;4(03): 196–205.
7. Buijse MA. Mechanisms of Wormholing in Carbonate Acidizing. In: *Proceedings of the International Symposium on Oilfield Chemistry, 18–21 February 1997, Houston, Texas*. p.SPE–37283–MS.
8. Akanni OO, Nasr-El-Din HA. The Accuracy of Carbonate Matrix-Acidizing Models in Predicting Optimum Injection and Wormhole Propagation Rates. In: *Proceedings of the SPE Middle East Oil & Gas Show and Conference, 8–11 March 2015, Manama, Bahrain*. p.SPE–172575–MS.
9. Glasbergen G, Kalia N, Nalbot M. The Optimum Injection Rate for Wormhole Propagation: Myth or Reality. In: *Proceedings of the 8th European Formation Damage Conference, 27–29 May 2009, Scheveningen, The Netherlands. p*.SPE–121464–MS.
10. McDuff D, Shuchart CE, Jackson S, Postl D, Brown JS. Understanding Wormholes in Carbonates: Unprecedented Experimental Scale and 3-D Visualization. In: *Proceedings of the SPE Annual Technical Conference and Exhibition, 19–22 September 2010, Florence, Italy*. p.SPE–134379–MS.
11. McDuff D, Shuchart CE, Postl D. Understanding Wormholes in Carbonates: Unprecedented Experimental Scale and 3D Visualization. *J Pet Technol*. 2010;62(10): 78–81.
12. Pasha P, Taghinia F, Nadalinia Chari F, Jalili B, Jalili P, Domiri Ganji D. Chemical reaction-diffusion model around a vessel for studying temperature and concentration of three chemical species by finite element method. *International Journal of Engineering, Transactions A: Basics*. 2023; 36(1): 171–181.
13. Kremleva TA, Smirnov AS, Fedorov KM. Simulation of carbonate acidizing process including wormholing. *Izvestia RAN. Fluid mechanics*. 2011;5: 76–84. (In Russian)
14. Gong M, El-Rabaa AM. Quantitative Model of Wormholing Process in Carbonate Acidizing. In: *Proceedings of the SPE Mid-Continent Operations Symposium, 28–31 March 1999, Oklahoma City, Oklahoma*. p.SPE–52165–MS.
15. Izgec O, Zhu D, Hill AD. Numerical and experimental investigation of acid wormholing during acidization of vuggy carbonate rocks. *Journal of Petroleum Science and Engineering*. 2010;74(1–2): 51–66.
16. Cohen CE, Ding D, Bazin B, Quintard M. A New Matrix-Acidizing Simulator Based on a Large-Scale Dual-Porosity Approach. In: *European Formation Damage Conference, 30 May–01 June 2007, Scheveningen, The Netherlands*. p.SPE-107755-MS.
17. Huang T, Zhu D, Hill AD. Prediction of wormhole population density in carbonate matrix acidizing. In: *SPE European Formation Damage Conference, 31 May–01 June 1999, Hague, The Netherlands*. p.SPE-54723-MS.
18. Wang Y, Hill AD, Schechter RS. The Optimum Injection Rate for Matrix Acidizing of Carbonate Formations. In: *SPE Annual Technical Conference and Exhibition, 3–6 October 1993, Houston, Texas*. p.SPE-26578-MS.
19. Jia C, Sepehrnoori K, Huang Z, Jun Y. Modeling and Analysis of Carbonate Matrix Acidizing Using a New Two-Scale Continuum Model. *SPE J*. 2021;26(05): 2570–2599.
20. Daccord G, Touboul E, Lenormand R. Carbonate Acidizing: Toward a Quantitative Model of the Wormholing Phenomenon. *SPE Production Engineering*. 1989;4(01): 63–68.
21. Al-Arji H, Al-Azman A, Le-Hussain F, Regenauer-Lieb K. Acid stimulation in carbonates: A laboratory test of a wormhole model based on Damköhler and Péclet numbers. *Journal of Petroleum Science and Engineering*. 2021;203: 108593.
22. Alarji H, Alazman A, Regenauer-Lieb K. The impact of effective tortuosity on carbonate acidizing and the validation of Damköhler and Péclet dimensionless phase space. *Journal of Petroleum Science and Engineering*. 2022;212: 110313.
23. Wang J, Mo S, Zhao B, Liu Z, Tian X. Modeling matrix acidizing in naturally fractured carbonate reservoirs. *Journal of Petroleum Science and Engineering*. 2020;186: 106685.

24. Monette M, Nguyen QP. An Experimental Study of Wormhole Morphology with a Novel Acid System in Ultra-High-Temperature Carbonate Reservoirs. *Transport in Porous Media.* 2023;149: 625–642.
25. Ali M, Ziauddin M. Carbonate acidizing: A mechanistic model for wormhole growth in linear and radial flow. *Journal of Petroleum Science and Engineering.* 2020;186: 106776.
26. Ghommem M, Zhao W, Dyer S, Qiu X, Brady D. Carbonate acidizing: Modeling, analysis, and characterization of wormhole formation and propagation. *Journal of Petroleum Science and Engineering.* 2015;131: 18–33.
27. Oyama ST, Lim H. An operability level coefficient (OLC) as a useful tool for correlating the performance of membrane reactors. *Chemical Engineering Journal.* 2009; 151(1–3): 351–358.
28. Dong K, Zhu D, Hill AD. Theoretical and Experimental Study of Optimal Injection Rates in Carbonate Acidizing. *SPE J.* 2017; 22(03): 892–901.
29. Panga MK, Ziauddin M, Balakotaiah V. Two-scale continuum model for simulation of wormholes in carbonate acidization. *AIChE Journal.* 2005;51(12): 3231–3248.
30. Hoefner ML, Fogler HS. Pore evolution and channel formation during flow and reaction in porous media. *AIChE Journal.* 1988;34(1): 45–54.
31. Lucas CRDS, Neyra JR, Araujo EA, da Silva DNN, Lima MA, Ribeiro DAM, Aum PTP. Carbonate acidizing–A review on influencing parameters of wormholes formation. *Journal of Petroleum Science and Engineering.* 2023;220: 111168.

About Authors

Rodion M. Ganopolskij
Candidate of Physical and Mathematical Sciences
Head of Department (University of Tyumen, Tyumen, Russia)

Konstantin M. Fedorov
Doctor of Physical and Mathematical Sciences
Professor (University of Tyumen, Tyumen, Russia)

Bulat R. Gilmutdinov
Candidate of Technical Sciences
Head of Department (Irkusk Oil Company LLC, Irkutsk, Russia)

Alexey E. Folomeev
Candidate of Technical Sciences
Head of Department (Irkusk Oil Company LLC, Irkutsk, Russia)

MATERIALS PHYSICS AND MECHANICS RESEARCH ARTICLE

Submitted: October 10, 2024 **Revised: October 25, 2024** **Accepted: December 1, 2024**

Periodic system of fullerenes: the column of six-fold symmetry

A.I. Melker [1] ✉, **M.A. Krupina** [2]

[1] St. Petersburg Academy of Sciences on Strength Problems, St. Petersburg, Russia

[2] Peter the Great St. Petersburg Polytechnic University, St. Petersburg, Russia

✉ ndtcs@inbox.ru

ABSTRACT

The possible ways of generation and growing the fullerenes having six-fold symmetry have been studied. Beginning with cyclohexane C_6H_{12}, benzol C_6H_6 and clusters C_6C_6, we obtained elementary fullerenes C_{12} and mini-fullerenes C_{24}, which produce the fullerenes from C_{24} to C_{84}; perfect (basic), as well as nanotubes. The basic fullerenes C_{24}, C_{36}, C_{48}, C_{60}, C_{72} and C_{84} have the ordinary six-fold symmetry. We have calculated their energies and discussed possible reasons for their dependence on a fullerene size and shape in the framework of the periodic system of fullerenes.

KEYWORDS

carbon • energy • fullerene • fusion reaction • graph representation • nanotube • periodic system single and double bonds • symmetry

Citation: Melker AI, Krupina MA. Periodic system of fullerenes: the column of six-fold symmetry. *Materials Physics and Mechanics*. 2024;52(5): 127–147.

http://dx.doi.org/10.18149/MPM.5252024_13

Introduction

Up to now an origin and growth of fullerenes and nanotubes is hotly debated [1–34]. The appearance of the periodic table of fullerenes [35,36] allowed change the strategy of investigation: phenomenological approach to fullerenes was replaced by task-oriented activity. The periodic table of fullerenes consists of horizontal series and vertical columns; they include fullerenes from C_{14} to C_{108}. The horizontal series form the Δn periodicities, Δn=2, 4, 6, 8, 10, 12, 14, 16, 18, where the fullerene structure changes from three-fold symmetry to six-fold through four and five ones. The vertical columns include the fullerenes of one and the same symmetry, the mass difference Δm for each column being equal to a double degree of symmetry, i.e. Δm=6, 8, 10, 12. We declare that the periodic system must be taken as a base for rigorous fullerene classification.

At first we have studied isomers of fullerenes from C_4 to C_{60} [37–41]. In parallel we have investigated nucleation and growth of the fullerenes referring to the columns of three-fold [42], four-fold [43] and five-fold symmetry [44]. In this contribution we present the results obtained for the fullerenes referring to the column of six-fold symmetry.

Nucleation and growth of embryos

We assume that the embryos of fullerenes of six-fold symmetry are similar to cyclic hydrocarbons of the same symmetry: cyclohexane (C_6H_{12}) or benzol (C_6H_6).

Cyclohexane

At first, cyclohexane was depicted as a molecule having a plane carbon ring. Later it was established that it has highly symmetric 'chair' configuration which belongs to the symmetry group D_{3d} (Fig. 1(a)). Here [45] four carbon atoms lie in one plane, two others are disposed bilaterally along the plane, all the valence angles CCC are tetrahedral, and all the C-H bonds of neighboring methylene groups are disposed in chess order with respect to each other. From twelve C-H bonds, six bonds are axial and parallel to the symmetry axis of the third order; other six bonds are equatorial. Geometric parameters of the molecule are as follows: r(C-C)=1.54 Å, r(C-H) = 1.09 Å. The chair is a stable conformation of cyclohexane. Another conformation is a boat (a bath) which belongs to the symmetry group C_{2v} and is shown in Fig. 1(b). It is unstable and at room temperature only one molecule from a thousand has a boat conformation. Chemical and physical methods are unable to fix each conformation separately; they see only an average picture. We have calculated their frozen structures and energy through the use of Avogadro package [46].

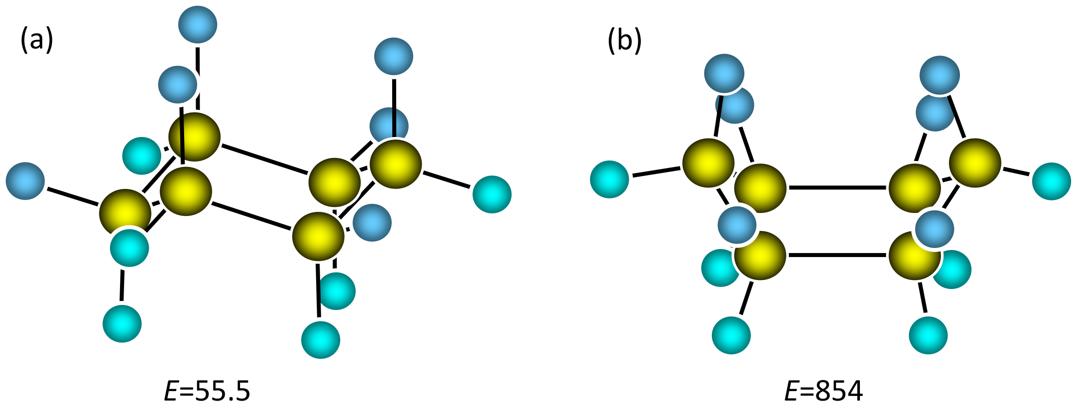

Fig. 1. Structure of a cyclohexane molecule: (a) chair conformation, (b) boat conformation. Large spheres are carbon atoms, small spheres are hydrogen atoms: E is energy, kJ/mol

Benzol

Another embryo of fullerenes of six-fold symmetry is similar to benzol (C_6H_6). For benzol it is customary to assume that the benzol molecule is a regular hexagon with D_{6h} symmetry [45,47] and not a system of alternating long and short bonds. It is believed that in this case there appear delocalized electrons which create bonds. This question is beyond the scope of our study. Nevertheless, it should be mentioned the following. As noted above, chemical and physical methods are unable to fix each electronic conformation separately; they see only an average picture. However, an electronic conformation can be fixed if the system is frozen. Such situation takes place in fullerenes, where the benzol hexagon is rigidly incorporated into a fullerene molecule. Here for fullerene C_{60} atomic force microscopy picture of one of the symmetry equivalent hexagons clearly shows the two different types of bonds [48]. The measured bond lengths are r_{hh} = 1.38 Å and r_{hp} = 1.4654 Å. For this reason, we take in consideration the bond-order discrimination in our study. We have calculated the frozen structure and energy of benzol through the use of Avogadro package [46]. The result is shown in Fig. 2.

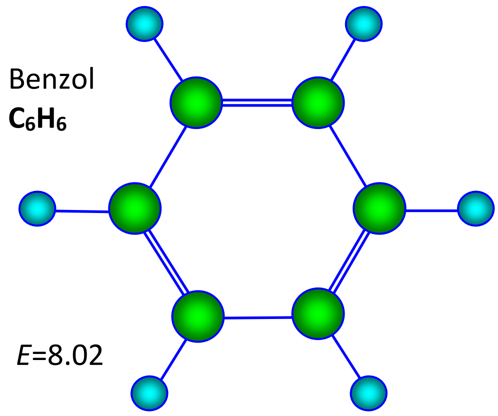

Fig. 2. Benzol: carbon ring and six hydrogen atoms on its periphery, *E* is energy, kJ/mol

Clusters

Suppose that we have removed hydrogen atoms from cyclohexane and added carbon atoms instead. In doing so we obtain clusters C_6C_6 with several types of carbon atoms. The carbon atoms of cyclohexane remain in the initial electronic state. The new added ones are reactive carbon atoms; they are connected with the initial carbon atoms by single or double bonds, being ionized to a different degree. Similar to cyclohexane, we can remove hydrogen atoms from benzol and add carbon atoms instead. In doing so we obtain also cluster C_6C_6 with several types of carbon atoms. We have calculated the optimized structures and energy of these compounds through the use of Avogadro package [46]. The results are presented in Fig. 3.

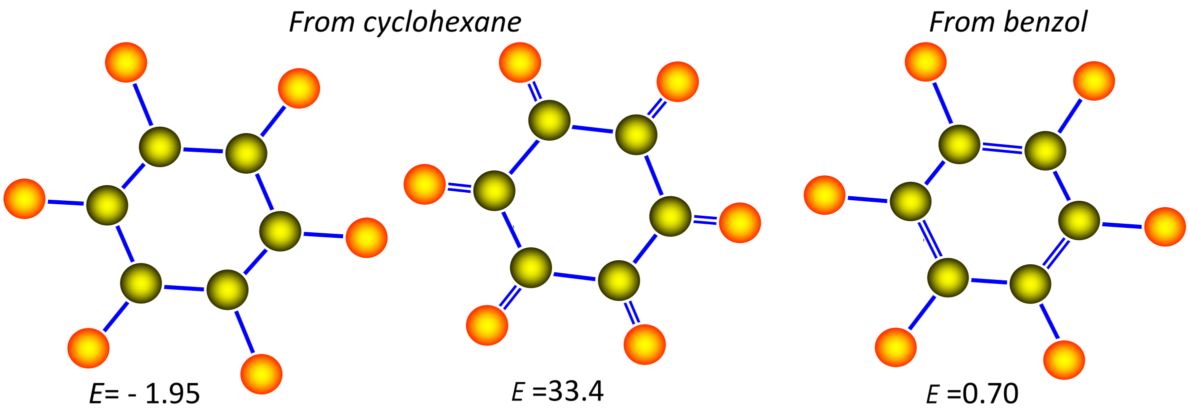

Fig. 3. Carbon clusters C_6C_6 obtained from cyclohexane and benzol, *E* is energy, kJ/mol

Folding and elementary fullerenes

One of the ways of further cluster evolution is folding and forming a hexa-angular prism (Fig. 4). Here and below, we use area-colored graphs because they gain a better understanding of the structures. In our case, six areas of the prisms are tetragons and they are grey painted, two areas are hexagons; they are yellow painted.

Consider cluster folding more closely. The folding produces a hexagonal prism of six-fold symmetry which may be thought over as an elementary fullerene. Several electronic configurations are presented in Fig. 4.

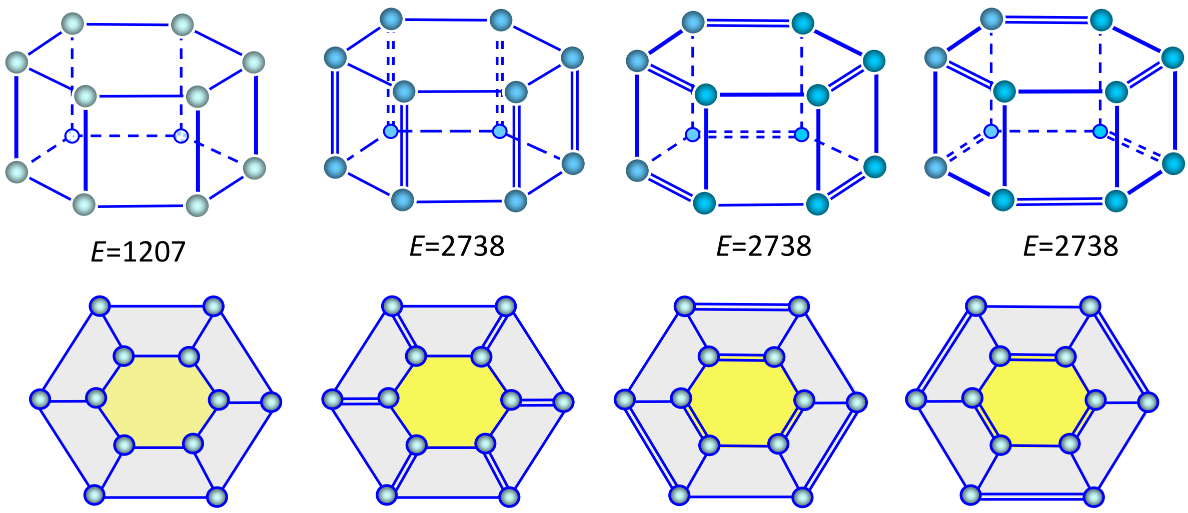

Fig. 4. Folding clusters into hexagonal prisms: structure and graphs; *E* is energy, kJ/mol

Fusion of prisms

From this point we will consider the prisms as elementary fullerenes. The fusion of two prisms with conserving their symmetry produces a fullerene which shape resembles a six-cornered barrel. The structure of several electronic isomers is shown in Fig. 5. To gain a better understanding of the fullerene structure, the graph areas are also painted in different colors: pentagons in goldish and hexagons in yellow as before.

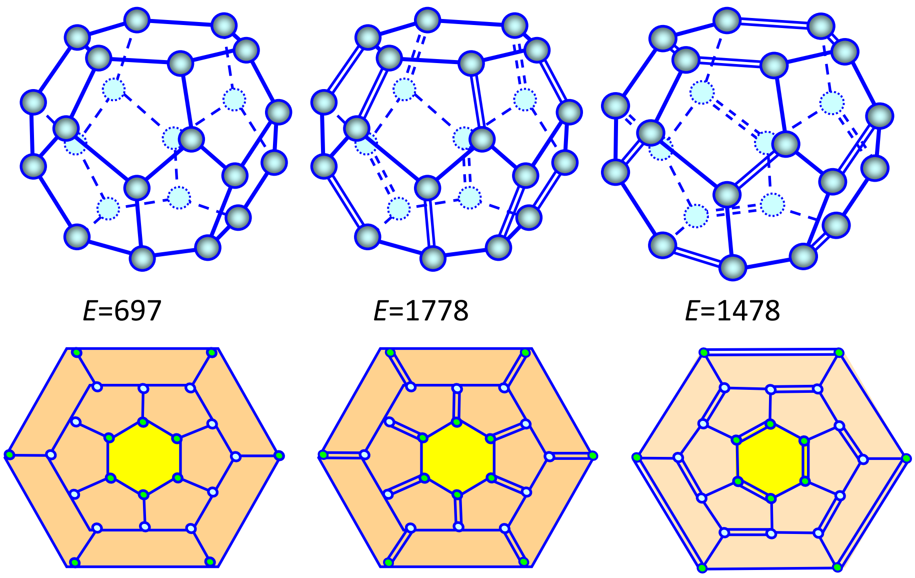

Fig. 5. Six-cornered barrel-shaped fullerene C_{24} as a result of prisms fusion; its graphs and energy *E*, kJ/mol

In its turn this barrel-shaped fullerene can continue the symmetry-conserving growth through the use of the above mentioned mechanism, i.e. joining with another hexagonal prism according to reaction $C_{24}+C_{12}$ (Fig. 6). The reaction is possible since the reacting structures have six-fold symmetry and therefore they are compatible with each other. The subsequent-fusion growth of the fullerene, C_{36}+C_{12} or C_{24}+C_{24}, is presented in Fig. 7. However further fusions create nanotubes.

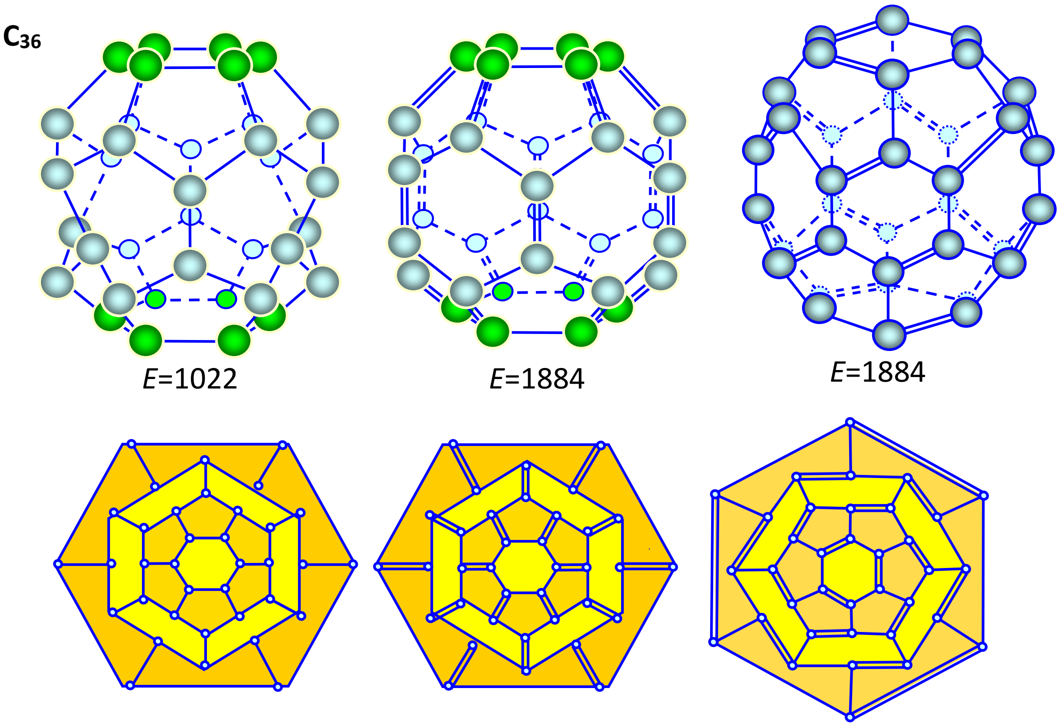

Fig. 6. Joining barrel-shaped fullerene C_{24} with prism C_{12}; structure, graphs; *E* is energy, kJ/mol

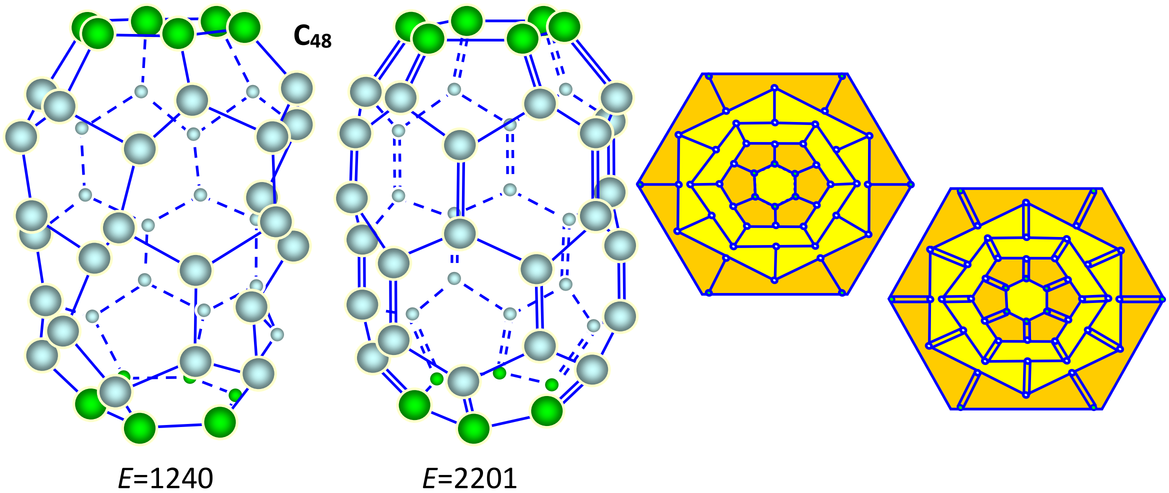

Fig. 7. Nanotube as joining two fullerenes C_{24}; structure and graphs; *E* is energy, kJ/mol

Cluster growth

Another way of looking at the gradual evolution of the clusters is the growth of initial clusters by joining single carbon atoms or carbon dimers. The complexes formed then transform into half-fullerenes (cupolas) conserving the symmetry of clusters [36].

Graphite

One additional comment is necessary for the six-fold-symmetry clusters. "Carbon atoms in graphite are arranged in plane paralleled layers which are slightly connected with each other. In each layer each carbon atom is bounded with three others by one double and two single bonds. A plane configuration of these bonds defines a plane structure of the entire layer. In reality all the three bonds are equivalent and valent angles are equal to 120°, since a double bond can occupy any of three possible positions around a carbon atom. This leads to indefinitely high number of different resonant structures of the layer (Fig. 8). Such description is equivalent to another, when an electron pair of each double bond displaces into a delocalized orbital enveloping the entire layer [49]. However, this does not influence on the geometry of a molecule which is dictated by the plane arrangement of three localized single bonds; the bonds being around each carbon atom". We assume that this phenomenon is referred to fullerenes too. In the following, we will use this fact in producing input data for calculations.

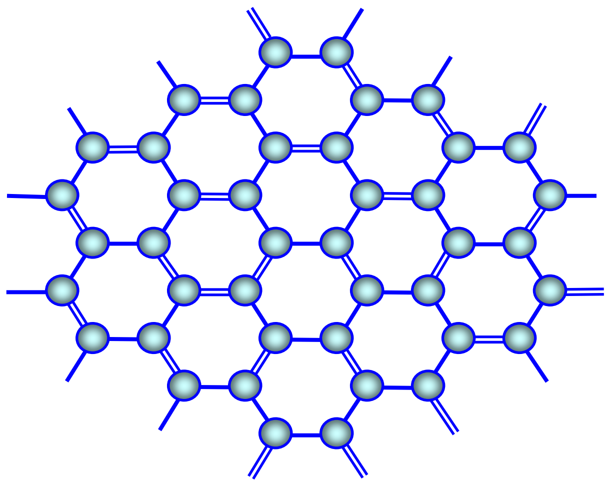

Fig. 8. One of possible resonant structures for a carbon-layer fragment in graphite. Based on [49]

Gaudi cupolas

They can be obtained by joining single carbon atoms to clusters C_6C_6 shown in Fig. 3. The result is presented in Fig. 9. From the figure it is seen that the cupolas have one and the same base of six atoms; they can combine with each other creating a new fullerene of six-fold symmetry. Reaction $C_{18}+C_{18}$ is equivalent to reaction $C_{24}+C_{12}$ considered above and has just the same result. The fullerene obtained is shown in Fig. 6.

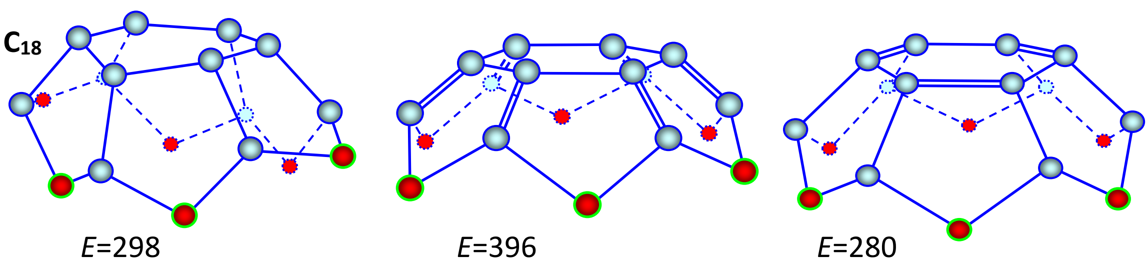

Fig. 9. Gaudi cupolas of six-fold symmetry: structure, *E* is energy, kJ/mol

Graphene fragments

Another way of looking at gradual evolution of the clusters C_6C_6 is the growth of initial clusters by joining carbon dimers, with producing graphene fragments conserving six-fold symmetry (Fig. 10).

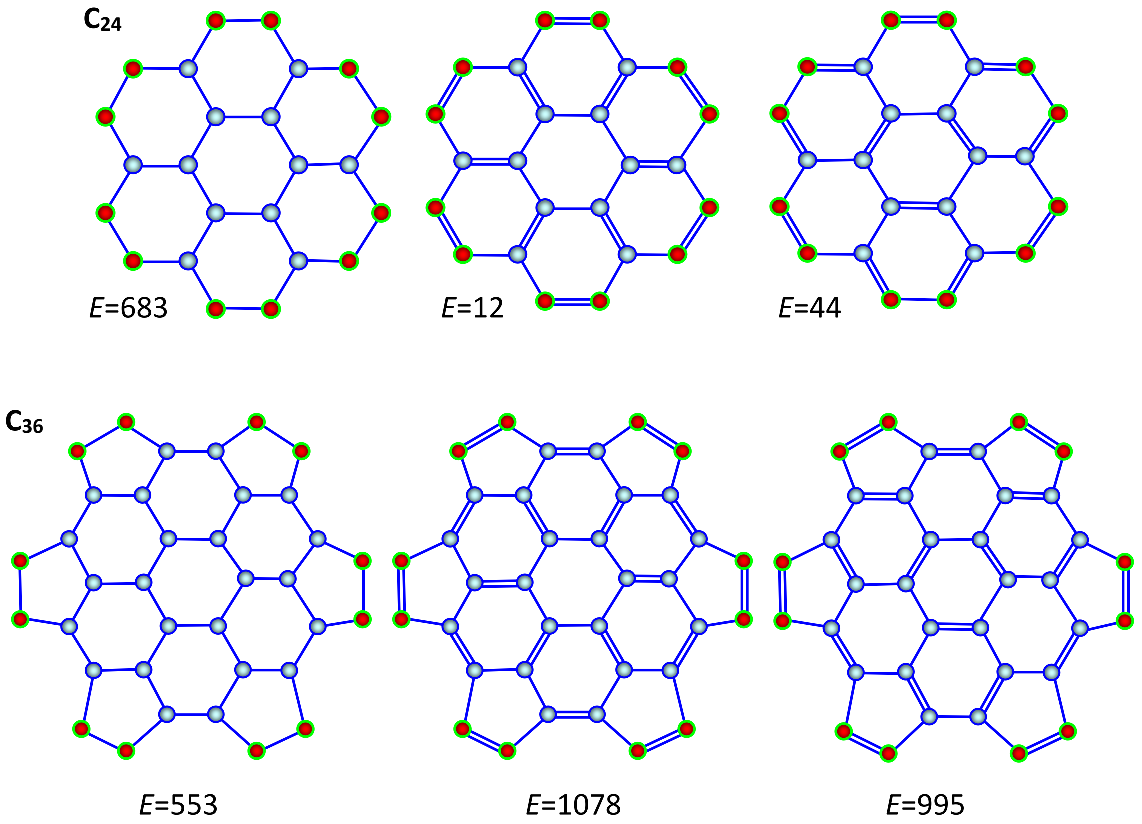

Fig. 10. Graphene fragments of six-fold symmetry: structure, *E* is energy, kJ/mol

Fuller cupolas

Beginning with C_{36} the graphene fragments contain pentagons. As a result of further growth transforms the plane surface into a curved one and the graphene fragments begin to grow as Fuller cupola (Fig. 11). From the figure it is seen that all the cupolas have one and the same base of twelve atoms; therefore, they can combine with each other creating new fullerenes.

Basic perfect and intermediate imperfect fullerenes

According to the periodic system of fullerenes [35,36], there are two main types of fullerenes; the basic perfect ones and intermediate imperfect ones. The basic perfect fullerenes have ideal structure and common symmetry. The intermediate imperfect fullerenes have extra carbon dimers. By analogy with crystal physics, we have assumed that these extra dimers play the role of defects which violate the common symmetry and create local imperfections. However, for defect crystals the long-range-order is observed experimentally. In order to underline this peculiarity, such long-range order is referred to as the topological long-range one [50]. Using analogous terminology, we have defined the imperfect fullerenes, which conserve the main axis of common symmetry, as having topological symmetry.

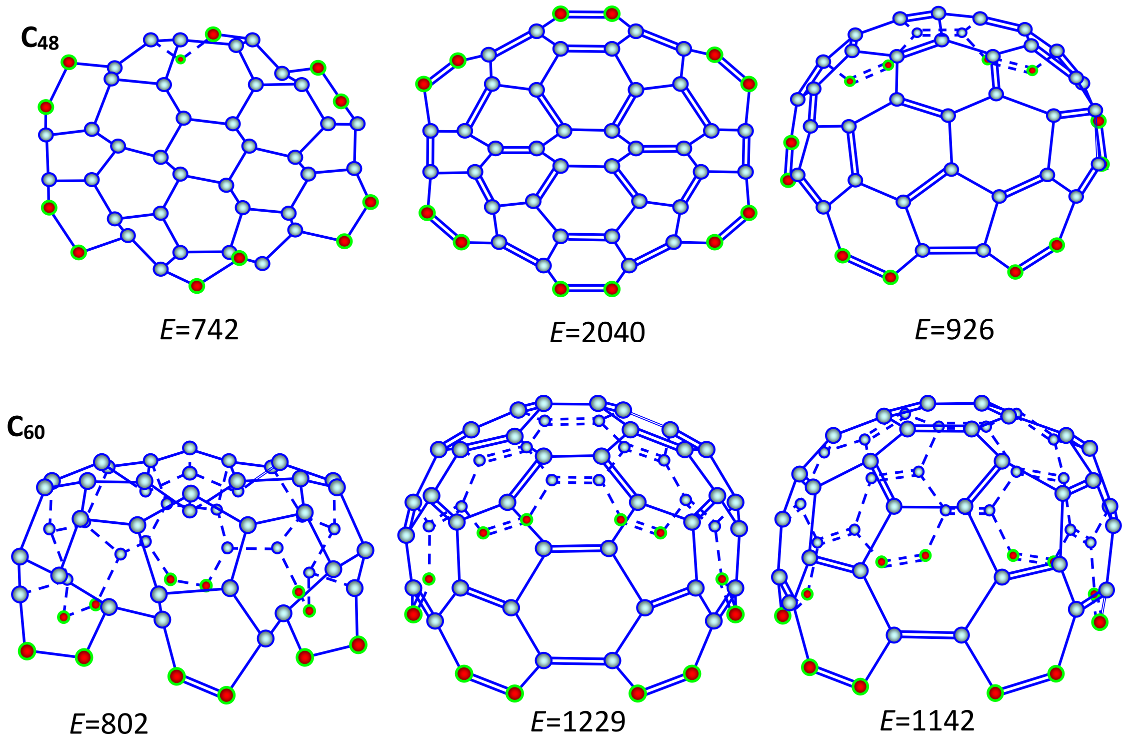

Fig. 11. Fuller cupolas of six-fold symmetry: structure, *E* is energy, kJ/mol

Perfect fullerenes

According to the first issue of periodic system of fullerenes in 2017 [36] there are the following basic perfect fullerenes and nanotubes of six-fold common symmetry: C_{36}, C_{48}, C_{60}, C_{72}, C_{84}, C_{96} and C_{108}. In 2018, we enlarged the system from above adding series Δn=2 and 4 [36]. Series Δn=2 contains the elementary fullerenes of similar shape (prisms) but having different symmetries. Series Δn=4 contains the barrel-shape fullerenes of different symmetries. As a result, the column of six-fold-symmetry fullerenes incorporated two new perfect fullerenes, C_{12} and C_{24}. Consider all these fullerenes in more detail.

Elementary fullerene C_{12}. It is a hexahedral right−angle prism (Fig. 4). Its generation was discussed above.

Barrel-shaped fullerene C_{24}. It is a barrel-shaped fullerene (Fig. 5). Other features are considered above,

Fullerene C_{36}. The fullerene was obtained by fusion barrel-shaped fullerene C_{24} with prism C_{12} (Fig. 6). There are other ways of producing this fullerene (Fig. 12), e.g. fusion of two cupolas C_{18}, or fusion of two graphene fragments C_{12} and C_{24}.

At first two molecules C_{18}, or C_{12} and C_{24}, are moving towards each other (Fig. 12(a,d)). Then the boundary atoms (dark-red) interact with each other producing a compound (Fig. 12(b,e)). During this process new covalent bonds (heavy red lines) are generated, distorted polyhedrons are formed; they relaxing into perfect polyhedrons (Figs. 12(c,f)).

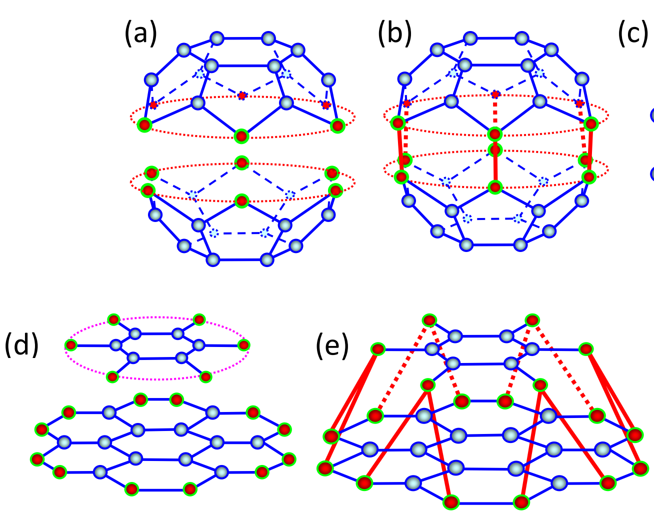

Fig. 12. C_{36} as joining two cupolas C_{18} (a,d) and two graphene fragments C_{12} (b,e) and C_{24} (c,f)

In the first case one obtains just the same fullerene as is shown in Fig. 6, having the same energy. In the second case we have an isomer of this fullerene (Fig. 13). The isomer obtained consists of six tetragons and fourteen hexagons; it contains twenty four faces. One may name this perfect isomer, having six-fold symmetry, a truncated six-angular bipyramid.

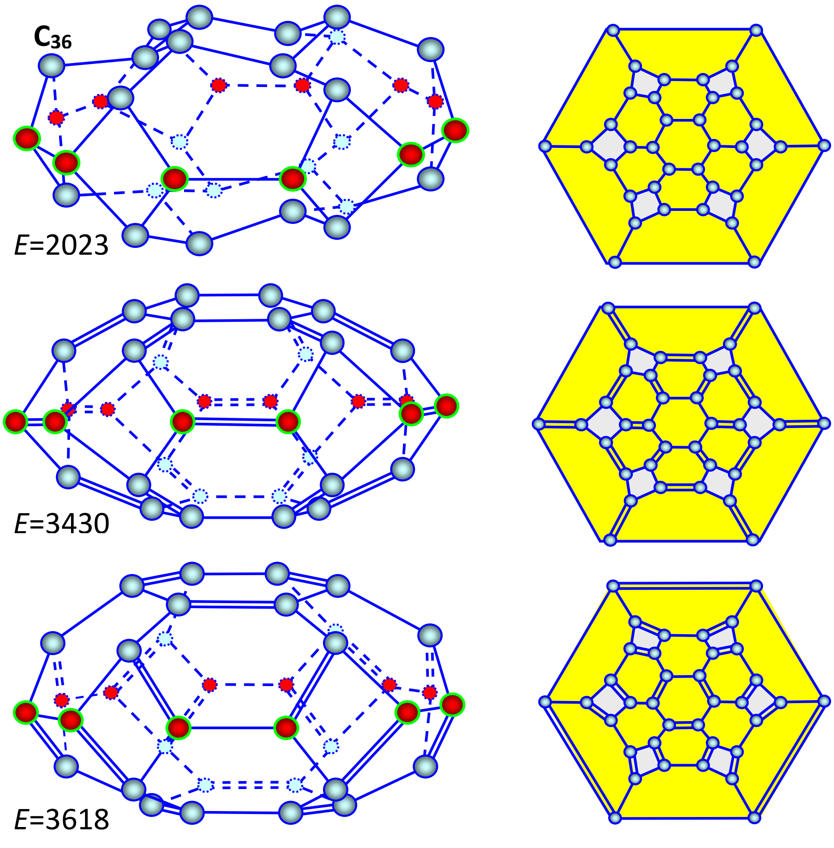

Fig. 13. Truncated six-angular bipyramid C_{36} and its graphs; *E* is energy, kJ/mol

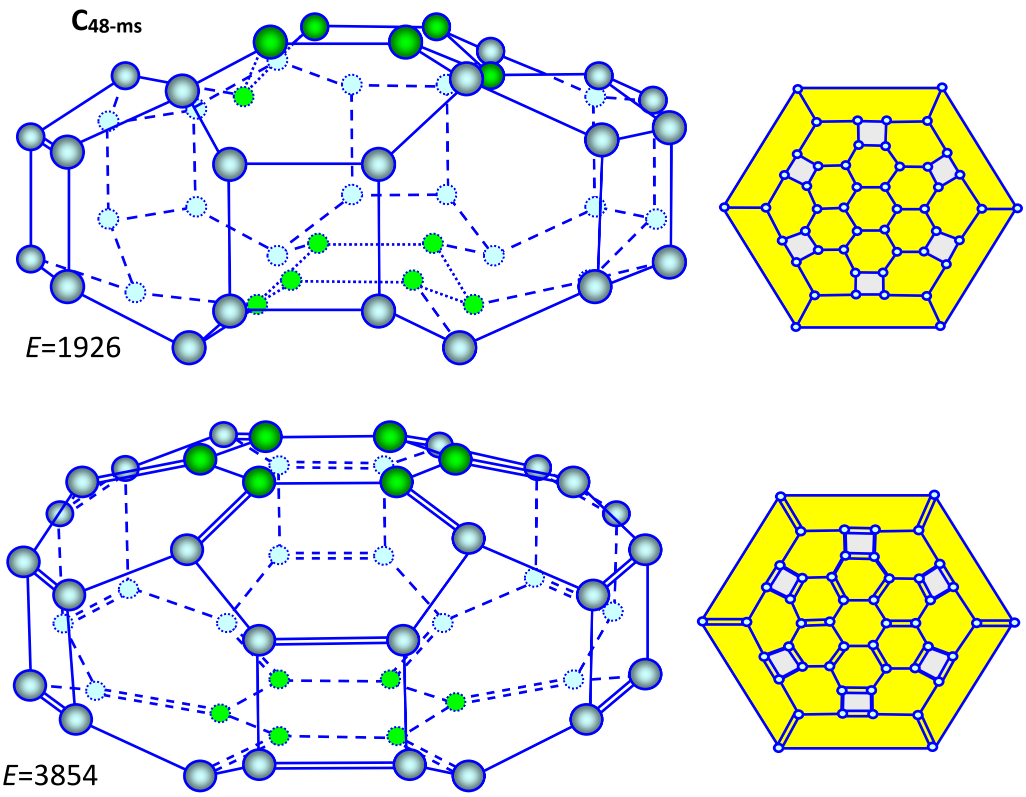

Fig. 14. Fullerene C_{48} as a result of joining two cupolas C_{24} of six-fold symmetry: the mirror symmetry fusion, structure and graphs; *E* is energy, kJ/mol

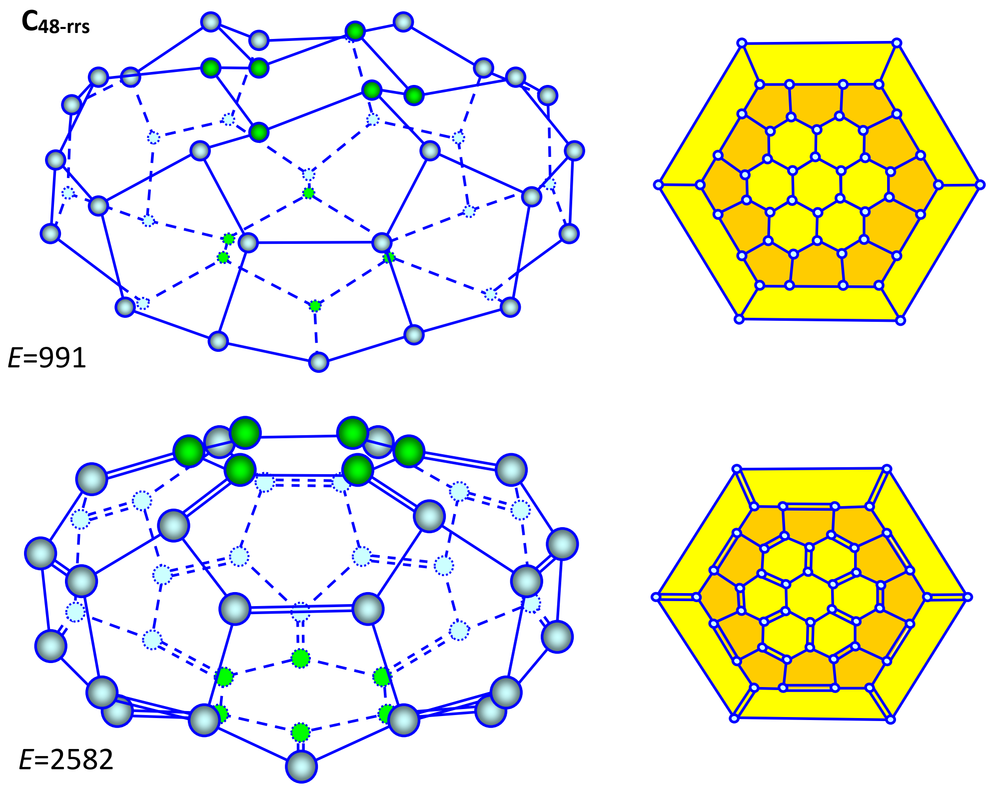

Fig. 15. Fullerene C_{48} as a result of fusion of two cupolas C_{24} having six-fold symmetry: rotation-reflection symmetry joining: structure, graphs, *E* is energy, kJ/mol

Fullerene C_{48}. One can design two isomers of six-fold-symmetry fullerene by two different ways of joining two cupolas C_{24}. It should be emphasized that there are two modes of cupola joining: mirror symmetry and rotation-reflection one. In the first case the lower cupola is a mirror copy of the upper one. The fullerene obtained consists of six tetragons and twenty hexagons (Fig. 14); it has twenty-six faces. It is a tetra$_6$-hexa$_{20}$ polyhedron. In the second case the lower cupola is a rotatory reflection of the upper one. The fullerene obtained contains twelve pentagons and ten hexagons, the number of faces being the same (Fig. 15). It is a penta$_{12}$-hexa$_{14}$ polyhedron. Its energy is less than that of the first fullerene.

Fullerene C_{60}. We have designed this fullerene of six-fold symmetry by fusion of a graphene fragment C_{24} and a cupola C_{36} (Fig. 16). The fullerene obtained contains six pairs of two adjacent pentagons and twenty hexagons (Fig. 17). It is a penta$_{12}$-hexa$_{20}$ polyhedron of six-fold symmetry.

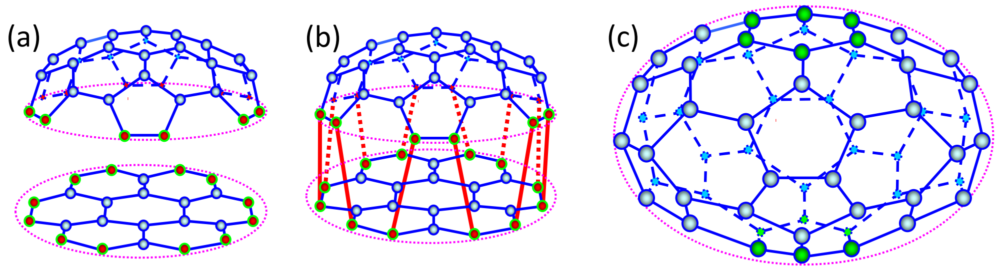

Fig. 16. Scheme of joining graphene fragment C_{24} and cupola C_{36}: (a) separate carbon components; (b) intermediate compounds; (c) polyhedron obtained

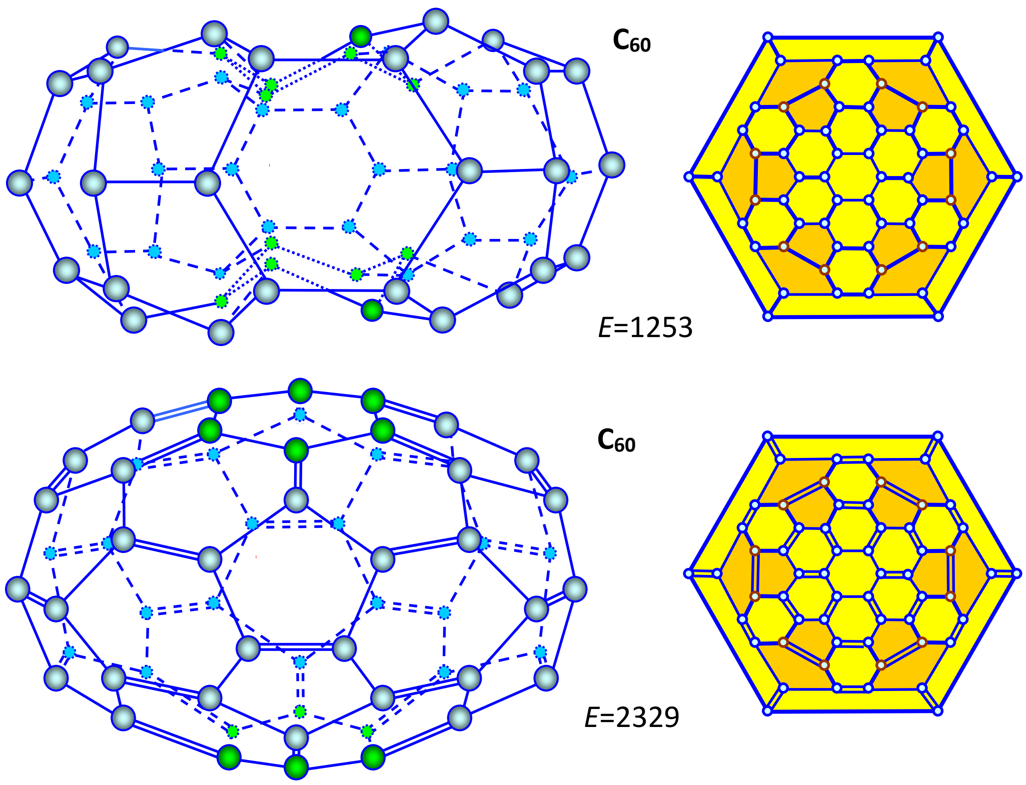

Fig. 17. Structure, energy and graphs of fullerene C_{60} with single and double bonds

Fullerene C_{72}. One can design this fullerene of six-fold symmetry by fusion of two cupolas C_{36} what is shown in Figs. 18–20. It should be emphasized that one of the graphs is reverse.

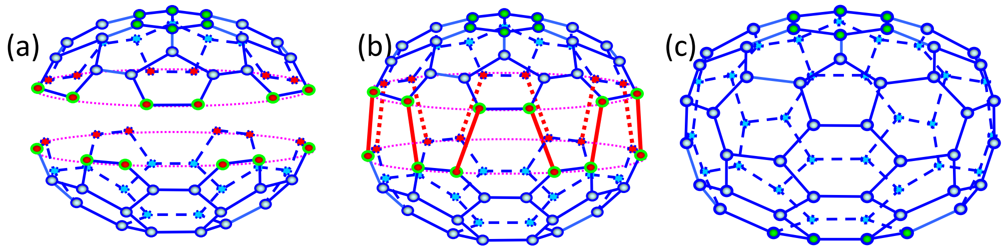

Fig. 18. Scheme of joining two half-fullerenes C_{36}:
(a) separate carbon cupolas; (b) intermediate compound; (c) polyhedron C_{72} obtained

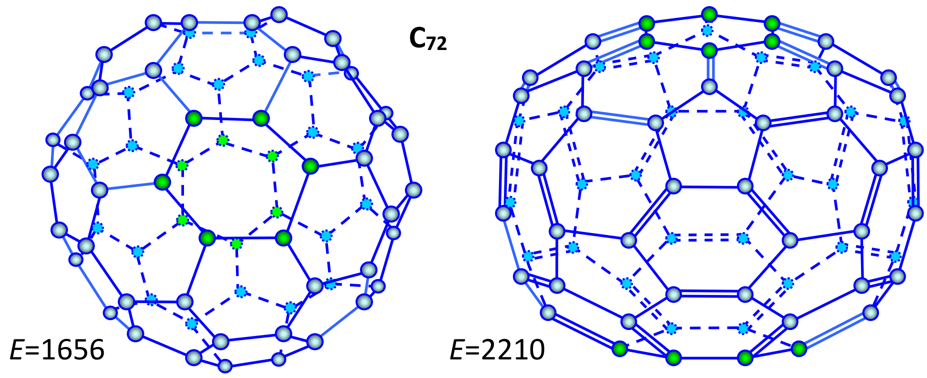

Fig. 19. Structure and energy *E* (kJ/mol) of fullerene C_{72}

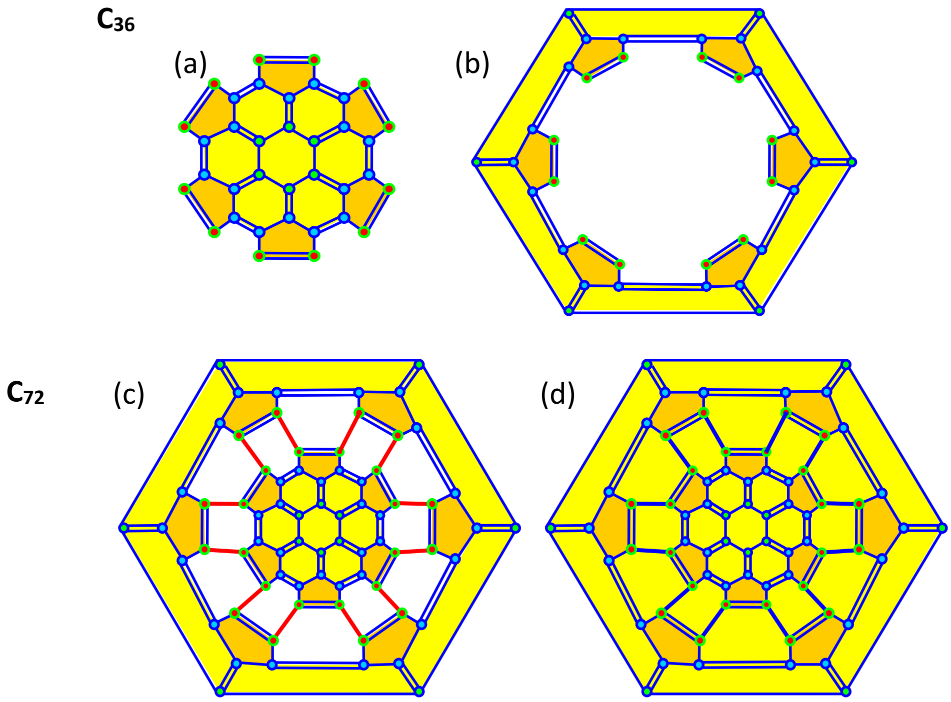

Fig. 20. Fusion reactions of cupolas C_{36} as graph embedding: (a) graph of cupola C_{36}; (b) reciprocal graph of cupola C_{36}; (c) graph embedding; (d) graph of fullerene C_{72}

Fullerene C_{84}. In a similar manner it is possible to construct this fullerene of six-fold symmetry by fusion of cupolas C_{36} and C_{48} what is shown in Figs. 21–23.

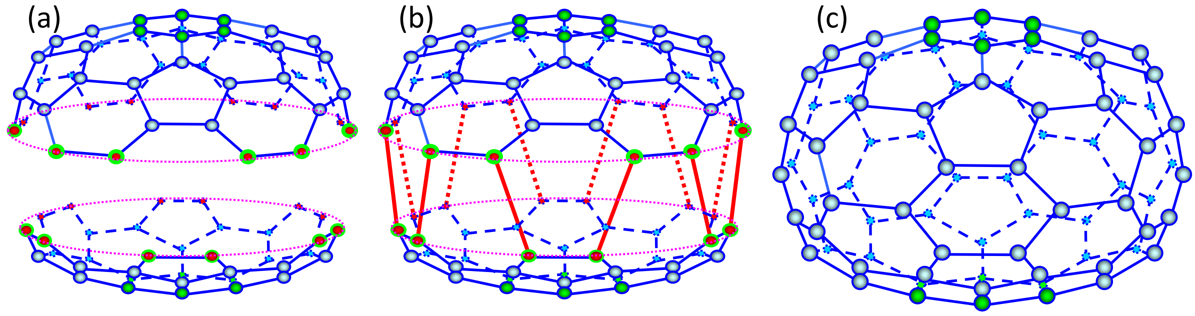

Fig. 21. Joining two half-fullerenes C_{36} and C_{48}, and fullerene C_{84} obtained: (a) separate carbon cupolas; (b) intermediate compound; (c) polyhedron after relaxation

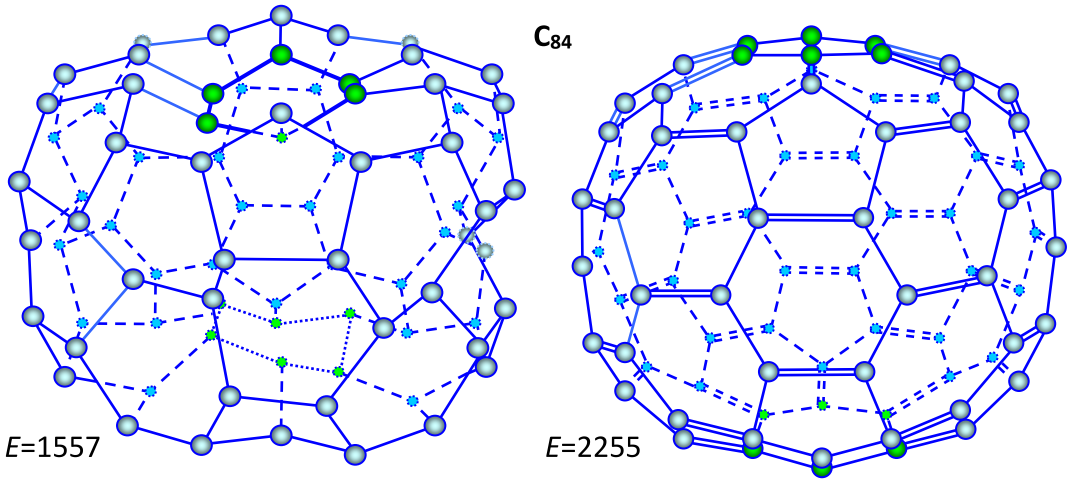

Fig. 22. Structure and energy *E* (kJ/mol) of fullerene C_{84}

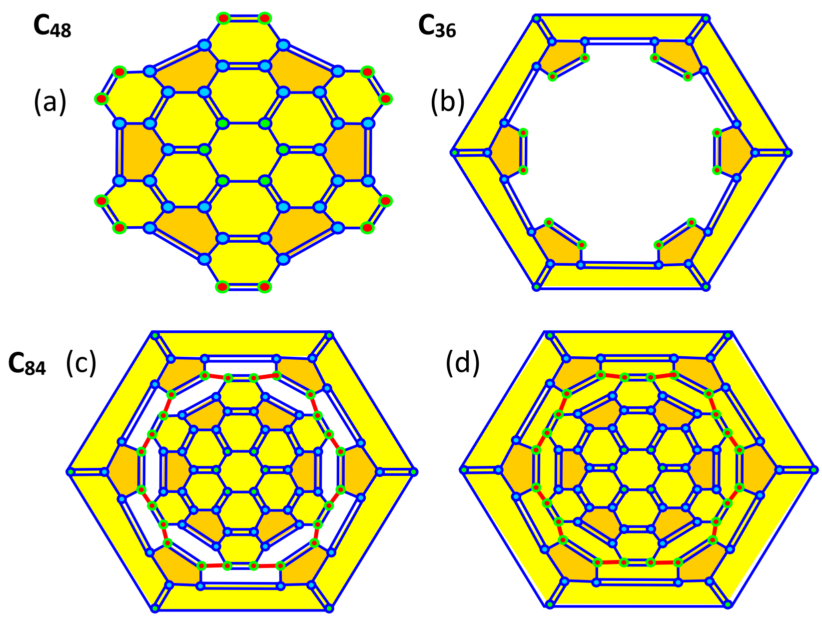

Fig. 23. Fusion reactions of cupolas C_{36} and C_{48} as graph embedding: (a) graph of cupola C_{48}; (b) reciprocal graph of cupola C_{36}; (c) graph embedding; (d) graph of fullerene C_{84}

Nanotube C_{96}. The next perfect fullerene is a nanotube. One can design this nanotube of six-fold symmetry by fusion of two cupolas C_{48} what is shown in Figs. 24–26. Let's analyze these figures. The question arises: what we have obtained, fullerenes or nanotubes? Where is the boundary between fullerenes and nanotubes? An intuitive idea says that a fullerene is a spheroid, whereas a nanotube with open ends is a cylinder and a nanotube with closed ends is a cylinder with two hemispheres. Each spheroid can be divided into three parts; two hemispheres. If the height of cylinder is less than the height of two hemispheres, we assume that it is a fullerene. On the contrary we have a nanotube. In its turn the cylinder height is defined by the number of adjacent hexagons. To form a cylinder one needs to have along its height at least one hexagon which is not connected with pentagons. Referring to the graphs shown, we admit that the nanotubes begin with the structure C_{96}.

It is worth noting that both fullerenes and a nanotube have one and the same number of pentagons, namely twelve, being equal to a double degree of symmetry.

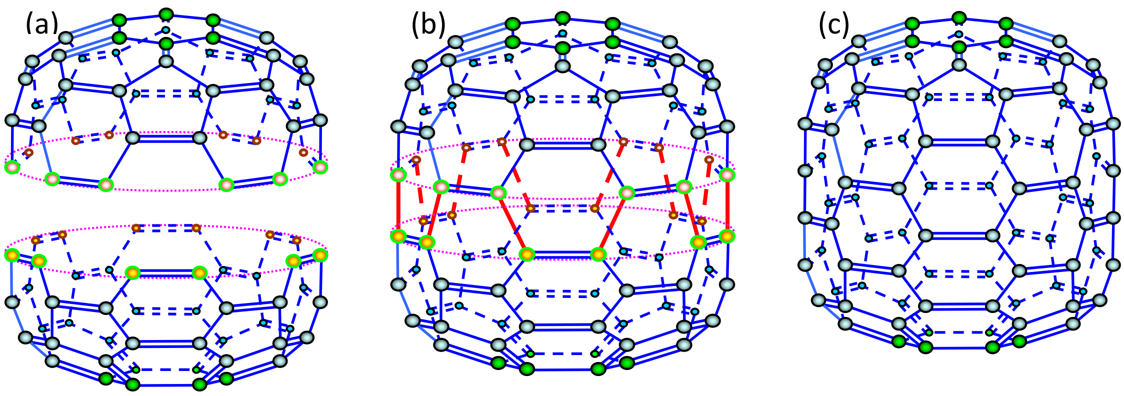

Fig. 24. Rotation-reflection-symmetry joining of two cupolas C_{48}: (a) separate cupolas C_{48}; (b) intermediate compound; (c) nanotube C_{96} obtained

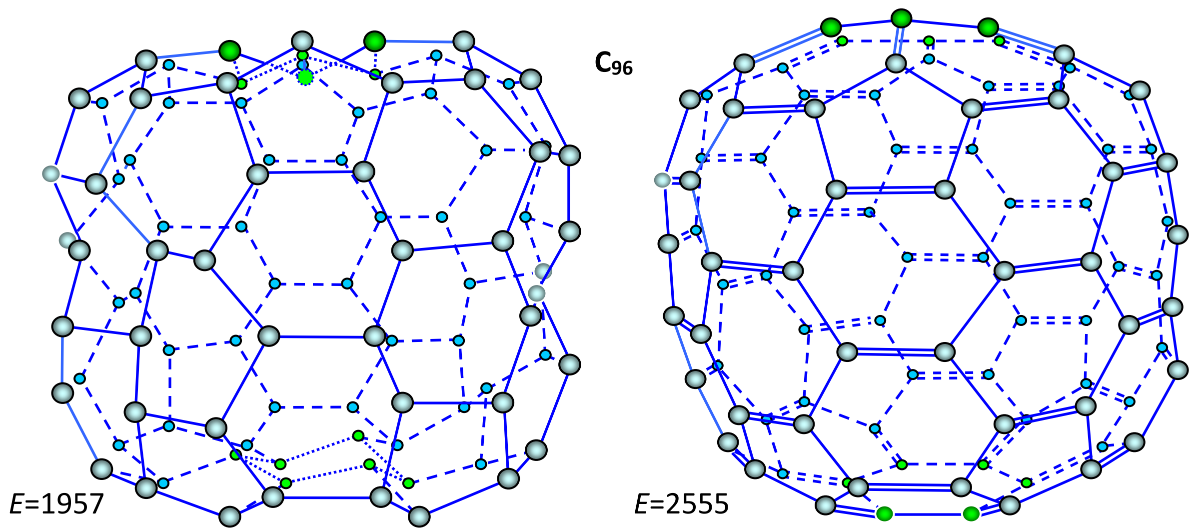

Fig. 25. Structure and energy *E* (kJ/mol) of nanotube C_{96}

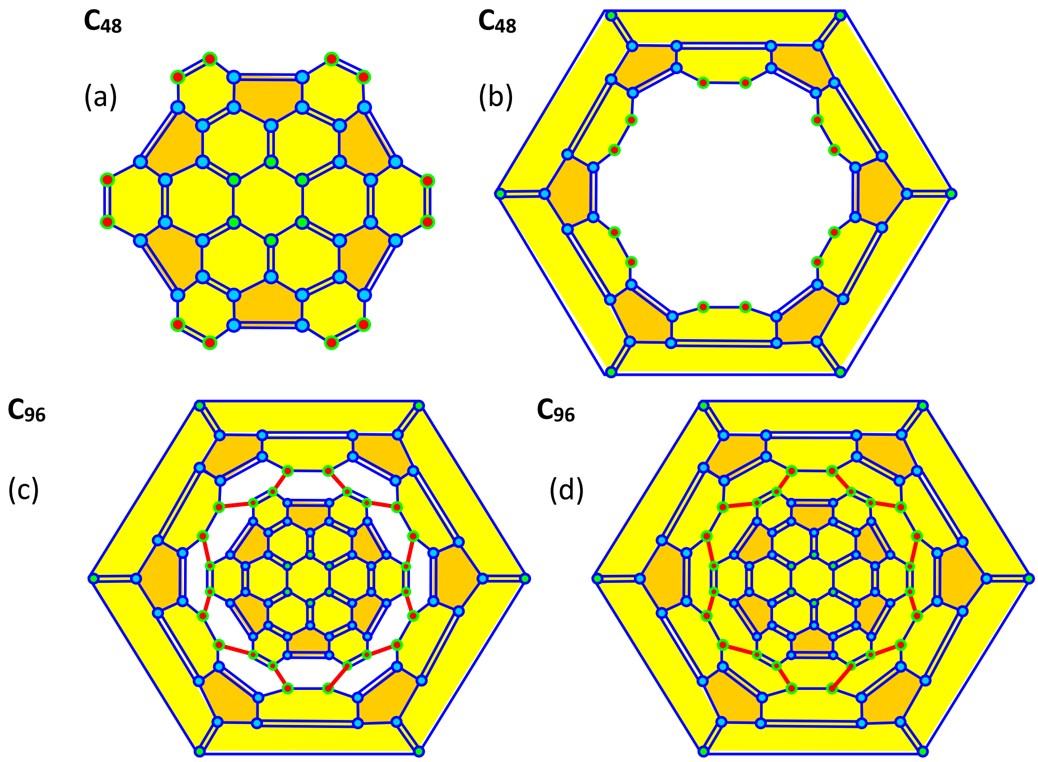

Fig. 26. Fusion reactions of cupolas C_{48} as graph embedding: (a) graph of cupola C_{48}; (b) reciprocal graph of cupola C_{48}; (c) graph embedding; (d) graph of nanotube C_{96}

Summary and Discussion

We have studied possible ways of generation and growing the fullerenes having six-fold symmetry. Beginning with cyclohexane C_6H_{12}, benzol C_6H_6 and clusters C_6C_6, we obtained at first elementary fullerenes C_{12} and mini-fullerenes C_{24}, and then the fullerenes from C_{36} to C_{96}, including a nanotube. We have calculated the energies of the possible fullerenes.

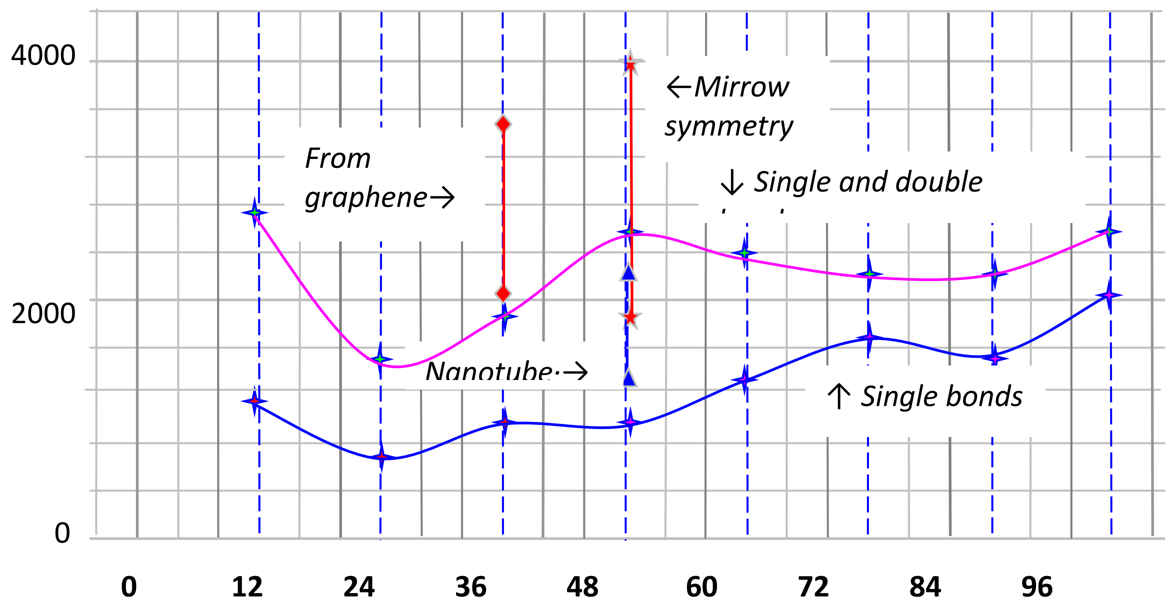

Fig. 27. Energy *E* of fullerenes in kJ/mol as a function of fullerene size and shape

In Table 1, the energies of fullerenes are presented, for fullerenes with single bonds only (above) and single and double bonds (below). The energies are also shown in Fig. 27.

Table 1. Energy of fullerenes in kJ/mol as a function of fullerene size and shape

C_{12}	C_{24}	C_{36}	$C_{36graph}$	$C_{48\ rrs}$	$C_{48\ ms}$	C_{48tube}	C_{60}	C_{72}	C_{84}	C_{96tube}
1207	697	1022	(2023)	991	(1926)	(1240)	1253	1656	1557	1957
2738	1478	1844	(3430)	2582	(3854)	(2201)	2329	2210	2255	2555

Continuity and discontinuity

These notions are connected with the Ionic and Pythagorean schools of philosophy (VI-IV century B.C.) [51]. Plato of Athens (Πλατων, 427 B.C.) has tried to combine both notions, putting five forms of matter (fire, air, earth, water, ether) into consistency to five regular polyhedra (tetrahedron, octahedron, cube, icosahedron, dodecahedron). According to Aristotle every thing is the unity of matter and form (*η ϋλη καί τό είδος*); the form being an active element produces movement [51].

In mathematics there are such notions as curvature, tensor of curvature [52]. The curvature is defined as the quantity which characterizes a deviation of a surface from a plane at a given point. The latter is defined in the following manner. Through the normal at a given point of surface all the possible planes are drawn. The sections of surface by these planes are called normal sections, the curvatures of normal sections being normal curvatures of the surface at a given point. Maximum and minimum curvatures are called principal curvatures. Their combinations give Gauss and average curvatures which are used for analysis of the surface curvature.

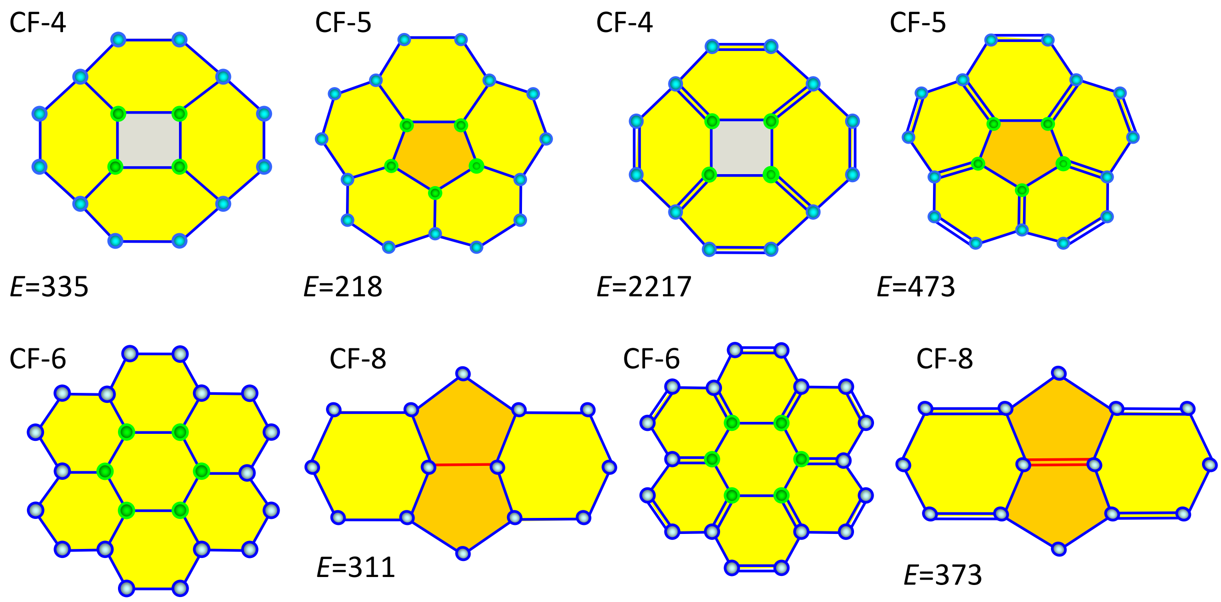

Fig. 28. Curvature fragments of fullerenes

Curvature of fullerenes

We will follow to Aristotle trying finding the forms of fullerenes, which define its surface curvature. In other words, we will search first of all “fragments of curvature”, but not a curvature value. Further we will use the following notions: curvature as continuity property and curvature fragments as discontinuity. Analysis of the fullerene structures shown before allows us to separate the following curvature fragments (Fig. 28). It should be emphasized that an isolated fragment CF-6 does not creates curvature; it becomes a curvature fragment under the influence of surroundings.

Different curvature fragments have their own symmetry. We name a center of symmetry "curvature concentration center". The study of its arrangement in different fullerenes has given the following picture (Fig. 29). The figures resemble rings (C_{12}, C_{48ms}), zig-zag ring (C_{48rrs}), prisms (C_{60}, C_{84}), Archimedes antiprisms (C_{24}, C_{72}) and a biantiprism (C_{36}).

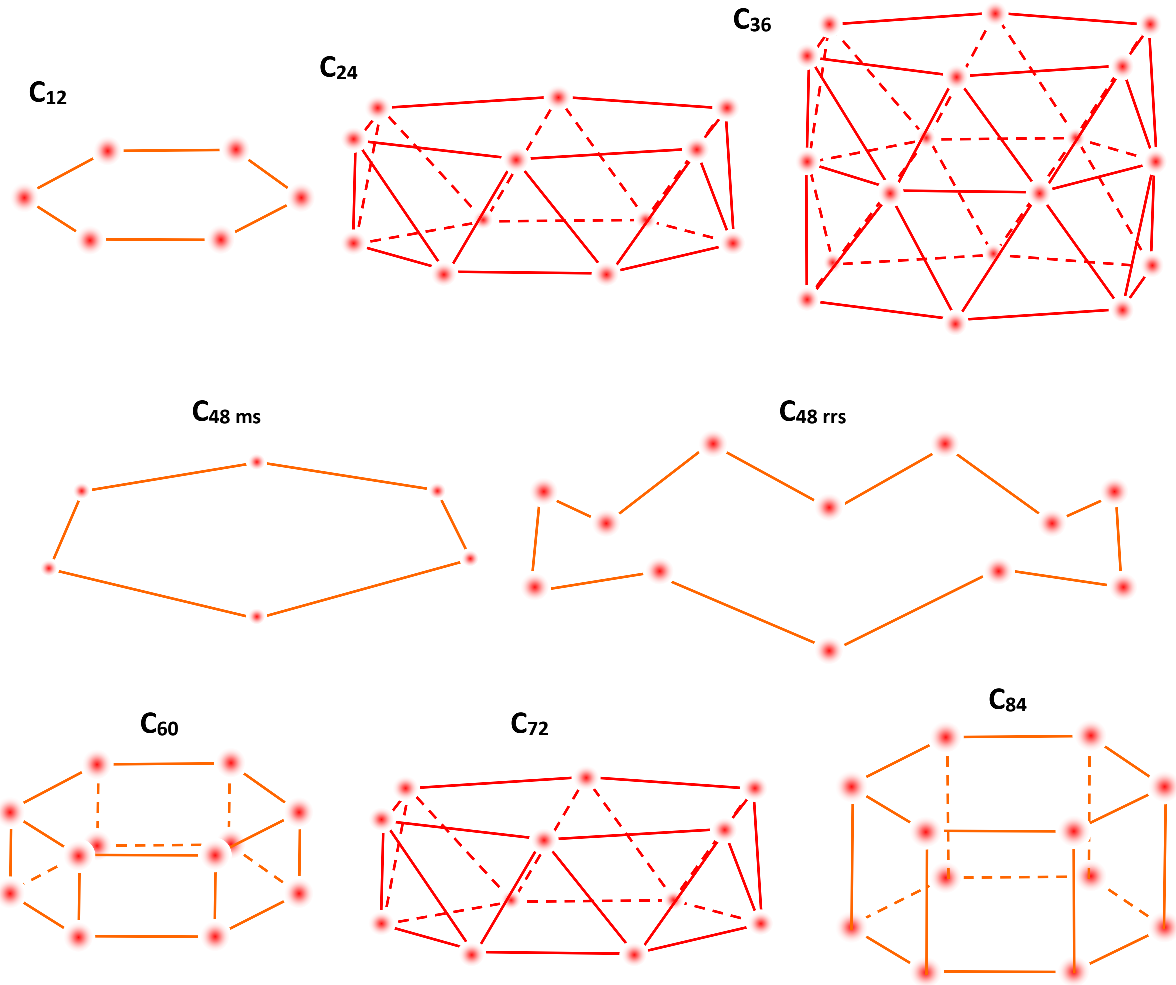

Fig. 29. Geometry of curvature concentration centers (CCC)

Curvature, strain and stress concentration

In mathematics [52], the surface is introduced as a bit of a plane subjected to continuous deformations (tension, compression, bending). In its turn, curvature is defined as the quantity which characterizes a deviation of a surface from a plane at a given point. In mechanics [53] for characteristics of deformation one introduces tensor of strain, which diagonal elements characterize volume change; non-diagonal elements show the change of a form. If stress is a function of strain in each point of continuum, such continuum is said to be an elastic body. In a simple case, the function which connects strain and stress is Hooke's law.

In mechanical engineering [54], the problem of weakening stress concentration is very important. Unloading local stress can be obtained through the use of a correct construction, in particular, a construction which consists of frames. Frame bridges were already used by Romans. An advance of the network of railway lines has led to widespread use of frame bridges and, as a consequence, to development of the methods of their designing. The first three farms are shown in Figs. 30–32. The problem was to design a farm in which the stress in farm rods would be minimum when a bridge is in work; the knots of systems being the centers of stress concentration.

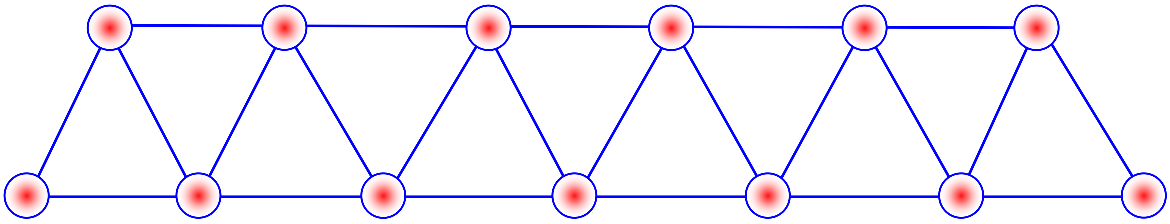

Fig. 30. Triangle lattice of Warren's frame (UK, 1846). Based on [54]

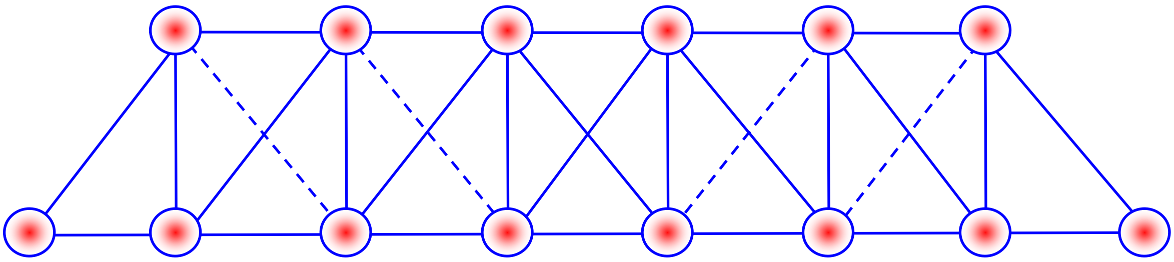

Fig. 31. Whipple's frame (USA, 1852). Based on [54]

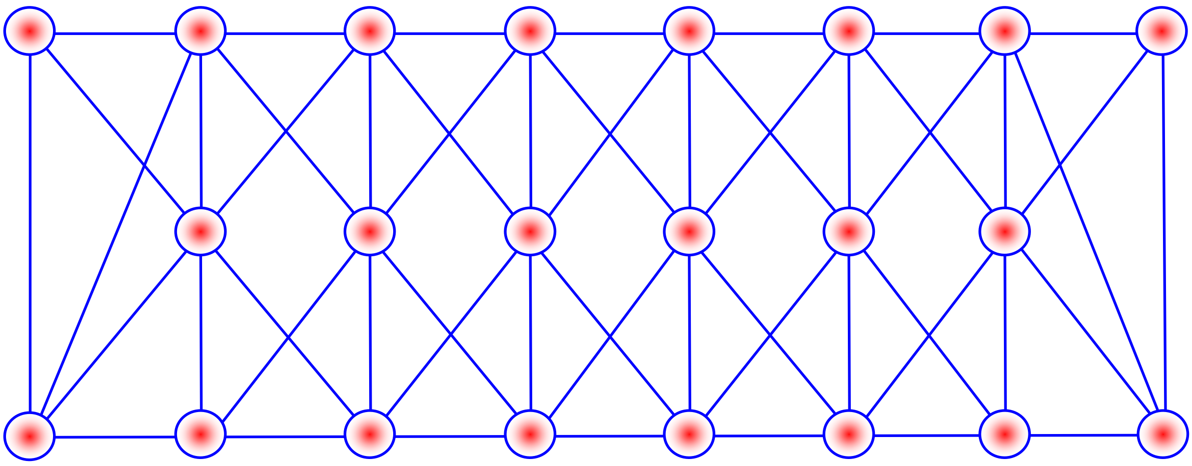

Fig. 32. Zhuravskiy's frame (Russia, 1850). Based on [54]

Studying cyclic molecules [36], we developed a procedure which shows their side view. It can be named the *method of cutting and unrolling*. The procedure allowed us to discover a new phenomenon: hidden symmetry of molecules. It is interesting to note that if to act in a similar manner, i.e. to cut the prisms shown in Fig. 29 along a vertical line going through one of its curvature concentration points, we obtain the figures resembling farm bridges.

Based on this similarity, we assume that in fullerenes the curvature concentration centers are strain centers and since strain is connected with stress, they are centers of stress concentration. Therefore, the energy of a fullerene consists of two parts: chemical energy of formation and strain energy of construction.

Now we are able to understand and explain the dependence of fullerene energy on size and form (Fig. 27). Fullerenes with single bonds relax through the transformation of plane hexagons into chair conformation and so their energy has incorporated only a small part of strain energy. As a result, the dependence of fullerene energy on size and shape is almost monotonic. Fullerenes with single and double bonds are rigid constructions, and here the contribution of strain energy is high. The fullerene shape is a result of self-organization and here there are possible several types of curvature. The most stress state is characteristic for fullerenes which curvature concentration centers (CCC) are plane hexagons, the least refers to CCC in the form of antiprisms which highly resemble farm bridges. The other fullerenes have intermediate strain energy.

Future investigations

We assume that first of all it is necessary to find the curvature concentration centers. In doing so, we gain the arrangement of stress concentration, can apply the elasticity theory not only to the fullerenes (this task is very cumbersome) but to the polyhedrons of curvature centers (the task is easier). Moreover, the energy of fullerenes can be considered not only as a global quantity, but as a surface distribution. Since the CCC polyhedrons resemble crystals, and the crystals are studied for years, we can use this knowledge for understanding such processes as, e.g. sublimation, fracture of fullerenes. As a result, we would be able to gain more profound insight into their nature.

References

1. Kroto HW, Hearth JR, O'Brien SC, Curl RF. Smalley RE, C60: Buckminsterfullerene. *Nature.* 1985;318: 162–163.
2. Kroto HW, The stability of the fullerenes Cn, with n=24, 28, 32, 36, 60, 60 and 70. *Nature.* 1987;329: 529–531.
3. Manolopoulos DE, May JC, Down SE. Theoretical studies of the fullerenes: C34 to C70. *Chem. Phys. Lett.* 1991;181(1–2): 105–111.
4. Zhang BL, Wang CZ, Ho KM, Xu CH, Chan CT. The geometry of small fullerene cages: C20 to C70. *J. Chem. Phys.* 1992;97(7): 5007–5011.
5. Kerner R. Nucleation and growth of fullerenes. *Comp. Mater. Sci.* 1994;2: 500–508.
6. Kerner R, Bennemann RH. Theory for the growth of fullerenes. *Fullerene Sci. Tech.* 1996;4(6): 1279–1285.
7. Goroff NS. Mechanism of fullerene formation. *Acc. Chem. Res.* 1996;29(2): 77–83.
8. Piskoti C, Yarger J, Zettl A. C36, a new carbon solid. *Nature.* 1998;393: 771–774.
9. Grossman JC, Cote M, Louie SG, Cohen ML. Electronic and structural properties of molecular C36. *Chem. Phys. Lett.* 1998;284(5–6): 344–349.
10. Jagadeesh MN, Chandrasekhar J. Computational studies on C36 and its dimer. *Chem. Phys. Lett.* 1999;305(5–6): 298–349.
11. Prinzbach H, Weiler A, Landenberger P, Wahl F, Wörth J, Scott LT, Gelmont M, Olevano D, Issendorf BV, Gas-phase production and photoelectron spectroscopy of the smallest fullerene C20. *Nature.* 2000;407: 60–63.

12. Paulus B, Electronic and structural properties of the cage-like molecules C20 to C36. *Phys. Chem. Chem. Phys.* 2003;5(16): 3364–3367.
13. Pattanayak J, Kar T, Scheiner S, Substitution patterns in mono BN-fullerenes: Cn (n = 20, 24, 28, 32, 36 and 40. *J. Phys. Chem. A.* 2004;108(38): 7681–7685.
14. Lu X, Chen Z, Curved pi-conjugation, aromaticity, and the related chemistry of small fullerenes (<C60) and single-walled carbon nanotubes. *Chem. Rev.* 2005;105: 3643–3696.
15. Khan SD, Ahmad S. Modelling of C2 addition rout to the formation of C60. *Nanotechnology.* 2006;17(18): 4654.
16. Malolepsza E, Witek HA, Irle S. Comparison of geometric, electronic, and vibrational fullerenes C20–C36. *J. Phys. Chem. A.* 2007;111: 6649–6657.
17. Yamaguchi Y, Colombo L, Growth of sp-sp^2 nanostructures in a carbon plasma. *Phys. Rev. B.* 2007;76: 134119.
18. Malolepsza E, Lee Y, Witek HA, Irle S, Lin C, Hsieh H, Comparison of geometric, electronic, and vibrational properties for all pentagon/hexagon-bearing isomers of fullerenes C38, C40, and C42. *Int. J. Quantum Chem.* 2009;109(9): 1999–2001.
19. Gan LH, Liu J, Hui Q, Shao SQ, Liu ZH, General geometrical rule for stability of carbon polyhedral. *Chem. Phys. Lett.* 2009(4–6);472: 224–227.
20. Lin F, Sørensen ES, Kallin C, Berlinsky AJ. C20, the smallest fullerene. In: Sattler KD. (ed.) *Handbook of Nanophysics. Clusters and Fullerenes.* CRC Press; 2010. p.29.
21. Chuvilin A, Kaiser U, Bichoutskaia E, Besley NA, Khlobystov AN. Direct transformation of grapheme to fullerene. *Nature Chem.* 2010;2: 450–453.
22. Gupta V, Graphene as intermediate phase in fullerene and carbon nanotube growth: a Young-Laplace surface-tension model. *Appl. Phys. Lett.* 2010;97(18): 181910.
23. Micelotta EL, Jones AP, Cami J, Peeters E. The formation of cosmic fullerenes from arophatic clusters. *Astrophys. J.* 2012;761(1): 35.
24. Deng SL, Xie SY, Huang RB, Zheng LS. The formation mechanism of fullerene. *Sci. Sinica Chim.* 2012;42: 1587–1597.
25. Irle S, Page AJ, Saha B, Wang Y, Chandrakumar KRS, Nishimoto Y, Qian HJ, Morokuma K, Atomistic mechanisms of carbon nanostructure self-assembly as predicted by nonequilibrium QM/MD simulations. In: Leszczynski J, Shukla MK. (Eds.) *Practical Aspects of Computational Chemistry II: An Overview of the Last Two Decades and Current Trends.* Springer; 2012.
26. Kharlamov A, Kharlamova G, Bondarenko M, Fomenko V. Joint synthesis of small carbon molecules (C3-C11), quasi-fullerenes (C40, C48, C52) and their hydrides. *Chem. Engng. Sci.* 2013;1(3): 32–40.
27. Zhen J, Castellanos P, Paardekooper DM. Laboratory formation of fullerenes from PAHs: top-down interstellar chemistry. *Astrophys. J. Lett.* 2014;797(2): L30.
28. Fujita J, Tachi M, Murakami K, Sakurai H, Morita Y, Higashibayashi S, Takeguchi M. Beam-induced graphitic carbon cage transformation from sumanene aggregates. *Appl. Phys. Lett.* 2014;104: 043107.
29. Xia K, Feng X, Tong Y, Wei GW, Persistent homology for the quantitative prediction of fullerene stability, *J. Comput. Chem.* 2015;36(6): 408-422.
30. Schwerdtfeger P, Wirz LN, Avery J. The topology of fullerenes. *WIREs Comput. Mol. Sci.* 2015;5(1): 96–145.
31. Jin Y, Perera A, Lotrich VF, Bartlett RJ. Couple cluster geometries and energies of C20 carbon cluster isomers. *Chem. Phys. Lett.* 2015;629: 76–80.
32. Bolboacă SD, Jäntschi L. Nanoquantitative structure-property relationship modeling on C_{42} fullerene isomers. *J. Chem.* 2016;2016: 1791756.
33. Sánchez-Bernabe FJ. Towards a periodic pattern in classical and nonclassical fullerenes with tetrahedral structure. *Materials Physics and Mechanics.* 2020;45(1): 79–86.
34. Melker AI. Isomers and isotopes of carbon. *Materials Physics and Mechanics.* 2020;45(1): 159–156.
35. Melker AI, Krupina MA. How the periodic table of fullerenes was born. *Nonlinear Dynamics and Applications.* 2022;28: 200–209.
36. Melker AI, Krupina MA. It's a long, long way to the periodic tables of fullerenes. *Perspective Materials.* 2023;10: 154–240. (In Russian)
37. Melker AI, Matvienko AN. Natural isomers of fullerenes from C_4 to C_{20}. *Materials Physics and Mechanics.* 2020;45(1): 38–48.
38. Melker AI, Matvienko AN. Natural isomers of fullerenes from C_{20} to C_{28}. *Materials Physics and Mechanics.* 2020;45(1): 49–59.
39. Melker AI, Matvienko AN. Natural isomers of fullerenes from C_{30} to C_{40}. *Materials Physics and Mechanics.* 2020;45(1): 60–78.

40. Melker AI, Krupina MA, Matvienko AN. Isomers of fullerenes from C_{50} to C_{56}. *Nonlinear Phenomena in Complex Systems*. 2023;26(1): 1–18.
41. Melker AI, Krupina MA, Matvienko AN. Isomers of fullerenes C_{58} and C_{60}. *Nonlinear Phenomena in Complex Systems*. 2024;27(2): 163–184.
42. Melker AI, Krupina MA, Matvienko AN. Nucleation and growth having three-fold T-symmetry. *Frontier Materials and Technologies*. 2022;2: 383–394.
43. Melker AI, Krupina MA, Matvienko AN, Nucleation and growth of fullerenes and nanotubes having four-fold symmetry. *Materials Physics and Mechanics*. 2021;47(1): 315–343.
44. Melker AI, Krupina MA, Matvienko AN, Nucleation and growth of fullerenes and nanotubes having five-fold symmetry. *Materials Physics and Mechanics*. 2022;49(1): 51–72.
45. Sverdlov LM, Kovner MA. Krainov EP. *Vibration Spectra of Many-Atomic Molecules*. Moscow: Nauka; 1970. (In Russian)
46. Hanwell MD, Curtis DE, Lonie DC, Vandermeersch T, Zurek E, Hutchison GR. Avogadro: an advanced semantic chemical editor, visualization, and analysis platform. *Journal of Cheminformatics*. 2012;4: 17
47. Murrell JN, Kettle SFA, Tedder JM. *Valence Theory*. London: John Wily & Sons; 1965.
48. Cross L, Mohn F, Moll N, Schuler B, Criado A, Guitián E, Peña, Gourdon A, Meyer G. Bond-order discrimination by atomic force microscopy. *Science*. 2012;337(6100): 1326-1329.
49. Gillespie RJ. *Molecular Geometry*. London: Van Nostrand Reinhold Co; 1972.
50. Kosevich AM, *Physical Mechanics of Real Crystals*. Kiev: Naukova Dumka; 1981. (In Russian)
51. Melker AI, *Dynamics of Condensed Matter*, *Vol. 3*, *Noophysics (Science and Scientists)*. St. Petersburg: St. Petersburg Academy of Sciences on Strength Problems; 2006. (In Russian)
52. Prokhorov AM. (Ed.) *Mathematical Encyclopedic Dictionary*. Moscow: Soviet Encyclopedia; 1988. (In Russian).
53. Muschelisvili NI. *Some Main Problems of the Mathematical Theory of Elasticity*. Moscow: Nauka; 1966. (In Russian)
54. Timoshenko SP. *History of Srength of Materials*. New York: McGraw-Hill; 1953.

About Authors

Alexander I. Melker Sc
Doctor of Physical and Mathematical Sciences
Professor (St. Petersburg Academy of Sciences on Strength Problems, St. Petersburg, Russia)

Maria A. Krupina iD Sc
Candidate of Physical and Mathematical Sciences
Associate Professor (Peter the Great St. Petersburg Polytechnic University, St. Petersburg, Russia)

MATERIALS PHYSICS AND MECHANICS RESEARCH ARTICLE

Submitted: October 15, 2024 Revised: November 5, 2024 Accepted: November 30, 2024

Changing symmetry during the growth of fullerenes originated from the nuclei of six-fold symmetry

A.I. Melker [1] ✉, **M.A. Krupina** [2], **E.O. Zabrodkin** [2]

[1] St. Petersburg Academy of Sciences on Strength Problems, St. Petersburg, Russia

[2] Peter the Great St. Petersburg Polytechnic University, St. Petersburg, Russia

✉ ndtcs@inbox.ru

ABSTRACT

The possible ways of generation and growing the fullerenes having at first six-fold symmetry has been studied. Beginning with a hexagonal prism (elementary fullerene C_{12}), six-cornered barrel-shaped fullerene C_{24} and high six-cornered barrel-shaped fullerene C_{36}, we obtained their direct descendants throw the use of Endo-Kroto's mechanism known as embedding carbon dimers. We have calculated the energies of the possible fullerenes and discussed possible reasons of their dependence on a fullerene size and shape.

KEYWORDS

carbon • center of curvature concentration • energy • fullerene • fusion reaction • graph representation periodic system • single and double bonds • symmetry

Citation: Melker AI, Krupina MA, Zabrodkin EO. Changing symmetry during the growth of fullerenes originated from the nuclei of six-fold symmetry. *Materials Physics and Mechanics*. 2024;52(5): 148–160. http://dx.doi.org/10.18149/MPM.5252024_14

Introduction

A fullerene is a molecule of carbon in the form of a hollow sphere, ellipsoid, tube, and many other shapes. The suffix "-ene" indicates that each carbon atom is covalently bounded to three others instead of the maximum of four. Fullerenes were conjectured more than fifty years ago independently in 1970 and 1973 [1–3]. They were discovered by mass spectrometry in 1985 [4], through laser evaporation of graphite in 1992 [5]. The discovery of fullerenes greatly expanded the number of known allotropes of carbon, which had previously been limited to graphite, diamond and amorphous carbon. From that time on the fullerenes have been the subjects of intense research, both for their chemistry and for their technological applications, especially in materials science, electronic, and nanotechnology. Nanostructure carbon, having many isomers, offers a great number of applications [6]. However, up to this point there is no clear and unique theory of fullerene growth, and therefore there is no standard way of obtaining desirable fullerene structures. The studies of fullerenes, in particular fullerene isomers, reflect only partial ways of their formation and have little in common; they are non universal [7–25].

The appearance of the periodic table of fullerenes [26] has changed the strategy of investigation: phenomenological approach to fullerenes was replaced by task-oriented activity. The periodic system of fullerenes gives a base for rigorous fullerene classification. It consists of horizontal series and vertical columns; they include fullerenes from C_{14} to C_{108}. The horizontal series form the Δn periodicities, where the fullerene structure changes from three-fold symmetry to six-fold through four and five ones. The vertical columns (groups) include the fullerenes of one and the same symmetry, the mass difference Δm for each column being equal to a double degree of symmetry.

On the base of periodic system, we have systemized possible ways of fullerene growth. It turned out that there are three the most natural types of growth mechanism [27]:

1. Endo-Kroto: embedding carbon dimers into the hexagons of initial fullerenes;
2. Melker-Vorobyeva: fusion of the carbon cupolas having the same symmetry;
3. Melker-Krupina: fusion of fullerenes having compatible symmetry.

The first mechanism creates both perfect and imperfect fullerenes; the second and third mechanisms do only perfect fullerenes.

Up to now we have considered so called "vertical growth" of fullerenes when a growing object conserves its symmetry, ordinary or topological. It resembles the growth of coniferous trees. Contrary to them deciduous trees grow sometimes in such manner that one of side branches begin to prevail over the main one. We have assumed that such situation was also possible for some fullerenes. In doing so, a fullerene is changing its symmetry, e.g., fullerene C_{44} having two-fold symmetry has transformed into fullerene C_{60} of six-fold symmetry.

To gain a better understanding of that phenomenon, we have decided to study it from the very beginning.

Elementary fullerene C_{12}

As was shown earlier [26–31], folding a plain cluster C_6C_6 produces a hexagonal prism of six-fold symmetry which may be thought over as an elementary fullerene C_{12}. Several electronic configurations are presented in Fig. 1. Here and below, we use area-colored graphs because they gain a better understanding of the structures. In our case, six areas of the prisms are tetragons, and they are grey painted, two areas are hexagons; they are yellow painted.

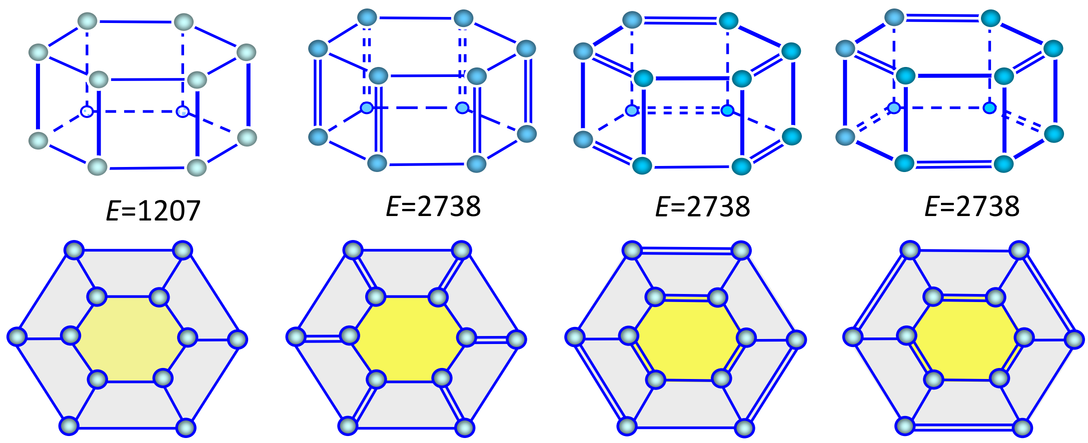

Fig. 1. Hexagonal prisms formed from clusters: structure and graphs; *E* is energy, kJ/mol

Mechanism of growth

The process of changing symmetry was obtained [32] through the use of the mechanism known as "embedding carbon dimers," which was suggested by M. Endo and the Nobel Prize winner H.W. Kroto in 1992 [33]. According to it, a carbon dimer, colored goldish, embeds into a hexagon of an initial fullerene. This leads to stretching and breaking the covalent bonds which are normal to the dimer and to creating new bonds with the dimer. As a result, there arises a new atomic configuration and there is a mass increase of two carbon atoms (Fig. 2).

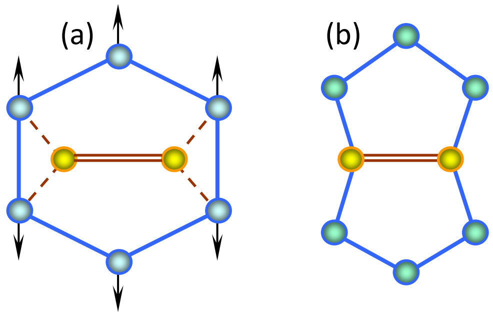

Fig. 2. Carbon dimer embedding into a hexagon (a) and forming two adjacent pentagons (b)

Growth of elementary fullerene C_{12}

The fullerenes produced during the growth of initial fullerene C_{12} through the use of the Endo-Kroto mechanism are illustrated in Figs. 3–7. Here the dimer embedding is made at the "frigid zone" near the axis of symmetry.

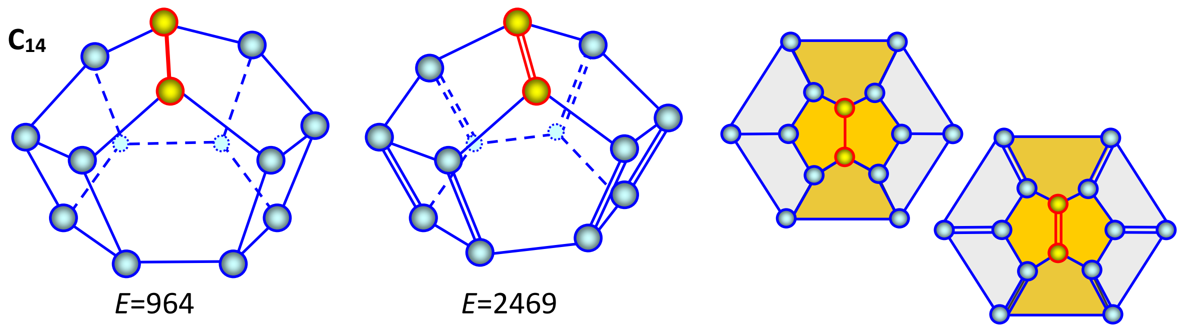

Fig. 3. Fullerene C_{14} as a result of a dimer embedding into a hexagonal prism; its graphs and energy E (kJ/mol)

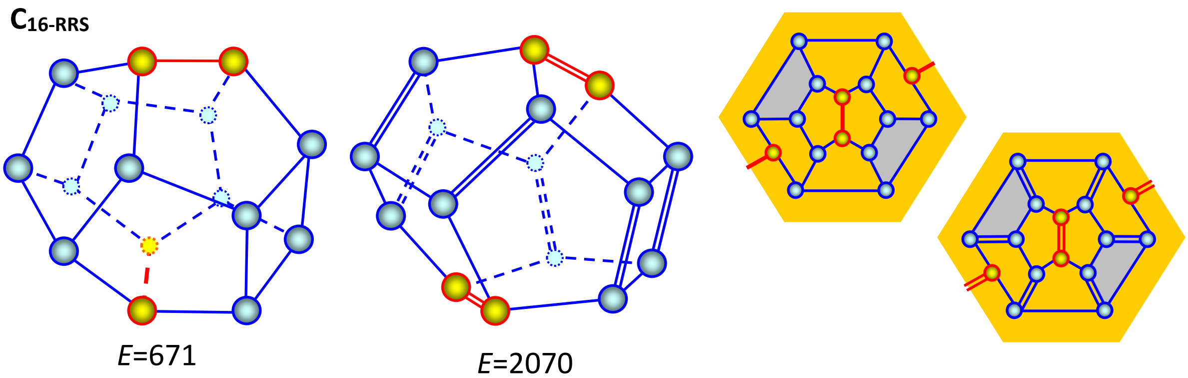

Fig. 4. Fullerene C_{16} produced by rotation-reflection-symmetry embedding two dimers into a hexagonal prism; its graphs and energy E (kJ/mol)

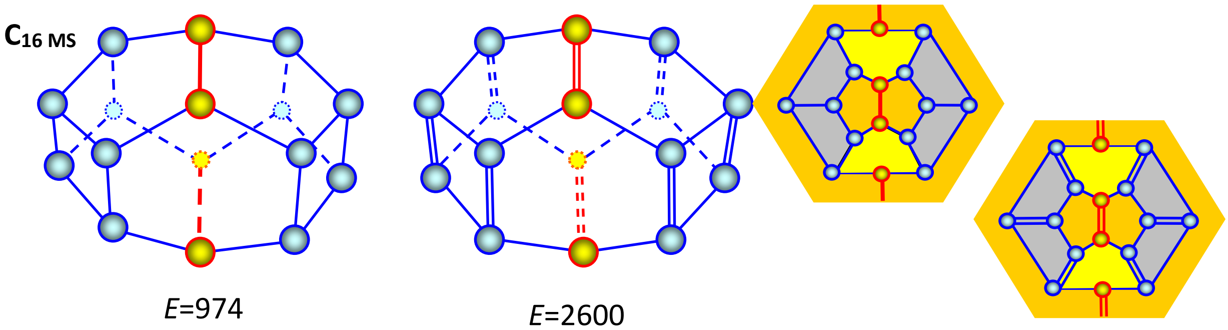

Fig. 5. Fullerene C_{16} produced by mirror-symmetry embedding two dimers into a hexagonal prism; its graphs and energy *E* (kJ/mol)

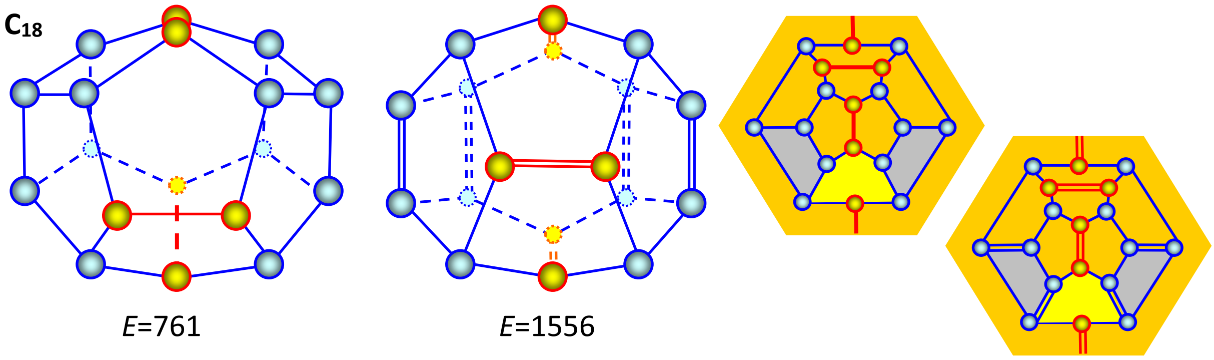

Fig. 6. Fullerene C_{18} as a result of three-dimers embedding into a hexagonal prism; its graphs and *E* (kJ/mol)

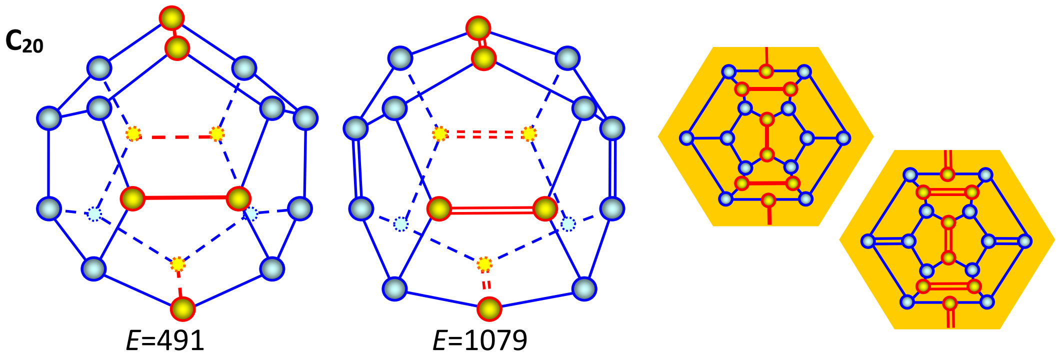

Fig. 7. Fullerene C_{20} as a result of four-dimers embedding into a hexagonal prism; its graphs and energy *E* (kJ/mol)

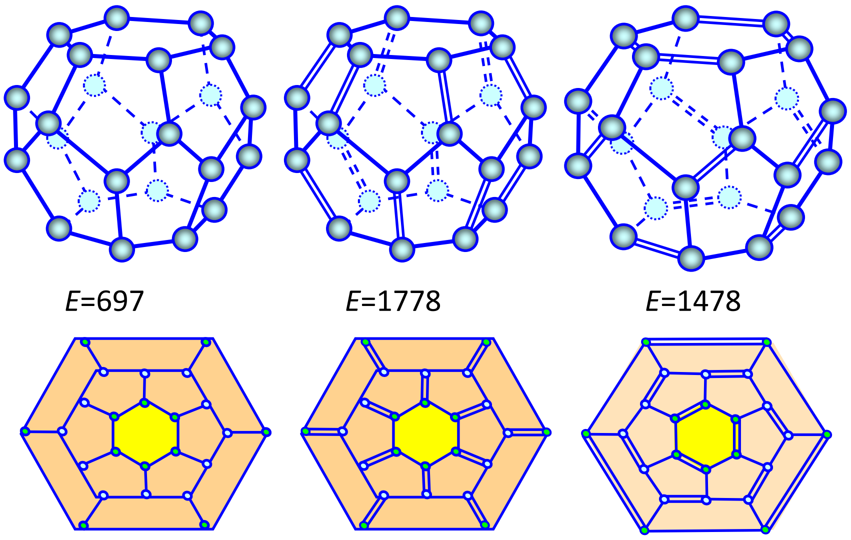

Fig. 8. Six-cornered barrel-shaped fullerene C_{24} as a result of prisms fusion; its graphs and energy *E* (kJ/mol)

Six-cornered barrel-shaped fullerene C_{24}

As was shown earlier [26], fusion of two prisms with conserving their symmetry produces a fullerene which shape resembles a six-cornered barrel. The structure of several electronic isomers is shown in Fig. 8; the structure and graph areas are painted as before in different colors.

Growth of six-cornered barrel-shaped fullerene C_{24}

The fullerenes C_{26} – C_{36} produced from the initial fullerene C_{24} through the use of the Endo-Kroto mechanism are illustrated in Fig. 9.

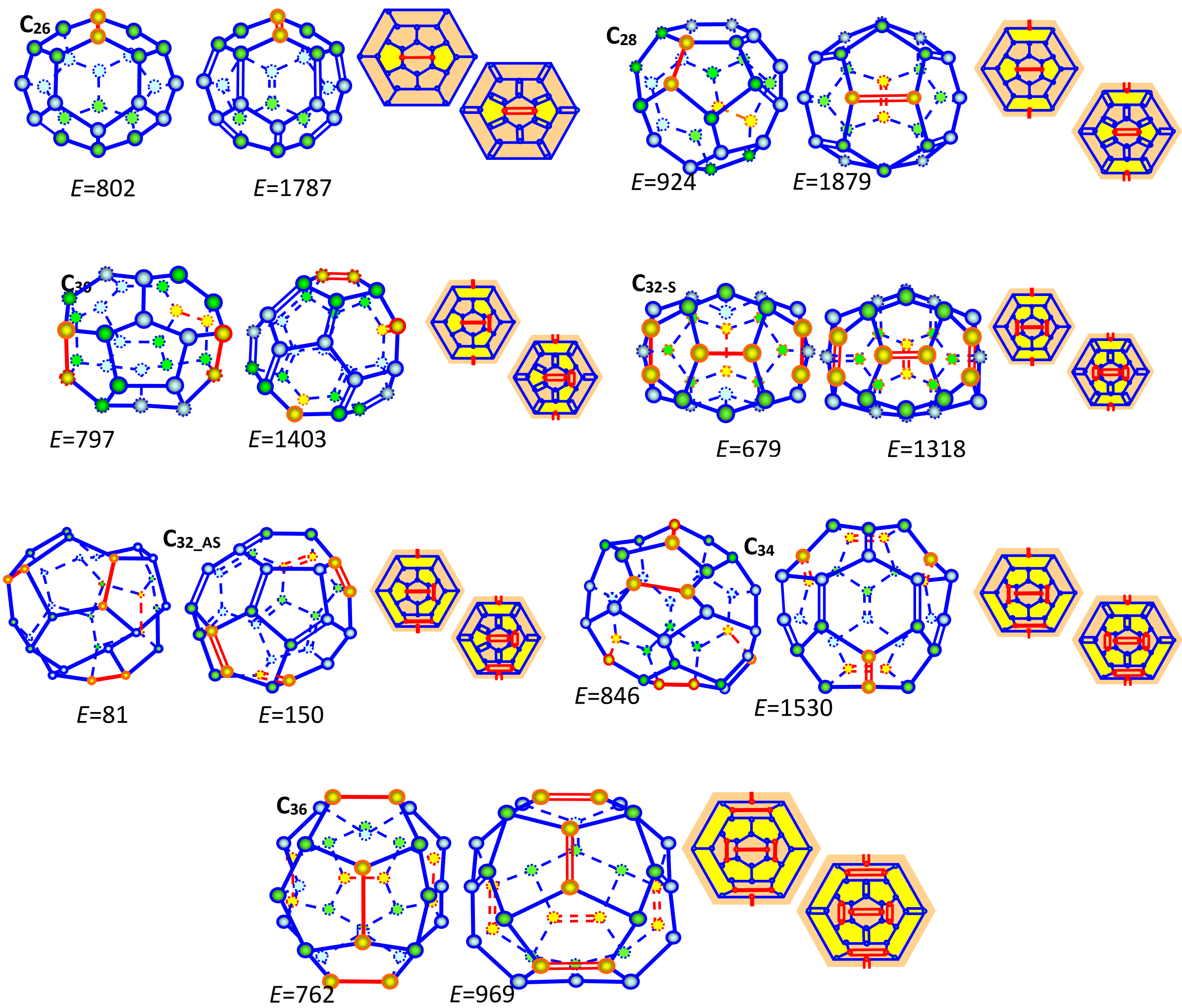

Fig. 9. Dimer embedding into fullerene C_{24}; graphs and energy in kJ/mol of C_{26}

High-six-cornered barrel-shaped fullerene C_{36}

As was shown earlier [26], fusion of two prisms with conserving their symmetry produces a fullerene which shape resembles a six-cornered barrel. The structure of several electronic isomers is shown in Fig. 10; the structure and graph areas are painted as before in different colors.

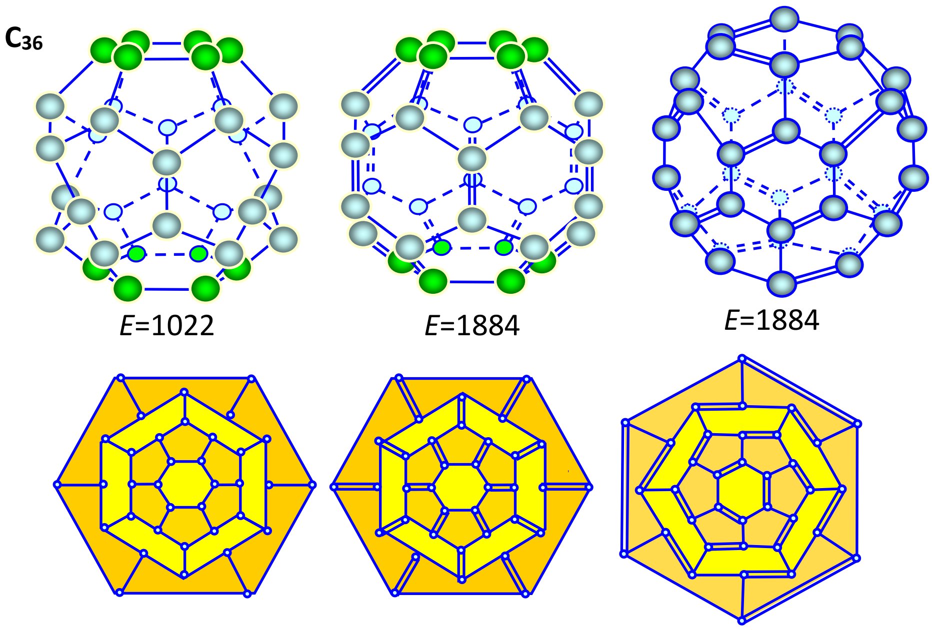

Fig. 10. Joining fullerene C_{24} with prism C_{12}; structure, graphs and energy *E* (kJ/mol)

Growth of high-six-cornered barrel-shaped fullerene C_{36}

The fullerenes produced during the growth of initial fullerene C_{36} through the use of the Endo-Kroto mechanism are illustrated in Fig. 11.

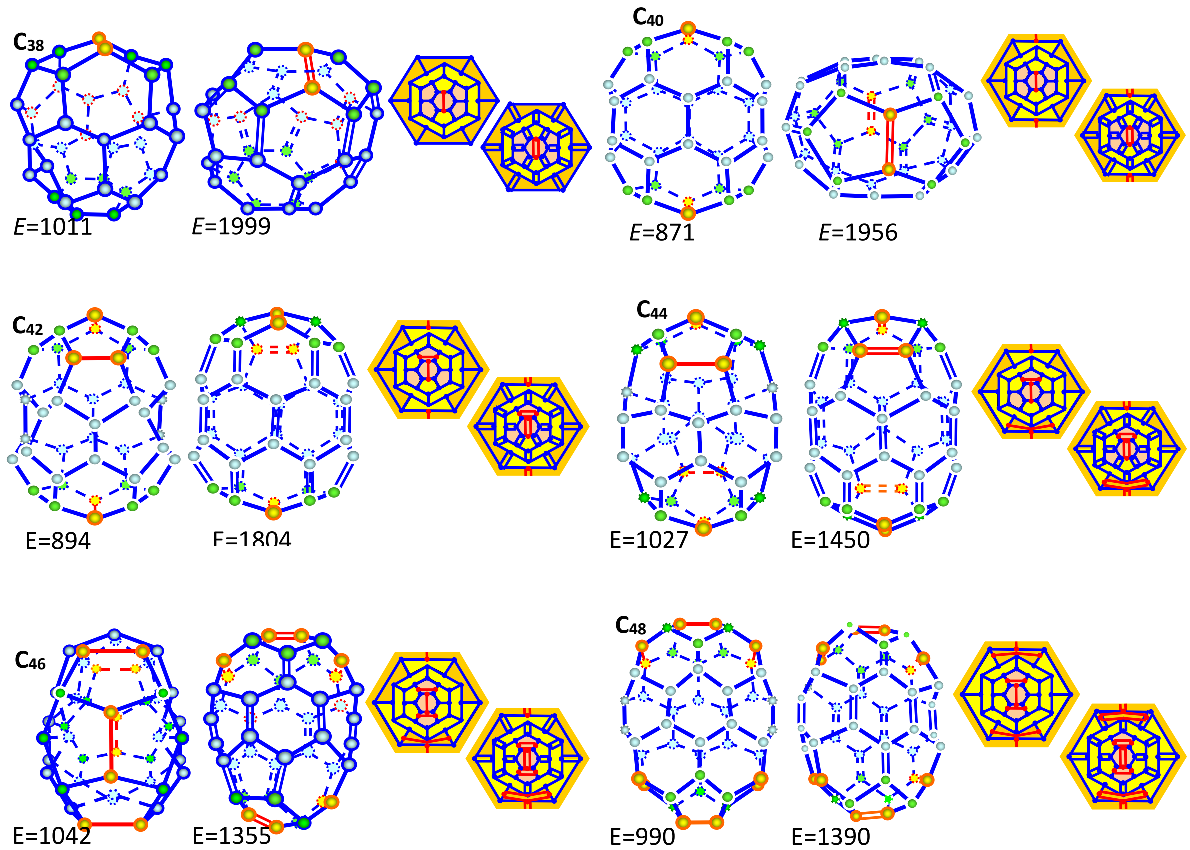

Fig. 11. Fullerenes produced by embedding carbon dimers into a fullerene C_{28}; their graphs and energy *E* (kJ/mol)

Summary

We have studied possible ways of generation and growing the fullerenes having at first six-fold symmetry. Beginning with a hexagonal prism (elementary fullerene C_{12}), six-cornered barrel-shaped fullerene C_{24} and high six-cornered barrel-shaped fullerene C_{36}, we obtained their direct descendants throw the use of Endo-Kroto's mechanism known ad embedding carbon dimers. We have calculated the structure and energy of the possible fullerenes.

In Tables 1, the calculated energies of fullerenes are presented, for fullerenes with single bonds only and single and double bonds.

Table 1. Energy of fullerenes in kJ/mol as a function of fullerene size and shape

Fullerenes	Single	Single+double
C_{12}	1207	2738
C_{14}	964	2469
$C_{16\ rrs}$	671	2070
$C_{16\ ms}$	(974)	(2600)
C_{18}	761	1556
C_{20}	491	1079
C_{24}	697	1778
C_{26}	802	1787
C_{28}	924	1879
C_{30}	787	1403
$C_{32\ s}$	679	1318
$C_{32\ as}$	817	1507
C_{34}	841	1530
C_{36}	762	969
C_{36}	1022	1884
C_{38}	1011	1999
C_{40}	871	1956
C_{42}	894	1804
C_{44}	1027	1450
C_{46}	1042	1355
C_{48}	990	1390

Continuity and discontinuity. Curvature of fullerenes

These notions are connected with the Ionic and Pythagorean schools of philosophy (VI-IV century B.C.) [34]. Plato of Athens (Πλατων, 427 B.C.) has tried to combine both notions, putting five forms of matter (fire, air, earth, water, ether) into consistency to five regular polyhedra (tetrahedron, octahedron, cube, icosahedron, dodecahedron). According to Aristotle every thing is the unity of matter and form (*η ϋλη καί τό είδος*); the form being an active element produces movement [34].

In mathematics, there are such notions as curvature, tensor of curvature [35]. The curvature is defined as the quantity which characterizes a deviation of a surface from a plane at a given point. The latter is defined in the following manner. Through the normal at a given point of surface all the possible planes are drawn. The sections of the surface by these planes are called normal sections, the curvatures of normal sections being normal curvatures of the surface at a given point. Maximum and minimum curvatures are called principal curvatures. Their combinations give Gauss and average curvatures which are used for analysis of the surface curvature.

We will follow to Aristotle trying finding such parts of fullerene's shape, which define surface curvature of a fullerene. In other words, we will search first of all "space fragments of curvature", but not a curvature value. Further we will use the following notions: curvature as a continuity property and curvature fragments as discontinuity. Analysis of the fullerene structures shown before allows us to separate the following curvature fragments (Fig. 12). It should be emphasized that an isolated fragment CF-6 does not creates curvature; it becomes a curvature fragment under the influence of surroundings. Different curvature fragments have their own symmetry. We name their center of symmetry "curvature concentration center" (CCC).

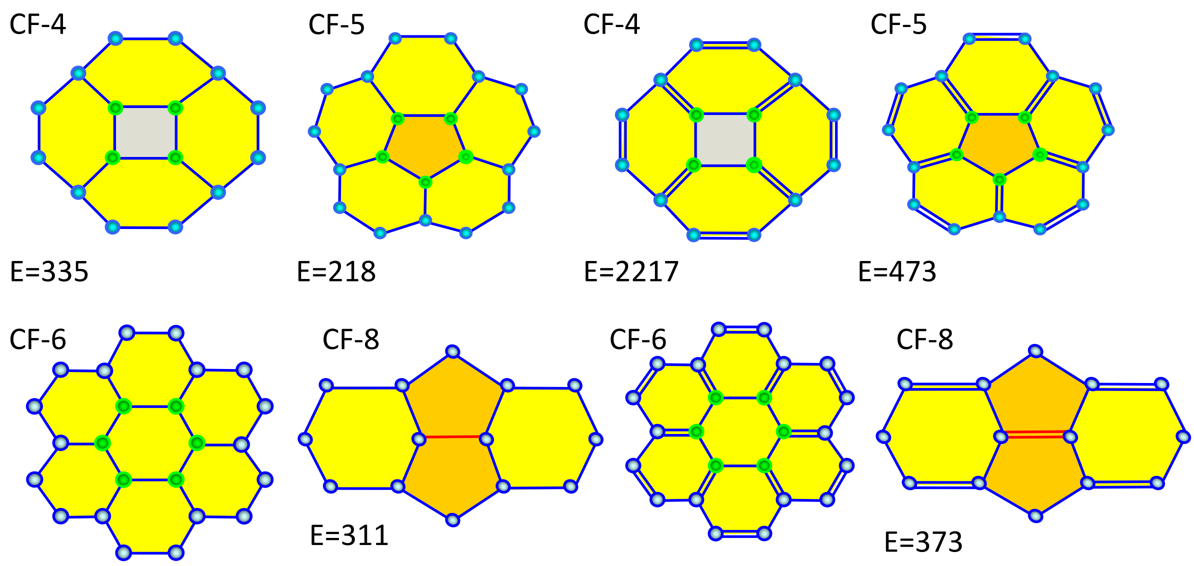

Fig. 12. Curvature fragments of fullerenes

In mathematics [35], surface is introduced as a bit of plane subjected to continuous deformations (tension, compression, bending). In its turn, curvature is defined as the quantity which characterizes a deviation of a surface from a plane at a given point. In mechanics [36] for characteristics of deformation one introduces tensor of strain, which diagonal elements characterize volume change; non-diagonal elements show the change of a form. If stress is a function of strain in each point of continuum, such continuum is said to be an elastic body. In a simple case, the function which connects strain and stress is Hooke's law.

We assume that in fullerenes the curvature concentration centers are strain centers and since strain is connected with stress, they are centers of stress concentration. Therefore the energy of a fullerene consists of two parts: chemical energy of formation and strain energy of construction.

Now we are able to understand and explain the dependence of fullerene energy on size and shape (Fig. 13). The study of the CCC arrangement for the family of fullerene C_{12} has given the following picture (Figs. 14,15). Fullerenes with single bonds relax through the transformation of plane hexagons into chair or boat conformation and so their energy has incorporated only a small part of strain energy. Fullerenes with single and double bonds are more rigid constructions, and here the contribution of strain energy is high.

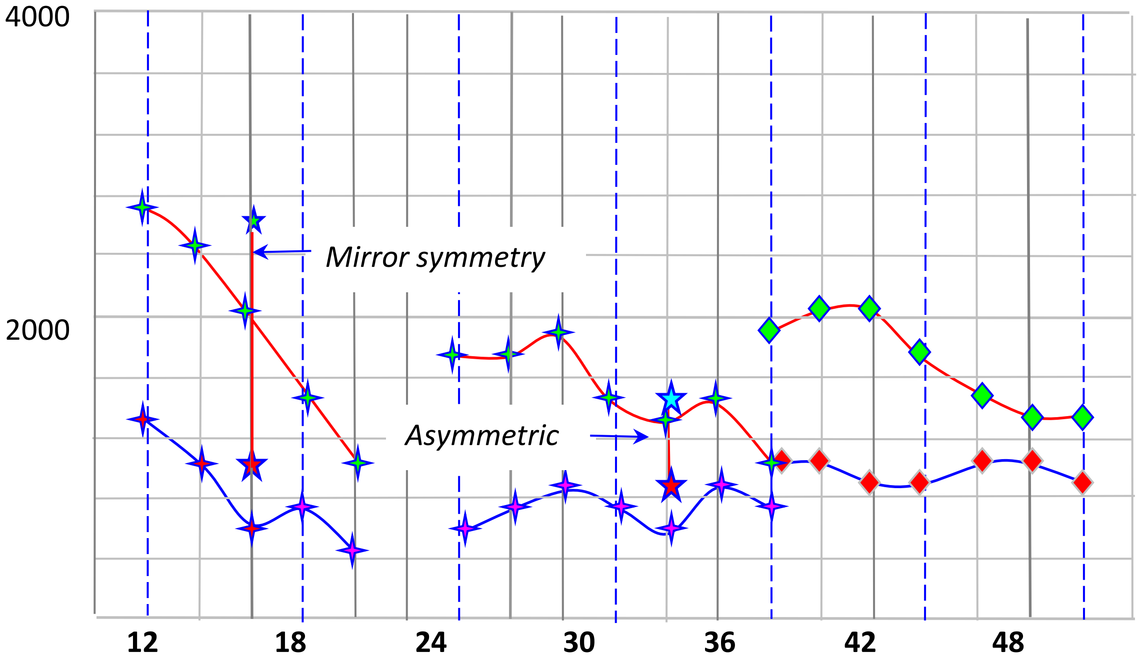

Fig. 13. Energy of fullerenes in kJ/mol as a function of fullerene size and shape

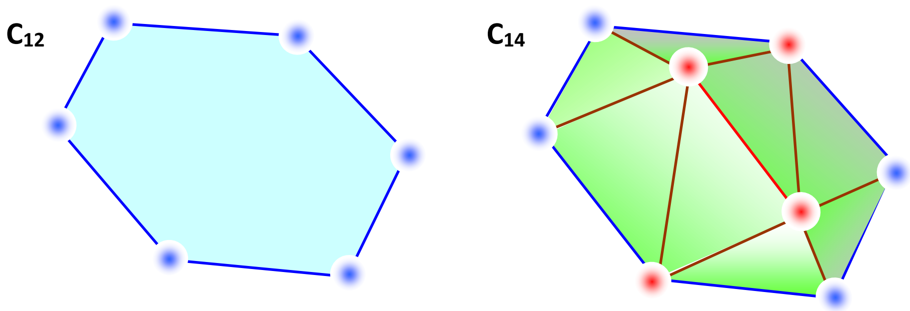

Fig. 14. Frames of CCC (curvature concentration centers) of fullerenes C_{12} and C_{14}

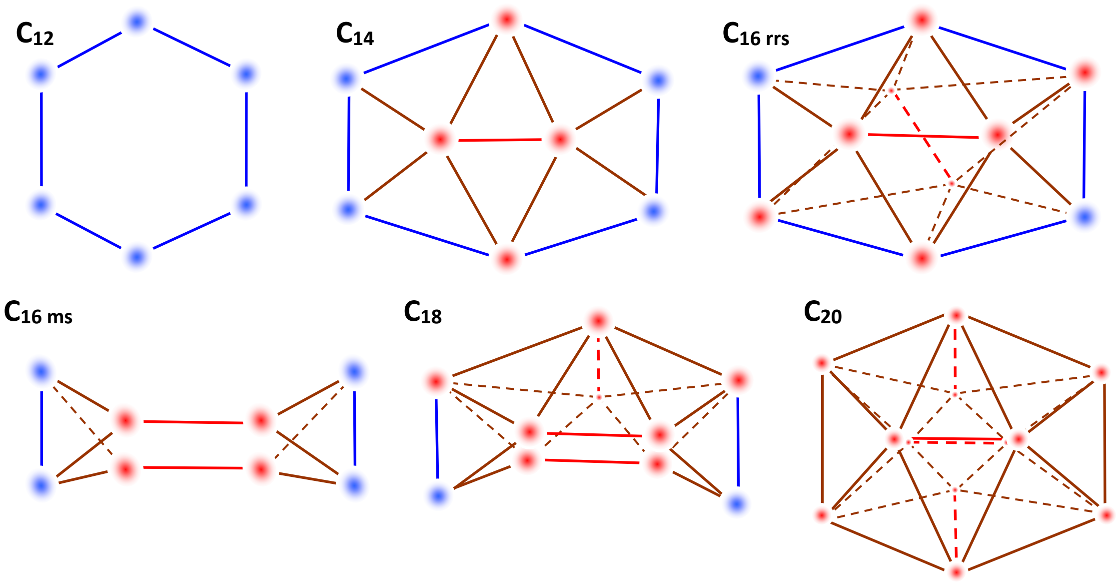

Fig. 15. Graphs of CCC (curvature concentration centers) for family C_{12}

It is worth noting some facts. The most energy (and therefore the most stress state) is characteristic for fullerenes which curvature concentration centers (CCC) compose plane hexagons. The least energy (and therefore the least stress state) refers to those having CCC in the form of an icosahedron. It must be remembered that the fullerene, creating such CCC, is a dodecahedron, an icosahedron and dodecahedron being dual.

Fullerene C_{16} ms has a larger energy in comparison with fullerene C_{16} rrs. Probably this phenomenon is associated with the fact that mirror symmetry doesn't create, as rotation reflection symmetry, a compact structure of CCC where the centers of stress concentration are compensated.

In a similar manner it is possible to explain the dependence of fullerene energy on size and shape for families C_{24} and C_{36}, if to design the structure of their CCC (Figs. 16–19). The local maxima of energy correspond to loose or asymmetric CCC structures; the local minima refer to compact ones.

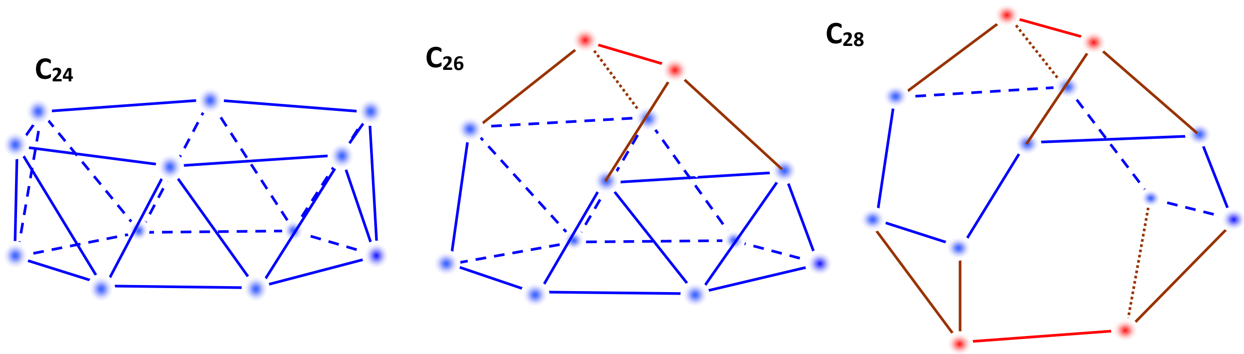

Fig. 16. Frames of CCC (curvature concentration centers) for fullerenes C_{24}, C_{26} and C_{28}

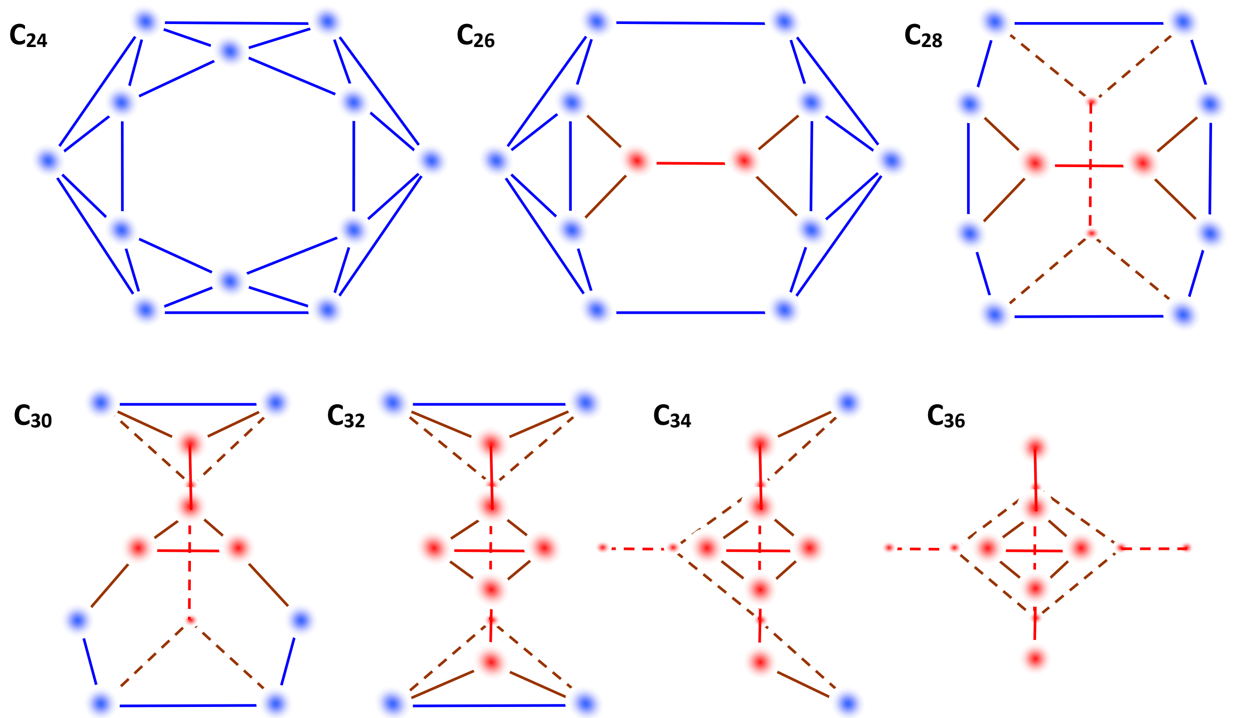

Fig. 17. Graphs of CCC (curvature concentration centers) for family of C_{24}

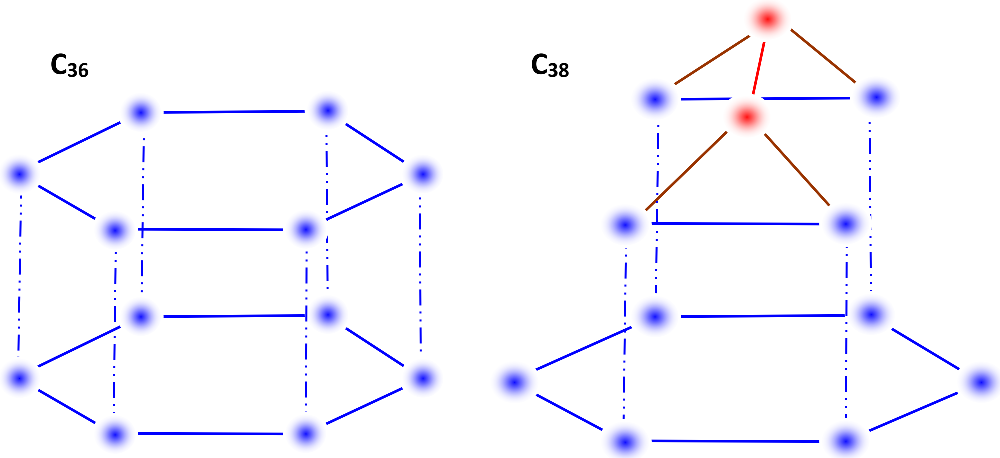

Fig. 18. Frames of CCC (curvature concentration centers) of fullerenes C_{36} and C_{38}

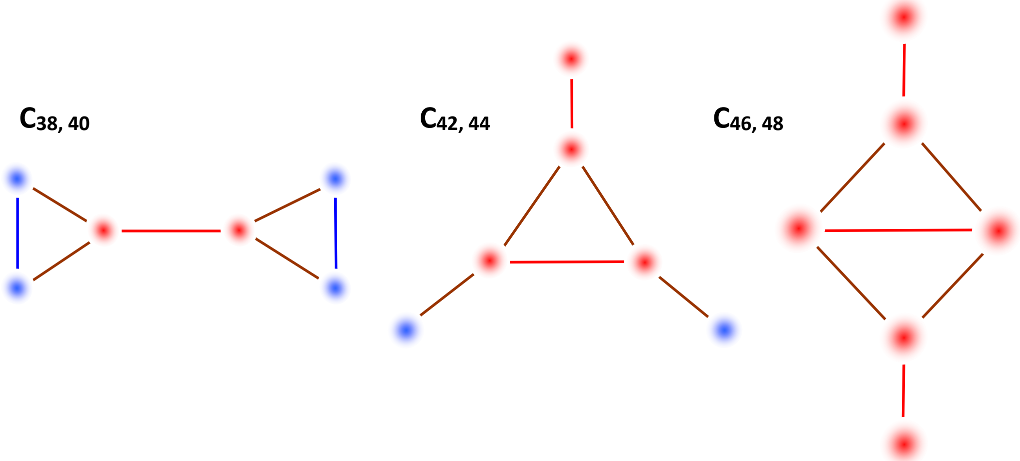

Fig. 19. Graphs of CCC (curvature concentration centers) for family of C_{26}
(only a half is shown; the second half is symmetric)

The fullerene shape is a result of self-organization and here there are possible several types of curvature. During the growth old CCC-s disappear, new CCC-s are generated, but the number of CCC-s remains constant for each family.

Future investigations

We assume that first of all it is necessary to find the curvature concentration centers. In doing so, we gain the arrangement of stress concentration, can apply the elasticity theory not only to the fullerenes (this task is very cumbersome) but to the polyhedrons of curvature concentration centers (the task is easier). Moreover, the energy of fullerenes can be considered not only as a global quantity, but as a surface distribution. Since the CCC polyhedrons resemble crystals, and the crystals are studied for years [37], we can use this knowledge for understanding such processes as, e.g. sublimation, fracture of fullerenes. As a result, we would be able to gain more profound insight into their nature.

References

1. Osawa E. Superarmacity. *Kagaku (Chemistry)* 1970;25: 854–863.
2. Bochvar DA, Gal'perin EG. Electronic structure of the molecules C20 and C60. *Proc Acad Sci SSSR* 1973;209: 239–241.
3. Stankevich I, Nikerov M, Bochvar D. Structural chemistry of crystalline carbon: geometry< stability, electronic spectrum. *Russ Chem Rev* 1984;53: 640–645.
4. Kroto HW, Hearth JR, O'Brien SC, Curl RF. Smalley RE, C60: Buckminsterfullerene. *Nature.* 1985;318: 162–163.
5. Kroto HW. C60: Buckminsterfullerene, the celestial sphere that fell to earth. *Angew Chem Int Ed.* 1992;31(2): 111–129.
6. Benedek G, Milani P, Ralchenko VG. *Nanostructured Carbon for Advanced Applications*. Dordrecht; Kluwer Academic Publishers; 2001.
7. Austin S, Fowler P, Hansen P, Monolopolus D, Zheng M. Fullerene isomers of C60. Kekulé counts vesus stability. *Chem Phys Lett.* 1994;228(4–5): 478–484.
8. Kirby E, Pisanski T. Aspect of topology, genus and isomerism in closed 3-valent networks. *J Math Chem.* 1998;23: 151–167.
9. Astakhova TY, Vinogradov GA. New isomerization operations for fullerene graphs. *J Mol Struct THEOCHEM.* 1998;430: 259–268.
10. Chen Z, Jiao H, Bühl M, Hirsch A, Thiel W. Theoretical investigation into structures and magnetic properties of smaller fullerenes and their heteroanalogues. *Theor. Chem. Acc.* 2001;106: 352–363.
11. Tagmatarchis N, Okada K, Tomiyama T, Kobayashi Y, Shinohara H. A catalytic synthesis and structural characterization of a new [84] fullerene isomer. *Chem. Commun.* 2001;15: 1366–1367.
12. Xu L, Cai W, Shao X. Prediction of low-energy isomers of large fullerenes from C132 to C160. *J Phys Chem A.* 2006;110: 9247–9253.
13. Shao N, Gao Y, Yoo S, An W, Zeng XC. Search for low-energy fullerenes: C98 to C110. *J Phys Chem A.* 2006;110(24): 7672–7676.
14. Shao N, Gao Y, Zeng XC. Search for low-energy fullerenes 2: C38 to C80 and C112 to C120. *J Phys Chem A.* 2007;111(48): 17671–17677.
15. Slanina Z, Uhlik F, Zhao X, Adamovich L, Nagase S. Relative stability of C74 isomers. *Fuller Nanotub Carbon Nanostruct.* 2007;15(3): 195–205.
16. Malolepsza E, Lee Y, Witek HA, Irle S, Lin C, Hsieh H, Comparison of geometric, electronic, and vibrational properties for all pentagon/hexagon-bearing isomers of fullerenes C38, C40, and C42. *Int. J. Quantum Chem.* 2009;109(9): 1999–2001.
17. Zhang H, Ye D, Lui Y. A combination of Clar number and Kekulé count as an indicator of relative stability of fullerene isomers of C60. *J Math Chem.* 2010;48: 733–740.
18. An J, Gan LH, Zhao JQ, Li R. A global search for the lowest energy isomer of C26. *J Chem Phys.* 2010;132(5): 154304.
19. Khamatgalimov AR, Kovalenko VI. Electronic structure and stability of fullerene C80 IPR isomer. *Fuller Nanotub Carbon Nanostruct.* 2011;19(7): 599–604.
20. Fedorov AS, Fedorov DA, Kuzubov AA, Avramov PV, Nishimura Y, Irle S, Witek HA. Relative isomer abundance of fullerenes and carbon nanotubes correlates with kinetic stability. *Phys Rev Lett.* 2011;107: 175506.
21. Gerasimov VI, Trofimov A, Proskurina O. Isomers of fullerene C60. *Materials Physics and Mechanics.* 2014;20(1): 25–32.
22. Jin Y, Perera A, Lotrich VF, Bartlett RJ. Couple cluster geometries and energies of C20 carbon cluster isomers. *Chem. Phys. Lett.* 2015;629: 76–80.
23. Schwerdtfeger P, Wirz LN, Avery J. The topology of fullerenes. *WIREs Comput. Mol. Sci.* 2015;5(1): 96–145.
24. Bolboacă SD, Jäntschi L. Nanoquantitative structure-property relationship modeling on C_{42} fullerene isomers. *J. Chem.* 2016;2016: 1791756.
25. Sánchez-Bernabe FJ. Towards a periodic pattern in classical and nonclassical fullerenes with tetrahedral structure. *Materials Physics and Mechanics*. 2020;45(1): 79–86.
26. Melker AI, Krupina MA. It's a long, long way to the periodic tables of fullerenes. *Perspective Materials.* 2023;10: 154–240. (In Russian)
27. Melker AI, Matvienko AN. Natural isomers of fullerenes from C_{20} to C_{28}. *Materials Physics and Mechanics*. 2020;45(1): 49–59.
28. Melker AI, Krupina MA, Matvienko AN, Nucleation and growth of fullerenes and nanotubes having four-fold symmetry. *Materials Physics and Mechanics.* 2021;47(1): 315–343.

29. Melker AI, Krupina MA, Matvienko AN. Nucleation and growth having three-fold T-symmetry. *Frontier Materials and Technologies.* 2022;2: 383–394.
30. Melker AI, Krupina MA, Matvienko AN, Nucleation and growth of fullerenes and nanotubes having five-fold symmetry. *Materials Physics and Mechanics.* 2022;49(1): 51–72.
31. Melker AI, Krupina MA, Matvienko AN. Isomers of fullerenes from C_{50} to C_{56}. *Nonlinear Phenomena in Complex Systems.* 2023;26(1): 1–18.
32. Melker AI, Krupina MA, Matvienko AN. Isomers of fullerenes C_{58} and C_{60}. *Nonlinear Phenomena in Complex Systems.* 2024;27(2): 163–184.
33. Endo M. Kroto HW. Formation of carbon nanofibers. *J. Phys. Chem.* 1992;96(17): 6941–6944
34. Melker AI, *Dynamics of Condensed Matter*, *Vol. 3*, *Noophysics (Science and Scientists).* St. Petersburg: St. Petersburg Academy of Sciences on Strength Problems; 2006. (In Russian)
35. Prokhorov AM. (Ed.) *Mathematical Encyclopedic Dictionary.* Moscow: Soviet Encyclopedia; 1988. (In Russian).
36. Muschelisvili NI. *Some Main Problems of the Mathematical Theory of Elasticity.* Moscow: Nauka; 1966. (In Russian)
37. Timoshenko SP. *History of Strength of Materials.* New York: McGraw-Hill; 1953.

About Authors

Alexander I. Melker Sc
Doctor of Physical and Mathematical Sciences
Professor (St. Petersburg Academy of Sciences on Strength Problems, St. Petersburg, Russia)

Maria A. Krupina Sc
Candidate of Physical and Mathematical Sciences
Associate Professor (Peter the Great St. Petersburg Polytechnic University, St. Petersburg, Russia)

Egor O. Zabrodkin
Master Student (Peter the Great St. Petersburg Polytechnic University, St. Petersburg, Russia)

МЕХАНИКА И ФИЗИКА МАТЕРИАЛОВ

52 (5) 2024

Учредители: Санкт-Петербургский политехнический университет Петра Великого,

Институт проблем Машиноведения Российской академии наук

Издание зарегистрировано федеральной службой по надзору в сфере связи, информационных технологий и массовых коммуникаций (РОСКОМНАДЗОР), свидетельство ПИ №ФС77-69287 от 06.04.2017 г.

Телефон редакции

+7(812)552 77 78, доб. 224

E-mail: mpmjournal@spbstu.ru

Компьютерная верстка Л.И. Гузилова

Подписано в печать 10.12.2024 г. Формат 60x84/8. Печать цифровая
Усл. печ. л. 10,0. Тираж 100. Заказ____.

Отпечатано с готового оригинал-макета, предоставленного автором
в Издательско-полиграфическом центре Политехнического университета Петра Великого. 195251, Санкт-Петербург, Политехническая ул., 29.
Тел.: +7(812)552 77 78, доб. 224.

MPM SCIENTIFIC JOURNAL

MPM, Vol. 52, No. 5, 2024